BEILSTEIN JOURNAL OF ORGANIC CHEMISTRY

Organic electron transport materials

Edited by Peter J. Skabara and Joseph Cameron

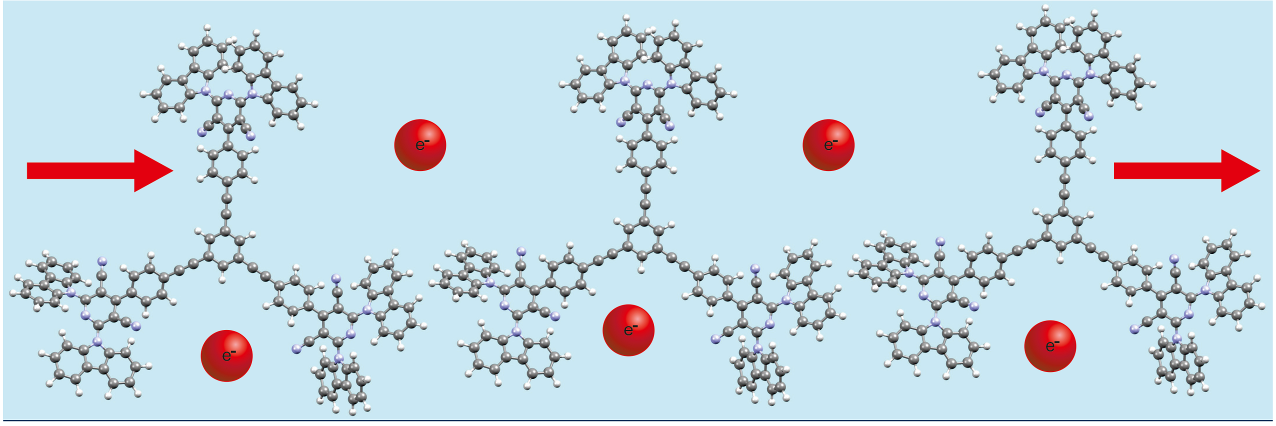

Imprint

Beilstein Journal of Organic Chemistry
www.bjoc.org
ISSN 1860-5397
Email: journals-support@beilstein-institut.de

The *Beilstein Journal of Organic Chemistry* is published by the Beilstein-Institut zur Förderung der Chemischen Wissenschaften.

Beilstein-Institut zur Förderung der
Chemischen Wissenschaften
Trakehner Straße 7–9
60487 Frankfurt am Main
Germany
www.beilstein-institut.de

BEILSTEIN JOURNAL OF ORGANIC CHEMISTRY

Organic electron transport materials

Joseph Cameron* and Peter J. Skabara*

Editorial

Address:
School of Chemistry, University of Glasgow, University Avenue,
Glasgow, G12 8QQ, UK

Email:
Joseph Cameron* - joseph.cameron@glasgow.ac.uk;
Peter J. Skabara* - peter.skabara@glasgow.ac.uk

* Corresponding author

Keywords:
acceptors; electron transport material; electron-deficient; n-type;
organic semiconductors

Beilstein J. Org. Chem. **2024,** *20,* 672–674.
https://doi.org/10.3762/bjoc.20.60

Received: 08 March 2024
Accepted: 21 March 2024
Published: 28 March 2024

This article is part of the thematic issue "Organic electron transport materials".

Associate Editor: P. J. Skabara

There has been much interest in developing electron transport materials for organic semiconductor devices due to their potential to be applied in various technologies. For example, such materials can be used to improve charge balance in the emissive layer of an organic light-emitting diode, charge extraction in perovskite solar cells or used as the semiconductor layer of n-type organic field-effect transistors.

Typically, an electron transport material should have a high electron mobility and a low-lying lowest unoccupied molecular orbital (LUMO) relative to vacuum. This is achieved by using electron-deficient units containing highly electronegative functionalities such as cyano groups [1]. This is one of the key advantages of organic electron transport materials compared with inorganic materials – the molecular structures can be easily tuned to achieve desired characteristics. The diversity of materials used as electron transport layers is also an advantage, meaning organic materials can be used effectively in a range of applications. For example, while a non-fullerene acceptor material might not be suitable as an electron transport layer in OPVs due to dissolution of layers, it can used in perovskite solar cells where it can be successfully deposited through orthogonal processing.

One of the biggest challenges with n-type materials is air stability. This is explained by the redox potentials of water (−0.66 V vs standard calomel electrode (SCE)) and oxygen (+0.024 V vs SCE, +0.57 V vs SCE) [2,3]. Therefore, it has been observed that once the overpotential required for these redox reactions to progress is taken into consideration, a lowest unoccupied molecular orbital (LUMO) energy ≤ -4.0 eV (relative to vacuum) is required for air stable electron transport materials [2] and this is a common target for researchers developing these types of materials. In general, this restriction also applies to n-dopants, compounds that reduce electron transport materials, which are important for increasing the electrical conductivity of n-type materials. However, there have been elegant solutions developed to counteract this, where air-stable dimers can be used which react with acceptors to produce reducing radical species, capable of reducing organic electron transport materials with a low electron affinity [4,5].

It is not only in modifying the molecular structure to improve the electron accepting ability that there is innovation in new organic electron transport materials. One of the potential benefits of organic semiconductors is the ability to use solution-processing techniques, which are more sustainable than thermal evaporation which is wasteful and requires high vacuum and temperature. Moreover, organic electron transport layers do not typically need treatment at the high temperatures required for metal oxide formation for example. However, making materials solution-processable can result in a trade-off in device performance and materials should be applicable to orthogonal processing to allow for solution-based fabrication of multilayer devices. Additionally, researchers should consider minimising the environmental footprint of the solvents and materials used in these processes. These challenges require novel approaches but there have already been some inspired works. For example, Wolfe et al. showed cathode interlayer materials can be developed to be soluble in ethyl acetate, a green solvent, and solution-processed for PM6:Y6 bulk-heterojunction solar cells with power conversion efficiency > 13% [6]. In addition to orthogonal processing, it has been shown that treatment with base [7] or photo-crosslinking [8] can insolubilise solution-processed layers and allow for the construction of efficient, solution-processed devices.

It is exciting to see how much of the work establishing n-type organic semiconductor materials for OFETs, for example, is now being applied to emerging technologies such as organic electrochemical transistors. In this case, materials might be modified with polar side chains [9], instead of the use of alkyl groups [10], and this allows for improved ion transport. A similar strategy has been used to improve the doping of n-type thermoelectric materials, where polar side chains on fullerene materials allow for better miscibility of the dopant [11] and therefore improved electrical conductivity. The overlap of desired characteristics for materials used in OECTs and organic thermoelectrics shows that there is a lot to be gained from the design of new electron transport materials.

Whilst there are challenges still to be overcome in developing materials for emerging technologies, researchers working on these issues should take inspiration from the rapid progress that was achieved in the development of non-fullerene acceptor materials as a replacement for $PC_{61}BM$ and $PC_{71}BM$ in organic solar cells which revitalised the research field as a result. This serves as a reminder that careful molecular design and thorough examination of the performance of electron transport materials can lead to unprecedented performance and move towards enabling important technologies.

We are delighted to act as guest editors for a collection of papers tackling many different aspects relating to organic electron transport materials from leaders across the world from this research community. We hope that these excellent works can act as inspiration for researchers looking to develop new materials or implement these in devices. We give our thanks to all the authors for their great contributions to this Thematic Issue and we thank the staff from the Beilstein-Institut for their support.

Joseph Cameron and Peter J. Skabara

Glasgow, March 2024

ORCID® iDs

Joseph Cameron - https://orcid.org/0000-0001-8622-8353
Peter J. Skabara - https://orcid.org/0000-0001-7319-0464

Data Availability Statement

Data sharing is not applicable as no new data was generated or analyzed in this study.

References

1. Leitonas, K.; Vigante, B.; Volyniuk, D.; Bucinskas, A.; Dimitrijevs, P.; Lapcinska, S.; Arsenyan, P.; Grazulevicius, J. V. *Beilstein J. Org. Chem.* **2023,** *19,* 1867–1880. doi:10.3762/bjoc.19.139
2. Griggs, S.; Marks, A.; Bristow, H.; McCulloch, I. *J. Mater. Chem. C* **2021,** *9,* 8099–8128. doi:10.1039/d1tc02048j
3. de Leeuw, D. M.; Simenon, M. M. J.; Brown, A. R.; Einerhand, R. E. F. *Synth. Met.* **1997,** *87,* 53–59. doi:10.1016/s0379-6779(97)80097-5
4. Mohapatra, S. K.; Marder, S. R.; Barlow, S. *Acc. Chem. Res.* **2022,** *55,* 319–332. doi:10.1021/acs.accounts.1c00612
5. Mohapatra, S. K.; Al Kurdi, K.; Jhulki, S.; Bogdanov, G.; Bacsa, J.; Conte, M.; Timofeeva, T. V.; Marder, S. R.; Barlow, S. *Beilstein J. Org. Chem.* **2023,** *19,* 1651–1663. doi:10.3762/bjoc.19.121
6. Wolfe, K. M.; Alam, S.; German, E.; Alduayji, F. N.; Alqurashi, M.; Laquai, F.; Welch, G. C. *Beilstein J. Org. Chem.* **2023,** *19,* 1620–1629. doi:10.3762/bjoc.19.119
7. Harding, C. R.; Cann, J.; Laventure, A.; Sadeghianlemraski, M.; Abd-Ellah, M.; Rao, K. R.; Gelfand, B. S.; Aziz, H.; Kaake, L.; Risko, C.; Welch, G. C. *Mater. Horiz.* **2020,** *7,* 2959–2969. doi:10.1039/d0mh00785d
8. Shi, Y.; McCarthy, D. P.; Lungwitz, D.; Jiang, F.; Taddei, M.; Contreras, H.; Lin, Y.; Mohapatra, A. A.; Tang, K.; Zhang, Y.; Barlow, S.; Kahn, A.; Marder, S. R.; Ginger, D. S. *Chem. Mater.* **2024,** *36,* 795–802. doi:10.1021/acs.chemmater.3c02295
9. Giovannitti, A.; Nielsen, C. B.; Sbircea, D.-T.; Inal, S.; Donahue, M.; Niazi, M. R.; Hanifi, D. A.; Amassian, A.; Malliaras, G. G.; Rivnay, J.; McCulloch, I. *Nat. Commun.* **2016,** *7,* 13066. doi:10.1038/ncomms13066
10. Yan, H.; Chen, Z.; Zheng, Y.; Newman, C.; Quinn, J. R.; Dötz, F.; Kastler, M.; Facchetti, A. *Nature* **2009,** *457,* 679–686. doi:10.1038/nature07727
11. Liu, J.; van der Zee, B.; Alessandri, R.; Sami, S.; Dong, J.; Nugraha, M. I.; Barker, A. J.; Rousseva, S.; Qiu, L.; Qiu, X.; Klasen, N.; Chiechi, R. C.; Baran, D.; Caironi, M.; Anthopoulos, T. D.; Portale, G.; Havenith, R. W. A.; Marrink, S. J.; Hummelen, J. C.; Koster, L. J. A. *Nat. Commun.* **2020,** *11,* 5694. doi:10.1038/s41467-020-19537-8

License and Terms

The definitive version of this article is the electronic one which can be found at:
https://doi.org/10.3762/bjoc.20.60

BEILSTEIN JOURNAL OF ORGANIC CHEMISTRY

Organic thermally activated delayed fluorescence material with strained benzoguanidine donor

Alexander C. Brannan[1], Elvie F. P. Beaumont[1], Nguyen Le Phuoc[2],
George F. S. Whitehead[1], Mikko Linnolahti[*2] and Alexander S. Romanov[*1]

Full Research Paper

Open Access

Address:
[1]Department of Chemistry, The University of Manchester, Manchester, United Kingdom and [2]Department of Chemistry, University of Eastern Finland, Joensuu, Finland

Email:
Mikko Linnolahti[*] - mikko.linnolahti@uef.fi; Alexander S. Romanov[*] - alexander.romanov@manchester.ac.uk

[*] Corresponding author

Keywords:
guanidine; organic; photoluminescence; TADF; yellow

Beilstein J. Org. Chem. **2023,** *19,* 1289–1298.
https://doi.org/10.3762/bjoc.19.95

Received: 27 June 2023
Accepted: 30 August 2023
Published: 07 September 2023

This article is part of the thematic issue "Organic electron transport materials".

Associate Editor: P. J. Skabara

Abstract

Organic thermally activated delayed fluorescence (TADF) materials have been widely investigated due to their impressive electronic properties and applied potential for the third generation of organic light-emitting diodes (OLED). We present organic TADF material (**4BGIPN**) based on the strained benzoguanidine donor and compare it with the benchmark carbazole-based material (**4CzIPN**). Extended π-conjugation in **4BGIPN** material results in yellow-green luminescence at 512 nm with a fast radiative rate of 5.5×10^{-5} s^{-1} and a photoluminescence quantum yield of 46% in methylcyclohexane solution. Such a nitrogen-rich **4BGIPN** material has a significantly stabilized highest occupied molecular orbital (HOMO) at −6.4 eV while the lowest unoccupied molecular orbital (LUMO) at −4.0 eV, indicating potential suitability for application as the electron transport layer or TADF class III emitter in OLEDs.

Introduction

Thermally activated delayed fluorescence (TADF) is a photoluminescence mechanism where excitons undergo thermally-assisted reverse-intersystem crossing from an excited triplet state to a higher-lying in energy singlet state to emit delayed fluorescence [1-3]. Organic TADF emitters have gained substantial attention in recent years for their prospective application in organic light-emitting diodes (OLEDs), photocatalysis, bioimaging, and sensors [4-6]. The ability to harvest both singlet and triplet excitons enable organic TADF emitters to compete with classic phosphorescent emitters that employ scarce metals such as iridium and platinum [7-9]. Since its first report in 2012 by Uoyama et al., 1,2,3,5-tetrakis(carbazol-9-yl)-4,6-dicyanobenzene (**4CzIPN**) has been a benchmark TADF emitter due to its high quantum yields and excellent performance in OLED devices [1]. **4CzIPN** is a donor–acceptor-type system where carbazole donor ligands are bound to the benzonitrile acceptor core moiety. In this work we have substituted the carbazole donors with 5*H*-benzo[*d*]benzo[4,5]imidazo[1,2-*a*]imidazole (benzoguanidine) ligands to give **4BGIPN**, see Figure 1. Benzoguanidine has an extended π-conjugation compared with carbazole and is more nitrogen-rich (three N-atoms vs one in carbazole). Thompson et al. recently reported a series of carbene–metal–amide (CMA) (metal = Cu, Ag, Au) emitters employing a benzoguanidine ligand [10]. The extended π-conjugation of benzoguanidine induced a larger hole–electron separation resulting in a smaller energy gap between the excited singlet and triplet states (S_1 and T_1) and ΔE_{ST} resulting in faster radiative rates. This study aimed to synthesize and explore the luminescent properties of the **4BGIPN** material containing a rigid benzoguanidine ligand in its molecular structure.

Results and Discussion

Synthesis and structure

4BGIPN was prepared in 70% yield by aromatic nucleophilic substitution reaction from 2,4,5,6-tetrafluoroisophthalonitrile and 5*H*-benzo[*d*]benzo[4,5]imidazo[1,2-*a*]imidazole (benzoguanidine) after deprotonation the latter with sodium hydride base. The compound shows poor solubility in most common organic solvents with moderate solubility in dichloromethane, 1,2-dichlorobenzene and dimethyl sulfoxide (DMSO). Compound **4BGIPN** was characterized by high-resolution mass spectrometry (HRMS), elemental analysis, and ^{1}H/^{13}C NMR spectroscopy. Proton NMR shows a complicated set of overlapping multiplets indicating that the reaction results in the formation of various isomers (rotamers) which are different by relative orientation of the benzoguanidine donor moieties with respect to each other (Figure 2, see Supporting Information File 1 for NMR). In DMSO-d_6 solution, **4BGIPN** isomers do not show interconversion even upon warming to 120 °C, resulting in a similar set of signals. Excellent fit between HRMS and elemental analysis further supports the formation of the isomeric mixture of **4BGIPN** as evidenced by the identical molecular peak ion and C, H, N values within acceptable deviation of 0.4%. The decomposition temperature (T_d, corresponds to 5% weight loss) was measured by thermogravimetric analysis (TGA) indicating excellent thermal stability for **4BGIPN** with T_d = 425 °C, which is similar to the benchmark material **4CzIPN**, having a T_d in the range of 402–449 °C (T_d range is dependent on the type of the **4CzIPN** polymorph) [11,12]. Differential scanning calorimetry (DSC) shows an endothermic process in the range of 237 to 265 °C which can be associated with the glass transition temperature (T_g) for the isomeric mixture of **4BGIPN**. This is expectedly higher than the analogous T_g of 176 °C for the **4CzIPN** material [13] due to a lower molecular mass of the latter (Figure S1, Supporting Information File 1).

Single crystals for X-ray diffraction study were obtained by slow layer diffusion of hexanes into dichloromethane solution for **4BGIPN** at room temperature (Figure 2). The title compound crystallizes with two independent molecules in the unit cell of the triclinic ($P{-}1$, Figure 2c, yellow plates) and monoclinic chiral space group $P2_1$ (Figure 2a,b,d, yellow blocks). Due to very weak reflection data, the structure of **4BGIPN** in triclinic form was refined in isotropic model, therefore, we do not discuss in detail the structural parameters. We only note that both forms are not due to the polymorphism but rather due to rotational isomerism of the **4BGIPN** material, i.e., different orientation of the benzoguanidine donor ligands above or below the central 4,6-dicyanobenzene ring. In the monoclinic form the two independent molecules of **4BGIPN** are related by a pseudo glide plane that do not completely align when superimposed through a glide operation. There is no evidence for systematic absences relating to the presence of a glide plane in the data

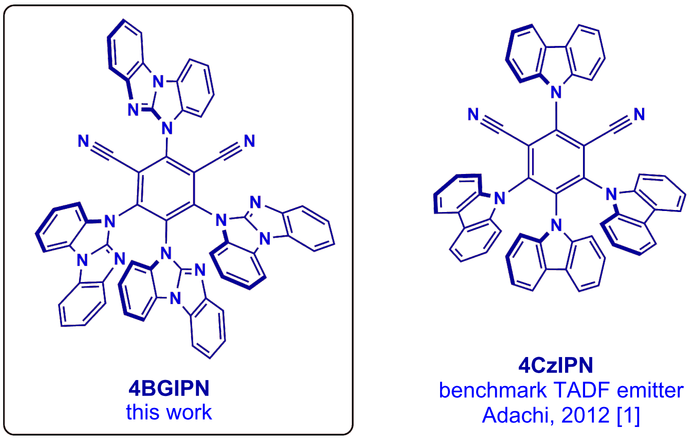

Figure 1: The molecular structures of the title compound **4BGIPN** and the benchmark TADF emitter **4CzIPN**.

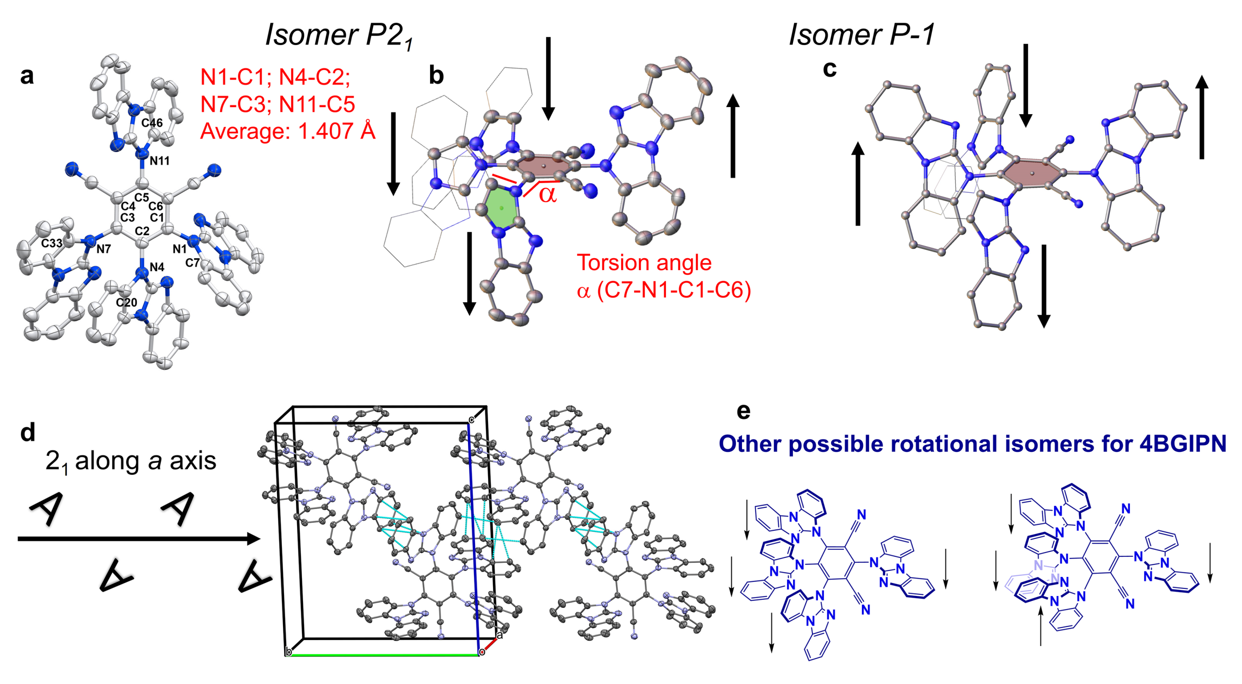

Figure 2: Crystal structure for compound **4BGIPN** in monoclinic form ((a) top view and (b) side view) where black arrows show opposite orientation of the benzoguanidine moieties around the central benzene ring. Representative example for the torsion angle α is shown in red; (c) Crystal structure for compound **4BGIPN** in triclinic form; (d) packing diagram with key geometrical parameters and intermolecular contacts shown as a cyan dashed line; (e) possible isomers for **4BGIPN** material. Ellipsoids are shown at the 50% level where hydrogen atoms are omitted for clarity.

supporting the refinement in the chiral $P2_1$ space group. The structure was refined as a two-component inversion twin; the crystal structure as a whole is a racemic mixture of both orientations. The $C_{benzene}$–$N_{benzoguanidine}$ bond length varies within the error of the experiment from 1.402(5) to 1.420(5), giving an average of 1.407(13) Å for **4BGIPN**, which is closely similar to 1.405(8) Å reported for the benchmark **4CZIPN** compound.

Unlike carbazole, the benzoguanidine ligand lacks C_2 rotational symmetry, thus enabling the benzoguanidine ligands to project above and below the plane of the central benzene ring. In both molecules in the asymmetric unit, the benzoguanidine moiety bound to the benzene carbon neighboring two nitrile groups, is orientated in the opposing projection about the plane of the benzene ring to the remaining benzoguanidine moieties (Figure 2b). Unlike monoclinic, the triclinic form of **4BGIPN** possesses two donor moieties pointing down at C1 and C3 carbon atoms while donor moieties at C2 and C5 are pointed up (Figure 2c). Several possible **4BGIPN** rotational isomers are demonstrated in Figure 2e, however, not isolated in this work. Compound **4BGIPN** possesses a twisted orientation between the donor (benzoguanidine) and acceptor (benzonitrile) ligands (Figure 2) due to steric hindrance imposed by benzoguanidine ligands and reflected by the torsion angle (α) laying in the range of 42.5(2)–64.3(2)°. We compared it with the more narrow torsion angle range of 55.1(2)–60.2(2)° for **4CzIPN** thus indicating that various carbazole donor ligands possess a very similar twist orientation [12]. The donor–acceptor twist angle has been demonstrated to be one of the key structural parameters enabling fast radiative rates for purely organic TADF materials since it's directly related with the overlap integral between HOMO and LUMO orbitals and influences the energy differences between first singlet and triplet excited states [14]. Therefore, we expect a marked difference in the photophysical properties for **4BGIPN**, vide infra.

Analysis of the intermolecular interactions revealed that **4BGIPN** molecules experience face to face intermolecular π–π stacking interactions between the benzoguanidine moieties similar to **4CzIPN** (reported by Etherington et al., [12]). The average interplanar distance for close neighbor benzoguanidine moieties in **4BGIPN** is 3.322(3) Å, which is significantly shorter (0.4 Å) than the 3.74(3) Å average distance between nearest neighbor carbazole ligands in **4CzIPN**, indicative for much stronger intermolecular interactions.

Cyclic voltammetry was used to analyze the redox behavior of **4BGIPN** in THF solution containing [n-Bu_4N]PF_6 as supporting electrolyte (Figure 3, Table 1). The reduction wave has a quasi-reversible character with the $E_{1/2}$ at −1.50 V, which is 260 mV shifted to higher potential when compared with **4CzIPN** (−1.76 V) under similar conditions in THF [15]. Com-

Table 1: Formal electrode potentials (peak position E_p for irreversible and $E_{1/2}$ for quasi-reversible processes (*), *V*, vs $FeCp_2$), onset potentials (*E*, *V*, vs $FeCp_2$), peak-to-peak separation in parentheses for quasi-reversible processes (ΔE_p in mV), E_{HOMO}/E_{LUMO} (eV) and band gap values (ΔE, eV) for the redox changes exhibited by **4BGIPN**.[a]

Complex	Reduction		E_{LUMO} eV^b	Oxidation		E_{HOMO} eV^b	ΔE eV
	E_{1st}	$E_{onset\ red}$		E_{1st}	$E_{onset\ ox}$		
4BGIPN	−1.50 (167)	−1.41	−3.98	+1.25	+1.01	−6.40	2.42

[a] In THF solution, recorded using a glassy carbon electrode, concentration 1.4 mM, supporting electrolyte $[n\text{-}Bu_4N][PF_6]$ (0.13 M), measured at 0.1 V s^{-1}. [b] Calculated according to $E_{HOMO} = -(E_{onset\ ox\ Fc/Fc+} + 5.39)$ and $E_{LUMO} = -(E_{onset\ red\ Fc/Fc+} + 5.39)$ eV.

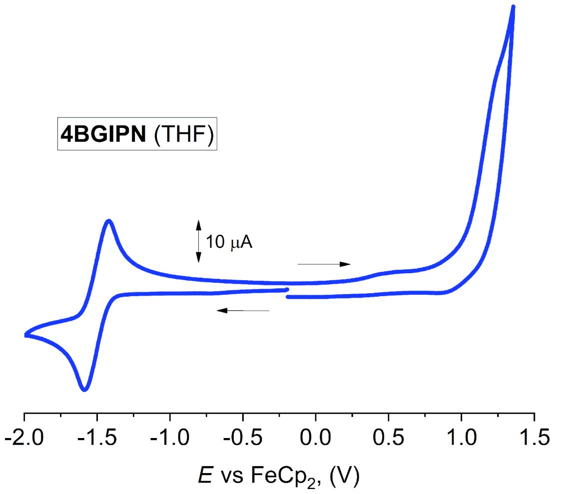

Figure 3: Full range cyclic voltammogram for **4BGIPN**. Recorded using a glassy carbon electrode in THF solution (1.4 mM) with $[n\text{-}Bu_4N]PF_6$ as supporting electrolyte (0.13 M), scan rate 0.1 Vs^{-1}.

pounds **4BGIPN** and **4CzIPN** experience a reduction process at the benzonitrile core (see, the LUMO isosurface in Figure 6, vide infra). Therefore, the higher reduction potential for **4BGIPN** suggests that the benzonitrile core has a lower electron density, which is likely associated with extended π-conjugation and two additional electron withdrawing aza-type nitrogen atoms in the benzoguanidine moieties. This explains the ca. 0.2 eV more stabilized LUMO energy level for compound **4BGIPN** compared with **4CzIPN**. Both **4CzIPN** and **4BGIPN** exhibit an irreversible oxidation wave observed at +1.25 V for **4BGIPN** in THF and +0.94 V for **4CzIPN** in MeCN [15]. A higher oxidation potential (E_p) for **4BGIPN** compared with the **4CzIPN** corroborates with the electron deficient nature of the benzoguanidine moiety thus making it harder to oxidize compared with the more electron-rich carbazole moiety. This results in stabilization of the HOMO energy level at −6.4 eV for **4BGIPN**. Significant stabilization for both HOMO and LUMO energy levels indicates the potential suitability of **4BGIPN** material for application not only as emitter in the emitting layer but also as an electron transport layer in the fabrication of OLEDs.

Photophysical properties and theoretical considerations

UV–vis and photoluminescence (PL) spectra for **4BGIPN** are shown in Figure 4 and Figure 5 while data in various media is collected in Table 2 and Table 3, respectively. UV–vis absorption spectra of **4BGIPN** show a strong π–π* intraligand transition (IL, benzoguanidine) at 290 nm with ε = 42000 M^{-1}cm^{-1}. Unlike **4CzIPN**, we do not observe any vibronically resolved carbazole absorption peaks which are commonly present at 325 nm [15]. Similar to **4CzIPN** [14,15], the UV–vis profile has two broad regions: localized charge transfer (^{lo}CT) over 320–380 nm region with ε up to 14000 M^{-1} cm^{-1} and a delocalized charge transfer (^{de}CT) broad shoulder over the region of ca. 380–460 nm with ε up to 1900 M^{-1} cm^{-1} (Table 2). Both ^{lo}CT and ^{de}CT bands are observed for the benchmark material **4CzIPN** [16] while originating from HOMO to LUMO transition in line with the theoretical calculations (Tables S1, S3, and S4, Supporting Information File 1). All CT bands experience a

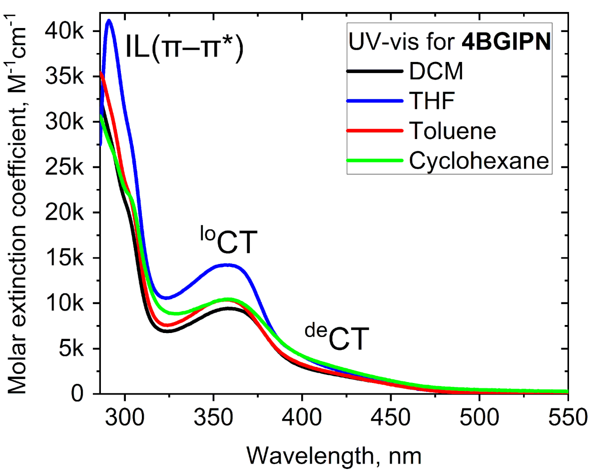

Figure 4: UV–vis absorption spectra for compound **4BGIPN** in various solvents.

Table 2: UV–vis data for compounds **4BGIPN** and **4CzIPN** [15,17] in various solvents.

	λ_{abs} [nm], (10^3 ε/M^{-1} cm^{-1})			
	DCM	THF	toluene	cyclohexane
4BGIPN	436 sh (1.5) 358 (9.5)	435 sh (1.8) 357 (14.2)	439 sh (1.4) 358 (10.4)	439 sh (1.9) 358 (10.5)
4CzIPN	448 (7) [15] 378 [17]	438 (8) [15] –	441 (6) [15] 375 [17]	N/A

very weak solvatochromic effect with increasing solvent polarity from cyclohexane to dichloromethane. This indicates only minor change of the dipole moment upon vertical excitation from S_0 (6.4 D) to S_1 (7.2 D) excited states according to the TD-DFT theoretical calculations (Table S2, Supporting Information File 1).

The photoluminescence (PL) characteristics of **4BGIPN** have been studied in methylcyclohexane solution (MCH, concentration 3.2×10^{-5} M) and Zeonex polymer films (0.1% concentration by weight) at 298 K and 77 K, which is shown in Figure 5 with data collected in Table 3. Compound **4BGIPN** exhibits a featureless yellow CT-type luminescence with λ_{max} = 525 nm

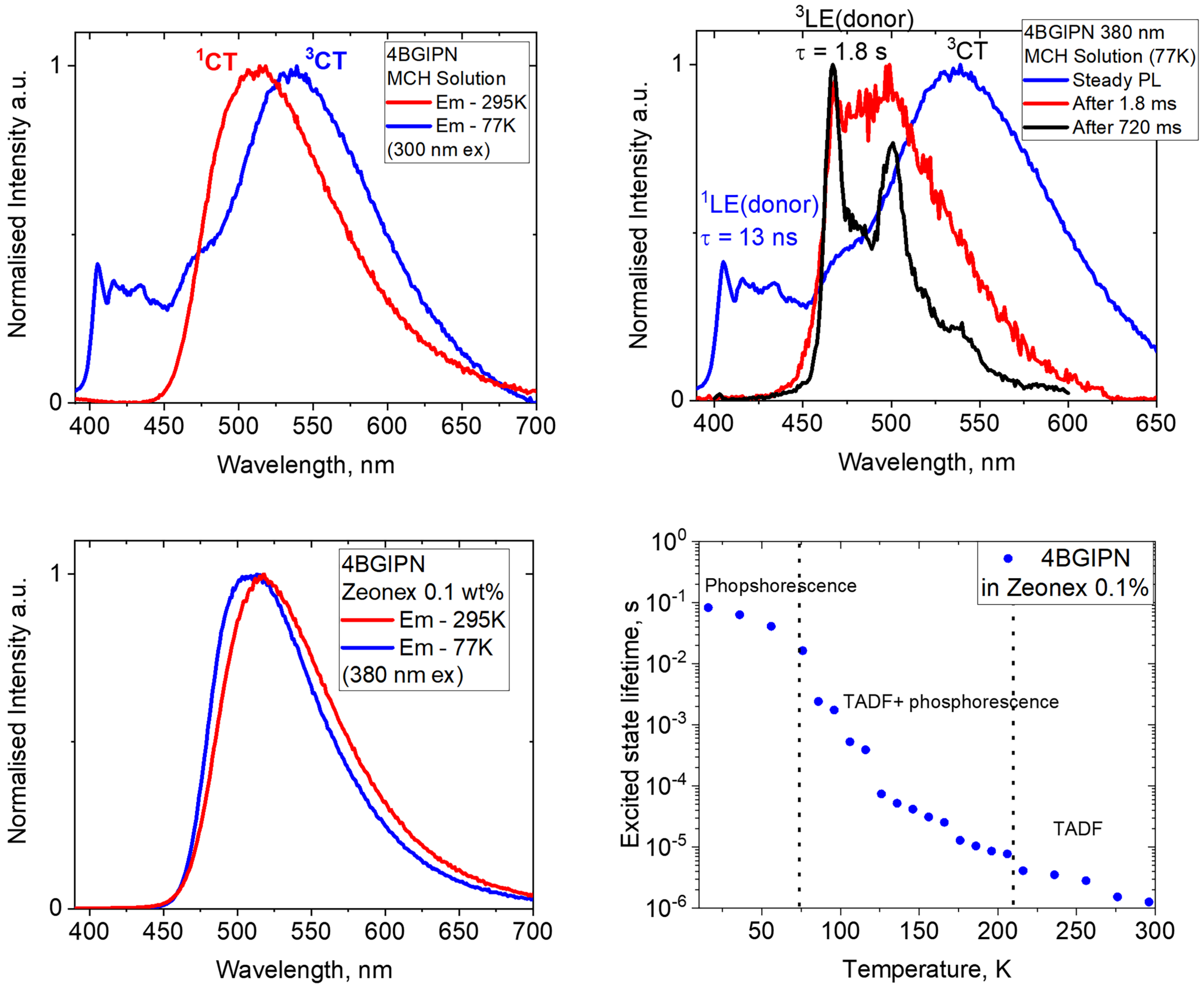

Figure 5: Photoluminescence spectra for **4BGIPN** at 295 and 77 K in (top left) MCH solution; (bottom left) Zeonex 0.1 wt % films; (top right) steady state and delayed PL in frozen glass MCH at 77 K with delays of 1.8 and 720 ms; (bottom right) excited state lifetime at various temperatures in the range from 16 to 296 K.

Table 3: Photophysical properties of **4BGIPN** in various media at 296 and 77 K.

	λ_{em} (nm)	τ (ns)	Φ (%)[a]	k_r (10^5 s^{-1})[b]	k_{nr} (10^5 s^{-1})[c]	^{1}LE/^{3}LE/^{1}CT (eV)[d]	λ_{em} (nm)	τ
methylcyclohexane (MCH) solution 296 K						77 K		
4BGIPN	512	13 (50%) 1666 (50%)	46 (N_2) (18 air)	5.48	6.43	3.12/2.73/2.70	405 (^{1}LE); 470 (^{3}LE); 530 (^{3}CT)	13 ns 1.8 s 126 (36%) µs 1038 (64%) µs
0.1 wt % Zeonex matrix 296 K 16 K								
4BGIPN	517	12 (35%) 2023 (75%)	39	2.56	4.0	–/–/2.66	498	4.35 (31%) ms 36.8 (37%) ms 212 (32%) ms

[a] Absolute quantum yields determined using an integrating sphere; [b] radiative rate constant $k_r = \Phi/\tau$; [c] nonradiative constant $k_{nr} = (1 - \Phi)/\tau$; [d] CT/LE energies based on the onset values of the emission spectra blue edge at 77 K and 295 K.

that is 44 and 25 nm red-shifted compared to **4CzIPN** (λ_{max} = 481 and 500 nm in Zeonex and MCH, respectively) [12]. The solution photoluminescent quantum yield (PLQY) of **4BGIPN** is 46% under inert atmosphere and decreases down to 18% in aerated MCH solution. The reduction in quantum yield on exposure to oxygen is due to quenching of the triplet excited states indicating a TADF luminescence mechanism. PLQY in Zeonex films is 39% in air, which is lower than the PLQY of 87% reported for **4CzIPN** [17].

The two-component excited state lifetime with prompt and delayed fluorescence is characteristic for the TADF-type luminescence [1]. The excited state lifetime of **4BGIPN** has a biexponential decay with a prompt fluorescence τ_p = 13 ns and a delayed fluorescence τ_d = 1655 ns components in MCH solution. Zeonex films of **4BGIPN** exhibit a similar prompt τ_p = 12 ns, but an almost two-fold longer delayed fluorescence τ_d = 2.4 µs when compared to MCH solution. The archetype material **4CzIPN** possesses a similar prompt fluorescence component of 8 ns, whereas a delayed component is nearly ten-times longer, 8.9 and 8.8 µs, in MCH and Zeonex films, respectively [12]. These measurements correlate well with lower PLQY values for **4BGIPN** compared with **4CzIPN**, thus indicating that the use of a larger benzoguanidine donor ligand may open more nonradiative processes. This is reflected in the larger distribution in the torsion angles for **4BGIPN** compared with **4CzIPN**, vide supra.

We collected steady state luminescence and PL after long time delays for **4BGIPN** at 77 K to further support the assignment of the TADF mechanism and attempt to characterize LE and CT triplet states. The emission profiles experienced minor narrowing upon cooling to 77 K, while the PL profile remained broad and featureless (Figure 5) in Zeonex matices. Notably, a frozen MCH glass exhibits a new vibronically resolved component at 405 and 470 nm, together with a broad CT profile. The first resolved high-energy PL component at 405 nm (Figure 5 top right) has a lifetime of 13 ns, which we assigned to singlet locally excited fluorescence (^{1}LE) from the benzoguanidine donor ligand. The second high-energy PL component at 470 nm becomes visible only after a long-time delay (720 ms, see Figure 5 black profile), therefore, we ascribed it to a phosphorescence from a higher lying ^{3}LE state localized on a donor benzoguanidine moiety. Unlike ^{1}LE-fluorescence, ^{3}LE-phosphorescence has a very long lifetime of 1.8 s. Excitation spectra of the broad and resolved bands for **4BGIPN** in MCH glass at 77 K (Figure S4, Supporting Information File 1) follow a mirror image rule when compared with emission spectra showing both broad and resolved components, thus supporting the assignments of the ^{3}CT and ^{3}LE(donor) excited states. The excited state lifetime of the broad CT component has a multiexponential decay with averaged lifetimes of 0.7 ms in MCH glass and up to 212 ms in Zeonex films, which we assigned as phosphorescence from a ^{3}CT state. A more than 100-fold increase in radiative lifetime on cooling to 77 K is characteristic for the organic TADF emitters [1]. Upon cooling Zeonex matrices of **4BGIPN** from 296 K to 16 K (Figure 5), the excited state lifetime shows an order of magnitude increase down to 60 K. However, only marginal increase of lifetime measured in the range of 60 to 16 K indicating a phosphorescence PL nature below 60 K.

The charge transfer singlet (^{1}CT) and local excited singlet (^{1}LE), triplet (^{3}LE) state energies were estimated from the onset values of the blue emission edge of the PL spectra at 295 K for ^{1}CT and 720 ms delayed PL at 77 K for ^{3}LE, respectively

(Figure 5 and Table 3). It was expected to have a large energy difference between the states of similar character (LE) but different multiplicity, i.e., ^{1}LE singlet state is 3.12 eV whereas ^{3}LE state is 2.73 eV. The energy of the singlet ^{1}CT state (2.70 eV) is only 0.03 eV lower compared to the energy of the ^{3}LE state. Therefore, we ascribe compound **4BGIPN** to the class III TADF material where the ^{3}LE is higher in energy than the manifold of the CT states as shown on Figure 6 [18]. The energy difference between singlet and triplet excited states is −0.03 eV for $\Delta E_{\text{1CT-3LE}}$. Such small energy ΔE_{ST} values further support the assignment of the TADF mechanism for the compound **4BGIPN**. Theoretical results (Tables S3 and S4, Supporting Information File 1) support our experimental observations, suggesting that low energy triplet states (T_1, T_2 and T_3) possess a mixed CT/LE character with an energy difference up to 0.2 eV to the first singlet state S_1. At the same time, class III TADF ($E_{\text{3LE}} > E_{\text{CT}}$) [19] and class II TADF materials ($E_{\text{3LE}} \approx E_{\text{CT}}$) [20] are reported to have shorter excited state lifetimes compared with class I TADF materials, for instance **4CzIPN** ($\Delta E_{\text{1CT-3LE}} = +0.09$ eV [12]). The short 1.6 microsecond excited state lifetime for **4BGIPN** (regardless of somewhat lower PLQY) is in line with those reported for other TADF class III systems [19]. We have been unable to resolve the ^{3}LE state for **4BGIPN** in Zeonex matrices regardless of numerous efforts and cooling the films down to 16 K and applying long time delays.

Conclusion

We have synthesized and characterized a donor–acceptor-type thermally activated delayed fluorescent emitter **4BGIPN** with four terminal benzoguanidine donor moieties surrounding the benzonitrile acceptor core. We found that the material is formed as a mixture of the rotational isomers that do not experience interconversion upon heating the **4BGIPN** solution in DMSO to 120 °C. Two rotational isomers were successfully crystallized to show different up and down orientations of the benzoguanidine donor ligands around the central 4,6-dicyanobenzene core. Unlike the **4CzIPN** compound, the **4BGIPN** emitter can crystallize in a chiral $P2_1$ space group due to the parallel and antiparallel orientation of the benzoguanidine donors with respect to each other, lack of C_2 rotational symmetry and extended π-conjugation. The twisted structure of the **4BGIPN** ensures that the donor groups accommodate the highest occupied molecular orbital (HOMO) while the acceptor 4,6-dicyanobenzene moiety contains the lowest unoccupied molecular orbital (LUMO) and is supported by the TD-DFT calcula-

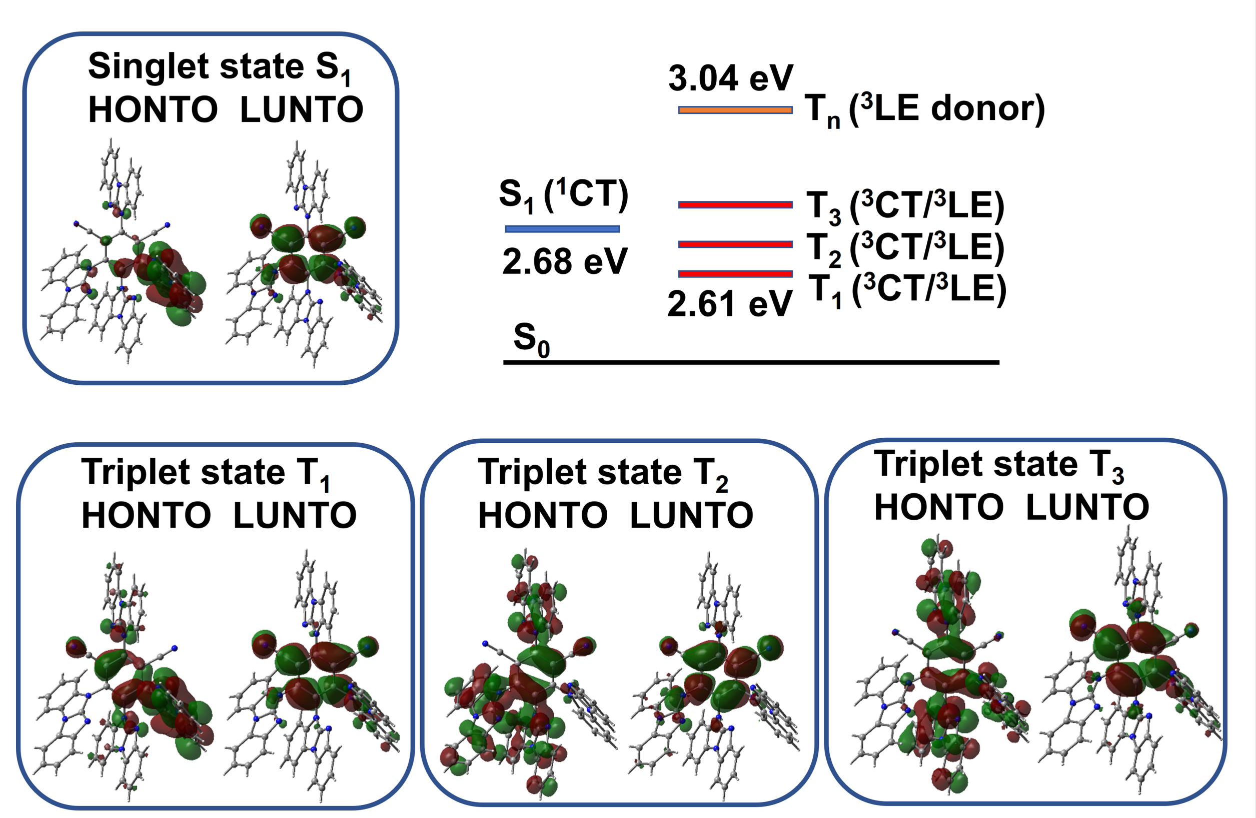

Figure 6: Energy state diagram and natural transition orbitals HONTO and LUNTO for compound **4BGIPN** in excited S_1, T_1, T_2 and T_3 states calculated from the crystal S_0 geometry.

tions. A comparison of the electronic parameters between benchmark **4CzIPN** and new **4BGIPN** materials revealed that benzoguanidine acts as a weaker donor ligand compared with carbazole, resulting in greater stabilization of the HOMO energy level down to −6.4 eV rather than LUMO. The significant stabilization of both HOMO and LUMO energy levels, along with multiple electron-withdrawing aza-nitrogen atoms in the structure of **4BGIPN**, suggests its potential suitability as an electron transport layer in OLED (organic light-emitting diode) devices. Variable temperature photoluminescence studies revealed that **4BGIPN** corresponds to the class III TADF system ($E_{3LE} > E_{1CT}$), while having a small energy difference between singlet and triplet excited states of −0.03 eV for $\Delta E_{1CT\text{-}3LE}$. Theoretical calculations support that the first three triplet excited states possess a mixed CT/LE character while benzoguanidine singlet ^{1}LE state is up to 0.4 eV higher in energy than the singlet ^{1}CT state. The high quantum yields of up to 46% indicate that the yellow-green **4BGIPN** emitter shows a high promise as a platform for developing bright **4BGIPN**-TADF class III type compounds with unity PLQY. Future works may benefit in isolating a particular isomer that could show superior photophysical TADF characteristics important for fabricating TADF OLED devices with improved operating stability.

Experimental

General considerations

All reactions were performed under a N_2 atmosphere. Solvents were dried as required. Sodium hydride was washed from mineral oil with diethyl ether and dried prior to use. 5*H*-Benzo[*d*]benzo[4,5]imidazo[1,2-*a*]imidazole (benzoguanidine) was obtained according to the literature protocol [10] while 2,4,5,6-tetrafluoroisophthalonitrile was purchased from Fluorochem Ltd. and used as received. ^{1}H and ^{13}C{^{1}H} NMR spectra were recorded using a Bruker AVIII HD 500 MHz NMR spectrometer. ^{1}H NMR spectra (500.19 MHz) and ^{13}C{^{1}H} (125.79 MHz) were referenced to dichloromethane-d_2 at δ 5.32 (^{13}C, δ 53.84). All electrochemical experiments were performed using an Autolab PGSTAT 302N computer-controlled potentiostat. Cyclic voltammetry (CV) was performed using a three-electrode configuration consisting of a glassy carbon macrodisk working electrode (GCE) (diameter of 3 mm; BASi, Indiana, U.S.A.) combined with a Pt wire counter electrode (99.99%; GoodFellow, Cambridge, U.K.) and an Ag wire pseudoreference electrode (99.99%; GoodFellow, Cambridge, U.K.). The GCE was polished between experiments using alumina slurry (0.3 µm), rinsed in distilled water and subjected to brief sonication to remove any adhering alumina microparticles. The metal electrodes were then dried in an oven at 100 °C to remove residual traces of water, the GCE was left to air dry and residual traces of water were removed under vacuum. The Ag wire pseudoreference electrodes were calibrated to the ferrocene/ferrocenium couple in THF at the end of each run to allow for any drift in potential, following IUPAC recommendations [16]. All electrochemical measurements were performed at ambient temperature under an inert N_2 atmosphere in THF containing the complex under study (0.14 mM) and the supporting electrolyte [*n*-Bu_4N][PF_6] (0.13 mM). Data were recorded with Autolab NOVA software (v. 1.11). Thermogravimetric analysis was performed by the Microanalysis Laboratory at the University of Manchester. Mass spectrometry data were obtained by the Mass Spectrometry Laboratory at the University of Manchester.

Synthesis of 4BGIPN. 5*H*-Benzo[*d*]benzo[4,5]imidazo[1,2-*a*]imidazole (benzoguanidine, [10]) (700 mg, 3.38 mmol) was added to a suspension of NaH (81.0 mg, 3.38 mmol) in anhydrous DMF (40 mL) at 0 °C under a stream of N_2. The reaction mixture was stirred for 1 h at room temperature. 2,4,5,6-Tetrafluoroisophthalonitrile (135 mg, 676 µmol) was added to the reaction mixture under N_2. The reaction mixture was heated to 140 °C and left to stir overnight. The reaction mixture was dried under vacuum to remove DMF. The crude product was extracted with DCM and washed with water. The organic phase was collected and dried with $MgSO_4$, filtered and concentrated under vacuo. The product was further purified by column chromatography (ethyl acetate/hexane 1:4) to give the pure product as a yellow powder in 70% yield (450 mg, 474 µmol). Single crystals suitable for X-ray diffraction were grown by layering a concentrated solution in DCM with hexane which was left for slow evaporation. ^{1}H NMR (700 MHz, DMSO-d_6) δ 8.46–8.35 (m), 8.23–8.22 (m), 8.16–8.06 (m), 7.94–6.86 (m), 6.82–6.80 (m), 6.59–6.54 (m), 6.47–6.41 (m), 6.35–6.29 (m), 6.24–6.23 (d, *J* = 7.9 Hz); ^{13}C{^{1}H} NMR (126 MHz, CD_2Cl_2) δ 151.17, 149.67, 146.84, 146.65, 146.27, 142.44, 142.29, 142.01, 134.45, 133.78, 133.00, 132.63, 131.91, 130.98, 128.91, 128.50, 127.82, 126.78, 126.58, 126.41, 126.24, 125.84, 124.85, 124.51, 124.39, 124.22, 124.11, 124.01, 123.82, 123.71, 123.53, 123.38, 123.30, 123.23, 122.97, 122.76, 121.99, 121.91, 121.61, 121.41, 121.28, 120.01, 119.91, 119.68, 119.43, 119.16, 117.13, 112.60, 112.41, 112.06, 112.00, 111.69, 111.33, 111.21, 111.11, 110.88, 110.82, 110.74, 110.44, 110.17 ppm; Anal. calcd. for $C_{60}H_{32}N_{14}$ (948.29): C, 75.94; H, 3.40; N, 20.66; found: C, 75.59; H, 3.54; N, 20.28; HRESIMS *m*/*z*: $[M + Na]^+$ calcd. for $C_{60}H_{32}N_{14}Na$, 971.2827; found, 971.2854.

X-ray crystallography

Crystals suitable for X-ray diffraction study were obtained by slow layer diffusion of hexanes/petroleum ether into dichloromethane solution for **4BGIPN** at room temperature. Crystals were mounted in oil on a MiTeGen loop and fixed on the diffractometer in a cold nitrogen stream. Data were collected using dual wavelength Rigaku FR-X rotating anode diffractometer using Cu Kα (λ = 1.54146 Å) radiation, equipped with an AFC-11 4-circle kappa goniometer, VariMAX^{TM} microfocus optics, a Hypix-6000HE detector and an Oxford Cryosystems 800 plus nitrogen flow gas system, at a temperature of 100 K. Data were collected and reduced using CrysAlisPro v42 [21,22]. Absorption correction was performed using empirical methods (SCALE3 ABSPACK) based upon symmetry-equivalent reflections combined with measurements at different azimuthal angles.

For the final refinement, the contribution of severely disordered CH_2Cl_2 molecules in the crystals of **4BGIPN** was accounted for by applying a solvent void mask calculated using BYPASS, implemented through Olex2 [23]. Structures were solved by direct method/intrinsic phasing and refined by the full-matrix least-squares against F^2. All non-hydrogen atoms were refined with anisotropic atomic displacement parameters. All hydrogen atoms were positioned geometrically and constrained to ride on their parent atoms with C–H = 0.95–1.00 Å, and U_{iso} = 1.2–1.5 U_{eq} (parent atom). All calculations were performed using the SHELXL software and Olex2 graphical user interface [22,23].

4BGIPN (monoclinic *P*2$_1$), CCDC number 2243340, $C_{60}H_{32}N_{14}$, monoclinic, space group $P2_1$ (no. 4), a = 17.4217(4) Å, b = 15.2552(3) Å, c = 20.8314(6) Å, β = 114.583(3)°, V = 5034.6(2) Å^3, Z = 4, d_{calc} = 1.252 g cm^{-3}, μ = 0.623 mm^{-1}, yellow block, 33714 reflections measured (4.664° ≤ 2Θ ≤ 152.79°), 17837 unique (R_{int} = 0.0314, R_{sigma} = 0.0512) which were used in all calculations. The final R_1 was 0.0462 (I > 2σ(I)) and wR_2 was 0.1190 (all data). *GOF* = 1.042, $\Delta\rho_{min}/\Delta\rho_{max}$ = 0.4/−0.2 e Å^{-3}.

4BGIPN (triclinic *P*−1), CCDC number 2287367, $C_{60}H_{32}N_{14}\cdot 0.5CH_2Cl_2$ (M = 991.46 g/mol): triclinic, space group P−1 (no. 2), a = 12.8390(16) Å, b = 21.536(3) Å, c = 23.149(5) Å, α = 65.321(17)°, β = 82.509(14)°, γ = 89.955(11)°, V = 5756.1(19) Å^3, Z = 4, T = 100.00(13) K, μ(Cu Kα) = 0.981 mm^{-1}, d_{calc} = 1.144 g/cm^3, 68407 reflections measured (4.244° ≤ 2Θ ≤ 151.924°), 22637 unique (R_{int} = 0.1849, R_{sigma} = 0.1991) which were used in all calculations. The final R_1 was 0.2870 (I > 2σ(I)) and wR_2 was 0.6519 (all data).

Computational results

Computations were performed using density functional theory (DFT) for the ground state and time-dependent DFT (TD-DFT) with Tamm–Dancoff approximation [24,25] for the excited states calculations, using the global hybrid MN15 functional by Truhlar [26] in combination with the def2-TZVP basis set by Ahlrichs [27,28]. TD-DFT calculations were performed to elucidate the nature of the excited state in a crystalline and optimized molecular geometry of **4BGIPN** with all data collected in Supporting Information File 1 (Tables S1–S4). All calculations were carried out by Gaussian 16 [29] and HOMO–LUMO overlap integrals were calculated using Multiwfn program [30].

Supporting Information

Supporting Information File 1

Additional experimental data.
[https://www.beilstein-journals.org/bjoc/content/supplementary/1860-5397-19-95-S1.pdf]

Supporting Information File 2

CIF file.
[https://www.beilstein-journals.org/bjoc/content/supplementary/1860-5397-19-95-S2.cif]

Acknowledgements

We are grateful to ZEON EUROPE GmbH for providing ZEONEX® 480 Cyclo Olefin Polymer (COP) used in our studies. We are grateful to Dr. Louise Natrajan at the University of Manchester for providing access to FLS-1000 fluorometer.

Funding

This work was supported by the Royal Society and the Academy of Finland. A.S.R. acknowledges support from the Royal Society (grant nos. URF\R1\180288 and RGF\EA\181008). M.L. acknowledges the Academy of Finland Flagship Programme, Photonics Research and Innovation (PREIN), decision 320166. N.L.P. acknowledges the Doctoral Programme in Science, Technology and Computing (Sciteco, University of Eastern Finland). (TD)-DFT computations were made possible by use of the Finnish Grid and Cloud Infrastructure resources (urn:nbn:fi:research-infras-2016072533). A.S.R. acknowledges the support from the EPSRC (grant code EP/K039547/1).

ORCID® iDs

Alexander C. Brannan - https://orcid.org/0000-0002-9640-2594
Elvie F. P. Beaumont - https://orcid.org/0009-0002-8553-306X
George F. S. Whitehead - https://orcid.org/0000-0003-1949-4250
Mikko Linnolahti - https://orcid.org/0000-0003-0056-2698
Alexander S. Romanov - https://orcid.org/0000-0003-2617-6402

Preprint

A non-peer-reviewed version of this article has been previously published as a preprint: https://doi.org/10.3762/bxiv.2023.26.v1

References

1. Uoyama, H.; Goushi, K.; Shizu, K.; Nomura, H.; Adachi, C. *Nature* **2012,** *492,* 234–238. doi:10.1038/nature11687
2. Endo, A.; Ogasawara, M.; Takahashi, A.; Yokoyama, D.; Kato, Y.; Adachi, C. *Adv. Mater. (Weinheim, Ger.)* **2009,** *21,* 4802–4806. doi:10.1002/adma.200900983
3. Parker, C. A.; Hatchard, C. G. *Trans. Faraday Soc.* **1961,** *57,* 1894–1904. doi:10.1039/tf9615701894
4. Yang, Z.; Mao, Z.; Xie, Z.; Zhang, Y.; Liu, S.; Zhao, J.; Xu, J.; Chi, Z.; Aldred, M. P. *Chem. Soc. Rev.* **2017,** *46,* 915–1016. doi:10.1039/c6cs00368k
5. Liu, Y.; Li, C.; Ren, Z.; Yan, S.; Bryce, M. R. *Nat. Rev. Mater.* **2018,** *3,* 18020. doi:10.1038/natrevmats.2018.20
6. Bryden, M. A.; Zysman-Colman, E. *Chem. Soc. Rev.* **2021,** *50,* 7587–7680. doi:10.1039/d1cs00198a
7. Wong, M. Y.; Zysman-Colman, E. *Adv. Mater. (Weinheim, Ger.)* **2017,** *29,* 1605444. doi:10.1002/adma.201605444
8. Lee, Y. H.; Park, S.; Oh, J.; Shin, J. W.; Jung, J.; Yoo, S.; Lee, M. H. *ACS Appl. Mater. Interfaces* **2017,** *9,* 24035–24042. doi:10.1021/acsami.7b05615
9. Kaji, H.; Suzuki, H.; Fukushima, T.; Shizu, K.; Suzuki, K.; Kubo, S.; Komino, T.; Oiwa, H.; Suzuki, F.; Wakamiya, A.; Murata, Y.; Adachi, C. *Nat. Commun.* **2015,** *6,* 8476. doi:10.1038/ncomms9476
10. Muniz, C. N.; Schaab, J.; Razgoniaev, A.; Djurovich, P. I.; Thompson, M. E. *J. Am. Chem. Soc.* **2022,** *144,* 17916–17928. doi:10.1021/jacs.2c06948
11. Kim, H. S.; Lee, J. Y.; Shin, S.; Jeong, W.; Lee, S. H.; Kim, S.; Lee, J.; Suh, M. C.; Yoo, S. *Adv. Funct. Mater.* **2021,** *31,* 2104646. doi:10.1002/adfm.202104646
12. Etherington, M. K.; Kukhta, N. A.; Higginbotham, H. F.; Danos, A.; Bismillah, A. N.; Graves, D. R.; McGonigal, P. R.; Haase, N.; Morherr, A.; Batsanov, A. S.; Pflumm, C.; Bhalla, V.; Bryce, M. R.; Monkman, A. P. *J. Phys. Chem. C* **2019,** *123,* 11109–11117. doi:10.1021/acs.jpcc.9b01458
13. Tsuchiya, Y.; Nakamura, N.; Kakumachi, S.; Kusuhara, K.; Chan, C.-Y.; Adachi, C. *Chem. Commun.* **2022,** *58,* 11292–11295. doi:10.1039/d2cc01467j
14. Chen, X.-K.; Tsuchiya, Y.; Ishikawa, Y.; Zhong, C.; Adachi, C.; Brédas, J.-L. *Adv. Mater. (Weinheim, Ger.)* **2017,** *29,* 1702767. doi:10.1002/adma.201702767
15. Bryden, M. A.; Millward, F.; Matulaitis, T.; Chen, D.; Villa, M.; Fermi, A.; Cetin, S.; Ceroni, P.; Zysman-Colman, E. *J. Org. Chem.* **2023,** *88,* 6364–6373. doi:10.1021/acs.joc.2c01137
16. Gritzner, G.; Kůta, J. *Electrochim. Acta* **1984,** *29,* 869–873. doi:10.1016/0013-4686(84)80027-4
17. Ishimatsu, R.; Matsunami, S.; Shizu, K.; Adachi, C.; Nakano, K.; Imato, T. *J. Phys. Chem. A* **2013,** *117,* 5607–5612. doi:10.1021/jp404120s
18. Etherington, M. K.; Gibson, J.; Higginbotham, H. F.; Penfold, T. J.; Monkman, A. P. *Nat. Commun.* **2016,** *7,* 13680. doi:10.1038/ncomms13680
19. Cui, L.-S.; Gillett, A. J.; Zhang, S.-F.; Ye, H.; Liu, Y.; Chen, X.-K.; Lin, Z.-S.; Evans, E. W.; Myers, W. K.; Ronson, T. K.; Nakanotani, H.; Reineke, S.; Bredas, J.-L.; Adachi, C.; Friend, R. H. *Nat. Photonics* **2020,** *14,* 636–642. doi:10.1038/s41566-020-0668-z
20. dos Santos, P. L.; Ward, J. S.; Congrave, D. G.; Batsanov, A. S.; Eng, J.; Stacey, J. E.; Penfold, T. J.; Monkman, A. P.; Bryce, M. R. *Adv. Sci.* **2018,** *5,* 1700989. doi:10.1002/advs.201700989
21. *Programs CrysAlisPro;* Oxford Diffraction Ltd.: Abingdon, UK, 2010.
22. Sheldrick, G. M. *Acta Crystallogr., Sect. C: Struct. Chem.* **2015,** *71,* 3–8. doi:10.1107/s2053229614024218
23. Dolomanov, O. V.; Bourhis, L. J.; Gildea, R. J.; Howard, J. A. K.; Puschmann, H. *J. Appl. Crystallogr.* **2009,** *42,* 339–341. doi:10.1107/s0021889808042726
24. Furche, F.; Rappoport, D. Density Functional Methods for Excited States: Equilibrium Structure and Electronic Spectra. In *Computational Photochemistry,* 1st ed.; Olivucci, M., Ed.; Elsevier: Amsterdam, Netherlands, 2005; Vol. 16, pp 93–128.
25. Hirata, S.; Head-Gordon, M. *Chem. Phys. Lett.* **1999,** *314,* 291–299. doi:10.1016/s0009-2614(99)01149-5
26. Yu, H. S.; He, X.; Li, S. L.; Truhlar, D. G. *Chem. Sci.* **2016,** *7,* 5032–5051. doi:10.1039/c6sc00705h
27. Weigend, F.; Häser, M.; Patzelt, H.; Ahlrichs, R. *Chem. Phys. Lett.* **1998,** *294,* 143–152. doi:10.1016/s0009-2614(98)00862-8
28. Weigend, F.; Ahlrichs, R. *Phys. Chem. Chem. Phys.* **2005,** *7,* 3297–3305. doi:10.1039/b508541a
29. *Gaussian 16,* Revision A. 03; Gaussian Inc.: Wallingford, CT, USA, 2016.
30. Lu, T.; Chen, F. *J. Comput. Chem.* **2012,** *33,* 580–592. doi:10.1002/jcc.22885

License and Terms

BEILSTEIN JOURNAL OF ORGANIC CHEMISTRY

A series of perylene diimide cathode interlayer materials for green solvent processing in conventional organic photovoltaics

Kathryn M. Wolfe[1], Shahidul Alam[2], Eva German[1], Fahad N. Alduayji[2], Maryam Alqurashi[2], Frédéric Laquai[*2] and Gregory C. Welch[*1,§]

Full Research Paper

Open Access

Address:
[1]Department of Chemistry, University of Calgary, 2500 University Drive N.W., Calgary, Alberta, T2N 1N4, Canada and [2]King Abdullah University of Science and Technology (KAUST), KAUST Solar Center (KSC), Physical Sciences and Engineering Division (PSE), Material Science and Engineering Program (MSE), Thuwal 23955-6900, Saudi Arabia

Email:
Frédéric Laquai[*] - frederic.laquai@kaust.edu.sa;
Gregory C. Welch[*] - gregory.welch@ucalgary.ca

* Corresponding author
§ Phone number: 1-403-210-7603

Keywords:
cathode interlayer materials; green solvent processing; organic photovoltaics

Beilstein J. Org. Chem. **2023,** *19,* 1620–1629.
https://doi.org/10.3762/bjoc.19.119

Received: 08 August 2023
Accepted: 13 October 2023
Published: 26 October 2023

This article is part of the thematic issue "Organic electron transport materials".

Associate Editor: P. J. Skabara

Abstract

Herein, we report on the design, synthesis, physical and chemical properties, and organic photovoltaic (OPV) device performance of four new cathode interlayer (CIL) materials based on bay N-annulated perylene diimides. Starting from the previously reported N-annulated perylene diimide (PDIN-H), the N-position was functionalized with a benzyl and pentafluorobenzyl group to make PDIN-B and PDIN-FB, respectively. Similarly, starting from the previously reported cyanated N-annulated perylene diimide (CN-PDIN-H), the N-position was functionalized with a benzyl and pentafluorobenzyl group to make CN-PDIN-B and CN-PDIN-FB, respectively. The materials exhibit solubility in the green solvent, ethyl acetate, and thus were processed into thin films using ethyl acetate as the solvent. The optoelectronic properties were assessed for both solution and film, and the electrochemical properties were probed in solution. To validate the potential as electron transporting layers, each film was used in conventional OPVs as the CIL with processing from ethyl acetate, while using a bulk heterojunction (BHJ) comprised of PM6:Y6. High power conversion efficiencies (PCEs) of 13% were achieved compared to control devices using the standard PFN-Br CIL.

Introduction

Organic photovoltaic (OPV) devices for energy harvesting or light recycling are of interest due to their low cost, fabrication via layer-by-layer printing, flexibility, and low carbon footprint [1,2]. Due to the processability of organic materials used in OPVs, the large-scale manufacturing of such devices at low cost with minimal environmental impact becomes viable, especially if processed from green solvents [3-5]. These devices have the opportunity to be integrated into buildings, automobiles, Internet of Things (IoT) devices, etc. This has motivated scientists to develop OPV technology over the past several decades, which resulted in power conversion efficiencies (PCEs) of OPVs reaching over 19% by using state-of-the-art organic photoactive materials in conjunction with hole and electron transporting "interlayers" that reside between the bulk heterojunction (BHJ) and the electrodes [6]. However, while progress has been made by increases in PCEs from ≈10% to ≈19% in the last decade, many of the materials used in OPVs suffer from low thermal and/or photostability, lengthy syntheses, high cost, and require harmful reagents for synthesis and processing. Therefore, it is necessary to design new materials with studious strategies to negate these issues and contribute to the movement for the commercialization of OPVs [7-9].

Cathode interlayers (CILs) have been recently recognized as a key component to realize highly efficient OPVs. Indeed, the highest efficiency to date reported at over 19% used a BHJ of PM6:BTP-eC9 with PFN-Br as the CIL [6]. CILs serve to increase device performance in various ways. First, polar functional groups (and induced dipole moments) serve to tune the work function of the cathode for a reduced energetic offset, thus reducing the Schottky barrier that is detrimental to device performance and long-term stability. Second, efficiency is increased by tuning the frontier molecular orbitals to block holes by a deep highest occupied molecular orbital (HOMO) and by promoting electron cascade with a deep lowest unoccupied molecular orbital (LUMO). Third, CILs prevent the donor material in the BHJ from coming in contact with the cathode, thus blocking holes and reducing recombination processes. Fourth, CILs can provide smooth surface morphologies for better contact with the cathode, as otherwise defects in the BHJ, such as pinholes, can occur [10-12]. Therefore, it is important to design CIL materials to have polar groups, appropriate FMO energetic levels, and functional groups known to promote ideal packing and intermolecular interactions with neighboring compounds.

Several CIL compounds stand out as top-performing materials, such as PFN-Br [13], PDIN [14], PDINO [14], and PDINN [15] (Figure 1), which have realized PCEs of ≈19% [6], ≈17% [16], ≈15% [17], and ≈17% [15], respectively, when implemented as CILs in conventional OPVs. While challenges exist for polymeric materials due to batch-to-batch variations, molecular materials are advantageous as they can be easily structurally characterized, have highly reproducible syntheses, and can exhibit high solubilities in common organic solvents for effective solution processing and thin film formation. Towards obtaining high-performance CIL materials, perylene diimides (PDIs) stand out as excellent candidates as they can form electron transporting films, have appropriate LUMO energy levels compatible with most photoactive acceptor molecules (LUMO levels residing between −3.5 eV to −4.0 eV) to promote electron cascade, have appropriate HOMO energy levels at −5.5 eV and below that serve to block hole transport, exhibit high thermal stability, are highly tunable in terms of their physical and chemical properties, and can be readily doped thereby increasing electronic conductivity. Some of the most widely used PDI materials for CILs are PDIN [14], PDINN [15], and PDINO (Figure 1a) [14,15]. Past work in our group has included N-annulated PDI materials, as seen in Figure 1b, where modifications to the PDIN-H CIL material include installation of a nitrile functional group on an open bay position for electrochemical tuning, and N-functionalization to provide several different side chains to study the impact of morphological changes on device performance [18,19]. With respect to the latter, we have introduced ethyl acetate as a suitable green solvent to process CILs onto high performance BHJs (e.g., PM6:Y6). Most CILs have been processed from alcohols as to not damage the underlying hydrophobic BHJ film, but use of such alcohol-based solvents limits the types of organic materials to be used as CILs. With ethyl acetate as a processing solvent a wider range of organic materials can be developed and studied as CILs.

Herein, we report on the design, synthesis, and application of four new CILs using the previously reported N-annulated PDI (PDIN-H) and nitrile functionalized N-annulated PDI (CN-PDIN-H) compounds (Figure 1c) as the scaffolds for modification [18]. The PDIN-H scaffold was modified by N-functionalization with a benzyl (PDIN-B) or pentafluorobenzyl group (PDIN-FB). Similarly, the CN-PDIN-H scaffold was functionalized with a benzyl (CN-PDIN-B) or pentafluorobenzyl group (CN-PDIN-FB). Addition of the benzyl and pentafluorobenzyl groups was to enhance solubility in green solvents, while nitrile functionalization was done to further stabilize the LUMO of the compounds. These materials are reported for the design strategy used, their synthesis, optoelectronic properties, electrochemical properties, and processability from ethyl acetate for thin film formation. Lastly, each new CIL material was tested in conventional OPVs by processing with ethyl acetate, a green solvent [20-22], where the BHJ used was PM6:Y6 and PCEs were found to be comparable to that of PFN-Br with PCEs of over ≈13%.

Results and Discussion

Design strategy

Previously, the benzyl-annulated dimers of the ethyl propyl perylene diimide (tPDI$_2$-N-R; Figure 2) were reported as non-fullerene acceptors for OPVs, reaching PCEs of ≈6% [23]. Realizing that these materials are suitable electron acceptors, it

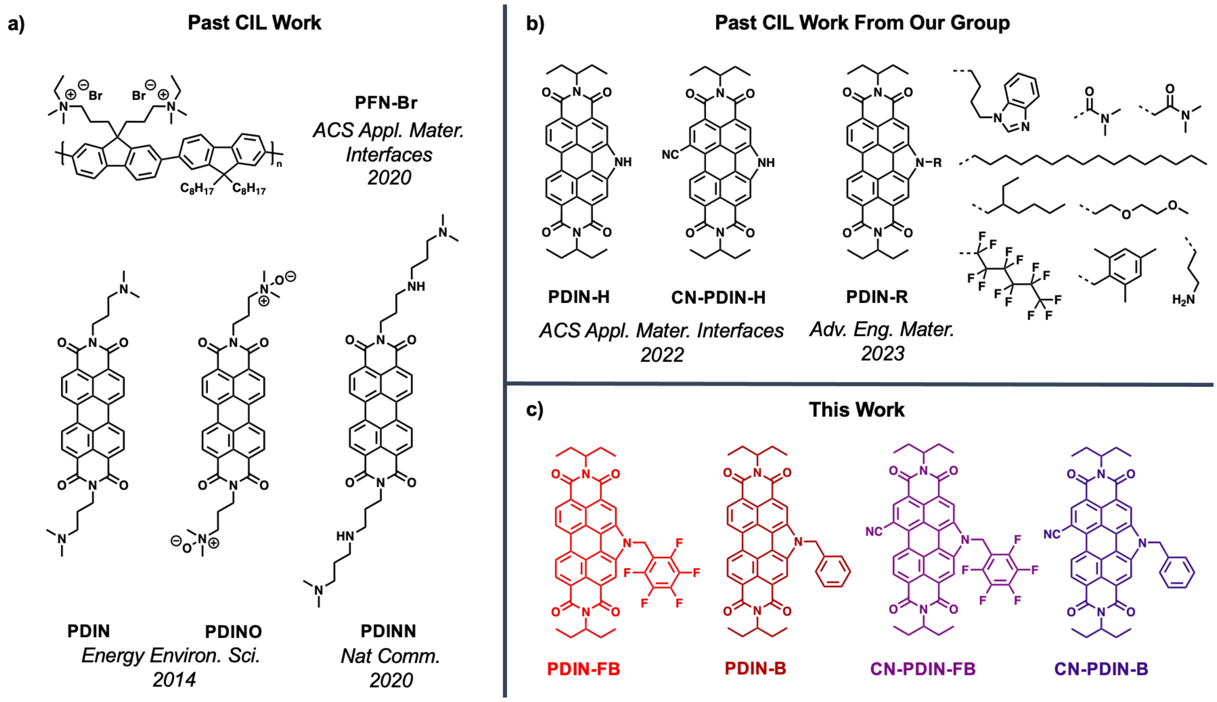

Figure 1: a) Select cathode interlayers used to make high-performance OPVs previously reported in the literature, including PFN-Br [13], PDIN [14], PDINO [14], and PDINN [15]. b) Cathode interlayers previously reported from our group including PDIN-H [18], CN-PDIN-H [18], and PDIN-R derivatives [19]. c) This work includes the CILs PDIN-FB, PDIN-B, CN-PDIN-FB, and CN-PDIN-B.

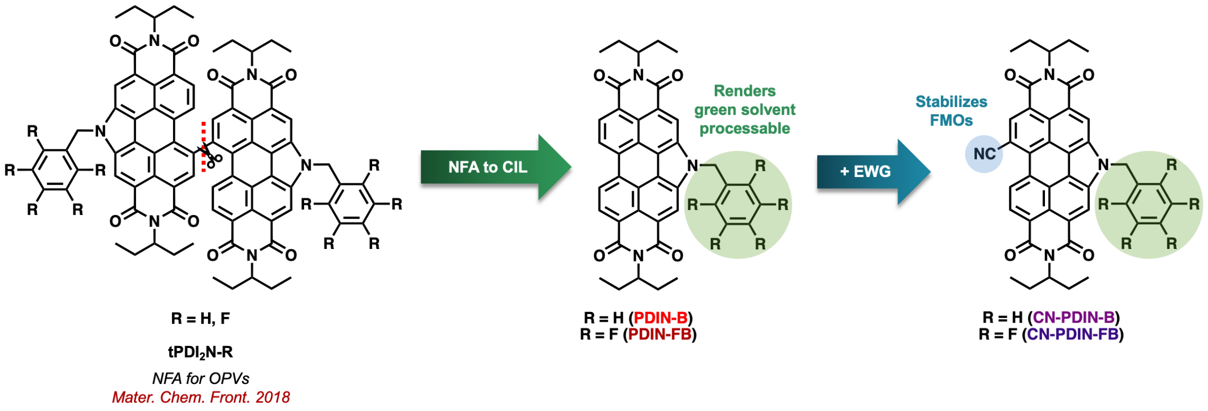

Figure 2: Evolution of the dimer tPDI$_2$N-R [23] as an NFA to PDIN-B/PDIN-FB monomers to serve as CILs, where the addition of nitrile functional group on the monomeric PDIN-B/PDIN-FB materials serve to stabilize FMOs.

was hypothesized that the monomeric species would be suitable candidates for use as CILs as the planar structure is more likely to induce ordered microstructures, which is ideal for CILs as a means to provide better contact with the cathode and BHJ acceptor materials. All derivatives (PDIN-FB, PDIN-B, CN-PDIN-FB, and CN-PDIN-B) have undergone N-functionalization to provide either a benzyl or pentafluorobenzyl group, which serves to alter the physical and chemical properties of the material. In terms of physical properties, the addition of benzyl and pentafluorobenzyl groups serve to break up NH···OH intermolecular bonding, which renders the materials soluble in a range of solvents suitable for solution processing [24]. Target organic solvents to use for the production of OPVs are those that are considered green, where a green solvent can be described as one that exhibits little to no toxicity to humans or animals, and has a minimal environmental impact when considering life-cycle assessments [21]. In terms of the electrochemical properties of the series, it was hypothesized that the addition of a nitrile functional group would stabilize both the HOMO and LUMO, where a deep-lying LUMO energy level is sought after for increased stability of electron-transporting materials [25]. Additionally, the presence of a nitrile group introduces an additional means for intermolecular bonding between the CILs and acceptor molecules (N···F and N···H bonding when using the acceptor Y6), as well as an induced dipole moment in the molecule for increased work function tuning of the cathode. The use of benzyl and pentafluorobenzyl substituents was to evaluate the impact of H vs F on the electrochemical properties and device performance.

Synthesis

The synthesis of the four CILs, PDIN-B (benzyl N-annulated ethyl propyl perylene diimide), PDIN-FB (pentafluorobenzyl N-annulated ethyl propyl perylene diimide), CN-PDIN-B (benzyl cyano N-annulated ethyl propyl perylene diimide), and CN-PDIN-FB (pentafluorobenzyl cyano N-annulated ethyl propyl perylene diimide) are reported within for the first time. Starting from PDIN-H, PDIN-B and PDIN-FB can be synthesized via N-alkylation by use of a base (K_2CO_3) in the presence of either benzyl bromide for PDIN-B or pentafluorobenzyl bromide for PDIN-FB (Scheme 1). Starting from CN-PDIN-H, CN-PDIN-B and CN-PDIN-FB can be synthesized by N-alkylation by use of a base (K_2CO_3) in the presence of either benzyl bromide for CN-PDIN-B or pentafluorobenzyl bromide for CN-PDIN-FB (Scheme 1). The products were collected by precipitating the product out of the reaction mixtures by adding a methanol/water mixture; thus, no lengthy purification steps were required for any of the syntheses. Yields of 52.4%, 80.2%, 58.1%, and 68.3% were obtained for PDIN-FB, PDIN-B, CN-PDIN-FB, and CN-PDIN-B, respectively. All compounds were structurally characterized using ^{1}H NMR spectroscopy, ^{13}C NMR spectroscopy, mass spectrometry, and elemental analysis. See Supporting Information File 1 for full synthetic and characterization details.

Optical properties

Using UV–visible spectroscopy, the optical properties for PDIN-FB, PDIN-B, CN-PDIN-FB, and CN-PDIN-FB in both solution and film form were obtained (Figure 3, Table 1), where solution spectra were done in ethyl acetate and the films were processed using ethyl acetate as the solvent and quartz as the substrate. Ethyl acetate was used due to being green and its use in OPV device fabrication (see below). When comparing the solution spectra of all the compounds, the spectrum of PDIN-FB shows an onset (in regard to the lowest energy transition at 0 → 0) at 532 nm (2.33 eV) with a λ_{max} of 515 nm, PDIN-B shows an onset of 536 nm (2.31 eV) with a λ_{max} of 520 nm, CN-PDIN-FB shows an onset of 549 nm (2.26 eV) with a λ_{max} of 528 nm, and CN-PDIN-B shows an onset of 554 nm (2.24 eV) with a λ_{max} of 533 nm. The shapes of all solution spectra are mostly retained across the compounds, which is expected due to the 0 → 0, 0 → 1, and 0 → 2 transition occurring on the perylene core [26]. In comparing the derivatives with a benzyl group on the pyrrolic position (PDIN-B, CN-PDIN-B) with those with a pentafluorobenzyl group (PDIN-FB, CN-PDIN-FB), a bathochromic shift of 0.02 eV is observed when going from the pentafluorobenzyl to the benzyl derivatives. When comparing the derivatives with (CN-PDIN-FB, CN-PDIN-B) and without (PDIN-FB, PDIN-B) a nitrile group, a bathochromic shift of 13 nm is observed for PDIN-FB → CN-PDIN-FB, and a bathochromic shift of 13 nm is observed for PDIN-B → CN-PDIN-B. The presence of the nitrile functional group results in a lowering of the energy of the optical band gap, which can be attributed to a higher degree of stabilization of the first excited state in relation to the stabilization of the ground state, which is observed in other PDIs when installing the electron-withdrawing nitrile group on the polycyclic aromatic core [27,28]. The molar extinction coefficients (ε) of all compounds in ethyl acetate were determined (see Supporting Information File 1, Figures S18–S25), where

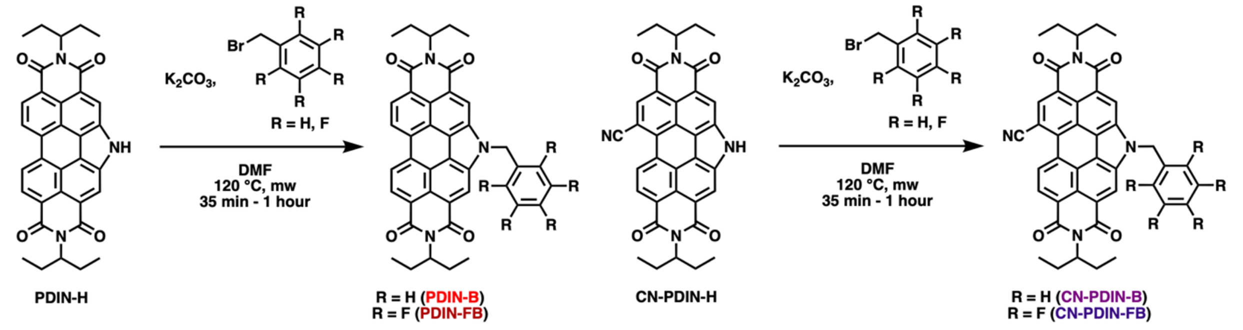

Scheme 1: Synthesis schematic for PDIN-FB, PDIN-B, CN-PDIN-FB, and CN-PDIN-B.

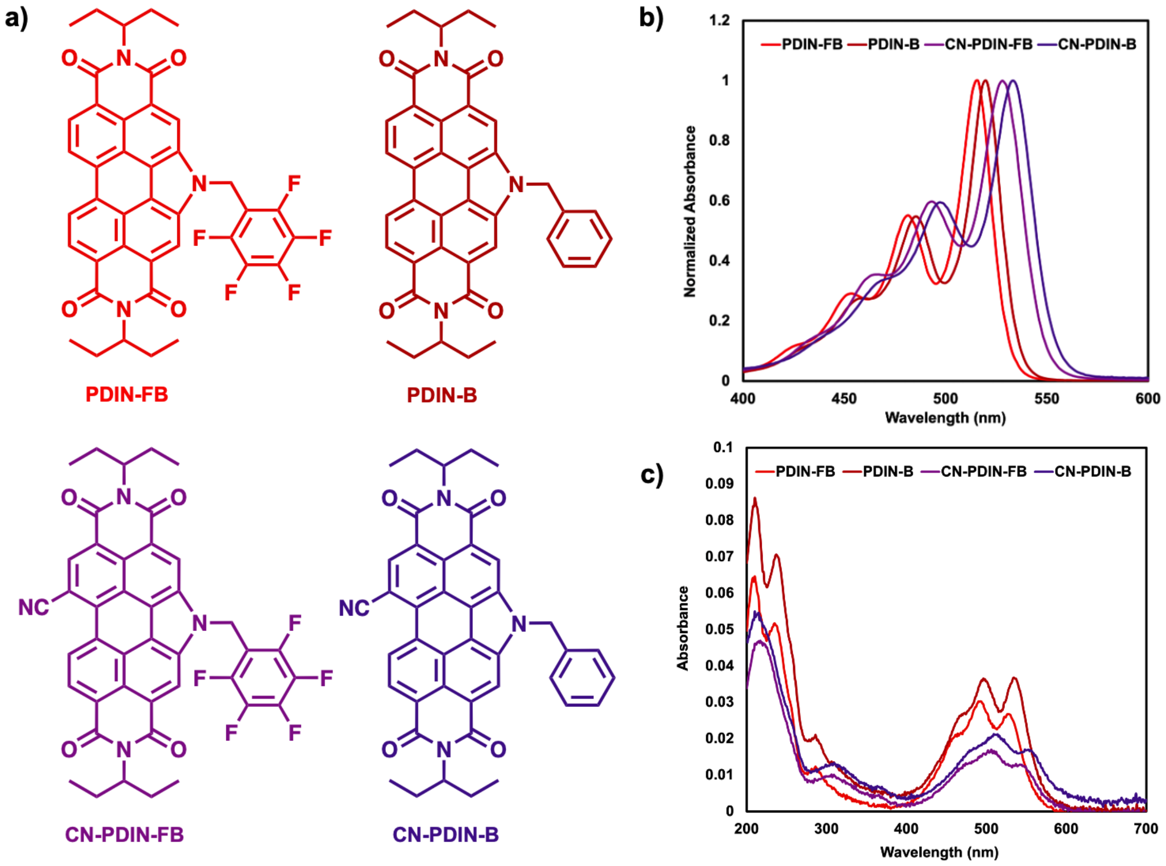

Figure 3: a) Structures of PDIN-FB, PDIN-B, CN-PDIN-FB, and CN-PDIN-B. b) Normalized solution UV–visible spectra using ethyl acetate as the solvent. c) UV–vis spectra for films on quartz substrates where films were cast from 1 mg/mL solutions using ethyl acetate as the solvent.

Table 1: Solution (in EtOAc) and film (on quartz) UV–visible spectra data and electrochemical data for PDIN-B, PDIN-FB, CN-PDIN-B, CN-PDIN-FB.

Compound	Solution λ_{max} (nm)	ε (M^{-1} cm^{-1})	Solution E_{optgap}	Film E_{optgap}	HOMO	LUMO
PDIN-FB	515	85,238	2.33 eV	2.22 eV	–5.9	–3.6
PDIN-B	520	74,489	2.31 eV	2.18 eV	–5.9	–3.6
CN-PDIN-FB	528	78,119	2.26 eV	2.13 eV	–6.1	–3.8
CN-PDIN-B	533	59,485	2.24 eV	2.09 eV	–6.1	–3.8

PDIN-FB has the highest ε at 85,238 M^{-1} cm^{-1}, CN-PDIN-FB the second highest ε at 78,119 M^{-1} cm^{-1}, PDIN-B the third highest ε at 74,489 M^{-1} cm^{-1}, and CN-PDIN-B the lowest ε at 59,485 M^{-1} cm^{-1}.

In terms of film spectra, all four materials were cast from a solution at a concentration of 1 mg/mL in ethyl acetate, where a concentration of 1 mg/mL was used due to CN-PDIN-FB exhibiting a maximum solubility of 1.2 mg/mL (see below). The PDIN-B film has the highest absorbance of 0.037 at its λ_{max} of 535 nm for the 0 → 0 transition and an onset of 570 nm (2.18 eV), the PDIN-FB film has the second highest absorbance of 0.030 at a λ_{max} of 495 nm for the 0 → 1 transition and an onset of 559 nm (2.22 eV), the CN-PDIN-B film has the third highest absorbance of 0.020 at a λ_{max} of 515 nm for the 0 → 1 transition and an onset of 593 nm (2.09 eV), and the CN-PDIN-FB film has the lowest absorbance of 0.017 at its λ_{max} of 509 nm for the 0 → 1 transition and an onset of 580 nm (2.13 eV). The film spectra (Figure 3) suggest that PDIN-B forms the thickest films while CN-PDIN-FB forms the thinnest films on quartz. The addition of a nitrile functional group impacts the shape of the UV–visible film spectra, leading to ill-defined 0 → 0, 0 → 1, and 0 → 2 transitions, while those without a nitrile group exhibit well-defined 0 → 0 and 0 → 1 transitions. Complex aggregation of these compounds is evident, and no clear indication of H- or J-aggregation can be concluded at this time.

Solution processing

All four compounds are soluble in ethyl acetate, and each was probed for its saturation point. This was done by adding each material to 1 mL of ethyl acetate until solids did not dissolve, where after this each solution was filtered with a 0.22 µm PTFE filter. The absorbance of each saturated solution was measured with a UV–visible spectrophotometer to determine the concentration using the Beer–Lambert law and the previously determined molar extinction coefficients. PDIN-FB reached a saturated solution at a concentration at 8.4 mg/mL, PDIN-B a saturated solution at 19.4 mg/mL, CN-PDIN-FB a saturated solution at 3.2 mg/mL, and CN-PDIN-FB a saturated solution at 1.2 mg/mL. The compounds are also soluble in other organic solvents such as toluene, *o*-xylenes, and chloroform at concentrations of >100 mg/mL. However, in conventional OPVs, it is critical that the CIL is cast from a solvent that does not dissolve the bottom layers as keeping each layer discrete is crucial for device performance. Therefore, ethyl acetate as a processing solvent for the CILs is ideal as films of PM6:Y6 are highly solvent resistant to ethyl acetate, and because the CILs are coated onto of the BHJ in this case [19]. Furthermore, ethyl acetate is considered a green solvent due to its low toxicity and minimal associated hazards [20,22,29]. We note that each compound has minimal solubility in methanol, the most common processing solvent for CILs, and instead encourage the use of other organic materials that are soluble in ethyl acetate as CILs in conventional type OPVs. Films of each CIL on quartz substrates processed from 1 mg/mL solutions in ethyl acetate are pictured in Supporting Information File 1, Figure S26.

Electrochemical properties

The electrochemical properties of the four CILs were probed using solution cyclic voltammetry (CV; Figure 4) and differential pulse voltammetry (DPV; Supporting Information File 1, Figures S27–S30), using dichloromethane as the solvent. For all reversible reduction or oxidation waves, HOMO and LUMO energy levels were determined using $E_{1/2}$ values with Fc/Fc$^+$ as the internal standard. All compounds exhibit two reversible reduction waves, where only PDIN-FB and PDIN-B exhibit a reversible oxidation wave. For CN-PDIN-FB and CN-PDIN-B, the HOMO is estimated using the optical band gap by subtracting the value in eV from the LUMO. This results in HOMO energy levels of −5.9 eV, −5.9 eV, −6.1 eV, and −6.1 eV for PDIN-FB, PDIN-B, CN-PDIN-FB, and CN-PDIN-B, respectively. Additionally, this results in LUMO energy levels of −3.6 eV, −3.6 eV, −3.8 eV, and −3.8 eV for PDIN-FB, PDIN-B, CN-PDIN-FB, and CN-PDIN-B, respectively. Both the HOMO and LUMO energy levels were confirmed using DPV, which are in agreeance with all values determined using CV (Supporting Information File 1, Figures S27–S30). The presence of a nitrile functional group stabilizes the FMOs in both CN-PDIN-FB and CN-PDIN-B by a factor of −0.2 eV (for both the HOMO and LUMO) when compared to PDIN-FB and PDIN-B, respectively. When comparing the benzyl versus pentafluorobenzyl groups, the FMOs are not significantly changed.

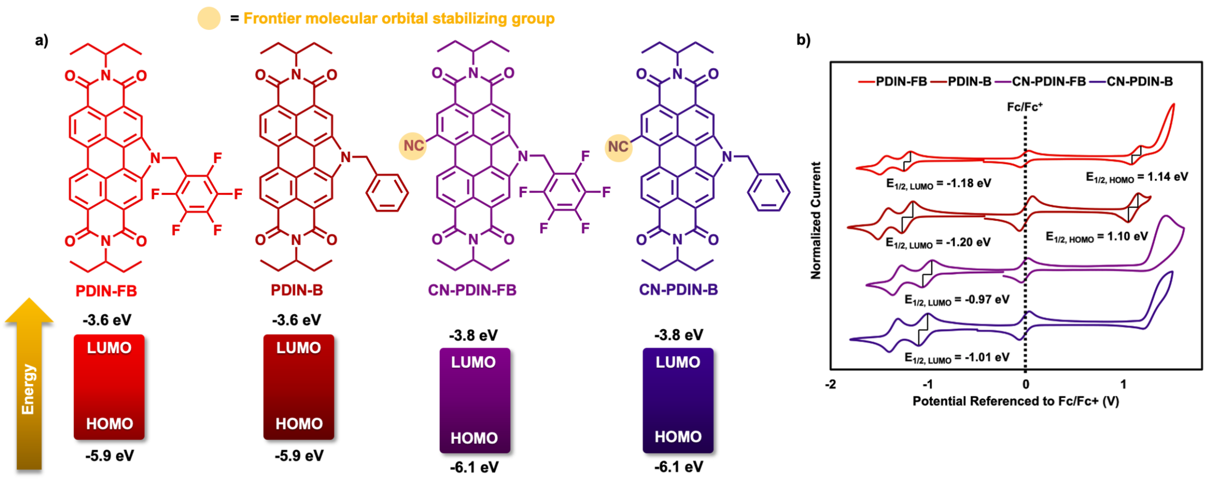

Figure 4: a) PDIN-FB, PDIN-B, CN-PDIN-FB, and CN-PDIN-B structures with their respective HOMO/LUMO level energies determined from CV $E_{1/2}$ values. b) Corresponding CVs for PDIN-FB, PDIN-B, CN-PDIN-FB, and CN-PDIN-B with $E_{1/2}$ values.

Photovoltaic device performance

OPV devices were fabricated using PDIN-FB, PDIN-B, CN-PDIN-FB, and CN-PDIN-B individually as CILs in conventional architecture devices with a layer stack of glass/ITO/PEDOT:PSS/PM6:Y6/CIL/Ag (Figure 5b). See Supporting Information File 1 for full device fabrication details. The BHJ materials, PM6:Y6 (Figure 5a), were selected due to their high photovoltaic performance and solvent resistance to ethyl acetate [19]. The energy level diagram of each respective layer in the device are represented in Figure 5c, where PEDOT:PSS, PM6, and Y6 work function and energy levels were taken from literature [17,30].

We evaluated the current density–voltage (*J*–*V*) in the dark and under illumination (AM1.5 G at 100 mW/cm^2), and we also assessed the devices' external quantum efficiency (EQE), which can be seen in Figure 6a and 6b. To make the necessary adjustments to the PCE, integrated J_{SC} (Supporting Information File 1, Figure S31) is computed for devices with their EQE values determined [31]. The estimated values of J_{SC} are consistent with those measured under an illumination similar to that of the sun. Table 2 provides a summary of all of the optoelectrical and photovoltaic characteristics that were derived from the measurements of sun *I*–*V* and EQE. All of the devices behaved like diodes, as shown by the dark *I*–*V* characteristics (Figure 6c), with a rectification ratio that was higher than three orders of magnitude when comparing the current density under reverse bias and forward bias and a blocking behavior that was reasonable when the current was flowing in the opposite direction. The solar cell devices exhibit good PCEs, approximately 14%, decent FF (≈65%), and J_{SC} (25 mA/cm^2). Figure S32 in Supporting Information File 1 displays the statistical evaluation of the photovoltaic (PV) parameters acquired from the *I*–*V* characteristics, and Supporting Information File 1, Table S1 summarizes the average PV parameters with standard deviation.

All of the devices are comparable to the PFN-Br CIL, which is the one that is employed the most for PM6:Y6 OPVs. PFN-Br is most often processed from methanol [32], which is a solvent that is not well suited for the production of large-area or environmentally friendly devices owing to a high vapor pressure that can lead to precipitation during coating and due to being a highly flammable and toxic solvent [20,33,34]. Figure S33 in Supporting Information File 1 compares the *J*–*V* characteristics of all N-annulated perylene diimides-based CILs cast from ethyl acetate and PFN-Br cast from methanol.

Figure 6d is a plot in double logarithmic scales that depicts the photocurrent density (J_{ph}) as a function of the effective voltage (V_{eff}). This was conducted to investigate the charge generation and extraction processes further. The J_{ph} was determined by

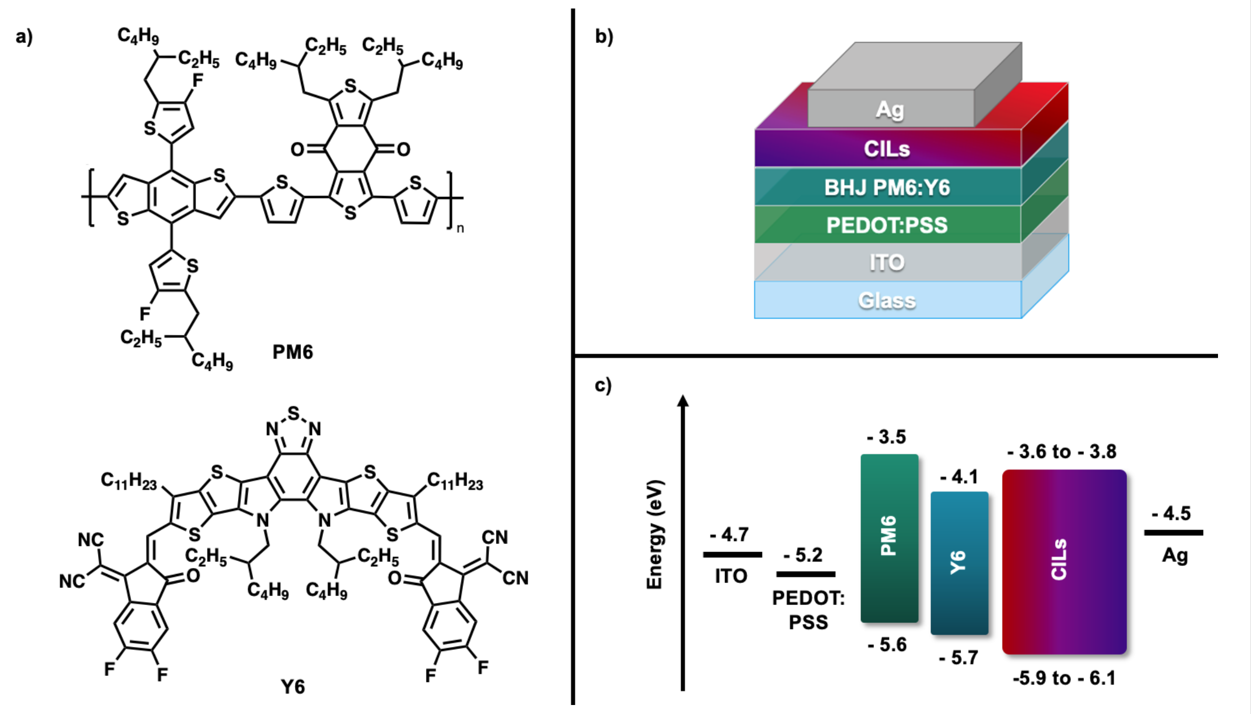

Figure 5: a) Chemical structures of BHJ donor material PM6 and acceptor material Y6, b) conventional OPV device structure used in this study, and c) the work functions of ITO, PEDOT:PSS, and Ag [30], as well as the energy levels of PM6, Y6, and the energy level range for the CILs used in this study.

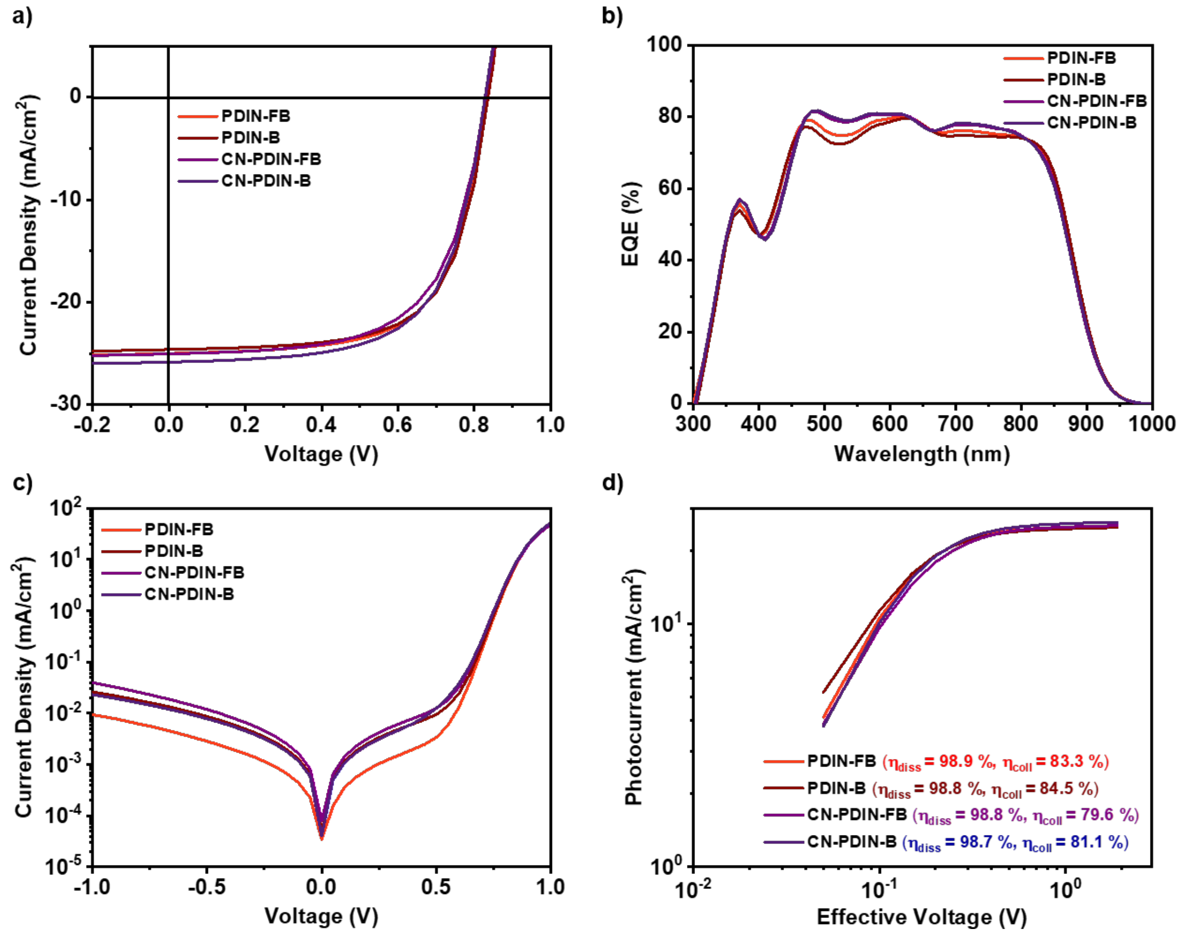

Figure 6: a) Current density-voltage (*I*–*V*) characterization under illumination, b) spectral response of the solar cells, c) *I*–*V* characteristics under dark, d) photocurrent vs effective voltage.

Table 2: Photovoltaic parameters corresponding to the OSCs varying CILs as cathode interlayers (EQE corrected). Here, the short circuit current is J_{SC}; the open circuit voltage is V_{OC}; the fill factor is FF, and the power conversion efficiency is η.

CIL	J_{SC} (mA/cm²)	J_{SC} (EQE) (mA/cm²)	V_{OC} (mV)	FF (%)	η (%)	η (EQE) (%)
PDIN-FB	24.99	**24.05**	835	65.5	13.67	**13.2**
PDIN-B	24.59	**23.85**	838	66.2	13.64	**12.4**
CN-PDIN-FB	25.02	**24.28**	831	62.9	13.07	**12.7**
CN-PDIN-B	25.807	**24.29**	831	64.1	13.74	**13.0**

subtracting the *J*–*V* characteristics measured in the light from those measured in the dark using the formula $J_{ph} = J_L - J_D$, where J_L denotes the current density measured in the light, and J_D represents the current density measured in the dark. The voltage (V_0) that prevails when J_{ph} is equal to zero was used in the calculation for V_{eff}, and the resulting value was then subtracted from the applied bias voltage (V_A). The exciton dissociation efficiency ($\eta_{diss} = J_{SC}/J_{sat}$) and the charge collecting efficiency ($\eta_{coll} = J_{MPP}/J_{sat}$) were calculated based on the conditions of a short circuit and the maximum power point, respectively. Supporting Information File 1 (section 12) provides a description of each step of the calculation procedure in detail [35]. All the devices exhibited a dissociation efficiency of more than 98% and a charge collection efficiency of more than 80%, confirming the moderate J_{SC} and FF acquired from the device. The devices showed no barriers between the active layer and the CIL interface, indicating efficient charge extractions.

In addition, to further confirm the charge extraction and recombination, the PAIOS (platform for all-in-one characterization of solar cells) tool from Fluxim was used to measure transient photocurrent (TPC) and light intensity-dependent IV (LID-IV) measurements. TPC measurements were performed to verify charge carrier transport properties, and current decay was monitored after 500 µs pulse. The normalized TPC data for all the devices is shown in Supporting Information File 1, Figure S34a. The photocurrent decay time under short circuit conditions is very similar for all devices, and we can see that most of the charges are extracted within two µs, thus indicating more significant extraction at the interface. *J–V* measurements based on the light's intensity were carried out to determine the possible recombination process that can occur within the device. The slope (alpha) was generated from the log–log plot shown in Supporting Information File 1, Figure S34b by applying a straightforward power law dependency to the J_{SC} vs light intensity (I) data. This dependence was written as $J_{SC} \propto I^{\alpha}$. The number of α near 1 suggests that non-geminate recombination does not substantially influence the J_{SC} at the recorded light intensity [36,37].

Conclusion

To summarize, four new CIL materials based on N-annulated perylene diimides were synthesized, structurally characterized, probed for their physical and chemical properties, and validated as electron transporting films by implementation in conventional OPV devices. In terms of device performance, the CIL is one of the crucial parameters influencing the quality of devices' extraction and, ultimately, the FF. The scope of this article is inadequate for a detailed investigation of the processes involved in the formation of the interfacial layer between the donor–acceptor and the charge transport layer. Nevertheless, based on all the optoelectrical characterization, proposed N-annulated perylene diimides-based CILs are suitable candidates for CILs that can be replaced with any traditional transport layer and are applicable for a wide range of high-efficiency OPVs. Furthermore, the CILs processed from ethyl acetate can be applied to fabricating fully environmentally friendly OPVs based on eco-friendly or green solvents, especially for indoor applications.

Supporting Information

Supporting Information File 1

Experimental part.
[https://www.beilstein-journals.org/bjoc/content/supplementary/1860-5397-19-119-S1.pdf]

Funding

This work was supported by the NSERC Green Electronics Network (GreEN) (NETGP 508526-17), NSERC DG program (2019-04392), the NSERC I2I Program (I2IPJ 561742-2021), the Canada Foundation for Innovation, the Western Economic Development fund, and the University of Calgary. This work was partially supported by the King Abdullah University of Science and Technology (KAUST) Office of Sponsored Research (OSR) under Award No. OSR-2018-CARF/CCF-3079. SA and FL are very grateful for the financial support for conducting the research.

ORCID® iDs

Kathryn M. Wolfe - https://orcid.org/0000-0002-6501-373X
Shahidul Alam - https://orcid.org/0000-0001-8491-2805
Maryam Alqurashi - https://orcid.org/0000-0002-7089-7445
Frédéric Laquai - https://orcid.org/0000-0002-5887-6158
Gregory C. Welch - https://orcid.org/0000-0002-3768-937X

References

1. Bernardo, G.; Lopes, T.; Lidzey, D. G.; Mendes, A. *Adv. Energy Mater.* **2021,** *11,* 2100342. doi:10.1002/aenm.202100342
2. Xie, L.; Song, W.; Ge, J.; Tang, B.; Zhang, X.; Wu, T.; Ge, Z. *Nano Energy* **2021,** *82,* 105770. doi:10.1016/j.nanoen.2021.105770
3. Xue, P.; Cheng, P.; Han, R. P. S.; Zhan, X. *Mater. Horiz.* **2022,** *9,* 194–219. doi:10.1039/d1mh01317c
4. Zhang, S.; Ye, L.; Zhang, H.; Hou, J. *Mater. Today* **2016,** *19,* 533–543. doi:10.1016/j.mattod.2016.02.019
5. Alam, S.; Islam, M. M.; Chowdhury, S.; Meitzner, R.; Kästner, C.; Schubert, U. S.; Hoppe, H. *Energy Technol. (Weinheim, Ger.)* **2020,** *8,* 2000116. doi:10.1002/ente.202000116
6. Fu, J.; Fong, P. W. K.; Liu, H.; Huang, C.-S.; Lu, X.; Lu, S.; Abdelsamie, M.; Kodalle, T.; Sutter-Fella, C. M.; Yang, Y.; Li, G. *Nat. Commun.* **2023,** *14,* 1760. doi:10.1038/s41467-023-37526-5
7. Lee, S.; Jeong, D.; Kim, C.; Lee, C.; Kang, H.; Woo, H. Y.; Kim, B. J. *ACS Nano* **2020,** *14,* 14493–14527. doi:10.1021/acsnano.0c07488
8. Wadsworth, A.; Moser, M.; Marks, A.; Little, M. S.; Gasparini, N.; Brabec, C. J.; Baran, D.; McCulloch, I. *Chem. Soc. Rev.* **2019,** *48,* 1596–1625. doi:10.1039/c7cs00892a
9. Zhao, F.; Zhou, J.; He, D.; Wang, C.; Lin, Y. *J. Mater. Chem. C* **2021,** *9,* 15395–15406. doi:10.1039/d1tc04097a
10. Yin, Z.; Wei, J.; Zheng, Q. *Adv. Sci.* **2016,** *3,* 1500362. doi:10.1002/advs.201500362
11. Ahmad, N.; Zhou, H.; Fan, P.; Liang, G. *EcoMat* **2022,** *4,* e12156. doi:10.1002/eom2.12156
12. Yao, J.; Chen, Q.; Zhang, C.; Zhang, Z.-G.; Li, Y. *SusMat* **2022,** *2,* 243–263. doi:10.1002/sus2.50
13. Shin, Y. S.; Yoon, Y. J.; Heo, J.; Song, S.; Kim, J. W.; Park, S. Y.; Cho, H. W.; Kim, G.-H.; Kim, J. Y. *ACS Appl. Mater. Interfaces* **2020,** *12,* 35740–35747. doi:10.1021/acsami.0c09968
14. Zhang, Z.-G.; Qi, B.; Jin, Z.; Chi, D.; Qi, Z.; Li, Y.; Wang, J. *Energy Environ. Sci.* **2014,** *7,* 1966. doi:10.1039/c4ee00022f
15. Yao, J.; Qiu, B.; Zhang, Z.-G.; Xue, L.; Wang, R.; Zhang, C.; Chen, S.; Zhou, Q.; Sun, C.; Yang, C.; Xiao, M.; Meng, L.; Li, Y. *Nat. Commun.* **2020,** *11,* 2726. doi:10.1038/s41467-020-16509-w

16. Song, H.; Hu, D.; Lv, J.; Lu, S.; Haiyan, C.; Kan, Z. *Adv. Sci.* **2022,** *9,* 2105575. doi:10.1002/advs.202105575
17. Yuan, J.; Zhang, Y.; Zhou, L.; Zhang, G.; Yip, H.-L.; Lau, T.-K.; Lu, X.; Zhu, C.; Peng, H.; Johnson, P. A.; Leclerc, M.; Cao, Y.; Ulanski, J.; Li, Y.; Zou, Y. *Joule* **2019,** *3,* 1140–1151. doi:10.1016/j.joule.2019.01.004
18. Farahat, M. E.; Anderson, M. A.; Martell, M.; Ratcliff, E. L.; Welch, G. C. *ACS Appl. Mater. Interfaces* **2022,** *14,* 43558–43567. doi:10.1021/acsami.2c12281
19. Hoff, A.; Martell, M.; Gasonoo, A.; Koenig, J. D. B.; Simón Marqués, P.; Cieplechowicz, E.; Pahlevani, M.; Welch, G. C. *Adv. Eng. Mater.* **2023,** *25,* 2201437. doi:10.1002/adem.202201437
20. Prat, D.; Hayler, J.; Wells, A. *Green Chem.* **2014,** *16,* 4546–4551. doi:10.1039/c4gc01149j
21. Clarke, C. J.; Tu, W.-C.; Levers, O.; Bröhl, A.; Hallett, J. P. *Chem. Rev.* **2018,** *118,* 747–800. doi:10.1021/acs.chemrev.7b00571
22. Armenta, S.; Esteve-Turrillas, F. A.; Garrigues, S.; de la Guardia, M. *Green Anal. Chem.* **2022,** *1,* 100007. doi:10.1016/j.greeac.2022.100007
23. Nazari, M.; Martell, M.; Welsh, T. A.; Melville, O.; Li, Z.; Cann, J.; Cieplechowicz, E.; Zou, Y.; Lessard, B. H.; Welch, G. C. *Mater. Chem. Front.* **2018,** *2,* 2272–2276. doi:10.1039/c8qm00487k
24. Harding, C. R.; Cann, J.; Laventure, A.; Sadeghianlemraski, M.; Abd-Ellah, M.; Rao, K. R.; Gelfand, B. S.; Aziz, H.; Kaake, L.; Risko, C.; Welch, G. C. *Mater. Horiz.* **2020,** *7,* 2959–2969. doi:10.1039/d0mh00785d
25. Anthony, J. E.; Facchetti, A.; Heeney, M.; Marder, S. R.; Zhan, X. *Adv. Mater. (Weinheim, Ger.)* **2010,** *22,* 3876–3892. doi:10.1002/adma.200903628
26. Würthner, F.; Saha-Möller, C. R.; Fimmel, B.; Ogi, S.; Leowanawat, P.; Schmidt, D. *Chem. Rev.* **2016,** *116,* 962–1052. doi:10.1021/acs.chemrev.5b00188
27. Jones, B. A.; Facchetti, A.; Wasielewski, M. R.; Marks, T. J. *J. Am. Chem. Soc.* **2007,** *129,* 15259–15278. doi:10.1021/ja075242e
28. Park, I. E.; Brixi, S.; Martell, M.; Ocheje, M. U.; Pettipas, R. D.; Harris, D. H.; Gelfand, B. S.; Rondeau-Gagné, S.; Lessard, B. H.; Welch, G. C. *J. Mater. Chem. C* **2021,** *9,* 13630–13634. doi:10.1039/d1tc03873g
29. Hong, S. U.; Wang, Y.; Soh, L. S.; Yong, W. F. *Green Chem.* **2023,** *25,* 4501–4512. doi:10.1039/d3gc00776f
30. Sokeng Djoumessi, A.; Madalaimuthu, J. P.; Alam, S.; Anand, A.; Sichwardt, A.; Fischer, P.; Rösch, R.; Schubert, U. S.; Hoppe, H. *Adv. Mater. Interfaces* **2022,** *9,* 2201150. doi:10.1002/admi.202201150
31. Alam, S.; Gavrik, A.; Meitzner, R.; Hoeppener, S.; Dyakonov, V.; Baumann, A.; Schubert, U. S.; Hoppe, H. *J. Phys. D: Appl. Phys.* **2019,** *52,* 475501. doi:10.1088/1361-6463/ab3b73
32. Karuthedath, S.; Firdaus, Y.; Scaccabarozzi, A. D.; Nugraha, M. I.; Alam, S.; Anthopoulos, T. D.; Laquai, F. *Small Struct.* **2022,** *3,* 2100199. doi:10.1002/sstr.202100199
33. C, A.; Dubey, D. K.; Pahlevani, M.; Welch, G. C. *Adv. Mater. Technol. (Weinheim, Ger.)* **2021,** *6,* 2100264. doi:10.1002/admt.202100264
34. Kong, T.; Wang, H.; Zhang, W.; Fan, P.; Yu, J. *J. Phys. D: Appl. Phys.* **2019,** *52,* 195104. doi:10.1088/1361-6463/ab092b
35. Alam, S.; Anand, A.; Islam, M. M.; Meitzner, R.; Djoumessi, A. S.; Slowik, J.; Teklu, Z.; Fischer, P.; Kästner, C.; Khan, J. I.; Schubert, U. S.; Laquai, F.; Hoppe, H. *J. Photonics Energy* **2022,** *12,* 035501. doi:10.1117/1.jpe.12.035501
36. Koster, L. J. A.; Mihailetchi, V. D.; Ramaker, R.; Blom, P. W. M. *Appl. Phys. Lett.* **2005,** *86,* 123509. doi:10.1063/1.1889240
37. Sokeng Djoumessi, A.; Alam, S.; Madalaimuthu, J. P.; Anand, A.; Slowik, J.; Pflug, T.; Meitzner, R.; Roesch, R.; Gnecco, E.; Horn, A.; Schubert, U. S.; Hoppe, H. *Energy Technol.* **2021,** *9,* 2100474. doi:10.1002/ente.202100474

License and Terms

The definitive version of this article is the electronic one which can be found at:
https://doi.org/10.3762/bjoc.19.119

BEILSTEIN JOURNAL OF ORGANIC CHEMISTRY

Benzoimidazolium-derived dimeric and hydride n-dopants for organic electron-transport materials: impact of substitution on structures, electrochemistry, and reactivity

Swagat K. Mohapatra*[1,2], Khaled Al Kurdi[1], Samik Jhulki[1], Georgii Bogdanov[3], John Bacsa[4], Maxwell Conte[1], Tatiana V. Timofeeva[3], Seth R. Marder*[1,5,6,7] and Stephen Barlow*[1,5,7]

Full Research Paper

Address:
[1]Center for Organic Photonics and Electronics and School of Chemistry and Biochemistry, Georgia Institute of Technology, Atlanta, GA 80007, United States, [2]Department of Industrial and Engineering Chemistry, Institute of Chemical Technology—Indian Oil Campus, ITT Kharagpur Extension Center, Bhubaneswar 751013 Odisha, India, [3]Department of Chemistry, New Mexico Highlands University, Las Vegas, New Mexico 87701, United States, [4]Crystallography Lab, Emory University, Atlanta, Georgia 30322, United States, [5]Renewable and Sustainable Energy Institute (RASEI), University of Colorado Boulder, Boulder, Colorado 80309, United States, [6]Department of Chemical and Biological Engineering and Department of Chemistry, University of Colorado Boulder, Boulder, Colorado 80309, United States and [7]National Renewable Energy Laboratory, Chemistry and Nanoscience Center, Golden, Colorado, 80401, United States

Email:
Swagat K. Mohapatra* - sk.mohapatra@iocb.ictmumbai.edu.in; Seth R. Marder* - seth.marder@colorado.edu; Stephen Barlow* - stephen.barlow@colorado.edu

* Corresponding author

Keywords:
benzoimidazole; crystal structure; kinetics; n-dopant; reduction

Beilstein J. Org. Chem. **2023,** *19,* 1651–1663.
https://doi.org/10.3762/bjoc.19.121

Received: 09 August 2023
Accepted: 17 October 2023
Published: 01 November 2023

This article is part of the thematic issue "Organic electron transport materials".

Associate Editor: P. J. Skabara

Abstract

1,3-Dimethyl-2,3-dihydrobenzo[*d*]imidazoles, **1H**, and 1,1',3,3'-tetramethyl-2,2',3,3'-tetrahydro-2,2'-bibenzo[*d*]imidazoles, $\mathbf{1_2}$, are of interest as n-dopants for organic electron-transport materials. Salts of 2-(4-(dimethylamino)phenyl)-4,7-dimethoxy-, 2-cyclohexyl-4,7-dimethoxy-, and 2-(5-(dimethylamino)thiophen-2-yl)benzo[*d*]imidazolium ($\mathbf{1g{-}i^+}$, respectively) have been synthesized and reduced with $NaBH_4$ to **1gH**, **1hH**, and **1iH**, and with Na:Hg to $\mathbf{1g_2}$ and $\mathbf{1h_2}$. Their electrochemistry and reactivity were compared to those derived from 2-(4-(dimethylamino)phenyl)- ($\mathbf{1b^+}$) and 2-cyclohexylbenzo[*d*]imidazolium ($\mathbf{1e^+}$) salts. $E(\mathbf{1^+}/\mathbf{1^\bullet})$ values for 2-aryl species are less reducing than for 2-alkyl analogues, i.e., the radicals are stabilized more by aryl groups than the cations, while 4,7-dimethoxy substitution leads to more reducing $E(\mathbf{1^+}/\mathbf{1^\bullet})$ values, as well as cathodic shifts in $E(\mathbf{1_2}^{\bullet+}/\mathbf{1_2})$ and $E(\mathbf{1H}^{\bullet+}/\mathbf{1H})$ values. Both the use of 3,4-dimethoxy and 2-aryl substituents accelerates the reaction of the **1H** species with $PC_{61}BM$. Because 2-aryl groups stabilize radicals, $\mathbf{1b_2}$ and $\mathbf{1g_2}$ exhibit weaker bonds than $\mathbf{1e_2}$ and $\mathbf{1h_2}$ and thus react with 6,13-bis(triisopropylsilylethynyl)pentacene (**VII**) via a “cleavage-first” pathway, while $\mathbf{1e_2}$ and $\mathbf{1h_2}$ react only via “electron-transfer-first”. $\mathbf{1h_2}$ exhibits the most cathodic $E(\mathbf{1_2}^{\bullet+}/\mathbf{1_2})$ value of the dimers considered here and, therefore, reacts more rapidly than any of the other dimers with **VII** via “electron-transfer-first”. Crystal structures show rather long central C–C bonds for $\mathbf{1b_2}$ (1.5899(11) and 1.6194(8) Å) and $\mathbf{1h_2}$ (1.6299(13) Å).

Introduction

Electrical doping of organic semiconductors can play an important role in tuning the properties of organic semiconductors for a variety of applications [1-5]. The most straightforward n-dopants for doping electron-transporting materials are simple one-electron reductants; however, to be effective for a wide range of semiconductors, they must exhibit low ionization energies and thus air sensitivity. One approach to circumvent this issue is to identify systems where the electron-transfer process is coupled to other chemical reactions, increasing the kinetic stability of the dopant to air, and thus increasing its ease of storage and handling.

Arguably, the most widely investigated air-inert n-dopants are 1,3-dimethyl-2,3-dihydrobenzo[*d*]imidazoles (DMBI-H, **1H**, Figure 1); these species have been known for decades (e.g., **1aH**, one of the simplest such derivatives, was first reported in 1954 [6]), but were only introduced in n-dopants in 2010, when Bao and co-workers reported the use of N-DMBI-H (**1bH**, Figure 1) to n-dope fullerenes [7]. Although widely used, due to their facile synthesis, structural tunability, and good air stability in the solid state, **1H** derivatives are relatively limited in dopant strength and their reactivity with organic semiconductors (SC) does not depend solely on the SC reduction potential, since the first step, at least in many cases, is a hydride transfer rather than an electron transfer [8,9]. Moreover, as well forming the desired semiconductor radical anion $SC^{\bullet-}$, and the stable $DMBI^+$ ($\mathbf{1}^+$) species, a hydrogen atom must be lost from the dopant, in some cases resulting in the incorporation of hydrogen-reduced side products into the semiconductor film [9], although in other cases it may be lost as H_2 [8,10,11].

The first report of a $(DMBI)_2$ dimer ($\mathbf{1_2}$, Figure 1) was of $\mathbf{1a_2}$ in 1984 [12]. More recently, dimers $\mathbf{1b_2}$–$\mathbf{1f_2}$ (Figure 1) have been used as n-dopants [13-20]. They behave similarly to the closed-shell dimers formed by certain 19-electron transition-metal sandwich compounds [21-23], exhibiting moderate air stability and acting as quite strong dopants, reacting with semiconductors more rapidly and predictably than hydride donors such as the corresponding **1H** species [8], cleanly only to give $SC^{\bullet-}$ and the corresponding monomeric cations. However, $\mathbf{1_2}$ dopants offer the possibility of more planar dopant ions than the organometallic dimers, which can be advantageous [19].

Although the impact of different 2-aryl Y groups on the reactivity of **1H** species have been examined [9,24], there has been no direct comparison of the solution reactivity (or doping behavior) of **1H** or $\mathbf{1_2}$ reductants with Y = aryl substituents to that of their Y = alkyl counterparts, while there has also been limited effort on examining the effects of substituents on the benzimidazole 6-membered ring in either class of reductant [16,24]. Furthermore, there has been little work on Y = 2-thienyl **1H** derivatives. Here, we report two new dimers ($\mathbf{1g_2}$ and $\mathbf{1h_2}$) and three new hydride donors (**1gH**, **1hH**, **1iH**). We also report crystal structures of several of these compounds and of several salts of the corresponding $\mathbf{1}^+$ cations, and compare the electrochemistry and reactivity of these species.

Results and Discussion

Synthesis

Although an unsymmetrical $\mathbf{1_2}$-like molecule, 2-diethoxyphosphoryl-1,1',3,3'-tetramethyl-2,2',3,3'-tetrahydro-2,2'-bibenzo[*d*]imidazole, has been obtained from addition of HPO_3Et_2 across the central C=C bond of bis(1,3-dimethylbenzoimidazolinidin-2-ylidene) [25], $\mathbf{1_2}$ dimers have generally been obtained by reductive electrochemical or chemical dimerization of $\mathbf{1}^+$ cations [12,13,16,19,26]. **1H** derivatives can be obtained in a number of ways, including direct condensation of *N,N'*-dimethylphenylene-1,2-diamine derivatives with the appropriate aldehydes, YCHO [24,27], or borohydride reduction of $\mathbf{1}^+$ salts [24]. The cations conversely can be obtained from **1H** derivatives, for example through hydride abstraction by Ph_3C^+ [13]. Alternatively, they can also be obtained by condensation of *N,N'*-dimethylphenylene-1,2-diamine derivatives with acid chlorides, YCOCl, or through the methylation of 2-substituted benzoimidazoles [24], which in turn can be obtained from condensation between phenylene-1,2-diamines and carboxylic acids YCO_2H [28], oxidative condensation between YCHO and phenylene-1,2-diamines [29], or reductive condensation between YCHO and 2-nitroanilines [24].

In this work we condensed the appropriate YCHO aldehyde (**II**) and 1,2-diaminobenzene (**I**) derivatives in the presence of sodium metabisulfite ($Na_2S_2O_5$) [29] to obtain the corresponding substituted benzimidazoles (**III**) in essentially quantitative yield (Scheme 1). In the absence of $Na_2S_2O_5$, but under otherwise similar conditions, we obtained in some cases the imines in which one of the amino groups condenses with the aldehyde but where the subsequent second condensation and oxidation does not take place, i.e., structures of type **IV** (Scheme 1), which are known to be converted to benzimidazoles by various oxidants

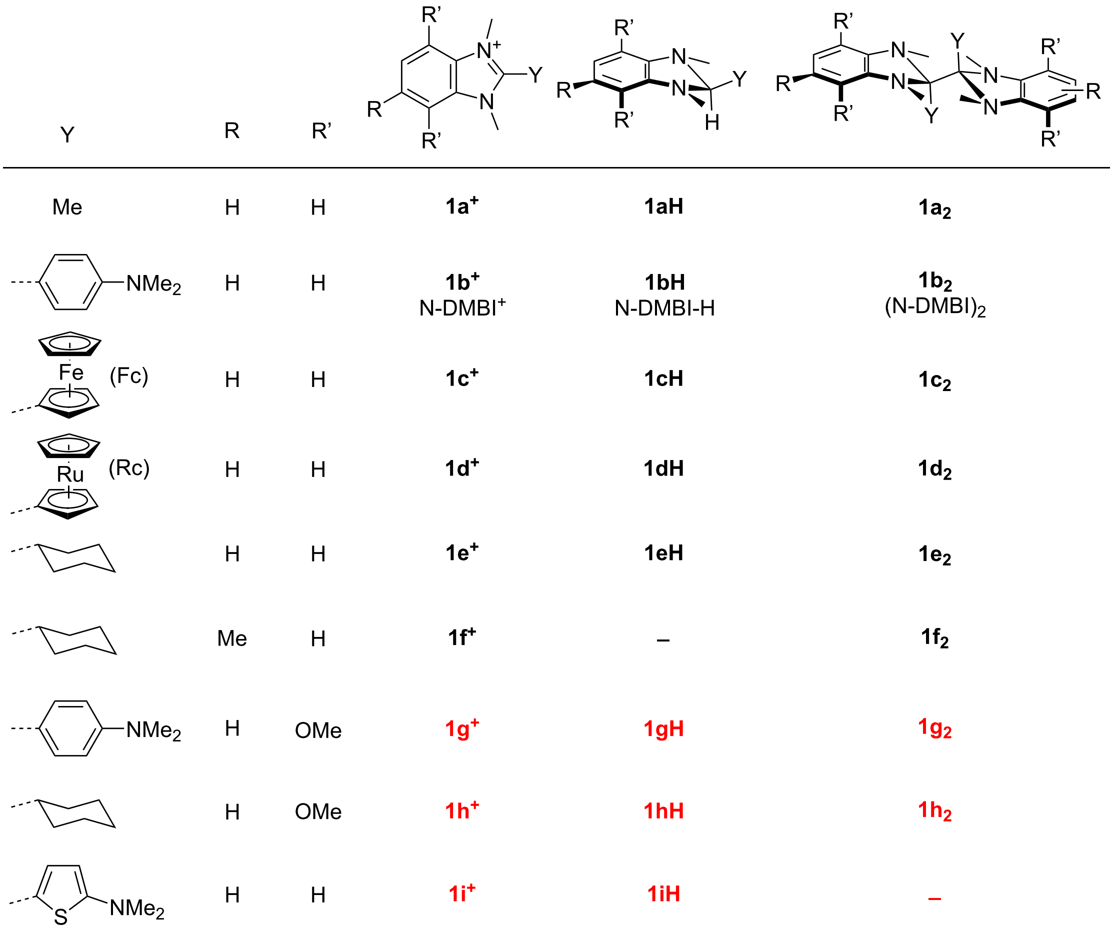

Y	R	R'			
Me	H	H	$\mathbf{1a^+}$	**1aH**	$\mathbf{1a_2}$
NMe$_2$	H	H	$\mathbf{1b^+}$ N-DMBI$^+$	**1bH** N-DMBI-H	$\mathbf{1b_2}$ (N-DMBI)$_2$
Fe (Fc)	H	H	$\mathbf{1c^+}$	**1cH**	$\mathbf{1c_2}$
Ru (Rc)	H	H	$\mathbf{1d^+}$	**1dH**	$\mathbf{1d_2}$
	H	H	$\mathbf{1e^+}$	**1eH**	$\mathbf{1e_2}$
	Me	H	$\mathbf{1f^+}$	–	$\mathbf{1f_2}$
NMe$_2$	H	OMe	$\mathbf{1g^+}$	**1gH**	$\mathbf{1g_2}$
	H	OMe	$\mathbf{1h^+}$	**1hH**	$\mathbf{1h_2}$
S NMe$_2$	H	H	$\mathbf{1i^+}$	**1iH**	–

Figure 1: DMBI$^+$, DMBI-H, and (DMBI)$_2$ derivatives discussed in this work (new compounds in red).

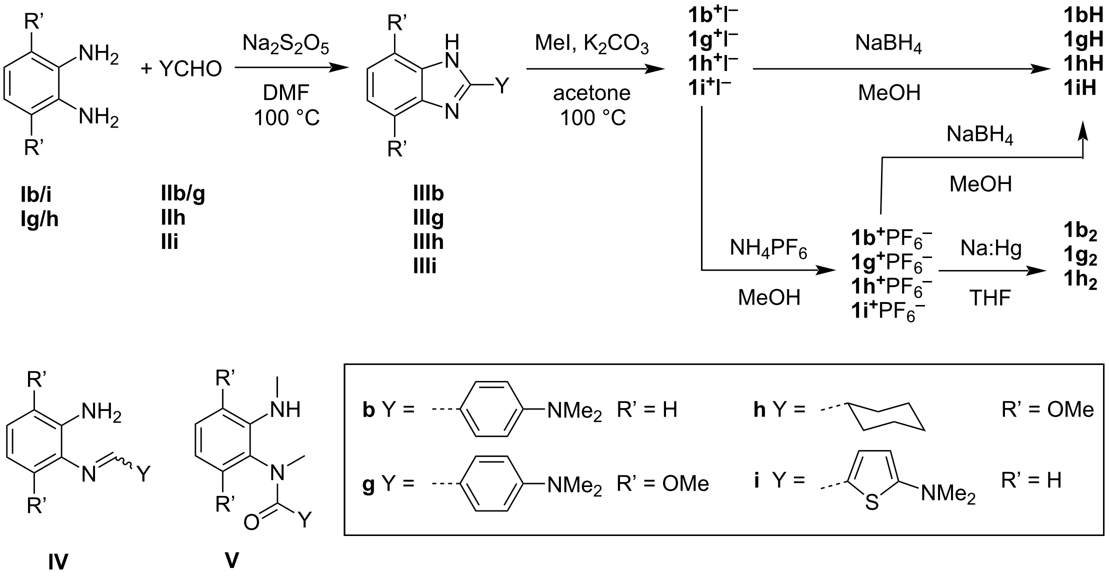

Scheme 1: Synthesis of DMBI-H and (DMBI)$_2$ derivatives and structures of side products.

and/or catalysts [30-32]. The benzimidazoles were then doubly methylated with iodomethane (or methyl tosylate) to afford the benzimidazolium iodides (or tosylates), $\mathbf{1}^+\mathrm{I}^-$ (or $\mathbf{1}^+\mathrm{OTs}^-$), which were metathesized to the corresponding hexafluorophosphates, $\mathbf{1}^+\mathrm{PF}_6^-$. Either I^- or PF_6^- salt can then be converted to the corresponding **1H** derivative using NaBH_4 in MeOH. The PF_6^- salts are somewhat more soluble than the iodides in THF, so were reductively dimerized to $\mathbf{1}_2$ in THF using Na:Hg, although reduction of $\mathbf{1i}^+\mathrm{PF}_6^-$ failed to afford $\mathbf{1i}_2$. As we have noted before for other $\mathbf{1}_2$ species, amides (**V**, Scheme 1) are encountered as both byproducts of dimer synthesis and dimer decomposition products [14]. **V** derivatives have also been obtained as pyrolysis products of a variety of Y = aryl **1H** derivatives [33], while **Vb** has also been found to be both a solution decomposition product of **1bH** [27,34] and a beneficial additive for a **1bH**-doped polymer [27], and has been crystallographically characterized [34]. In the case of molecules with aryl Y-substituents – $\mathbf{1b}_2$ and $\mathbf{1g}_2$ – the room-temperature ^{1}H and ^{13}C NMR spectra (see Supporting Information File 1, Figures S2, S26 and S27, and reference [26]) display more resonances than expected based on the highest symmetry possible for the molecule indicating that the sample represents neither solely a high-symmetry conformer, nor a mixture of rapidly exchanging lower symmetry conformers. In the case of $\mathbf{1b}_2$ all the proton resonances are rather broad, and variable-temperature experiments (see Supporting Information File 1, Figure S2) showed further broadening and then coalescence of some of these peaks on increasing the temperature, consistent with the room-temperature spectrum being affected by restricted rotation; interestingly the crystal structure of $\mathbf{1b}_2$ contains molecules with two very different conformations (see below).

The $\mathbf{1}_2$ dimers are somewhat more sensitive to air than the corresponding **1H** hydrides, but are all sufficiently stable as solids that they can briefly be handled in air, for example, for weighing. The solids do decompose slowly in air, although we have not quantified this; in inert atmosphere, however, they are completely stable (at least 4 months for solid $\mathbf{1b}_2$). Both **1H** and $\mathbf{1}_2$ derivatives decompose more rapidly on exposure to air in solution. In CDCl_3 decomposition is rapid, consistent with the reactivity of many reductants with that solvent. In $\mathrm{C}_6\mathrm{D}_6$ these compounds are more stable, allowing, for example, rapid acquisition of a ^{1}H NMR spectrum; however, handling under nitrogen is advisable as these species completely decompose to **V** (and perhaps $\mathbf{1}^+$ species) on timescales of hours to days (see Supporting Information File 1, Figures S3–S5).

Crystal structures

We have determined the structures of two $\mathbf{1}_2$ dimers, four **1H** derivatives (including **1bH**, the structure of which has previously been reported, but with somewhat lower precision than in the present work [34]), and three salts of $\mathbf{1}^+$ cations using single-crystal X-ray diffraction. Here, we briefly discuss some of the more interesting structural findings; a more detailed comparison of structural parameters is given in the Supporting Information File 1, Table S2. In particular, we are aware of only two previously reported crystal structures of DMBI dimers [14], although several related structures of organic dimers, including those of benzothiazoline, benzoxazoline, acridanyl, morpholinonyl dimers ($\mathbf{2}_2$–$\mathbf{5}_2$, respectively, Figure 2) have been reported in different chemical contexts [35-38]. The crystal structure of $(\mathrm{N\text{-}DMBI})_2$, $\mathbf{1b}_2$ (Figure 3), contains two crystallographically inequivalent molecules that are geometrically rather different from each other. One of the molecules has crystallographic inversion (C_i) symmetry, and approximate molecular C_{2h} symmetry, and so has a perfectly staggered conformation around the central C–C bond and thus a Y–C–C–Y torsion angle of precisely 180°; the structure closely resembles those of the two inequivalent molecules in the structure of the previously reported Y = ferrocenyl derivative, $\mathbf{1c}_2$ [14], or the molecule in the structure $\mathbf{2}_2$ [35], all three of which also have C_i symmetry. The other conformer present, although also staggered, has no crystallographic, or even approximate molecular,

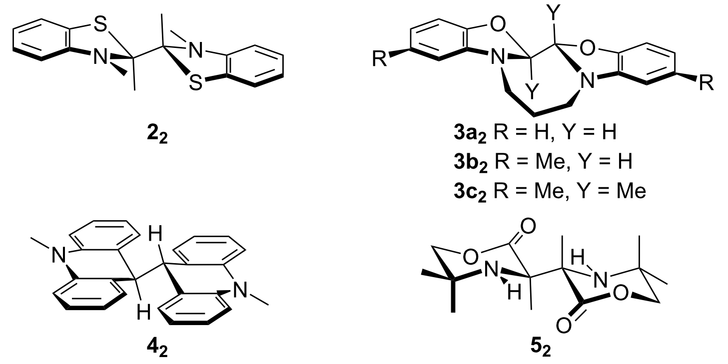

$\mathbf{2}_2$

$\mathbf{3a}_2$ R = H, Y = H
$\mathbf{3b}_2$ R = Me, Y = H
$\mathbf{3c}_2$ R = Me, Y = Me

$\mathbf{4}_2$

$\mathbf{5}_2$

Figure 2: Crystallographically characterized molecules related to DMBI dimers.

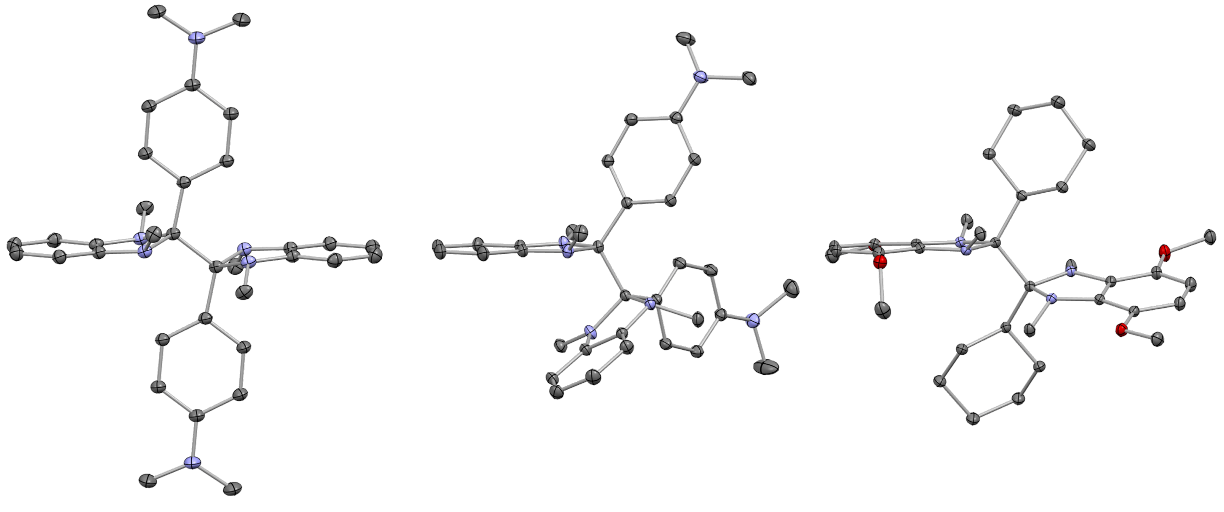

Figure 3: Molecular structures from the single crystal structures of **$1b_2$** (two crystallographically inequivalent molecules, left and center) and **$1h_2$** (right), shown with 50% thermal ellipsoids and excluding disorder in **$1h_2$** and hydrogen atoms for clarity.

symmetry and is characterized by a Y–C–C–Y torsion angle of 60.3°. The conformation found in the structure of the Y = cyclohexyl, R' = OMe derivative, **$1h_2$** (Figure 3), is somewhat similar to that previously reported for its non-methoxylated analogue **$1e_2$** [14]; the **$1h_2$** molecule does not have the crystallographic C_2 symmetry of the latter, but does have approximate molecular C_2 symmetry, while the Y–C–C–Y torsion angles for **$1h_2$** and **$1e_2$** are 149.4° and 140.3°, respectively, and thus both intermediate between the perfectly staggered (180° torsion) and neighboring eclipsed conformation (120°). The imidazole rings in the previously reported and present dimer structures are mostly somewhat folded towards a puckered envelope conformation, generally with the Y group in a pseudo-axial position and the 1,3-methyl groups and the central C–C bond in pseudo-equatorial positions, although for one of the monomers in the unsymmetrical conformer in the structure of $(N\text{-DMBI})_2$, **$1b_2$,** the Y and central bond are pseudo-equatorial and pseudo-axial, respectively. However, this folding is generally much less pronounced than in **1H** derivatives (see below, Figure 4, and Table S2 in Supporting Information File 1) presumably since in the dimers both 2-substituents (Y and the other monomer unit) are fairly bulky, whereas in the hydrides there is a large difference in bulk between the hydridic H-atom and theY-group and thus a strong preference for Y to occupy a pseudo-equatorial position.

As with other **1_2** species [14] and related organic [35,37,38] and organometallic dimers [22,39-46], the central C–C bond of the present dimers are rather long compared to typical C–C bonds, although not remarkably so given that these are hexasubstituted ethane derivatives. Values of 1.5899(11) and 1.6194(8) Å are found for the symmetrical and unsymmetrical conformers of **$1b_2$**, respectively, while a value of 1.6299(13) Å is found for **$1h_2$**; these may be compared to hexasubstituted central C–C bond length values of 1.595(5) and 1.601(5) Å for the two inequivalent molecules of the Y = Fc, R = R' = H derivative **$1c_2$** [14], 1.640(4) Å for the Y = cyclohexyl, R = R' = H derivative **$1e_2$** [14], 1.573 Å for **2_2** [35], and 1.591 Å for **5_2** [38], while $(PhEt_2C)_2$, a simple hexa-substituted ethane, exhibits a central C–C bond length of 1.635 Å [47]. The tetrasubstituted central C–C bond of **4_2** is also rather long (1.58 Å) [37]. Bridged benzoxazoline dimers, **3_2**, have, on the other hand, relatively short C–C central bonds, perhaps due to the influence of the propanediyl tether; the hexasubstituted bond of **$3c_2$** is only 1.549(6) Å in length, while the tetrasubstituted bonds of **$3a_2$** and **$3b_2$** are even shorter [36].

The crystallographically determined central C–C bond lengths for **$1b_2$** are shorter than that previously reported for the Y = cyclohexyl, R = R' = H derivative **$1e_2$** (1.640(4) Å) [14], despite DFT calculations indicating that the former dimer is considerably more weakly bonded [8,14] and kinetic evidence for the "cleavage-first" mechanism occurring in doping reactions using **$1b_2$** but not **$1e_2$** (see below). We have previously noted a similar lack of correlation between bond length and bond dissociation energy in comparing the structures of **$1c_2$** (Y = Fc; R = R' = H) and **$1e_2$** (Y = cyclohexyl; R = R' = H) [14], and in comparing those of different organometallic dimers [22,46]. As noted in our previous work [14,22,46], the bond length depends on orbital overlap and steric strain in the dimer, whereas dissociation energetics also depend on the stability of the monomeric odd-electron species, which vary considerably; in the case of **$1^•$** radicals an important factor is the ability of the Y substituent to delocalize spin density.

The **1H** structures (Figure 4) are similar to those of other DMBI-H structures in the literature [34,48-50] (and are compared in more detail in Supporting Information File 1, Table S2); in all cases the imidazole ring is folded in a “puckered envelope” conformation with the 2-Y and 1,3-dimethyl substituents in pseudo-equatorial positions and the reactive hydridic 2-H-atom pesudo-axial. The cation structures (Figure 5) give some insight into the variety of dopant-ion shapes and sizes that can be afforded by these types of dopants. The angle between the imidazolium ring and the aromatic ring of the $\mathbf{1g}^+\mathrm{I}^-$ is 41.5°, close to the range of values previously reported for $\mathbf{1b}^+$ salts (42.5–52.5°) [19,34] and for salts of Y = Ph, R = R' = H cations with different counterions (42.0–54.9°) [51-53]. As expected, owing to reduced steric interactions associated with the five-membered rather than six-membered aromatic ring, the structure of $\mathbf{1i}^+\mathrm{PF}_6{}^-$ contains a somewhat more planar cation (31.9°). Finally, we note that the new structures reported here mean that the **1b** and **1h** systems join the **1c** (Y = Fc; R = R' = H) system [50] as families for which $\mathbf{1}^+$, **1H**, and $\mathbf{1_2}$ members are all crystallographically characterized.

Electrochemistry

The $\mathbf{1}^+$, **1H**, and $\mathbf{1_2}$ species were investigated using cyclic voltammetry in THF/0.1 M $\mathrm{Bu_4NPF_6}$ at a scan rate of 50 mV s^{-1}. The voltammograms (shown for one series of compounds in Figure 6) were qualitatively similar to those reported and shown elsewhere for other compounds of the same classes [9,13,19,24], and the redox potentials are summarized in Table 1. The cations exhibit features assigned to $E(\mathbf{1}^+/\mathbf{1}^\bullet)$ that are non-reversible owing to the rapid dimerization of $\mathbf{1}^\bullet$. These values are important in determining the overall thermodynamic reducing power of the dimers according to:

$$E(\mathbf{1}^+/0.5\mathbf{1_2}) = E(\mathbf{1}^+/\mathbf{1}^\bullet) + \Delta G_{\mathrm{diss}}(\mathbf{1_2})/2F, \qquad (1)$$

where $\Delta G_{\mathrm{diss}}(\mathbf{1_2})$ is the free-energy change for dissociation of $\mathbf{1_2}$ to $\mathbf{1}^\bullet$ (dissociation energetics are not estimated in the present work, but have been estimated using DFT calculations for $\mathbf{1b–e_2}$ in previous works [8,14] and, in favorable cases, can be experimentally estimated using electron spin resonance [14] or using dissociation and dimerization barriers from reaction kinetics and variable scan-rate electrochemistry, respectively [54]) and where F is the Faraday constant. Similarly, at least for cases where the reactive hydrides of **1H** derivatives are ultimately lost as $\mathrm{H_2}$, the strength of **1H** dopants is given by:

$$\begin{aligned} E(\mathbf{1}^+,0.5\mathrm{H}_2/\mathbf{1H}) = E(\mathbf{1}^+/\mathbf{1}^\bullet) &+ \Delta G_{\mathrm{diss}}(\mathbf{1H})/F \\ &- \Delta G_{\mathrm{diss}}(\mathrm{H}_2)/2F, \end{aligned} \qquad (2)$$

where $\Delta G_{\mathrm{diss}}(\mathbf{1H})$ is the free-energy change for dissociation of **1H** to $\mathbf{1}^\bullet$ and $\mathrm{H}^\bullet$ (again, not discussed in this work), and

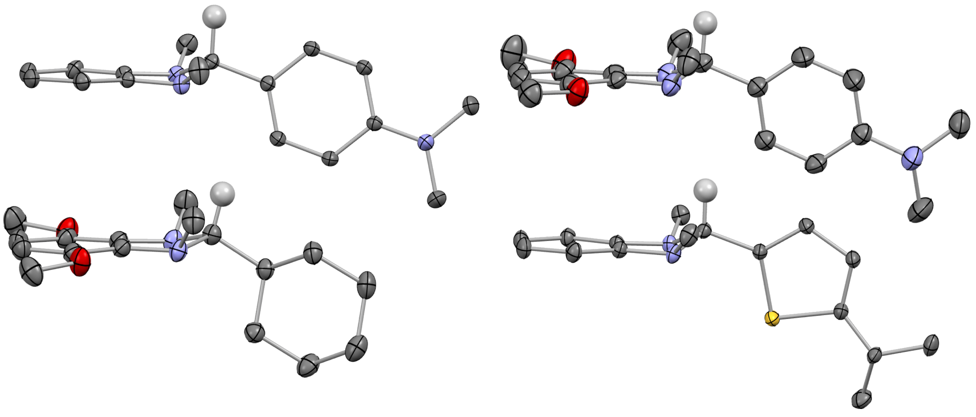

Figure 4: Molecular structures from the single crystal structures of **1bH** (upper left), **1gH** (upper right), **1hH** (lower left), and **1iH** (lower right), shown with 50% thermal ellipsoids and excluding hydrogen atoms for clarity, except for the hydridic 2-hydrogen atoms (located and refined for **1bH**, geometrically placed for the others).

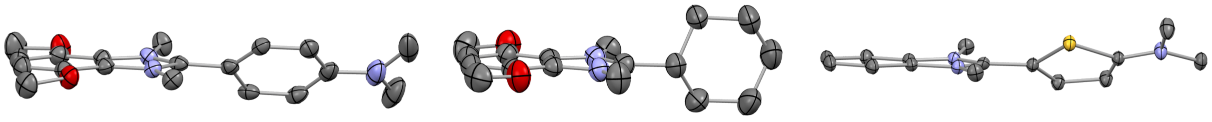

Figure 5: Structures of the cations from the single crystal structures of $\mathbf{1g}^+\mathrm{I}^-$ (left), $\mathbf{1h}^+\mathrm{PF}_6{}^-$ (center), and $\mathbf{1i}^+\mathrm{PF}_6{}^-$ (right), shown with 50% thermal ellipsoids and excluding hydrogen atoms and counter anions.

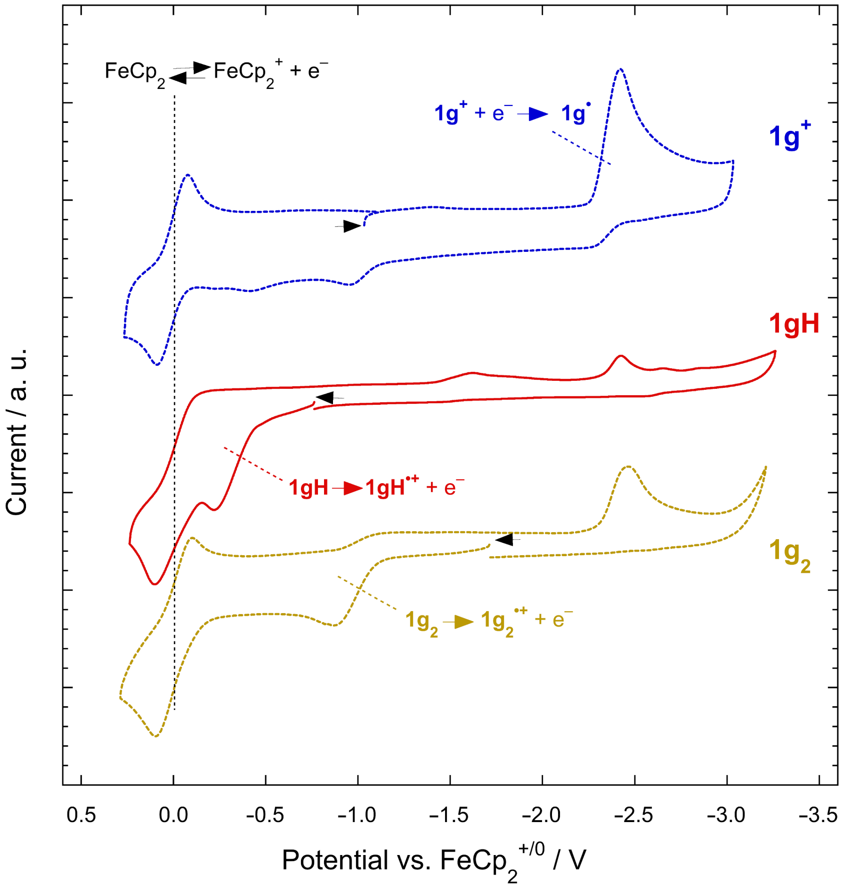

Figure 6: Cyclic voltammograms (50 mV s^{-1}, THF, 0.1 M Bu_4NPF_6) of **1g**$^+$$PF_6^-$, **1gH**, and **1g$_2$**, in each case containing ferrocene as an internal reference. Black arrows indicate the starting point and scan initial direction for each voltammograms. Note that the oxidation peak of **1g$_2$** is seen in the voltammogram of **1g**$^+$$PF_6^-$ following scanning of the reduction peak, while the reduction peak of the cation is seen in the voltammograms of both **1gH** and **1g$_2$** following scanning of the irreversible oxidation peaks.

Table 1: Electrochemical potentials (V) for DMBI derivatives[a].

	E_{red}(**1**$^+$/**1**$^•$)	E_{ox}(**1H**$^{•+}$/**1H**)	E_{ox}(**1$_2$**$^{•+}$/**1$_2$**)
1b (Y = C_6H_4-4-NMe_2; R = R' = H)	−2.38[b]	−0.13[c]	−0.75[b]
1c (Y = Fc; R = R' = H)	−2.24[d]	−0.06[e]	−0.89[d]
1d (Y = Rc; R = R' = H)	−2.29[d]	−0.07[e]	−0.59[d]
1e (Y = cy-C_6H_{11}; R = R' = H)	−2.45[d]	−0.06	−0.64[d]
1g (Y = C_6H_4-4-NMe_2; R = H; R' = OMe)	−2.42	−0.22	−0.87
1h (Y = cy-C_6H_{11}; R = H; R' = OMe)	−2.56	−0.11	−0.92
1i (Y = 2-C_4H_3S-5-NMe_2; R = R' = H)	−2.05	−0.22	–

[a]vs $FeCp_2^{+/0}$ in THF, 0.1 M Bu_4NPF_6; [b]data from reference [19]; [c]data from reference [8]; [d]data from reference [14]; [e]data from reference [50].

$\Delta G_{diss}(H_2)$ the free-energy change for dissociation of dihydrogen. The values of E(**1**$^+$/**1**$^•$) are also relevant to the kinetics of steps in doping reactions that involve **1**$^•$, in particular for doping reactions in which the initial step is dimer dissociation and the second step is an electron transfer from **1**$^•$ to SC (or SC$^{•-}$). The E(**1**$^+$/**1**$^•$) potentials for the Y = 4-dimethylaminophenyl **1b**$^+$/**1b**$^•$ and **1g**$^+$/**1g**$^•$ systems are both somewhat less reducing than those for their Y = cyclohexyl counterparts, **1e**$^+$/**1e**$^•$ and **1h**$^+$/**1h**$^•$, respectively. These differences are also similar to those previously seen in the comparison of Y = metallocenyl systems **1c**$^+$/**1c**$^•$ and **1d**$^+$/**1d**$^•$ with **1e**$^+$/**1e**$^•$ (and in the DFT-calculated ionization energies of **1c–e**$^•$) [14,50] and are perhaps surprising since 4-(dimethylamino)phenyl and metallocenyl groups are π-donors, unlike cyclohexyl, and thus might be expected to be better able to stabilize an adjacent cation. However, aryl and metallocenyl substituents also stabilize adjacent radicals more effectively than alkyl groups and this effect is presumably dominant in the present case. The importance of radical stabilization may in part be because the positive charges in Y = H or alkyl **1**$^+$ ions is already substantially stabilized by the aromaticity of the benzimidazolium ions, whereas the spin densities of the corresponding **1**$^\bullet$ radicals are highly localized; indeed DFT calculations for the Y = alkyl **1e**$^\bullet$ derivative indicate spin density almost entirely on the 2-position of the five-membered ring, while for Y = aryl and metallocenyl examples **1b**$^\bullet$, **1c**$^\bullet$, and **1d**$^\bullet$ there is substantial spin delocalization onto the Y-substituents [14,55]. Different extents of deviation from planarity in cations and radicals, as well as inductive effects, may also play a role.

The **1i**$^+$/**1i**$^\bullet$ (Y = 5-(dimethylamino)-2-thienyl; R = R' = H) potential is less reducing than that of **1b**$^+$/**1b**$^\bullet$ (Y = 4-dimethylaminophenyl; R = R' = H). 5-(Dimethylamino)-2-thienyl is more strongly π-donating than 4-dimethylaminophenyl, at least according to NMR and DFT data for molecules in which the (hetero)aryl group is more or less coplanar with a π-acceptor [56], although some tabulated Swain–Lupton substituent constants do suggest phenyl can be a stronger π-donor than thienyl towards another aryl ring [57]. Presumably inductive effects destabilizing **1i**$^+$, different extents of planarization, and improved radical stabilization by the 5-(dimethylamino)-2-thienyl susbtituent play a role. As expected, R' = OMe groups on the six-membered benzimidazolium ring *do* have a net cation-stabilizing effect, resulting in **1g**$^\bullet$ and **1h**$^\bullet$ being more reducing monomers than their non-methoxylated analogues **1b**$^\bullet$ and **1e**$^\bullet$, respectively.

Cyclic voltammograms of both **1H** and **1**$_2$ both reveal irreversible oxidations (with the corresponding **1**$^+$ reductions seen in subsequent reductive cycles, see Figure 6 for examples). These **1H**$^{\bullet+}$/**1H** and **1**$_2^{\bullet+}$/**1**$_2$ potentials are relevant to the air stability of the hydrides and dimers, respectively, as well as to other processes in which **1H** or **1**$_2$ acts as an electron donor, such as the initation step proposed for the radical-chain dehalogenation of α-dihaloketones by a **1H** derivative [58] and dimer n-doping reactions that proceed via the "ET-first" mechanism (see below). In all cases the dimers are more easily oxidized, consistent with their greater air sensitivity. The impact of the Y-substituents on both **1H**$^{\bullet+}$/**1H** and **1**$_2^{\bullet+}$/**1**$_2$ potentials is not straightforward; one would expect π-conjugated substituents to make little contribution to the HOMO of either **1H** or **1**$_2$ (as shown in calculated molecular orbitals for several examples [14,50,55,59,60]) and so the dependence of these potentials on Y is likely to be due to a combination of inductive effects and perhaps steric effects on the molecular conformation. As expected, methoxy R' substituents lead to **1H**$^{\bullet+}$/**1H** and **1**$_2^{\bullet+}$/**1**$_2$ potentials that are more reducing than those for analogous species without these groups. **1h**$_2$ (Y = cyclohexyl, R = H, R' = MeO) is the most easily oxidized DMBI dimer that we have examined to date; however, it is a little less easily oxidized than [RuCp*(1,3,5-$Me_3C_6H_3$)]$_2$ (−1.09 V) [61] and, like [RuCp*(1,3,5-$Me_3C_6H_3$)]$_2$, can still be handled in air.

Reactivity

To compare the reactivity of the new compounds towards relevant organic semiconductors (SC), we have examined the reactions of the **1H** derivatives with the solubilized fullerene PC$_{61}$BM (**VI**, Figure 7) and that of the **1**$_2$ derivatives with 6,13-bis(triisopropylsilylethynyl)pentacene (TIPS-pentacene, **VII**, Figure 7), since we have previously found that these dopant class/SC combinations often react on a timescale suitable for monitoring using UV–vis–NIR spectroscopy (**1H** derivatives do not react significantly with **VII** in solution at room temperature, while the reactions of **1**$_2$ derivatives and **VI** are very rapid) [9,14,50,61]. Figure 8a compares the evolution of the absorbance at 1030 nm, corresponding to a **VI**$^{\bullet-}$ absorption maximum, when doping excess **VI** with **1H** derivatives in chlorobenzene at 293 K in the absence of light, air, and water. In each case the reaction is apparently first order in dopant, consistent with the rate law:

$$d\left[\mathbf{VI}^{\bullet-}\right]/dt = k\left[\mathbf{1H}\right]\left[\mathbf{VI}\right] \qquad (3)$$

previously demonstrated for **1bH** and **VI** [9]. The rate constants, *k*, obtained assuming this rate law are shown in Table 2 (the value for **3b** being similar to that previously determined [9]). One can anticipate, extending the Hammond postulate, that increased driving forces should correlate with reduced barriers

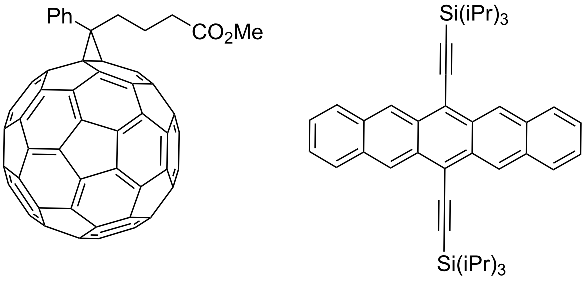

VI
PC$_{61}$BM

VII
TIPS-pentacene

Figure 7: Acceptors used to examine reactivity of DMBI-H and (DMBI)$_2$ derivatives.

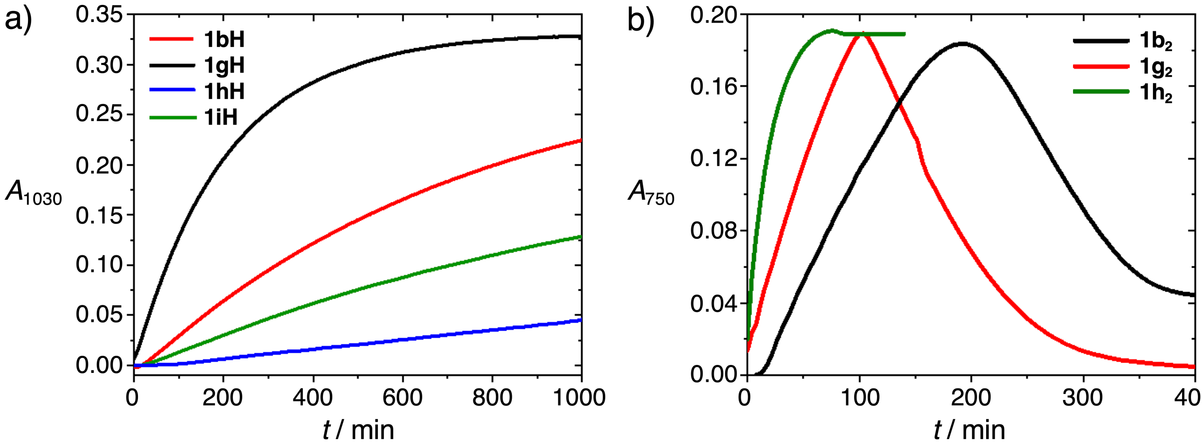

Figure 8: a) Temporal evolution of the absorbance at 1030 nm, corresponding to an absorption maximum of $\mathbf{VI}^{\bullet-}$, when $PC_{61}BM$ (**VI**, 2.7 mM) is reacted with different **1H** derivatives (0.4 mM) in chlorobenzene at room temperature. b) Temporal evolution of the absorbance at 750 nm, corresponding to one of the absorption maxima of $\mathbf{VII}^{\bullet-}$, when TIPS-pentacene (**VII**, 0.026 mM) is reacted with different $\mathbf{1_2}$ derivatives (0.37 mM) in chlorobenzene at room temperature.

Table 2: Rate constants for the reaction of DMBI-H derivatives and $PC_{61}BM$.

	k [M^{-1} min^{-1}]
1bH (Y = C_6H_4-4-NMe_2; R = R' = H)	0.26
1gH (Y = C_6H_4-4-NMe_2; R = H; R' = OMe)	0.48
1hH (Y = cy-C_6H_{11}; R = H; R' = OMe)	0.04
1iH (Y = 2-C_4H_3S-5-NMe_2; R = R' = H)	0.13

and increased rate constants. Values of *k* do *not* correlate with the $\mathbf{1H}^{\bullet+}$/**1H** potentials, but, at least when comparing aryl and alkyl Y substituents and when comparing R' = H and R' = OMe examples, do correlate with the expected stability of the resultant $\mathbf{1}^{+}$ cations, which is also expected to correlate with the hydride donor strength of **1H**. This is consistent with previous findings that the first and rate-determining step of several **1H**/SC reactions, including **1H**/**VI** reactions, is *not* an electron transfer, but a hydride transfer [8,9]. There is conflicting evidence in the literature regarding the π-donor characteristics of phenyl and thienyl groups [56,57], while thienyl is more inductively electron-withdrawing [57], as noted in the electrochemical section; however, the observed rate constants for **1bH** and **1iH** suggest that 5-dimethylamino-2-thienyl affords less net charge stabilization than 4-dimethylaminophenyl.

Two reaction pathways have been established for the oxidation of organometallic and organic dimers. A "cleavage-first" mechanism, whereby the dimer is in equilibrium with a small concentration of the corresponding odd-electron monomer, which can then rapidly react with an acceptor such as an organic semiconductor (SC) through an exergonic electron transfer (ET), has been observed for the reactions of several relatively weakly bonded dimeric dopants (the Y = metallocenyl DMBI dimers $\mathbf{1c_2}$ and $\mathbf{1d_2}$ as well as various organometallic dimers) with **VII** [14,46,61], as well as in the oxidation of bis(3,5,5-trimethyl-2-morpholinon-3-yl), $\mathbf{5_2}$ (Figure 2), by isatin derivatives [62]. In the alternative "ET-first" mechanism the first step is an endergonic dimer-to-SC ET; subsequent rapid cleavage of the odd-electron dimer cation affords the stable monomer cation and an odd-electron monomer, the latter then undergoing an exergonic ET to another SC molecule. The "ET-first" mechanism occurs in parallel with the "cleavage-first" mechanism for many of the **VII** doping reactions mentioned above and is the only mechanism seen for dimeric dopants that are more strongly bound ($\mathbf{1e_2}$, as well as various organometallic dimers including $[RuCp^*(1,3,5\text{-}Me_3C_6H_3)]_2$) [14,46,61], as well as being observed in different contexts in, for example, the oxidation of $\mathbf{4_2}$ by various quinone derivatives [63]. For both mechanisms, the first steps are typically rate determining and thus, in general, the rate law is:

$$d\left[\mathrm{SC}^{\bullet-}\right]/dt = 2k_1\left[\mathbf{1_2}\right] + 2k_2\left[\mathbf{1_2}\right]\left[\mathrm{SC}\right], \quad (4)$$

where k_1 and k_2 are rate constants for the first steps of the "cleavage first" and "ET-first" pathways respectively, k_1 being negligible in the case of strongly bound dimers.

Figure 8b compares the evolution of one of the distinctive **VII** $^{\bullet-}$ absorptions when doping **VII** with excess $\mathbf{1_2}$ derivatives in chlorobenzene at 293 K in the absence of light, air, and water. In the case of the Y = 4-dimethylaminophenyl dimers $\mathbf{1b_2}$ and $\mathbf{1g_2}$, the $\mathbf{VII}^{\bullet-}$ absorption grows in and then falls approximately linearly at a comparable rate. This type of plot is a signature of dimer/**VII** combinations for which the "cleavage-first" pathway is important and has previously been seen for the reactions of **VII** with $\mathbf{1c_2}$, $\mathbf{1d_2}$, $(RhCp^*Cp)_2$, and one of the isomers of $[RuCp^*\{1,4\text{-}(Me_2N)_2C_6H_4\}]_2$, all of which are calculated to be relatively weakly bonded [14,46,61]. Specifically, this behavior is consistent with a "cleavage-first" mechanism in which the initial cleavage is rate determining and for which the resultant one-electron monomers are capable of reducing *both* **VII** to $\mathbf{VII}^{\bullet-}$ (−1.55 V) *and* $\mathbf{VII}^{\bullet-}$ to $\mathbf{VII}^{2-}$ (−1.93 V); since the cleavage is rate determining, **VII** will be converted to $\mathbf{VII}^{\bullet-}$ and then, when excess dimer is used, to $\mathbf{VII}^{2-}$ with a comparable rate constant. Indeed spectra obtained at long-reaction times (see Supporting Information File 1, Figure S7) are similar to those previously attributed to $\mathbf{VII}^{2-}$ [14,46,61], such as the reaction product of **VII** and Na:K. On the other hand, when *only* the "ET-first" mechanism is operative, the conversion of $\mathbf{VII}^{\bullet-}$ to $\mathbf{VII}^{2-}$ will be much slower, if it is even observable, than the initial formation of $\mathbf{VII}^{\bullet-}$ from **VII** due to the considerably greater endergonicity expected for this step. This is seen for the solution reaction of $\mathbf{1h_2}$, where, as in the case of non-methoxylated analogue $\mathbf{1e_2}$, only the formation of $\mathbf{VII}^{\bullet-}$ is seen and the growth in its absorbance can be fitted as first order in **VII**. Returning to the case of $\mathbf{1b_2}$ and $\mathbf{1g_2}$, we note that the rise in $\mathbf{VII}^{\bullet-}$ absorption is neither zero-order nor first-order in **VII**, consistent with *both* mechanisms contributing, as previously demonstrated by more extensive investigations in the case of $\mathbf{1c_2}$, $\mathbf{1d_2}$, and $(RhCp^*Cp)_2$ [14,61]. Thus, the Y = alkyl derivative ($\mathbf{1h_2}$, "ET-first" only) appears to be more strongly bonded than its Y = aryl counterparts ($\mathbf{1b_2}$, $\mathbf{1g_2}$, both mechanisms), consistent with previous DFT calculations for $\mathbf{1b_2}$ and $\mathbf{1e_2}$ (ΔU_{diss} = 163 and 210 kJ mol^{-1}, respectively) and with the expected impact of the different Y substituents on monomer radical stability. In addition, the reaction of $\mathbf{1h_2}$ and **VII** to form $\mathbf{VII}^{\bullet-}$ under the conditions used in the present study is complete much sooner than reactions using $\mathbf{1b_2}$ or $\mathbf{1g_2}$, consistent with the ET-first reaction of $\mathbf{3h_2}$ being more rapid than that for either $\mathbf{1b_2}$ or $\mathbf{1g_2}$. Furthermore, the presumed "cleavage-first" reductions of $\mathbf{VII}^{\bullet-}$ to $\mathbf{VII}^{2-}$ proceed only slightly faster for $\mathbf{1g_2}$ than for its non-methoxylated analogue $\mathbf{1b_2}$, suggesting the OMe groups only slightly weaken the bond in the latter and that the difference in the rates of formation of $\mathbf{VII}^{\bullet-}$ with these two dimers is largely due to differences in the rate of the $\mathbf{1_2}$-to-**VII** ET reaction. Furthermore, the ordering of ET-first rates ($\mathbf{1h_2}$ > $\mathbf{1g_2}$ > $\mathbf{1b_2}$ > $\mathbf{1e_2}$, that for $\mathbf{1e_2}$ being estimated by extrapolating previously reported parameters to the present conditions of temperature and concentration) reflecting the trend expected based on the $E(\mathbf{1_2}^{\bullet+}/\mathbf{1_2})$ values of Table 1.

It is worth noting that, although we see evidence for the "cleavage-first" mechanism in the reactions of $\mathbf{1b_2}$ and $\mathbf{1g_2}$ with **VII** at these specific concentrations, the "ET-first" mechanism will dominate these reactions (as well as those of the same dopants with more readily reduced SCs) under typical doping conditions, where SC and sub-stoichiometric dimer are mixed in solution prior to spin-coating at much higher concentrations. However, as we have previously noted, there are potential advantages and disadvantages for dimers for which the cleavage-first pathway is viable and those for which it is not. For the former class, doping in solution will proceed as long as $E(\text{SC/SC}^{\bullet-})$ is less reducing than $E(\mathbf{1}^+/0.5\mathbf{1_2})$, whereas in the latter this limit can only be reached as long as the $\mathbf{1_2}$-to-SC ET step is kinetically feasible under the reaction conditions. Moreover, for a given monomer redox potential, $E(\mathbf{1}^+/\mathbf{1}^\bullet)$, a weakly bound dimer will be thermodynamically stronger (Equation 1) although, in some cases the effects of structural change on $E(\mathbf{1}^+/\mathbf{1}^\bullet)$ and $\Delta G_{\text{diss}}(\mathbf{1_2})$ partially cancel one another, as in the comparison of $\mathbf{1b_2}$ vs $\mathbf{1e_2}$ or $\mathbf{1g_2}$ vs $\mathbf{1h_2}$ (i.e., for Y = 4-dimethylaminophenyl, dimers are more weakly bound and monomers less reducing that for Y = cyclohexyl). Conversely, the combination of a strongly bound dimer and an acceptor with $E(\text{SC/SC}^{\bullet-})$ with the reach of $E(\mathbf{1}^+/0.5\mathbf{1_2})$, but sufficiently cathodic that ET is very slow, could permit activation of doping by an external stimulus, such as photoexcitation, when desired, for example subsequent to processing.

Conclusion

In conclusion we have reported a number of new DMBI-H and $(DMBI)_2$ reductants and compared their structures, electrochemistry, and reactivity with those of previously reported analogues. The structures show similar features to other related compounds, notably the dimers show long central C–C bonds. The $E(\mathbf{1}^+/\mathbf{1}^\bullet)$ potentials depend strongly on the 2-substituents (Y), become increasing reducing (more negative) in the order Y = 5-(dimethylamino)thiophen-2-yl < 4-(dimethylamino)phenyl < cyclohexyl, indicating the effects of radical stabilization are more important than those of cation stabilization, while the $E(\mathbf{1H}^{\bullet+}/\mathbf{1H})$ and $E(\mathbf{1_2}^{\bullet+}/\mathbf{1_2})$ potentials are less strongly and clearly affected by the 2-substituents. On the other hand, methoxy R' substituents lead to more reducing values of $E(\mathbf{1}^+/\mathbf{1}^\bullet)$, $E(\mathbf{1H}^{\bullet+}/\mathbf{1H})$, and $E(\mathbf{1_2}^{\bullet+}/\mathbf{1_2})$ than for R' = H analogues. The reaction rates of **1H** with $PC_{61}BM$ (**VI**) increase in the order Y = cyclohexyl < 5-(dimethylamino)thiophen-2-yl < 4-(dimethylamino)phenyl and R’ = H < MeO, broadly consistent with the anticipated influence of these substituents on the $DMBI^+$ stability, as expected for a hydride-transfer reaction. The rates of reactions of the dimers with TIPS-pentacene (**VII**) follow a more complex pattern: examples with Y = cyclohexyl react solely via an “electron-transfer-first” mechanism, consistent with a relatively strongly bonded dimer, whereas Y = 4-(dimethylamino)phenyl derivatives also react by a “cleavage-first” mechanism, consistent with a weaker central bond, which in turn is consistent with stabilization of the monomeric radicals by the 2-aryl substituents. The Y = cyclohexyl, R’ = OMe dimer reacts most rapidly with TIPS-pentacene via the “ET-first” mechanism, consistent with this dimer also exhibiting the most cathodic value of $E(\mathbf{1_2}^{\bullet+}/\mathbf{1_2})$. Overall, this study gives insight into how substituents have different effects on the reactivity of DMBI-H derivatives and of $(DMBI)_2$ species, and may help provide guidance for dopant selection and for future dopant design.

Supporting Information

Supporting Information File 1

Synthetic and other experimental procedures, details of crystal-structure determinations, variable-temperature NMR data, stability data, optical spectra for reactivity studies, and NMR spectra of new compounds.
[https://www.beilstein-journals.org/bjoc/content/supplementary/1860-5397-19-121-S1.pdf]

Acknowledgements

This work is partly based on the Ph.D. thesis of KAK [64].

Funding

The work was primarily supported by the National Science Foundation through award DMR-1807797/2216857. Diffraction studies at New Mexico Highlands University were supported by the National Science Foundation’s PREM program through DMR-2122108. SJ was supported by Fulbright-Nehru Postdoctoral Fellowship from the United States-India Educational Foundation and Institute of International Education for (grant no. 2266/FNPDR/2017). This work was also authored in part by the National Renewable Energy Laboratory (NREL), operated by Alliance for Sustainable Energy, LLC, for the U.S. Department of Energy (DOE) under Contract No. DE-AC36-08GO28308; specifically, some of the data analysis was carried out as part of a Laboratory Directed Research and Development (LDRD) Program at NREL. The views expressed in the article do not necessarily represent the views of the DOE or the U.S. Government. The U.S. Government retains and the publisher, by accepting the article for publication, acknowledges that the U.S. Government retains a nonexclusive, paid-up, irrevocable, worldwide license to publish or reproduce the published form of this work, or allow others to do so, for U.S. Government purposes.

ORCID® iDs

Swagat K. Mohapatra - https://orcid.org/0000-0002-4485-3967
Georgii Bogdanov - https://orcid.org/0000-0002-8655-3102
Tatiana V. Timofeeva - https://orcid.org/0000-0001-7475-3206
Seth R. Marder - https://orcid.org/0000-0001-6921-2536
Stephen Barlow - https://orcid.org/0000-0001-9059-9974

References

1. Walzer, K.; Maennig, B.; Pfeiffer, M.; Leo, K. *Chem. Rev.* **2007,** *107,* 1233–1271. doi:10.1021/cr050156n
2. Russ, B.; Glaudell, A.; Urban, J. J.; Chabinyc, M. L.; Segalman, R. A. *Nat. Rev. Mater.* **2016,** *1,* 16050. doi:10.1038/natrevmats.2016.50
3. Lüssem, B.; Keum, C.-M.; Kasemann, D.; Naab, B.; Bao, Z.; Leo, K. *Chem. Rev.* **2016,** *116,* 13714–13751. doi:10.1021/acs.chemrev.6b00329
4. Wang, Z.-K.; Liao, L.-S. *Adv. Opt. Mater.* **2018,** *6,* 1800276. doi:10.1002/adom.201800276
5. Barlow, S.; Marder, S. R.; Lin, X.; Zhang, F.; Kahn, A. Electrial Doping of Organic Semiconductors with Molecular Oxidants and Reductants. In *Conjugated Polymers,* 4th ed.; Skotheim, T. A.; Reynolds, J.; Thompson, B. C., Eds.; CRC Press: Boca Raton, FL, USA, 2019. doi:10.1201/9780429190520-2
6. Wahl, H. *Bull. Soc. Chim. Fr.* **1954,** 251–253.
7. Wei, P.; Oh, J. H.; Dong, G.; Bao, Z. *J. Am. Chem. Soc.* **2010,** *132,* 8852–8853. doi:10.1021/ja103173m
8. Jhulki, S.; Un, H.-I.; Ding, Y.-F.; Risko, C.; Mohapatra, S. K.; Pei, J.; Barlow, S.; Marder, S. R. *Chem* **2021,** *7,* 1050–1065. doi:10.1016/j.chempr.2021.01.020
9. Naab, B. D.; Guo, S.; Olthof, S.; Evans, E. G. B.; Wei, P.; Millhauser, G. L.; Kahn, A.; Barlow, S.; Marder, S. R.; Bao, Z. *J. Am. Chem. Soc.* **2013,** *135,* 15018–15025. doi:10.1021/ja403906d
10. Guo, H.; Yang, C.-Y.; Zhang, X.; Motta, A.; Feng, K.; Xia, Y.; Shi, Y.; Wu, Z.; Yang, K.; Chen, J.; Liao, Q.; Tang, Y.; Sun, H.; Woo, H. Y.; Fabiano, S.; Facchetti, A.; Guo, X. *Nature* **2021,** *599,* 67–73. doi:10.1038/s41586-021-03942-0
11. Pallini, F.; Mattiello, S.; Manfredi, N.; Mecca, S.; Fedorov, A.; Sassi, M.; Al Kurdi, K.; Ding, Y.-F.; Pan, C.-K.; Pei, J.; Barlow, S.; Marder, S. R.; Nguyen, T.-Q.; Beverina, L. *J. Mater. Chem. A* **2023,** *11,* 8192–8201. doi:10.1039/d3ta00231d
12. Ludvík, J.; Pragst, F.; Volke, J. *J. Electroanal. Chem. Interfacial Electrochem.* **1984,** *180,* 141–156. doi:10.1016/0368-1874(84)83576-5
13. Naab, B. D.; Zhang, S.; Vandewal, K.; Salleo, A.; Barlow, S.; Marder, S. R.; Bao, Z. *Adv. Mater. (Weinheim, Ger.)* **2014,** *26,* 4268–4272. doi:10.1002/adma.201400668
14. Zhang, S.; Naab, B. D.; Jucov, E. V.; Parkin, S.; Evans, E. G. B.; Millhauser, G. L.; Timofeeva, T. V.; Risko, C.; Brédas, J.-L.; Bao, Z.; Barlow, S.; Marder, S. R. *Chem. – Eur. J.* **2015,** *21,* 10878–10885. doi:10.1002/chem.201500611
15. Naab, B. D.; Gu, X.; Kurosawa, T.; To, J. W. F.; Salleo, A.; Bao, Z. *Adv. Electron. Mater.* **2016,** *2,* 1600004. doi:10.1002/aelm.201600004

16. Yuan, D.; Huang, D.; Zhang, C.; Zou, Y.; Di, C.-a.; Zhu, X.; Zhu, D. *ACS Appl. Mater. Interfaces* **2017,** *9,* 28795–28801. doi:10.1021/acsami.7b07282
17. Schwarze, M.; Gaul, C.; Scholz, R.; Bussolotti, F.; Hofacker, A.; Schellhammer, K. S.; Nell, B.; Naab, B. D.; Bao, Z.; Spoltore, D.; Vandewal, K.; Widmer, J.; Kera, S.; Ueno, N.; Ortmann, F.; Leo, K. *Nat. Mater.* **2019,** *18,* 242–248. doi:10.1038/s41563-018-0277-0
18. Al Kurdi, K.; Gregory, S. A.; Jhulki, S.; Conte, M.; Barlow, S.; Yee, S. K.; Marder, S. R. *Mater. Adv.* **2020,** *1,* 1829–1834. doi:10.1039/d0ma00406e
19. Un, H.-I.; Gregory, S. A.; Mohapatra, S. K.; Xiong, M.; Longhi, E.; Lu, Y.; Rigin, S.; Jhulki, S.; Yang, C.-Y.; Timofeeva, T. V.; Wang, J.-Y.; Yee, S. K.; Barlow, S.; Marder, S. R.; Pei, J. *Adv. Energy Mater.* **2019,** *9,* 1900817. doi:10.1002/aenm.201900817
20. Lungwitz, D.; Joy, S.; Mansour, A. E.; Opitz, A.; Karunasena, C.; Li, H.; Panjwani, N. A.; Moudgil, K.; Tang, K.; Behrends, J.; Barlow, S.; Marder, S. R.; Brédas, J.-L.; Graham, K.; Koch, N.; Kahn, A. *J. Phys. Chem. Lett.* **2023,** *14,* 5633–5640. doi:10.1021/acs.jpclett.3c01022
21. Guo, S.; Kim, S. B.; Mohapatra, S. K.; Qi, Y.; Sajoto, T.; Kahn, A.; Marder, S. R.; Barlow, S. *Adv. Mater. (Weinheim, Ger.)* **2012,** *24,* 699–703. doi:10.1002/adma.201103238
22. Mohapatra, S. K.; Fonari, A.; Risko, C.; Yesudas, K.; Moudgil, K.; Delcamp, J. H.; Timofeeva, T. V.; Brédas, J.-L.; Marder, S. R.; Barlow, S. *Chem. – Eur. J.* **2014,** *20,* 15385–15394. doi:10.1002/chem.201404007
23. Mohapatra, S. K.; Marder, S. R.; Barlow, S. *Acc. Chem. Res.* **2022,** *55,* 319–332. doi:10.1021/acs.accounts.1c00612
24. Zhu, X.-Q.; Zhang, M.-T.; Yu, A.; Wang, C.-H.; Cheng, J.-P. *J. Am. Chem. Soc.* **2008,** *130,* 2501–2516. doi:10.1021/ja075523m
25. Küçükbay, H.; Çetinkaya, E.; Çetinkaya, B.; Lappert, M. F. *Synth. Commun.* **1997,** *27,* 4059–4066. doi:10.1080/00397919708005451
26. Pham, P. H.; Barlow, S.; Marder, S. R.; Luca, O. R. *Chem Catal.* **2023,** *3,* 100675. doi:10.1016/j.checat.2023.100675
27. Pallini, F.; Mattiello, S.; Cassinelli, M.; Rossi, P.; Mecca, S.; Tan, W. L.; Sassi, M.; Lanzani, G.; McNeill, C. R.; Caironi, M.; Beverina, L. *ACS Appl. Energy Mater.* **2022,** *5,* 2421–2429. doi:10.1021/acsaem.1c03893
28. Lim, C.-H.; Ilic, S.; Alherz, A.; Worrell, B. T.; Bacon, S. S.; Hynes, J. T.; Glusac, K. D.; Musgrave, C. B. *J. Am. Chem. Soc.* **2019,** *141,* 272–280. doi:10.1021/jacs.8b09653
29. Ghosh, R.; Kushwaha, A.; Das, D. *J. Phys. Chem. B* **2017,** *121,* 8786–8794. doi:10.1021/acs.jpcb.7b05947
30. Crippa, G. B.; Maffei, S. *Gazz. Chim. Ital.* **1941,** *71,* 194–200.
31. Balachandran, K. S.; George, M. V. *Indian J. Chem.* **1973,** *11,* 1267–1271.
32. Speier, G.; Párkányi, L. *J. Org. Chem.* **1986,** *51,* 218–221. doi:10.1021/jo00352a016
33. Reddy, A. P. R.; Veeranagaiah, V.; Ratnam, C. V. *Indian J. Chem.* **1985,** *B24,* 367–371.
34. Bardagot, O.; Aumaître, C.; Monmagnon, A.; Pécaut, J.; Bayle, P.-A.; Demadrille, R. *Appl. Phys. Lett.* **2021,** *118,* 203904. doi:10.1063/5.0047637
35. Miler-Srenger, E. *Acta Crystallogr., Sect. B: Struct. Crystallogr. Cryst. Chem.* **1973,** *29,* 1119–1124. doi:10.1107/s0567740873003973
36. Ramirez-Montes, P. I.; Ochoa, M. E.; Rodríguez, V.; Santillan, R.; García-Ortega, H.; Rodríguez, P.; Farfán, N. *Tetrahedron Lett.* **2012,** *53,* 5887–5890. doi:10.1016/j.tetlet.2012.08.094
37. Preuss, J.; Zanker, V.; Gieren, A. *Acta Crystallogr., Sect. B: Struct. Crystallogr. Cryst. Chem.* **1977,** *33,* 2317–2319. doi:10.1107/s0567740877008346
38. Haltiwanger, R. C.; Koch, T. H.; Olesen, J. A.; Kim, C. S.; Kim, N. K. *J. Am. Chem. Soc.* **1977,** *99,* 6327–6331. doi:10.1021/ja00461a026
39. Andrianov, V. G.; Struchkov, Y. T.; Petrakova, V. A.; Vol'kenau, N. A. *Koord. Khim.* **1986,** *12,* 978–980.
40. Gaudet, M. V.; Hanson, A. W.; White, P. S.; Zaworotko, M. J. *Organometallics* **1989,** *8,* 286–293. doi:10.1021/om00104a004
41. Lee, S.; Lovelace, S. R.; Arford, D. J.; Geib, S. J.; Weber, S. G.; Cooper, N. J. *J. Am. Chem. Soc.* **1996,** *118,* 4190–4191. doi:10.1021/ja952217c
42. Hsu, S. C. N.; Yeh, W.-Y.; Lee, G.-H.; Peng, S.-M. *J. Am. Chem. Soc.* **1998,** *120,* 13250–13251. doi:10.1021/ja982773h
43. Hitchcock, P. B.; Lappert, M. F.; Protchenko, A. V. *J. Am. Chem. Soc.* **2001,** *123,* 189–190. doi:10.1021/ja005580e
44. Shao, L.; Geib, S. J.; Badger, P. D.; Cooper, N. J. *J. Am. Chem. Soc.* **2002,** *124,* 14812–14813. doi:10.1021/ja027081e
45. Tamm, M.; Bannenberg, T.; Fröhlich, R.; Grimme, S.; Gerenkamp, M. *Dalton Trans.* **2004,** 482–491. doi:10.1039/b314347c
46. Longhi, E.; Risko, C.; Bacsa, J.; Khrustalev, V.; Rigin, S.; Moudgil, K.; Timofeeva, T. V.; Marder, S. R.; Barlow, S. *Dalton Trans.* **2021,** *50,* 13020–13030. doi:10.1039/d1dt02155a
47. Kratt, G.; Beckhaus, H.-D.; Lindner, H. J.; Rüchardt, C. *Chem. Ber.* **1983,** *116,* 3235–3263. doi:10.1002/cber.19831160921
48. Beauchamp, A. L.; Montgrain, F.; Wuest, J. D. *Acta Crystallogr., Sect. C: Cryst. Struct. Commun.* **1987,** *43,* 1557–1560. doi:10.1107/s0108270187091108
49. Mas-Marzá, E.; Poyatos, M.; Sanaú, M.; Peris, E. *Inorg. Chem.* **2004,** *43,* 2213–2219. doi:10.1021/ic035317p
50. Zhang, S.; Moudgil, K.; Jucov, E.; Risko, C.; Timofeeva, T. V.; Marder, S. R.; Barlow, S. *Inorg. Chim. Acta* **2019,** *489,* 67–77. doi:10.1016/j.ica.2019.02.003
51. Wright, A. G.; Weissbach, T.; Holdcroft, S. *Angew. Chem., Int. Ed.* **2016,** *55,* 4818–4821. doi:10.1002/anie.201511184
52. Mehrotra, S.; Raje, S.; Jain, A. K.; Angamuthu, R. *ACS Sustainable Chem. Eng.* **2017,** *5,* 6322–6328. doi:10.1021/acssuschemeng.7b01495
53. Li, X.; Hao, P.; Shen, J.; Fu, Y. *Dalton Trans.* **2018,** *47,* 6031–6035. doi:10.1039/c8dt00829a
54. Moudgil, K.; Mann, M. A.; Risko, C.; Bottomley, L. A.; Marder, S. R.; Barlow, S. *Organometallics* **2015,** *34,* 3706–3712. doi:10.1021/acs.organomet.5b00327
55. Uebe, M.; Yoshihashi, Y.; Noda, K.; Matsubara, M.; Ito, A. *J. Mater. Chem. C* **2018,** *6,* 6429–6439. doi:10.1039/c8tc01280f
56. Kwon, O.; Barlow, S.; Odom, S. A.; Beverina, L.; Thompson, N. J.; Zojer, E.; Brédas, J.-L.; Marder, S. R. *J. Phys. Chem. A* **2005,** *109,* 9346–9352. doi:10.1021/jp054334s
57. Hansch, C.; Leo, A.; Taft, R. W. *Chem. Rev.* **1991,** *91,* 165–195. doi:10.1021/cr00002a004
58. Tanner, D. D.; Chen, J. J. *J. Org. Chem.* **1989,** *54,* 3842–3846. doi:10.1021/jo00277a020
59. Riera-Galindo, S.; Orbelli Biroli, A.; Forni, A.; Puttisong, Y.; Tessore, F.; Pizzotti, M.; Pavlopoulou, E.; Solano, E.; Wang, S.; Wang, G.; Ruoko, T.-P.; Chen, W. M.; Kemerink, M.; Berggren, M.; di Carlo, G.; Fabiano, S. *ACS Appl. Mater. Interfaces* **2019,** *11,* 37981–37990. doi:10.1021/acsami.9b12441
60. Zeng, Y.; Zheng, W.; Guo, Y.; Han, G.; Yi, Y. *J. Mater. Chem. A* **2020,** *8,* 8323–8328. doi:10.1039/d0ta01087a

61. Guo, S.; Mohapatra, S. K.; Romanov, A.; Timofeeva, T. V.; Hardcastle, K. I.; Yesudas, K.; Risko, C.; Brédas, J.-L.; Marder, S. R.; Barlow, S. *Chem. – Eur. J.* **2012,** *18,* 14760–14772. doi:10.1002/chem.201202591
62. Bennett, R. W.; Wharry, D. L.; Koch, T. H. *J. Am. Chem. Soc.* **1980,** *102,* 2345–2349. doi:10.1021/ja00527a036
63. Colter, A. K.; Lai, C. C.; Parsons, A. G.; Ramsey, N. B.; Saito, G. *Can. J. Chem.* **1985,** *63,* 445–451. doi:10.1139/v85-073
64. Al Kurdi, K. Investigating Charge Transport in Conjugated Organic Materials. Ph.D. Thesis, Georgia Institute of Technology, Atlanta, GA, USA, 2021.

License and Terms

The definitive version of this article is the electronic one which can be found at:
https://doi.org/10.3762/bjoc.19.121

BEILSTEIN JOURNAL OF ORGANIC CHEMISTRY

A deep-red fluorophore based on naphthothiadiazole as emitter with hybridized local and charge transfer and ambipolar transporting properties for electroluminescent devices

Suangsiri Arunlimsawat[1], Patteera Funchien[1], Pongsakorn Chasing[1], Atthapon Saenubol[1], Taweesak Sudyoadsuk[2] and Vinich Promarak*[1]

Full Research Paper

Address:
[1]Department of Materials Science and Engineering, School of Molecular Science and Engineering, Vidyasirimedhi Institute of Science and Technology, Wangchan, Rayong 21210, Thailand and [2]Frontier Research Center, Vidyasirimedhi Institute of Science and Technology, Wangchan, Rayong 21210, Thailand

Email:
Vinich Promarak* - vinich.p@vistec.ac.th

* Corresponding author

Keywords:
ambipolar material; deep red fluorophore; hybridized local and charge transfer; naphthothiadiazole; OLED; organic light-emitting diode

Beilstein J. Org. Chem. **2023,** *19,* 1664–1676.
https://doi.org/10.3762/bjoc.19.122

Received: 11 July 2023
Accepted: 20 October 2023
Published: 03 November 2023

This article is part of the thematic issue "Organic electron transport materials".

Associate Editor: P. J. Skabara

Abstract

Herein, we report the synthesis and characterization of an efficient ambipolar charge-carrier-transporting deep-red fluorophore (**TPECNz**) based on a donor–acceptor–donor (D–A–D)-type molecule and its application as a non-doped emitter in an organic light-emitting diode (OLED). The fluorophore **TPECNz** contains naphtho[2,3-*c*][1,2,5]thiadiazole (Nz) as a strong acceptor unit symmetrically functionalized with *N*-(4-(1,2,2-triphenylvinyl)phenyl)carbazole as a donor and aggregation-induced emission (AIE) luminogen. The experimental (solvatochromic and emission in THF/water mixtures studies) and theoretical investigations prove that **TPECNz** retains cooperative hybridized local and charge transfer (HLCT) and weak AIE features. Thanks to its D–A–D-type structure with a proper twist angle between the D and A units, a strong electron deficiency of the Nz unit, and electron-donating and hole-transporting natures of carbazole, **TPECNz** exhibits a strong deep red emission (λ_{em} = 648 nm) with a high fluorescence quantum yield of 96%, outstanding thermal property (T_g = 236 °C), and ambipolar charge-carrier-transporting property with a decent balance of mobility of electrons (1.50×10^{-5} cm^2 V^{-1} s^{-1}) and holes (4.42×10^{-6} cm^2 V^{-1} s^{-1}). **TPECNz** is successfully employed as a non-doped emitter in an OLED which displays deep red electroluminescent emission peaked at 659 nm with CIE coordinates of (0.664, 0.335)), an EQE$_{max}$ of 3.32% and exciton utilization efficiency (EUE) of 47%.

Introduction

Recently, organic fluorophores with efficient deep-red/near-infrared (DR/NIR) emission properties (λ_{em} = 650–900 nm) have received much attention due to their potential applications in several different fields such as chemosensing [1-3], bioimaging/biosensing [4-8], photodynamic therapy [9], optical communication [10], NLO materials [11], laser dyes [12], and DR/NIR electroluminescent devices [13-18]. However, DR/NIR chromophores typically suffer from low photoluminescent quantum yields (PLQY) because of their intrinsic small band-gap energy causing larger vibronic coupling between the ground and excited states, particularly when they are applied as emitters in organic light-emitting diodes (OLEDs) [19]. Therefore, with such a constrained number of efficient emitters, the current advance of DR/NIR OLEDs largely trails behind the visible light emission OLEDs [20,21]. So far, remarkable efforts have been made in designing new DR/NIR organic fluorophores in combination with device engineering to build up the performance of DR/NIR OLEDs. In general, to realize high fluorescence in the DR/NIR region from the organic fluorophores, the challenges of their pronounced non-radiative processes, and high planarity and extended π-conjugation lengths which eventually favor the undesired formation of poorly emissive molecular aggregates must be overcome. Alternatively, donor–acceptor (D–A)-type organic fluorophores have been introduced and successfully exploited for the development of fluorophores with DR/NIR emissions without lengthy extension of their π-conjugation systems due to a broadening of both the valence and the conduction bands and a consequent narrowing of the energy gap [22-25]. The D–A characters also offer a tunability of optoelectronic properties such as energy levels, optical bandgap (E_g), and charge-transport properties, which could be done by selecting different D and A moieties [22,26-28]. In these fluorophores, the emission generally derives from intramolecular charge-transfer (CT) states at lower energy. Nonetheless, the formed CT state between D and A in such materials normally caused a lesser Φ_{PL} because of the separated frontier molecular orbitals [29,30]. Recently, the reports by Ma et al. revealed that by designing suitable twist-angles between D and A and D–A strength, frontier molecular orbitals of D–A fluorophores are not completely separated due to overlap between the transition orbitals [31-33]. In these molecules, the lowest excited state still shows moderate or large oscillator strengths or a mixing of two excited-state components, locally excited (LE) state and CT excited state. This kind of excited state was later known as a hybridized local and charge transfer (HLCT) state, in which the CT component can provide a high-lying reversed intersystem crossing (hRISC) pathway for fast and effective triplet utilization in the device, and the LE component can contribute good PLQY [34-36]. So far, based on this concept, several D–A-type fluorophores have been designed and investigated including some DR/NIR materials [37-41]. Inevitably, these materials displayed high PLQY and exceptional OLED device performance [42-45]. Even though the radiative transition rate is improved for the HLCT fluorophores, the non-radiative transition process is still an obstacle to lowering the PLQY, particularly for the DR/NIR emitters [20,46]. Therefore, to enhance the performance of HLCT-based DR/NIR fluorophores the non-radiative transition process of the exited state needs to be resolved. This could be managed by the molecular design of the D–A structure. It has been reported that the performance of HLCT fluorophores greatly depends on the strength of donors, acceptors, and π spacers and the building blocks of HLCT should be carefully selected to regulate appropriate electron push–pull strength [32,35,47,48].

Here, a novel chromophore, 4,9-bis(9-(4-(1,2,2-triphenylvinyl)phenyl)-9*H*-carbazol-3-yl)naphtho[2,3-*c*][1,2,5]thiadiazole (**TPECNz**), built on a D–A–D type structure was designed and synthesized (Scheme 1). The D–A–D configuration was constructed by incorporating a second symmetrical donor in the D–A framework, which could further reduce the energy gap between HOMO/LUMO hybrid orbits and drive fluorescence emission to longer wavelengths [48,49]. In this molecular design, the strong electron-deficient naphtho[2,3-*c*][1,2,5]thiadiazole (Nz) [13,50,51] as an acceptor and the strong electron-donating carbazole [52] as a donor unit were used in the D–A–D structure to further reduce the bandgap, thereby red-shifting the absorption and emission wavelengths. In addition, the strong electron affinity of Nz and the electron-donating and hole-transporting ability of carbazole would build in the good ability to transport electrons and holes, respectively, providing well-balanced ambipolar characteristics. On the other hand, the attached 4-(1,2,2-triphenylvinyl)phenyl (TPE) moiety would induce aggregation-induced emission (AIE) as feature into the molecule. It was suspected that AIE would restrain the aggregation-caused quench (ACQ) and the energy loss through the vibronic coupling natures of the DR/NIR fluorophores [53]. As a result, **TPECNz** effectively possesses a strong deep-red emission with combined HLCT, weak AIE, and ambipolar transporting properties, which enabled its application as non-doped emitter. The **TPECNz**-based non-doped deep-red OLED realized a maximum external quantum efficiency (EQE_{max}) of 3.32% with an emission peak at 659 nm.

Results and Discussion

The designed **TPECNz** molecule was synthesized by a multi-step reaction as described in Scheme 1. Initially, an Ullmann coupling reaction of bromo-TPE **1** and carbazole provided TPE-*N*-carbazole **2** in good yield (87%). Compound **2** was then converted to the boronic ester intermediate **3** in 41% yield over two steps: monobromination at the carbazole unit of **2** with NBS/THF at low temperature giving the unisolated mixed brominated product followed by borylation with bis(pinacolato)diboron catalyzed by Pd(dpf)Cl_2/KOAc. Finally, **TPECNz** was obtained as red solid in a reasonable yield by a Suzuki-type cross-coupling reaction between **3** and 4,9-dibromonaphtho[2,3-*c*][1,2,5]thiadiazole. The chemical structure and purity of com-

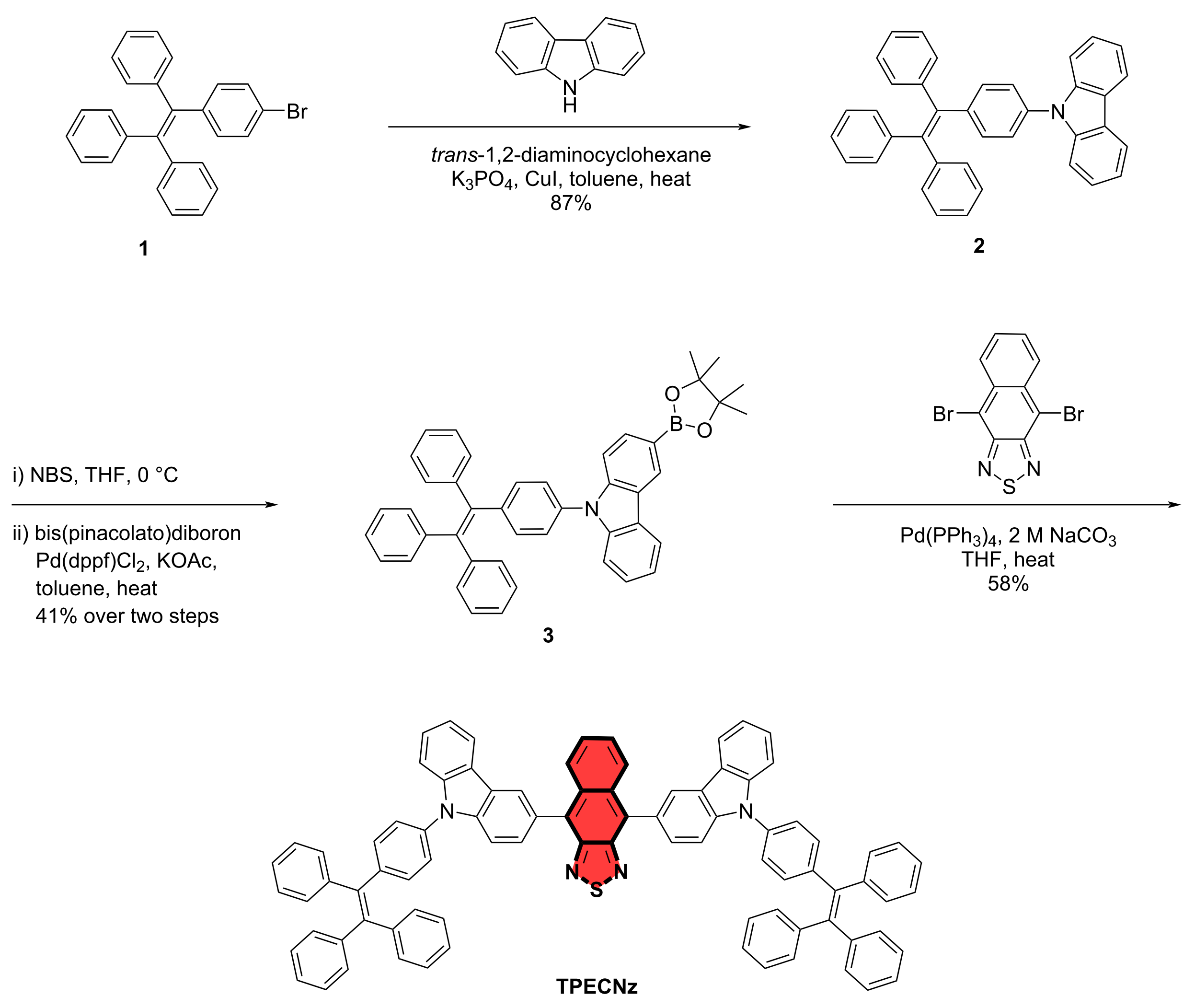

Scheme 1: Synthesis of D–A–D chromophore **TPECNz**.

pound **3** were verified by ^{1}H NMR, ^{13}C NMR, and high-resolution MALDI-TOF-MS techniques.

To examine the electronic properties of D–A **TPECNz**, density functional theory (DFT) calculations at the B3LYP level of theory with the 6-31G(d,p) basis set were performed. It has been previously reported that the twist angle of the D–A segment has a significant role in controlling the CT component in the HLCT state [54]. A suitable twisted angle (40–80°) allocated an appropriate tuning between the complete π-conjugation and the pure CT transition character to form the HLCT state. As depicted in Figure 1a, the optimized structure of **TPECNz** revealed a twisted molecular configuration with dihedral angles of 54–56° between the planes of the terminal carbazole donors and the Nz acceptor that are beneficial for the state mixing between the LE and CT states. The lowest unoccupied molecular orbital (LUMO) was mainly localized on the Nz ring, while the highest occupied molecular orbital (HOMO) was delocalized over the Nz core and the attached carbazole moieties. There was an overlap between the HOMO and LUMO orbitals over the Nz fragment, which is likely to promote the LE component and consequently gives rise to a faster radiative decay and thus a higher luminescence efficiency. To further figure out excited-state properties of **TPECNz**, the natural transition orbitals (NTOs) of singlet (S) and triplet (T) excited states were executed based on time-dependent (TD)-DFT calculations at the CAM-B3LYP/6-31G(d) level of theory. As shown in Figure 1b, the hole and particle of **TPECNz** are similar to its HOMO and LUMO orbitals, respectively. The $S_0 \rightarrow S_1$ transition with oscillator strength (f) of 0.476 clearly showed HLCT transition characteristics, in which a certain overlap between hole and particle wavefunctions on the Nz ring represented for LE component inducing a high luminescence efficiency, while a significant spatial separation be-

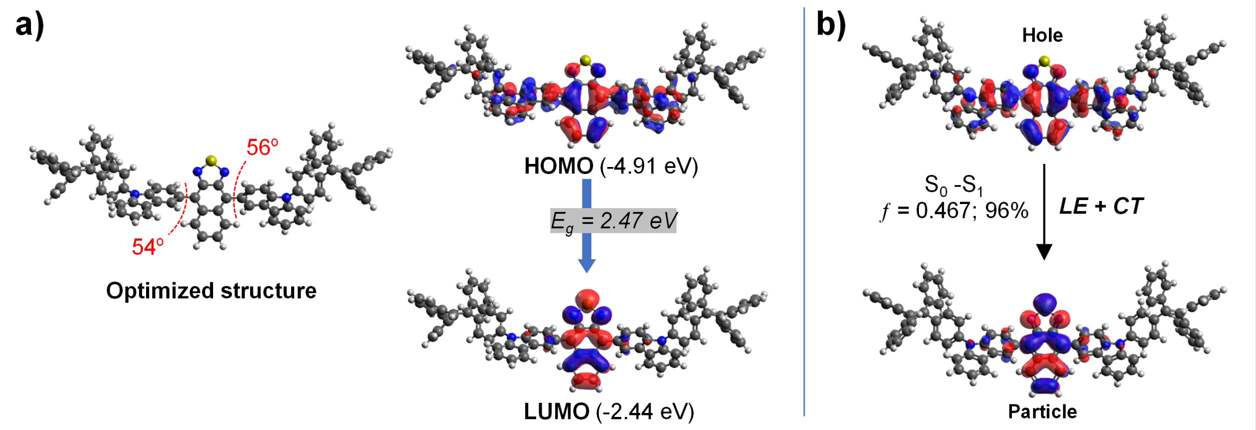

Figure 1: a) The optimized structure and HOMO/LUMO distributions calculated by B3LYP/6-31G(d,p) method. b) The natural transition orbits (NTOs) of the $S_0 \rightarrow S_1$ transition computed by CAM-B3LYP/6-31G(d) method. The percentage is the proportion of transition and ƒ is the oscillator strength.

tween hole and particle wavefunctions considered for CT component promoting RISC process along high-lying excitation state for enhancing an exciton utilization efficiency (EUE).

The photophysical properties of **TPECNz** were studied in solution, thin film, and solid powder. As shown in Figure 2a, the UV–vis absorption spectrum in diluted toluene solution displays intense absorption peaks in the high energy region (<380 nm) and a much weaker absorption peak at 508 nm attributed to the π–π* transition of the conjugated aromatic backbone and intramolecular charge-transfer (ICT) transition from carbazole donor to Nz acceptor, respectively. Such weak ICT absorption peak (ε = 17,000 M^{-1} cm^{-1}) as compared to the π–π* absorption peak (ε = 95,300 M^{-1} cm^{-1}) symbolizes a weak electronic coupling between the carbazole donor and the Nz acceptor parts because of the twisted configuration between them as observed in the optimized structure (Figure 1a) [47]. In solution, **TPECNz** exhibits a strong deep-red emission with the PL spectrum (λ_{em} = 648 nm) described by a broad PL band (FWHM = 120 nm) that reflects the corresponding ICT absorption band well, featuring no significant vibronic structure, and a considerably large Stokes shift of 140 nm. The UV–vis absorption and PL spectra of spin-coated films were similar to those of dilute solutions. Based on the onset energy of this UV–vis spectrum, the optical band gap (E_g^{opt}) was estimated to be 2.04 eV. **TPECNz** in thin film and solid powder also displayed deep-red emission observed by PL maxima at 668 and 665 nm, respectively (Figure 2b). As listed in Table 1, the **TPECNz** solution shows an excellent absolute PL quantum yield (PLQY) of 96%, whereas the spin-coated thin film exhibits a red-shifted spectrum with the PLQY dropped to 35% due to intermolecular interactions. However, the emission efficiency of the molecule

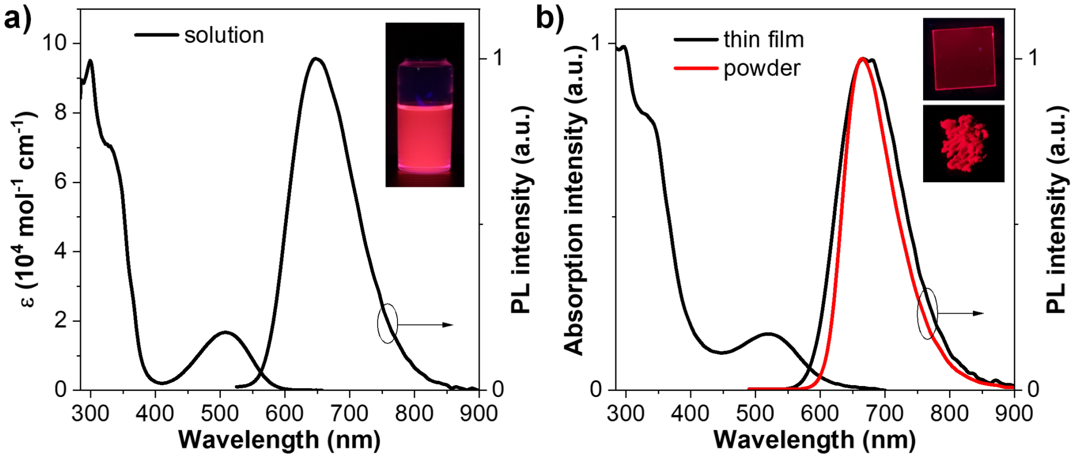

Figure 2: UV–vis absorption and PL spectra in a) toluene solution (≈1 × 10^{-5} M) and b) thin film spin-coated on fused silica substrate and solid powder (insert: fluorescence images of the solution, thin film, and solid powder under UV light at 356 nm).

Table 1: Optical and physical data of **TPECNz**.

λ_{PL} (nm) sol[a]/film[b]/solid[c]	τ (ns)[d] sol[a]/film[b]	PLQY (%)[e] sol[a]/film[b]/solid[c]	k_r/k_{nr} (10^7 s^{-1})[a]	k_r/k_{nr} (10^7 s^{-1})[b]	$E_{1/2}$ vs Ag/Ag$^+$ (V)[f]	E_g^{opt}/E_g^{ele} (eV)[g]	HOMO/LUMO (eV)[h]
648/668/664	13.4/11.1	96/35/64	7.16/0.30	3.15/5.86	−1.26, 1.05, 1.47, 1.72	2.04/2.17	−5.44/−3.40

[a] Measured in diluted toluene solution (1×10^{-5} M); [b] measured in thin film; [c] measured in solid powder; [d] transient PL decay lifetime with excitation at 475 nm; [e] absolute PL quantum yield measured by an integrating sphere; [f] obtained from differential pulse voltammetry (DPV) peak; [g] band-gap energy from UV absorption (E_g^{opt}) and electrochemical (E_g^{ele}) results; [h] calculated from HOMO (eV) = −(4.44 + E_{onset}^{ox}) and LUMO (eV) = HOMO + E_g^{opt}.

is enhanced in the solid powder form with a PLQY of 64% owing to its AIE nature.

To gain more information about the effect of the solvent on the optical properties of **TPECNz**, the absorption and emission behaviors were investigated in several solvents as illustrated in Figure 3a. The results showed that, while the UV–vis absorption spectra were nearly unaffected by the nature of the solvent due to the LE nature, the emission spectra exhibited a noticeable positive solvatochromism, with maxima shifting towards longer wavelengths with increasing solvent polarities. Particularly, the maximum PL peaks in low polar solvents showed little shifts because of the LE character, whereas red shifts of the PL maxima apparently occurred in higher polar solvents due to CT excited state; therefore, the molecule contains both the intrinsic LE and CT excited states or demonstrates HLCT char-

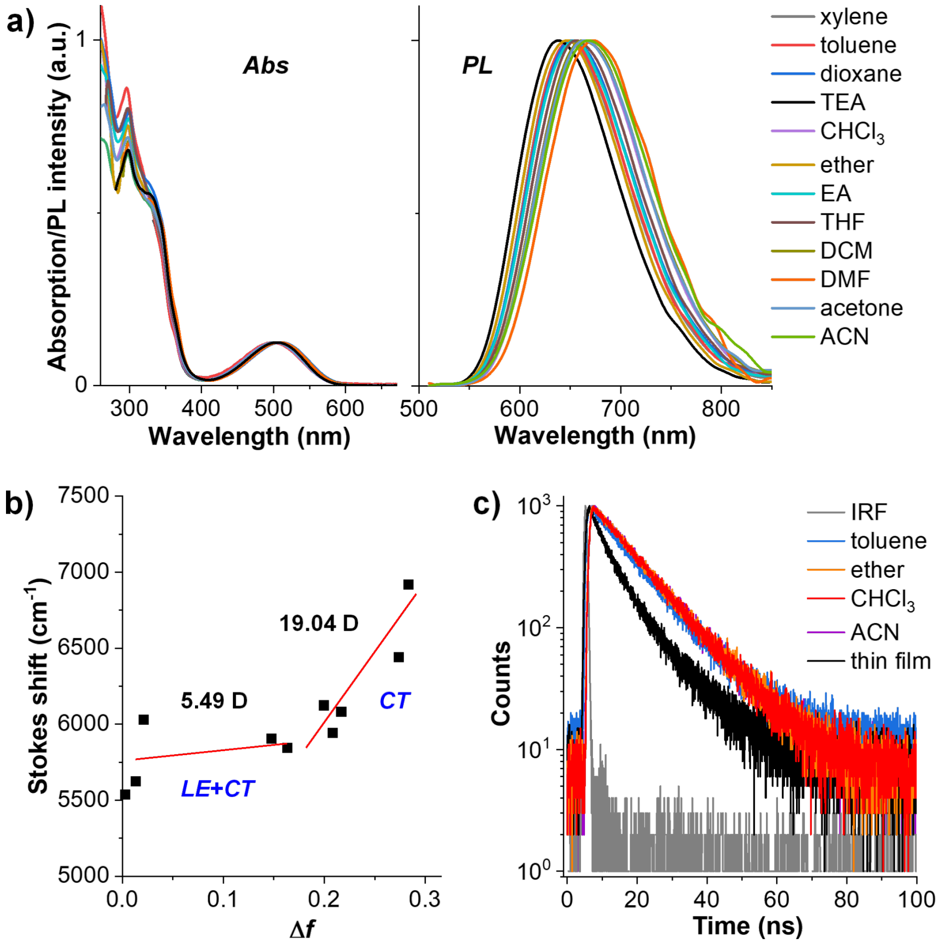

Figure 3: a) Normalized UV–vis absorption/PL spectra in different solvents. b) Lippert–Mataga plot of Stokes shift vs solvent polarity function (Δ*f*). c) Transient PL decay traces in various solvents and thin film. IRF = instrument response function.

acteristics. Besides, the Stokes shifts between absorption and emission spectra were plotted as a function of solvent polarity function (Δf) corresponding to the Lipper–Mataga model which defines the interactions between the solvent and dipole moment of the chromophore (Figure 3b). The Lippert–Mataga plot showed two linear slopes indicating the presence of two different excited states in the molecule. In the high-polarity region, the excited-state dipole moment (μ_e) was 19.04 D, which was close to that of a typical CT molecule 4-(*N*,*N*-dimethylamino)benzonitrile (μ_e = 23 D) [55], suggesting a CT state-dominated character in high-polarity solvents. Besides, in the low-polarity region, the μ_e value was 5.49 D, which is slightly higher than the ground-state dipole moment (μ_g = 1.30 D) estimated using B3LYP/6-31G(d,p) calculation. Nevertheless, this value was significantly smaller than that of the high-polarity region, indicating that the S_1 state in low-polarity solvents contained both CT and LE components simultaneously, which underwent interstate coupling forming a new HLCT emissive state. Additionally, transient PL decay spectra of **TPECNz** in solvents of different polarities showed a single exponential decay in nanosecond ranges (Figure 3c), signifying that the excited state responsible for the PL emission originates from the hybridization between LE and CT excited states or HLCT state, not a simple mix-up of the two states [56].

Furthermore, to further understand the PLQY of the molecule in solution and thin film, the radiative rate constant (k_r) and non-radiative rate constant (k_{nr}) were calculated from the PLQY values and PL lifetimes (τ) according to Equation 1 and Equation 2.

$$k_r = \frac{\Phi_{PL}}{\tau} \qquad (1)$$

$$\Phi_{PL} = \frac{k_r}{k_r + k_{nr}} \qquad (2)$$

As can be seen from Table 1, the k_r of **TPECNz** in solution is larger than k_{nr}, which is consistent with the the observerd high PLQY in solution. On the other hand, k_{nr} of **TPECNz** in thin films is significantly higher than the k_{nr} of solution, explaining the drop of PLQY in thin films as compared to the PLQY in solution. However, the moderate PLQY in thin films still makes **TPECNz** suitable for the deep-red OLEDs.

In addition, the AIE characteristic of **TPECNz** was further investigated by observing its PL emissions in water/THF mixtures with different water fractions (f_w = 0–95%). In such diverse solvent mixtures, the molecule will demonstrate different degrees of aggregation since it can dissolve really well in THF but is insoluble in water, resulting in colloidal nanoaggregates being formed in solutions with high water contents. As shown in Figure 4a and 4b, in pure THF, **TPECNz** deep-red emission color with the PL peaked at 658 nm. With the increase of f_w, the PL emission maxima suddenly dropped. At f_w = 40%, the PL intensity reached the lowest point, as well as the PL peak being red-shifted. This could be attributed to the twisted ICT emission characteristics of the molecule described by a red-shifted PL emission and a weakened emission intensity with the increased solvent polarity [57,58]. As the f_w was further raised to 95%, the PL emissions became more intense and were blue-shifted. This was attributable to the formation of nanoaggregates and suppression of the ICT process. This finding proves that both **TPECNz** is an AIE-active fluorophore, however, the AIE effect in **TPECNz** might not be as strong as for the standard AIE molecules, whose emissions are completely quenched

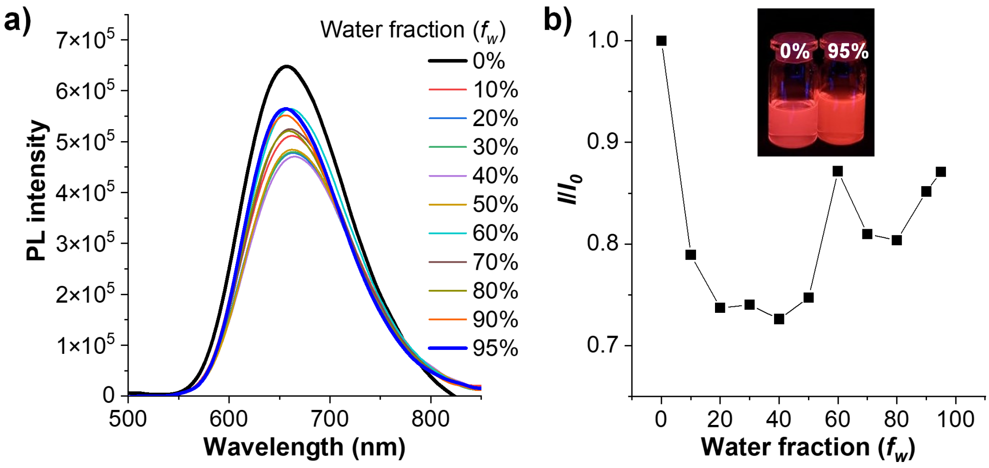

Figure 4: a) PL spectra in THF/water mixtures (5 μM) with different water fractions (f_w). b) Plot of relative PL intensity (I/I_0) vs % of water fraction (f_w) (insert: photographs of the solutions @ f_w of 0% and 95% taken under UV illumination).

in solutions and brightened by aggregate formation, as a result of the restriction of intramolecular motions (RIM) caused by intermolecular steric interaction [53]. The weak AIE characteristic of **TPECNz** in the aggregate state could be attributed to the competition between the twisted ICT and AIE properties in the molecule [57,58].

The thermal properties of **TPECNz** were studied by thermogravimetric analysis (TGA) and differential scanning calorimetry (DSC) under N_2 atmosphere at a scanning rate of 10 °C min^{-1}. As displayed in Figure 5a, the compound has a high thermal stability with a decomposition temperature at 5% weight loss (T_{5d}) of 498 °C, a glass transition temperature (T_g) of 236 °C, and a melting temperature (T_m) of 376 °C. The high T_g may enhance the morphological thin film stability and film integrity of **TPECNz** during device fabrication. While the high T_m suggests that **TPECNz** can withstand the latent heat generated during the device fabrication and operation. These results signaled that **TPECNz** may be suitable for optoelectronic devices. The electrochemical behavior of **TPECNz** was analyzed by cyclic voltammetry (CV) and differential pulse voltammetry (DPV) in CH_2Cl_2 containing 0.1 M n-Bu_4NPF_6 as a supporting electrolyte. As illustrated in Figure 5b, the molecule shows multiple quasi-reversible oxidation and reduction behavior in the potential window from −1.5 eV to 2.0 eV. The reduction wave appeared at a half-wave potential ($E_{1/2}$) of −1.26 eV assigned to the reduction of an electron-deficient Nz core as observed in the calculated LUMO orbital [39]. The first oxidation wave occurred at $E_{1/2}$ of 1.05 eV and was ascribed to the oxidation of the π-conjugated backbone along the Nz core and end-capped carbazole moieties as seen in the computed HOMO orbital, while the second oxidation wave at $E_{1/2}$ of 1.47 eV was attributed to the oxidation of the π-conjugated TPE–carbazole fragment as depicted in the calculated HOMO−1 orbital. In addition, the oxidation and reduction onsets of **TPECNz** were 1.00 eV and −1.17 eV, respectively. Hence, the electrochemical energy gap (E_g^{ele}) defined as the difference between the oxidation and reduction onset potentials was calculated to be 2.17 eV, which is slightly higher than the E_g^{opt} estimated from the UV–vis absorption onset (Table 1). The HOMO energy level was calculated from the oxidation onset potential to be −5.44 eV. Further, the calculated LUMO energy level was found to be −3.40 eV. The relatively low LUMO level of **TPECNz** is conceivably associated with a high electron deficiency of the Nz moiety originating from its localized distribution of electrons and the high electronegativities of the N and S atoms, whereas its high HOMO level is attributed to the electron-donating property of the attached carbazoles and the π-conjugation of the carbazole–Nz–carbazole fragment. Such proper energy levels will benefit the efficient charge injections from the electrodes in OLEDs.

To evaluate charge-carrier mobility in **TPECNz**, hole (μ_h) and electron (μ_e) mobilities were initially measured using metal-insulator-semiconductor (MIS) diodes in combination with charge extraction in linearly increasing voltage (CELIV) or MIS-CELIV technique [59-61]. Electron- and hole-only MIS devices were fabricated with the structures of indium tin oxide (ITO)/magnesium fluoride (MgF_2) (20 nm)/**TPECNz** (100 nm)/lithium fluoride (LiF) (1 nm)/aluminum (Al) (100 nm) and ITO/MgF_2 (20 nm)/**TPECNz** (100 nm)/molybdenum trioxide (MoO_3) (6 nm)/Al (100 nm), respectively (Figure 6a), where the MgF_2 layer was employed as an insulator. During the measurements, varied maximum voltages were applied during the pulse for extracting the charges while keeping the pulse duration and offset voltage of 10 µs and 5 V for the electron-only

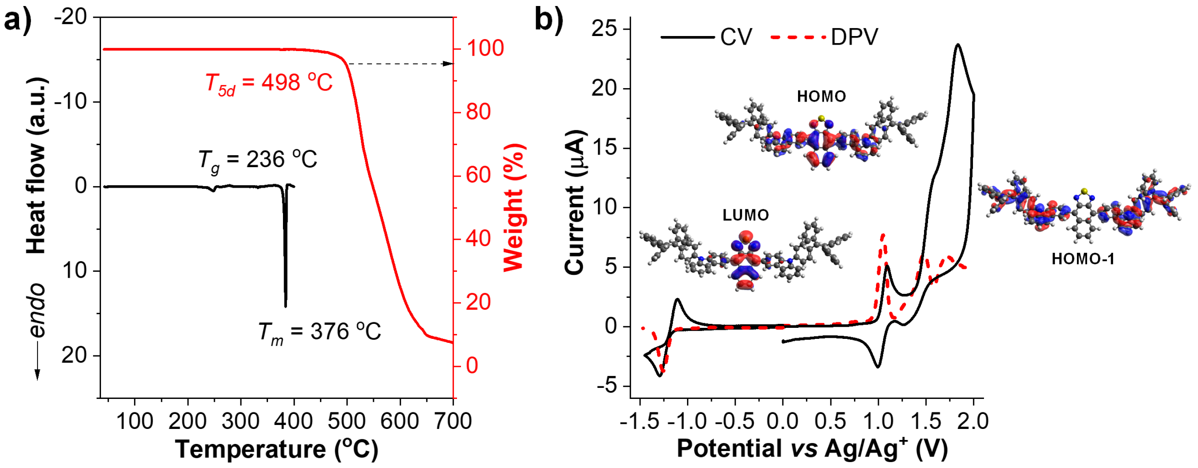

Figure 5: a) DSC and TGA thermograms measured at a heating rate of 10 °C min^{-1} under N_2 flow. b) Cyclic voltammogram (CV) and differential pulse voltammogram (DPV) analyzed in dry CH_2Cl_2 at a scan rate of 50 mV s^{-1} under an argon atmosphere (insert: HOMO/HOMO−1/LUMO orbitals).

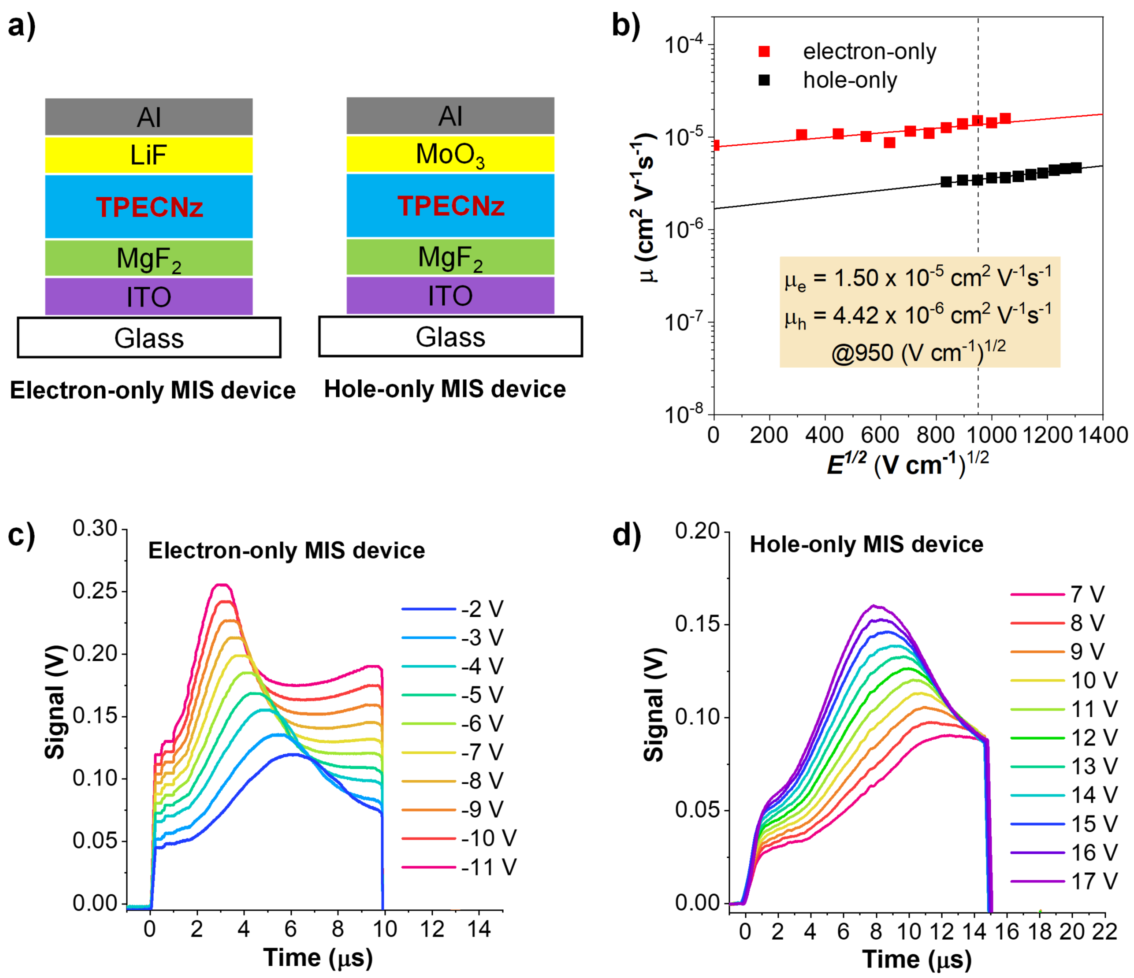

Figure 6: a) Schematic structure of the hole-only and electron-only MIS devices. b) Electric-field dependence of the hole and electron mobilities. Transient signals at different applied maximum voltages for c) electron-only MIS device and d) hole-only MIS device.

MIS device and 15 μs and −5 V for the hole-only MIS device, respectively, and their MIS-CELIV signal transient plots as a function of time are shown in Figure 6c and 6d. As the applied voltage increased, it was found that the transient peak shifted to slightly shorter times indicating an increasing carrier mobility. The hole and electron mobilities (μ) were calculated and plotted as a function of electric field ($E^{1/2}$). As illustrated in Figure 6b, the mobility (μ) of both holes and electrons is electric field dependent and gradually increases on increasing the electric field, which is explained as the Poole–Frenkel effect obeying the relationship, $\log \mu \propto E^{1/2}$ [59]. The measured mobilities of the holes (μ_h) and electrons (μ_e) of **TPECNz** thin film at 950 $(\mathrm{V\ cm^{-1}})^{1/2}$ electric field were 4.42×10^{-6} and 1.50×10^{-5} $\mathrm{cm^2\ V^{-1}\ s^{-1}}$, respectively. This result suggested that **TPECNz** was an ambipolar material with the mobility of electrons somewhat greater than that of holes. The pronounced ability of **TPECNz** to transport electrons could be accredited to a strong-electron affinity of the Nz core, while its ability to transport holes could be derived from the attached carbazole moieties.

To evaluate the electroluminescent (EL) performance of **TPECNz**, non-doped OLED employing **TPECNz** as an emissive layer (EML) was fabricated through thermal evaporation of the optimized device configuration of ITO/1,4,5,8,9,11-hexaazatriphenylene-hexacarbonitrile (HAT-CN) (6 nm)/*N*,*N*'-bis(naphthalen-1-yl)-*N*,*N*'-bis(phenyl)benzidine (NPB) (30 nm)/tris(4-carbazoyl-9-ylphenyl)amine (TCTA) (10 nm)/**TPECNZ** (60 nm)/1,3,5-tris(1-phenyl-1*H*-benzimidazol-2-yl)benzene (TPBi) (40 nm)/LiF (1 nm)/Al (100 nm), in which ITO and Al served as anode and cathode, respectively (Figure 7a). Herein, HAT-CN and LiF were used as the hole- and electron-injection layers, respectively, NPB and TPBi were applied as the hole- and electron-transporting layers, respectively, and TCTA owing to its high-lying LUMO energy level (LUMO = 2.3 eV) and low electron mobility was utilized as an electron-blocking layer

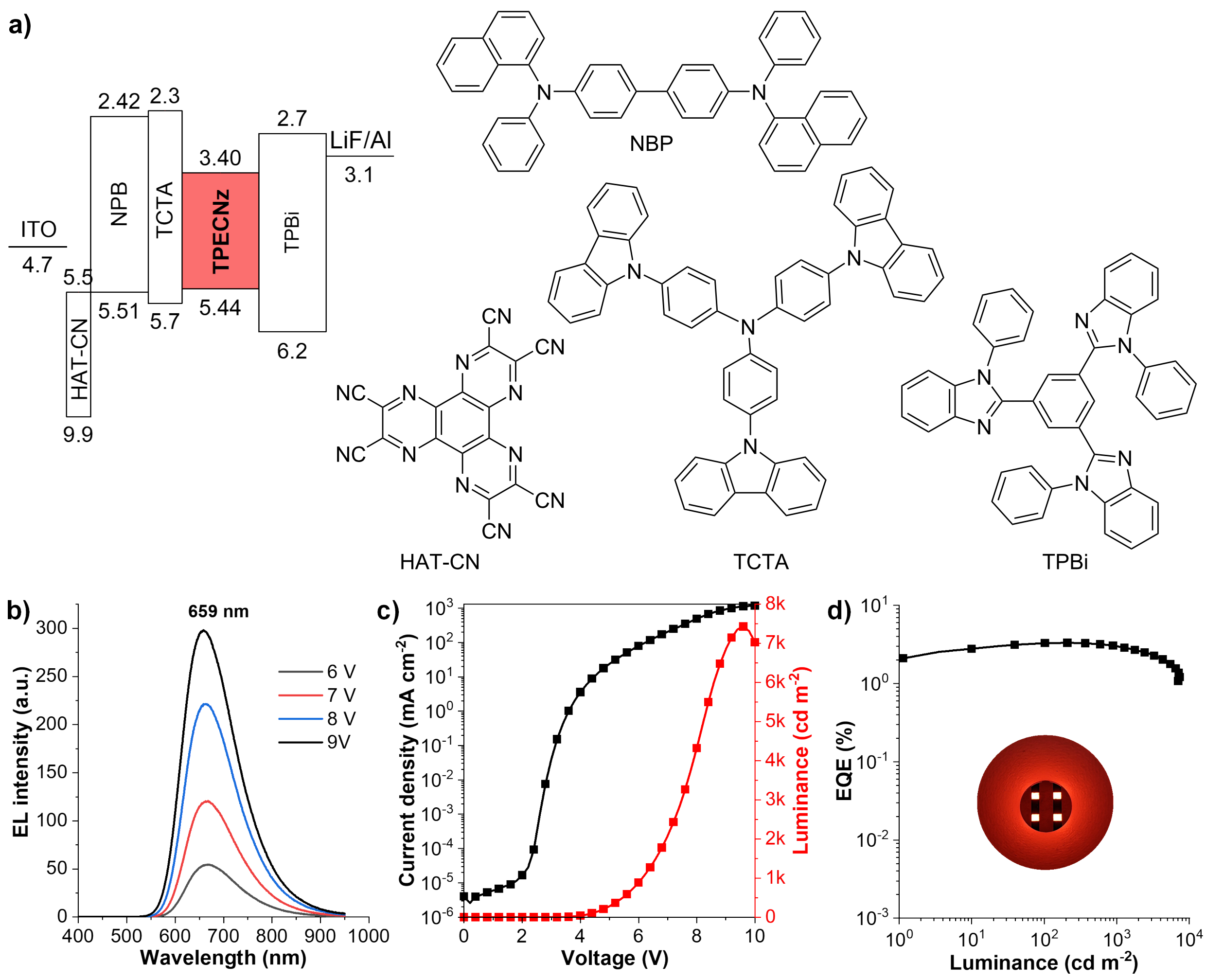

Figure 7: a) Schematic energy diagram of OLED and organic materials used in the device. b) EL spectra at various applied voltages. c) Current density–voltage–luminance (*J*–*V*–*L*) characteristics. d) External quantum efficiency–luminance (EQE–*L*) plot (insert: photograph of OLED under operation).

[62]. Owing to a narrow band gap stemming from its strong D–A characteristic, **TPECNz**-based non-doped OLED successfully displayed deep-red emission with a maximum EL peak at 659 nm and Commission Internationale de L'Eclairage (CIE) coordinates of (0.664, 0.335), which were very close to the standard red CIE coordinates of (0.67, 0.33) [63]. The device demonstrated high emission stability with EL spectra under different operating voltages (6–9 V) revealing an unchanged profile with a single emission band (Figure 7b), indicating the recombination zone of the excitons confined inside the EML. No emission peaks at low wavelengths from the supporting layers (NPB at 440 nm [64], TCTA at 410 nm [65], and TPBi at 390 nm [66]) and at longer wavelengths due to the excimer/exciplex emissions at the interfaces of NPB-TCTA/EML and EML/TPBi were observed, signifying that the OLED possessed a well-balanced electron and hole transport. Moreover, due to the efficient ambipolar charge-carrier-transporting property of **TPECNz** EML and good charge balance in the device, the non-doped OLED was turned on at a low voltage of 3.2 V and achieved decent device EL performance as presented in Figure 7c and 7d. The device exhibited a maximum luminance (L_{max}) of 7430 cd m^{-2}, a maximum external quantum efficiency (EQE$_{\mathrm{max}}$) of 3.32%, and a maximum luminance efficiency (LE$_{\mathrm{max}}$) of 2.87 cd A^{-1}, with a little efficiency roll-off of 9% at 1000 cd m^{-2}. Furthermore, its exciton utilization efficiency (EUE) was calculated using EUE = EQE/($\eta_{\mathrm{out}} \times \eta_{\mathrm{rec}} \times$ PLQY) (light outcoupling efficiency: η_{out} = 20%, PLQY in a thin film = 35%, and charge recombination: η_{rec} = 100%) to be 47%. This EUE was higher than the 25% theoretical upper limit of spin statistics for typical fluorescent emitters, indicating that the triplet excitons have been utilized via an HLCT mechanism to contribute to the EL in this device.

Conclusion

In summary, a new D–A–D-type fluorophore as a deep-red emitter has been designed and synthesized by exploiting a strong electron-accepting naphtho[2,3-*c*][1,2,5]thiadiazole (Nz) as A unit and *N*-(4-(1,2,2-triphenylvinyl)phenyl)carbazole as D unit. The integration of 4-(1,2,2-triphenylvinyl)phenyl (TPE) moiety as an AIE luminogen helped to provide the fluorophore with AIE feature, while its D–A–D structure with a proper twist angle (54–56°) between the Nz acceptor and carbazole donor promotes a state mixing between close-lying LE and CT states or HLCT property. The combined characteristics of HLCT and weak AIE were clearly evidenced by a solvatochromic study, emission in THF/water investigation, and theoretical calculations. These synergetic properties could benefit for effective utilization of excitons in the OLED. A collaborative consequence of its D–A–D-type structure, a strong electron affinity of Nz unit, and electron donating and hole-transporting properties of carbazole nurtured the molecule to exhibit an intense deep-red emission with decent PL quantum yield, superior thermal property, and ambipolar charge-carrier-transporting property with a good balance of mobility of electrons and holes, which were desirable properties for OLED application. It was efficiently utilized as a non-doped emitter in OLEDs. The device presented a strong deep-red electroluminescent (EL) emission (peak at 659 nm and CIE coordinates of (0.664, 0.335)) with a maximum luminance of 7430 cd m^{-2}, EQE_{max} of 3.32%, and EUE of 47%. This work successfully established that an ambipolar D–A–D-type fluorophore having combined AIE–HLCT features could be a promising design to develop future deep-red or near-infrared OLEDs.

Experimental

Materials and Methods

All chemical reagents and solvents were purchased from commercial resources and used without further purification. ^{1}H NMR and ^{13}C NMR spectra were recorded with a Bruker AVANCE III HD 600 (600 MHz for ^{1}H and 151 MHz for ^{13}C) using $CDCl_3$ as a solvent containing TMS as an internal standard. High-resolution mass spectrometry (HRMS) analysis was performed using either a Bruker LC-Quadrupole-Time-of Flight tandem mass spectrometer or a Bruker Autoflex MALDI-TOF mass spectrometer. UV–vis spectra were recorded using a Perkin Elmer Lambda 1050 UV–vis–NIR spectrometer. Luminescence emission spectra and lifetimes were analyzed using an Edinburgh Instruments FLS980 Spectrometer. Absolute PL quantum yield (PLQY) was measured using a calibrated integrating sphere incorporated with Edinburgh Instruments FLS980 Spectrometer. Electrochemical studies were carried out using an Autolab PGSTA101 potentiostat equipped with three electrodes (Pt, glassy carbon, and Ag/AgCl) in dry CH_2Cl_2 containing 0.1 M n-Bu_4NPF_6 as a supporting electrolyte under argon. Thermogravimetric analysis (TGA) and differential scanning calorimetry (DSC) were recorded using a Rigaku STA8122 thermogravimetric analyzer and a PerkinElmer DSC 8500 Lab System, respectively. Melting points were measured using a Krüss KSP1N melting point meter and are uncorrected.

Quantum chemical calculations were executed using the Gaussian 16 package [67]. Density functional theory (DFT) calculations at the B3LYP level of theory with the 6-31G(d,p) basis set were performed to realize the ground state geometry, HOMO and LUMO distributions, and HOMO and LUMO energy levels. Natural transition orbitals (NTOs) were calculated for the excited states using time-dependent (TD)-DFT calculations at the CAM-B3LYP/6-31G(d) level of theory.

Device fabrication and testing

The patterned ITO-coated glass substrate with a sheet resistance of 12 Ω sq^{-1} was pre-cleaned carefully and cured with UV/O_3 for 20 min. The OLED with an active diode area of 0.04 cm^{-2} was fabricated using a Kurt J. Lasker mini SPECTROS 100 thin film deposition system under vacuum conditions with a base pressure lower than 1×10^{-5} bar and a thermal evaporation rate of 0.2–0.3 Å s^{-1} for MgF_2, HATCN, NPB, TCTA, **TPECNz**, and TPBi, 0.05–0.1 Å s^{-1} for LiF, and about 1 Å s^{-1} for Al layer. The thickness of each layer was monitored by a quartz oscillator thickness sensor. All devices were measured without encapsulation under an ambient atmosphere at room temperature. They were analyzed by a Keithley 2400 source meter, a Hamamatsu Photonics PMA-12 multichannel analyzer, and an integrating sphere equipped with a Hamamatsu Photonics C9920-12 EQE measurement system. The hole and electron mobility were investigated using MIS-CELIV measurement. A pulse delay generator (Stanford Research System DG535) and a single channel arbitrary/function generator (AFG 3021B) were used to generate the CELIV triangle pulse with adjustable voltage slope and offset, as well as amplified the signal by WMA-320 high voltages amplifier. For photo-CELIV, a delay generator (Stanford Research System DG535) was also used for pulse synchronization along with an LED driver (THORLABS, LEDD1B). The signal was recorded by a 3-series mixed domain oscilloscope (Tektronix, MDO32).

Synthesis of 9-(4-(1,2,2-triphenylvinyl)phenyl)-9*H*-carbazole (2): [68] A mixture of **1** (2.00 g, 4.86 mmol), carbazole (2.44 g, 14.58 mmol), K_3PO_4 (5.17 g, 24.313 mmol), ±-*trans*-1,2-diaminocyclohexane (1.46 mL, 12.17 mmol) and CuI (1.85 g, 9.72 mmol) in dry toluene (50 mL) was degassed with N_2 for 10 min. The reaction mixture was stirred at reflux under N_2 atmosphere for 18 h. After being cooled to room temperature, the mixture was diluted with water (100 mL) and extracted with CH_2Cl_2 (50 mL × 3). The combined organic layer was washed with water, brine solution, dried over anhydrous Na_2SO_4, filtered, and concentrated under reduced pressure. The crude product was then purified by column chromatography over silica gel eluting with CH_2Cl_2/hexane 1:4 to give white solids (2.11 g, 87%). ^{1}H NMR (600 MHz, $CDCl_3$) δ 8.12 (d, *J* = 7.7 Hz, 2H), 7.40 (t, *J* = 7.8 Hz, 2H), 7.34 (d, *J* = 8.2 Hz, 2H), 7.28 (t, *J* = 8.0 Hz, 4H), 7.24 (d, *J* = 8.1 Hz, 2H), 7.21–7.07 (m, 15H); ^{13}C NMR (151 MHz, $CDCl_3$) δ 143.55, 143.41, 143.30, 142.94, 141.84, 140.74, 140.12, 135.68, 132.67, 131.42, 131.37, 131.32, 127.85, 127.77, 127.72, 126.73, 126.69, 126.62, 126.12, 125.83, 123.32, 120.25, 119.84, 109.80; HRMS–APCI–TOF (*m/z*): $[M + H]^+$ calcd for $C_{38}H_{28}N$, 498.2216; found, 498.2233.

Synthesis of 3-(4,4,5,5-tetramethyl-1,3,2-dioxaborolan-2-yl)-9-(4-(1,2,2-triphenylvinyl)phenyl)-9*H*-carbazole (3): A round-bottomed flask containing a solution of compound **2** (1.81 g, 3.63 mmol) in THF (200 mL) was covered with aluminum foil and cooled in an ice bath. A solution of NBS (646 mg, 3.63 mmol) in THF (100 mL) was added dropwise into the solution over a period of 2 h, while monitoring the reaction by TLC (CH_2Cl_2/hexane 1:4). Then, the reaction was quenched with water (100 mL) and the mixture extracted with CH_2Cl_2 (50 mL × 3). The combined organic layer was washed with water, brine, dried over anhydrous Na_2SO_4, filtered, and concentrated under reduced pressure. The residue was crystallized from CH_2Cl_2/methanol to obtain compound **3** as a mixture with unreacted starting material and dibrominated product which was used in the next step without further purification. White solid (1.34 g, 2.32 mmol). HRMS–APCI–TOF *m/z*: $[M + H]^+$ calcd for $C_{38}H_{28}N$, 498.2216; found, 498.2217; $[M + H]^+$ calcd for $C_{38}H_{27}BrN$, 576.1321; found, 576.1331; $[M + H]^+$ calcd for $C_{38}H_{26}Br_2N$, 654.0427; found, 654.0438.

The mixture of the above crude product (1.00 g), bis(pinacolato)diboron (881 mg, 3.47 mmol), KOAc (2.04 g, 20.81 mmol), and Pd(dppf)Cl_2 (70.8 mg, 0.087 mmol) in dry toluene (50 mL) was degassed with N_2 for 10 min. The reaction mixture was stirred at a refluxing temperature under N_2 atmosphere for 48 h. After being cooled to room temperature, the mixture was diluted with water (100 mL) and extracted with CH_2Cl_2 (50 mL × 3). The combined organic layer was washed with water, brine, dried over anhydrous Na_2SO_4, filtered, and concentrated under reduced pressure. The crude product was then purified by column chromatography over silica gel eluting with CH_2Cl_2/hexane 3:7 to give compound **3** as white solid (928 mg, 41% over two steps). ^{1}H NMR (600 MHz, $CDCl_3$) δ 8.61 (s, 1H), 8.15 (d, *J* = 7.7 Hz, 1H), 7.85 (d, *J* = 8.2 Hz, 1H), 7.39 (t, *J* = 7.7 Hz, 1H), 7.34–7.22 (m, 7H), 7.22–7.04 (m, 15H), 1.40 (s, 12H); ^{13}C NMR (151 MHz, $CDCl_3$) δ 143.54, 143.38, 143.24, 143.13, 142.88, 141.95, 140.91, 140.13, 135.48, 132.70, 132.35, 131.43, 131.38, 131.32, 127.88, 127.77, 127.73, 127.70, 126.75, 126.72, 126.65, 126.15, 125.86, 123.54, 123.06, 120.50, 120.25, 109.83, 109.19, 83.66, 24.95; HRMS–APCI–TOF (*m/z*): $[M + H]^+$ calcd for $C_{44}H_{39}BNO_2$, 624.3068; found, 624.3078.

Synthesis of 4,9-bis(9-(4-(1,2,2-triphenylvinyl)phenyl)-9*H*-carbazol-3-yl)naphtho[2,3-*c*][1,2,5]thiadiazole (TPECNz): A mixture of **3** (834 mg, 1.34 mmol), 4,9-dibromonaphtho[2,3-*c*][1,2,5]thiadiazole (200 mg, 0.58 mmol), Pd(PPh_3)$_4$ (80.6 mg, 0.070 mmol) and 2 M Na_2CO_3 (8.7 mL, 17.44 mmol) in THF (50 mL) was degassed with N_2 for 3 min. The reaction mixture was stirred at refluxing temperature under N_2 atmosphere for 48 h. After being cooled to room temperature, the mixture was diluted with water (100 mL) and extracted with CH_2Cl_2 (50 mL × 3). The combined organic layer was washed with water, brine, dried over anhydrous Na_2SO_4, filtered, and concentrated under reduced pressure. The crude product was then purified by column chromatography over silica gel eluting with CH_2Cl_2/hexane 3:7, followed by recrystallization from a CH_2Cl_2/methanol mixture to obtain **TPECNz** as red solid (396.0 mg, 58%). Mp > 360 °C; ^{1}H NMR (600 MHz, $CDCl_3$) δ 8.43 (s, 2H), 8.15 (td, *J* = 7.1, 3.5 Hz, 4H), 7.74 (dd, *J* = 8.3, 1.7 Hz, 2H), 7.60 (d, *J* = 8.3 Hz, 2H), 7.45 (t, *J* = 7.6 Hz, 2H), 7.41 (t, 6H), 7.35 (dd, *J* = 7.2, 3.2 Hz, 2H), 7.30 (d, *J* = 8.3 Hz, 6H), 7.24–7.07 (m, 30H); ^{13}C NMR (151 MHz, $CDCl_3$) δ 152.04, 143.54, 143.40, 143.29, 143.19, 141.93, 141.27, 140.62, 140.10, 135.60, 132.78, 132.46, 131.43, 131.38, 131.31, 130.75, 129.14, 128.16, 127.87, 127.81, 127.72, 127.43, 126.78, 126.71, 126.63, 126.22, 126.17, 123.56, 123.35, 123.21, 120.53, 120.11, 110.03, 109.89; HMRS–MALDI–TOF (*m/z*): $[M]^+$ calcd for $C_{86}H_{56}N_4S$, 1176.4226; found, 1176.4221.

Supporting Information

Supporting Information File 1

Energy diagram of singlet and triplet excited states estimated by CAM-B3LYP/6-31G(d,p) calculations and copies of ^{1}H NMR, ^{13}C NMR, and HRMS spectra of the synthesized compounds.
[https://www.beilstein-journals.org/bjoc/content/supplementary/1860-5397-19-122-S1.pdf]

Acknowledgements

We thank VISTEC for the scholarship support for S. A. and A. S.

Funding

This work was financially supported by the National Research Council of Thailand (NRCT) (no. N42A650196).

ORCID® iDs

Taweesak Sudyoadsuk - https://orcid.org/0000-0002-9160-1578
Vinich Promarak - https://orcid.org/0000-0003-4805-9944

Preprint

A non-peer-reviewed version of this article has been previously published as a preprint: https://doi.org/10.3762/bxiv.2023.29.v1

References

1. Zhao, M.; Guo, Y.-S.; Xu, W.-N.; Zhao, Y.-F.; Xie, H.-Y.; Li, H.-J.; Chen, X.-F.; Zhao, R.-S.; Guo, D.-S. *TrAC, Trends Anal. Chem.* **2020,** *122,* 115704. doi:10.1016/j.trac.2019.115704
2. Gomes, L. J.; Carrilho, J. P.; Pereira, P. M.; Moro, A. J. *Sensors* **2023,** *23,* 471. doi:10.3390/s23010471
3. Laramie, M. D.; Levitz, A.; Henary, M. *Sens. Actuators, B* **2017,** *243,* 1191–1204. doi:10.1016/j.snb.2016.12.051
4. Shen, Q.; Wang, S.; Yang, N.-D.; Zhang, C.; Wu, Q.; Yu, C. *J. Lumin.* **2020,** *225,* 117338. doi:10.1016/j.jlumin.2020.117338
5. Feng, X.; Wei, L.; Liu, Y.; Chen, X.; Tian, R. *Adv. Healthcare Mater.* **2023,** *12,* 2300537. doi:10.1002/adhm.202300537
6. Miao, W.; Guo, X.; Yan, X.; Shang, Y.; Yu, C.; Dai, E.; Jiang, T.; Hao, E.; Jiao, L. *Chem. – Eur. J.* **2023,** *29,* e202203832. doi:10.1002/chem.202203832
7. Zhang, F.; Tang, B. Z. *Chem. Sci.* **2021,** *12,* 3377–3378. doi:10.1039/d1sc90046c
8. Li, J.; Dong, Y.; Wei, R.; Jiang, G.; Yao, C.; Lv, M.; Wu, Y.; Gardner, S. H.; Zhang, F.; Lucero, M. Y.; Huang, J.; Chen, H.; Ge, G.; Chan, J.; Chen, J.; Sun, H.; Luo, X.; Qian, X.; Yang, Y. *J. Am. Chem. Soc.* **2022,** *144,* 14351–14362. doi:10.1021/jacs.2c05826
9. Chen, L.; Chen, M.; Zhou, Y.; Ye, C.; Liu, R. *Front. Chem. (Lausanne, Switz.)* **2021,** *9,* 629062. doi:10.3389/fchem.2021.629062
10. Minotto, A.; Haigh, P. A.; Łukasiewicz, Ł. G.; Lunedei, E.; Gryko, D. T.; Darwazeh, I.; Cacialli, F. *Light: Sci. Appl.* **2020,** *9,* 70. doi:10.1038/s41377-020-0314-z
11. Patil, D.; Jadhav, M.; Avhad, K.; Gawale, Y.; Sekar, N. *J. Lumin.* **2018,** *204,* 436–447. doi:10.1016/j.jlumin.2018.08.031
12. Aoki, R.; Komatsu, R.; Goushi, K.; Mamada, M.; Ko, S. Y.; Wu, J. W.; Placide, V.; D'Aléo, A.; Adachi, C. *Adv. Opt. Mater.* **2021,** *9,* 2001947. doi:10.1002/adom.202001947
13. Wan, Q.; Tong, J.; Zhang, B.; Li, Y.; Wang, Z.; Tang, B. Z. *Adv. Opt. Mater.* **2020,** *8,* 1901520. doi:10.1002/adom.201901520
14. Ye, H.; Kim, D. H.; Chen, X.; Sandanayaka, A. S. D.; Kim, J. U.; Zaborova, E.; Canard, G.; Tsuchiya, Y.; Choi, E. Y.; Wu, J. W.; Fages, F.; Bredas, J.-L.; D'Aléo, A.; Ribierre, J.-C.; Adachi, C. *Chem. Mater.* **2018,** *30,* 6702–6710. doi:10.1021/acs.chemmater.8b02247
15. Xiao, Y.; Wang, H.; Xie, Z.; Shen, M.; Huang, R.; Miao, Y.; Liu, G.; Yu, T.; Huang, W. *Chem. Sci.* **2022,** *13,* 8906–8923. doi:10.1039/d2sc02201j
16. Therdkatanyuphong, P.; Chasing, P.; Kaiyasuan, C.; Boonnab, S.; Sudyoadsuk, T.; Promarak, V. *Adv. Funct. Mater.* **2020,** *30,* 2002481. doi:10.1002/adfm.202002481
17. Lee, W. W. H.; Zhao, Z.; Cai, Y.; Xu, Z.; Yu, Y.; Xiong, Y.; Kwok, R. T. K.; Chen, Y.; Leung, N. L. C.; Ma, D.; Lam, J. W. Y.; Qin, A.; Tang, B. Z. *Chem. Sci.* **2018,** *9,* 6118–6125. doi:10.1039/c8sc01377b
18. Lo, Y.-C.; Yeh, T.-H.; Wang, C.-K.; Peng, B.-J.; Hsieh, J.-L.; Lee, C.-C.; Liu, S.-W.; Wong, K.-T. *ACS Appl. Mater. Interfaces* **2019,** *11,* 23417–23427. doi:10.1021/acsami.9b06612
19. Caspar, J. V.; Kober, E. M.; Sullivan, B. P.; Meyer, T. J. *J. Am. Chem. Soc.* **1982,** *104,* 630–632. doi:10.1021/ja00366a051
20. Zampetti, A.; Minotto, A.; Cacialli, F. *Adv. Funct. Mater.* **2019,** *29,* 1807623. doi:10.1002/adfm.201807623
21. Liu, J.-F.; Wang, X.-Q.; Yu, Y.-J.; Zou, S.-N.; Yang, S.-Y.; Jiang, Z.-Q.; Liao, L.-S. *Org. Electron.* **2021,** *91,* 106088. doi:10.1016/j.orgel.2021.106088
22. Malina, I.; Kampars, V.; Turovska, B.; Belyakov, S. *Dyes Pigm.* **2017,** *139,* 820–830. doi:10.1016/j.dyepig.2017.01.017
23. Sugihara, Y.; Inai, N.; Taki, M.; Baumgartner, T.; Kawakami, R.; Saitou, T.; Imamura, T.; Yanai, T.; Yamaguchi, S. *Chem. Sci.* **2021,** *12,* 6333–6341. doi:10.1039/d1sc00827g
24. Tang, X.; Li, X.-L.; Liu, H.; Gao, Y.; Shen, Y.; Zhang, S.; Lu, P.; Yang, B.; Su, S.-J.; Ma, Y. *Dyes Pigm.* **2018,** *149,* 430–436. doi:10.1016/j.dyepig.2017.10.033
25. Kumsampao, J.; Chaiwai, C.; Chasing, P.; Chawanpunyawat, T.; Namuangruk, S.; Sudyoadsuk, T.; Promarak, V. *Chem. – Asian J.* **2020,** *15,* 3029–3036. doi:10.1002/asia.202000727
26. Redon, S.; Eucat, G.; Ipuy, M.; Jeanneau, E.; Gautier-Luneau, I.; Ibanez, A.; Andraud, C.; Bretonnière, Y. *Dyes Pigm.* **2018,** *156,* 116–132. doi:10.1016/j.dyepig.2018.03.049
27. Rémond, M.; Hwang, J.; Kim, J.; Kim, S.; Kim, D.; Bucher, C.; Bretonnière, Y.; Andraud, C.; Kim, E. *Adv. Funct. Mater.* **2020,** *30,* 2004831. doi:10.1002/adfm.202004831
28. Li, Y.; Zhu, H.; Wang, X.; Cui, Y.; Gu, L.; Hou, X.; Guan, M.; Wu, J.; Xiao, Y.; Xiong, X.; Meng, X.; Hong, X. *CCS Chem.* **2022,** *4,* 3735–3750. doi:10.31635/ccschem.022.202101547
29. Essam, Z. M.; Ozmen, G. E.; Setiawan, D.; Hamid, R. R.; Abd El-Aal, R. M.; Aneja, R.; Hamelberg, D.; Henary, M. *Org. Biomol. Chem.* **2021,** *19,* 1835–1846. doi:10.1039/d0ob02313b
30. Zhao, F.; Sun, T.; Wang, Y.; Yang, W.; Zhan, Y. *Dyes Pigm.* **2021,** *194,* 109542. doi:10.1016/j.dyepig.2021.109542
31. Li, W.; Pan, Y.; Xiao, R.; Peng, Q.; Zhang, S.; Ma, D.; Li, F.; Shen, F.; Wang, Y.; Yang, B.; Ma, Y. *Adv. Funct. Mater.* **2014,** *24,* 1609–1614. doi:10.1002/adfm.201301750
32. Li, W.; Pan, Y.; Yao, L.; Liu, H.; Zhang, S.; Wang, C.; Shen, F.; Lu, P.; Yang, B.; Ma, Y. *Adv. Opt. Mater.* **2014,** *2,* 892–901. doi:10.1002/adom.201400154
33. Jiang, J.; Li, X.; Hanif, M.; Zhou, J.; Hu, D.; Su, S.; Xie, Z.; Gao, Y.; Yang, B.; Ma, Y. *J. Mater. Chem. C* **2017,** *5,* 11053–11058. doi:10.1039/c7tc03978f
34. Loythaworn, T.; Petdee, S.; Chasing, P.; Chantanop, N.; Therdkatanyuphong, P.; Waengdongbung, W.; Sudyoadsuk, T.; Promarak, V. *Mater. Chem. Front.* **2022,** *6,* 3225–3236. doi:10.1039/d2qm00401a
35. Liu, T.; Chen, X.; Zhao, J.; Wei, W.; Mao, Z.; Wu, W.; Jiao, S.; Liu, Y.; Yang, Z.; Chi, Z. *Chem. Sci.* **2021,** *12,* 5171–5176. doi:10.1039/d1sc00272d

36. Sudyoadsuk, T.; Petdee, S.; Chasing, P.; Therdkatanyuphong, P.; Kaiyasuan, C.; Waengdongbung, W.; Namuangruk, S.; Promarak, V. *Dyes Pigm.* **2021,** *195,* 109712. doi:10.1016/j.dyepig.2021.109712
37. Tagare, J.; Vaidyanathan, S. *J. Mater. Chem. C* **2018,** *6,* 10138–10173. doi:10.1039/c8tc03689f
38. Yu, Y.; Cang, M.; Cui, W.; Xu, L.; Wang, R.; Sun, M.; Zhou, H.; Yang, W.; Xue, S. *Dyes Pigm.* **2021,** *184,* 108770. doi:10.1016/j.dyepig.2020.108770
39. Kongsabay, S.; Funchien, P.; Chasing, P.; Sudyodsuk, T.; Promarak, V. *J. Lumin.* **2022,** *248,* 118921. doi:10.1016/j.jlumin.2022.118921
40. Yu, Y.; Chao, X.; Xie, M.; Zhou, Y.; Ma, C.; Zhou, H.; Sun, Q.; Pan, Y.; Yang, W.; Xue, S. *Dyes Pigm.* **2023,** *215,* 111306. doi:10.1016/j.dyepig.2023.111306
41. Jairam, T.; Hong, W. P. *J. Mater. Chem. C* **2022,** *10,* 16173–16217. doi:10.1039/d2tc03601k
42. Liu, Y.; Liu, H.; Bai, Q.; Du, C.; Shang, A.; Jiang, D.; Tang, X.; Lu, P. *ACS Appl. Mater. Interfaces* **2020,** *12,* 16715–16725. doi:10.1021/acsami.0c01846
43. Liu, Y.; Man, X.; Bai, Q.; Liu, H.; Liu, P.; Fu, Y.; Hu, D.; Lu, P.; Ma, Y. *CCS Chem.* **2022,** *4,* 214–227. doi:10.31635/ccschem.021.202000627
44. Wang, C.; Li, X.; Pan, Y.; Zhang, S.; Yao, L.; Bai, Q.; Li, W.; Lu, P.; Yang, B.; Su, S.; Ma, Y. *ACS Appl. Mater. Interfaces* **2016,** *8,* 3041–3049. doi:10.1021/acsami.5b10129
45. Sudyoadsuk, T.; Petdee, S.; Waengdongbung, W.; Loythaworn, T.; Chasing, P.; Kongsabay, S.; Therdkatanyuphong, P.; Promarak, V. *Adv. Photonics Res.* **2023,** *4,* 2200195. doi:10.1002/adpr.202200195
46. Li, Y.; Yao, J.; Wang, C.; Zhou, X.; Xu, Y.; Hanif, M.; Qiu, X.; Hu, D.; Ma, D.; Ma, Y. *Dyes Pigm.* **2020,** *173,* 107960. doi:10.1016/j.dyepig.2019.107960
47. Chen, X.; Ma, D.; Liu, T.; Chen, Z.; Yang, Z.; Zhao, J.; Yang, Z.; Zhang, Y.; Chi, Z. *CCS Chem.* **2022,** *4,* 1284–1294. doi:10.31635/ccschem.021.202100900
48. Xia, H.; Xu, X.; Guo, J.; Qian, C.; Zhang, K.; Zhu, M.; Zhang, B.; Peng, W.; Peng, Q.; Zhu, W. *Dyes Pigm.* **2021,** *186,* 108950. doi:10.1016/j.dyepig.2020.108950
49. Huang, X.; Zhang, G.; Zhou, C.; Liu, S.; Zhang, J.; Ying, L.; Huang, F.; Cao, Y. *New J. Chem.* **2015,** *39,* 3658–3664. doi:10.1039/c4nj02350a
50. Fan, J.; Zhang, Y.; Zhang, K.; Liu, J.; Jiang, G.; Li, F.; Lin, L.; Wang, C.-K. *J. Mater. Chem. C* **2019,** *7,* 8874–8887. doi:10.1039/c9tc02144b
51. Funchien, P.; Chasing, P.; Sudyoadsuk, T.; Promarak, V. *Chem. Commun.* **2020,** *56,* 6305–6308. doi:10.1039/d0cc01648a
52. Kaewpuang, T.; Chaiwai, C.; Chasing, P.; Wongkaew, P.; Sudyoadsuk, T.; Namuangruk, S.; Manyum, T.; Promarak, V. *J. Photochem. Photobiol., A* **2021,** *420,* 113509. doi:10.1016/j.jphotochem.2021.113509
53. Tu, L.; Xie, Y.; Li, Z.; Tang, B. *SmartMat* **2021,** *2,* 326–346. doi:10.1002/smm2.1060
54. Pan, Y.; Huang, J.; Li, W.; Gao, Y.; Wang, Z.; Yu, D.; Yang, B.; Ma, Y. *RSC Adv.* **2017,** *7,* 19576–19583. doi:10.1039/c7ra01270e
55. Grabowski, Z. R.; Rotkiewicz, K.; Rettig, W. *Chem. Rev.* **2003,** *103,* 3899–4032. doi:10.1021/cr940745l
56. Li, W.; Liu, D.; Shen, F.; Ma, D.; Wang, Z.; Feng, T.; Xu, Y.; Yang, B.; Ma, Y. *Adv. Funct. Mater.* **2012,** *22,* 2797–2803. doi:10.1002/adfm.201200116
57. Sun, H.; Tang, X.-X.; Zhang, R.; Sun, W.-H.; Miao, B.-X.; Zhao, Y.; Ni, Z.-H. *Dyes Pigm.* **2020,** *174,* 108051. doi:10.1016/j.dyepig.2019.108051
58. Nicol, A.; Qin, W.; Kwok, R. T. K.; Burkhartsmeyer, J. M.; Zhu, Z.; Su, H.; Luo, W.; Lam, J. W. Y.; Qian, J.; Wong, K. S.; Tang, B. Z. *Chem. Sci.* **2017,** *8,* 4634–4643. doi:10.1039/c7sc00908a
59. Katagiri, C.; Yoshida, T.; White, M. S.; Yumusak, C.; Sariciftci, N. S.; Nakayama, K.-i. *AIP Adv.* **2018,** *8,* 105001. doi:10.1063/1.5045711
60. Suzuki, Y.; Adachi, S.; Suenobu, T.; Suzuki, M.; Nakayama, K.-i. *Jpn. J. Appl. Phys.* **2020,** *59,* SDDB01. doi:10.7567/1347-4065/ab5506
61. Gao, M.; Burn, P. L.; Pivrikas, A. *J. Appl. Phys.* **2019,** *126,* 035501. doi:10.1063/1.5100313
62. Peng, H.; Wang, W.; Chen, S. *IEEE Electron Device Lett.* **2015,** *36,* 369–371. doi:10.1109/led.2015.2398850
63. Li, Z.; Hu, X.; Liu, G.; Tian, L.; Gao, H.; Dong, X.; Gao, T.; Cao, M.; Lee, C.-S.; Wang, P.; Wang, Y. *J. Phys. Chem. C* **2021,** *125,* 1980–1989. doi:10.1021/acs.jpcc.0c10769
64. Chan, L.-H.; Lee, R.-H.; Hsieh, C.-F.; Yeh, H.-C.; Chen, C.-T. *J. Am. Chem. Soc.* **2002,** *124,* 6469–6479. doi:10.1021/ja0255150
65. Ji, W.; Jing, P.; Xu, W.; Yuan, X.; Wang, Y.; Zhao, J.; Jen, A. K.-Y. *Appl. Phys. Lett.* **2013,** *103,* 053106. doi:10.1063/1.4817086
66. Juang, F.-S.; Yao, M.-Q.; Mondal, T.; Saha, S. K. *IEEE Access* **2020,** *8,* 216986–216993. doi:10.1109/access.2020.3041358
67. *Gaussian 16,* Revision C.01; Gaussian Inc.: Wallingford, CT, 2016.
68. Nasiri, S.; Cekaviciute, M.; Simokaitiene, J.; Petrauskaite, A.; Volyniuk, D.; Andruleviciene, V.; Bezvikonnyi, O.; Grazulevicius, J. V. *Dyes Pigm.* **2019,** *168,* 93–102. doi:10.1016/j.dyepig.2019.04.045

License and Terms

BEILSTEIN JOURNAL OF ORGANIC CHEMISTRY

Quinoxaline derivatives as attractive electron-transporting materials

Zeeshan Abid[1], Liaqat Ali[1], Sughra Gulzar[1], Faiza Wahad[1], Raja Shahid Ashraf[1]
and Christian B. Nielsen*[2]

Review

Open Access

Address:
[1]Institute of Chemical Sciences, Department of Chemistry, Government College University, Lahore, Pakistan and [2]Department of Chemistry, Queen Mary University of London, London, United Kingdom

Email:
Christian B. Nielsen* - c.b.nielsen@qmul.ac.uk

* Corresponding author

Keywords:
electron transport materials; non-fullerene acceptors; n-type semiconductors; organic electronics; quinoxalines

Beilstein J. Org. Chem. **2023,** *19,* 1694–1712.
https://doi.org/10.3762/bjoc.19.124

Received: 14 July 2023
Accepted: 03 November 2023
Published: 09 November 2023

This article is part of the thematic issue "Organic electron transport materials".

Associate Editor: P. J. Skabara

Abstract

This review article provides a comprehensive overview of recent advancements in electron transport materials derived from quinoxaline, along with their applications in various electronic devices. We focus on their utilization in organic solar cells (OSCs), dye-sensitized solar cells (DSSCs), organic field-effect transistors (OFETs), organic-light emitting diodes (OLEDs) and other organic electronic technologies. Notably, the potential of quinoxaline derivatives as non-fullerene acceptors in OSCs, auxiliary acceptors and bridging materials in DSSCs, and n-type semiconductors in transistor devices is discussed in detail. Additionally, their significance as thermally activated delayed fluorescence emitters and chromophores for OLEDs, sensors and electrochromic devices is explored. The review emphasizes the remarkable characteristics and versatility of quinoxaline derivatives in electron transport applications. Furthermore, ongoing research efforts aimed at enhancing their performance and addressing key challenges in various applications are presented.

Introduction

Organic semiconductors have emerged as a fascinating class of materials with significant implications for numerous scientific disciplines, including electronics, photonics, and energy conversion. These materials, composed of carbon-based molecules or polymers, offer remarkable flexibility, tunability, and processability compared to their inorganic counterparts [1,2]. Charge transport in organic semiconductors is a fundamental aspect that governs the performance and functionality of various organic semiconductor devices, such as organic solar cells (OSCs), organic field-effect transistors (OFETs), organic light-emitting diodes (OLEDs), and bio/chemo-sensing devices. The movement of charge carriers through these materials occurs via a complex interplay of electronic, structural, and energetic phenomena, presenting intriguing challenges and opportunities for scientific exploration [3,4].

Quinoxalines (Qxs) have emerged as a promising class of heterocyclic compounds for charge transport applications, owing to two crucial factors. Firstly, their structural diversity enables precise customization of molecular structures, allowing for fine-tuning of their properties and optimization of performance for specific applications. Secondly, the feasibility of synthesizing quinoxalines contributes immensely to their appeal. Qxs can be readily prepared through simple condensation reactions, enabling convenient experimental studies and cost-effective bulk production [5]. The availability of inexpensive and accessible starting materials further enhances the practicality and commercial viability of Qxs for charge transport applications [6-10]. Figure 1 shows a few Qx scaffolds used in development of Qx derivatives.

The utilization of Qxs as a charge transporting material, whether as a hole transport material (HTM) or an electron transport material (ETM), is largely dependent on its functionalization. Although the Qx material has primarily been recognized for its effectiveness in hole transport, several studies have unveiled its significant potential as an ETM [6,7,11,12], exhibiting desirable characteristics such as high electron mobility and efficient charge transfer. In particular, Qx derivatives find use as non-fullerene acceptors (NFAs) in OSCs and as essential building blocks in sensitizers for DSSCs. The significance of Qx extends beyond to thermally activated delayed fluorescence (TADF) emitters and chromophores in the development of organic light-emitting diodes (OLEDs), sensors, and electrochromic devices [8,13,14].

In this review, we have comprehensively examined the recent advancements of Qx-derived ETMs in various applications within the organic semiconductor device field over the past five to six years. Furthermore, we have briefly discussed the integration of Qx derivatives into relevant materials to enhance electron transport. The review also sheds light on future research directions and potential challenges in this area, emphasizing the importance of further exploration and innovation. Overall, this review presents a first detailed account of the electron transport properties of Qx derivatives in recent times, offering valuable insights into their potential as promising ETMs.

Review

Quinoxalines as polymer acceptors

The development of efficient and high-performing polymer materials based on Qxs is of significant interest in the field of

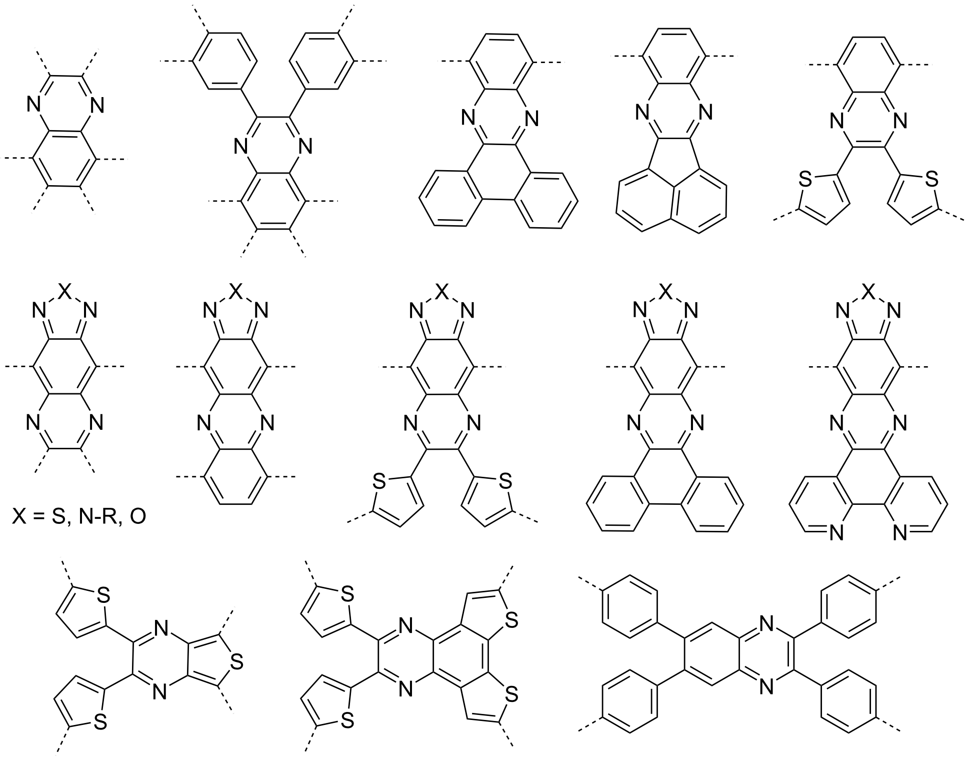

Figure 1: Structures of some of the most versatile Qx scaffolds; dashed lines indicate the substitution sites for core expansion.

organic electronics. A compelling indication of this potential is the remarkable achievements made by a relatively simple polymer, poly[(thiophene)-*alt*-(6,7-difluoro-2-(2-hexyldecyloxy)quinoxaline)] (PTQ10). PTQ10 has demonstrated impressive power conversion efficiencies (PCEs) of over 12% in polymer solar cells (PCS) when paired with the IDT acceptor [15], over 16% with the Y6 acceptor [16,17] and a champion PCE of 21.2% in perovskite solar cells [18]. This outstanding performance is attributed to the versatile and tunable nature of the Qx moiety, wherein researchers substituted alkoxy chains to enhance solubility and difluoro groups to lower the highest occupied molecular orbital (HOMO) energy level.

Qx-derived polymer acceptors have witnessed significant progress in recent years, driven by a contextual understanding of the major issues hindering their performance as electron acceptors. Researchers have focused on improving multidimensional electron transport, enhancing electron injection, addressing stability concerns, optimizing side chain engineering, and refining fabrication processes. One notable study by Wang et al. demonstrated the importance of designing molecular structures that can overcome aggregation-related limitations and enhance charge transport properties in all-polymer solar cells (all-PSCs). The team incorporated twisted perylenediimide units into the polymeric backbone of (naphthalenediimide/quinoxaline)thieno[3,2-*b*]thiophene in different ratios to produce three copolymers, **Qx1a**, **Qx1b** and **Qx1c** (Figure 2). This strategy reduced aggregation and improved the performance and stability of copolymers, with **Qx1c** achieving a PCE of 4.81% with PTB7-Th donor in an all-PSC device. Moreover, the broadened absorption band indicated an expanded spectral response, suggesting potential for harvesting a wider range of photons [19].

You and co-workers demonstrated the effectiveness of introducing electron-withdrawing cyanide (CN) groups at the 6- and 7-positions of the Qx moiety, named QxCN to address various concerns related to charge transport. The copolymers, **Qx2**, **Qx3**, and **Qx4**, formed by combining QxCN with different aryl groups showed down-shifting of lowest unoccupied molecular orbital (LUMO) levels and enhanced electron injection and transport. Furthermore, the dipole moment introduced by the CN groups improved charge separation by reducing Coulomb attraction and exciton binding energy. The resulting enhancement in exciton dissociation and reduced charge recombination contribute to the improved performance of polymer acceptors, especially **Qx2** which achieved PCE of 5.32% with PBDB-T donor in an all-PSC device [20]. In a recent study by Eedugurala et al., a terachlorobenzene ring were fused to the [1,2,5]thiadiazolo[3,4-*g*]quinoxaline unit in the polymer backbone of **Qx6** which enhanced the stability of the polymer and led to its high-spin configuration compared to the analogous material **Qx5** featuring 6,7-dimethyl-[1,2,5]thiadiazolo[3,4-*g*]quinoxaline in its polymer backbone. The transition from a closed-shell aromatic state to a high-spin quinoidal form resulted in favorable changes in the bandgap, electron affinity, and delocalization of spin density. These changes have the potential to improve charge transport and efficient charge separation in all-PSCs such as switching from p-type dominated behaviour of polymer **Qx5** to n-type dominated behaviour of Q6, with no off state due to presence of free charge carriers in the latter case [21].

Besides optimizing polymer structures, side chain engineering, introduction of electron-withdrawing terminal acceptor units, and careful selection of solvents and annealing processes have also been demonstrated as potential solutions to improve charge transport and refine the device fabrication processes. You et al. found that the position of alkoxy side chains on the pendant benzene rings significantly influenced the performance of **Qx2** acceptors. Three variants of **Qx2**, i.e., **Qx7** and **Qx8** were synthesized with alkoxy side chains located at the *meta* and *para* positions of the pendant benzene rings. **Qx7** exhibited efficient exciton dissociation, good electron-transporting ability, and a PCE of 5.07% in an all-PSC device with the PBDB-T donor, whereas **Qx8** showed poor charge transport, severe charge recombination, and a PCE of 1.62%. This highlighted the significance of side chain engineering in achieving high-performance polymer acceptors [22].

In addition to the importance of side-chain modification, the study by Zhou et al. showcases the importance of solvent choice and annealing techniques in optimizing the performance of all-PSCs using **Qx9** and **Qx10**. While both polymers served as donors in all-PSC devices, the study primarily focused on side chain engineering of the electron-deficient Qx unit. The combination of thermal annealing treatment and the use of THF as a non-halogenated solvent led to improvements in photovoltaic performance and charge carrier transport. Additionally, the impact of side chain modification on device characteristics, such as lower HOMO and higher circuit voltage (V_{oc}), underscored the influence of the molecular structure [23].

A recent development by Liang et al. introduced Qx-derived double-cable conjugated polymers as a promising approach for improving the performance of single-component-OSCs (SCOSCs). They replaced the traditional benzothiadiazole core of Y-series acceptor with the Qx moiety (Y-O6) and copolymerized it with the PBDB-T donor in two ratios to give **Qx11a** and **Qx11b**. This approach enhanced charge transport and nanophase separation, resulting in a record PCE of 13.02% in an

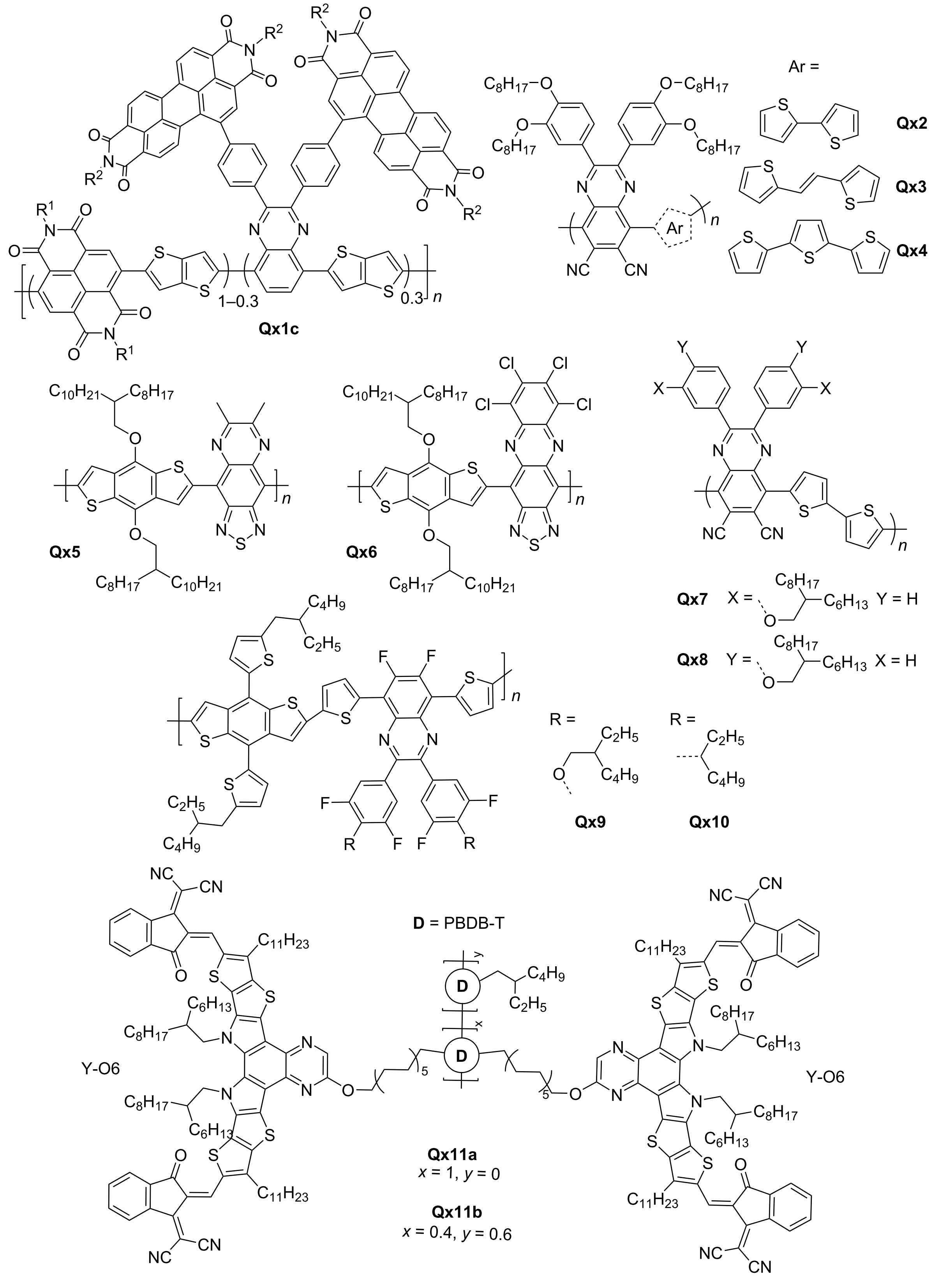

Figure 2: Qx-derived polymer acceptors.

SCOSC device made of **Qx11b** with diluted YO6 component [24].

Table 1 enlists the photovoltaic device performance of recently reported Qx materials. The structures of reviewed NFAs are drawn in Figure 2. The reviewed findings highlight that, despite limitations in the device performance, Qx derivatives possess significant potential for improvement. With further advancements and optimization, Qx polymer acceptors are expected to evolve into high-performance materials for organic electronics.

Quinoxalines as NFAs

Fullerene acceptors have long dominated OSCs until the emergence of NFAs; nonetheless, researchers have attempted to improve fullerenes and address their limitations, as demonstrated by Elavarasan and colleagues. Their team synthesized **TQT-C_{60}** and anchored it to fullerene molecules (Figure 3) to prevent aggregation during thermal aging. The researchers found that **TQT-C_{60}** demonstrated enhanced morphological stability and thermal resistance compared to the phenyl-C61-butyric acid methyl ester (PCBM) acceptor when used in bulk heterojunction polymer solar cell devices with poly(3-hexylthiophene) (P3HT) as the donor material. This improvement was attributed to the anchoring effect of the bulkier groups present in **TQT-C_{60}**, which hindered the movement and aggregation of fullerene molecules within the polymer matrix [25].

Small molecule NFAs have significantly advanced the field of OSCs. Notably, the fused-ring electron acceptors (FREAs) have exhibited exceptional promise, heralding a new era of possibilities for OSC technology. In 2019, Yuan et al. reported on a new class of FREAs called Y6. Y6 utilizes a ladder-type electron-deficient core-based central fused ring (dithienothiophen[3.2-*b*]pyrrolobenzothiadiazole) and achieved a remarkable efficiency of 16% in OSCs [26]. Building upon this breakthrough, Liu et al. blended Y6 with their polymer D18, resulting in an efficiency of 18% and marking a significant advancement in OSC research [27].

Zhou and co-workers synthesized Y6-type NFA acceptors, **Qx12** and **Qx13**, by substituting Y6's benzothiadiazole ring with a Qx moiety. **Qx13** exhibited a stronger π–π interaction compared to **Qx12**, which facilitated enhanced electron hopping and reduced geminate recombination. **Qx12** and **Qx13** achieved remarkable PCEs of 13.31% and 16.64%, respectively, with PBDB-TF donor in OSC devices [28]. Zhu et al. reported a modification in **Qx13** by incorporating an imide-functionalized Qx moiety in its core and end-capping groups with fluorinated or chlorinated compounds, producing **Qx14** and **Qx15**, respectively. This modification aimed to improve the device performance by enhancing aggregation control and optimizing the open-circuit voltage. The introduction of functional groups provided a strategic means to tailor the molecular structure, resulting in improved photovoltaic properties and overall PCEs (12.12–13.3%) [29]. Researchers have explored Y6 derivatives for hydrogen production. Zhang and co-workers synthesized a two-dimensional polycyclic material by merging two Y6 molecules with a Qx unit. They blended the newly formed compound with the donor polymer PM6 to create BHJ nanoparticles and employed it in the hydrogen evolution reaction. This approach substantially reduced trap density, increasing the hydrogen evolution rate by 2–3 times compared to conventional inorganic/organic hybrid photocatalysts [30].

Computational chemistry offers a cost-effective and time-efficient means of screening and selecting promising candidates for experimental exploration. Bhattacharya et al. employed density functional theory (DFT) approach to explore structural modulation for tuning the optoelectronic properties of **Qx13**. Their designed molecule series, **Qx16**, featured a 1,4-dihydro-2,3-

Table 1: Photovoltaic performance of Qx-derived polymer acceptors in PSCs.

Active layer	V_{oc} (mV)	J_{sc} (mA/cm^3)	FF (%)	PCE (%)	Ref.
PTB7-Th:**Qx1a**	0.8	10.58	50.5	4.27	[19]
PTB7-Th:**Qx1b**	0.81	11.11	51.28	4.61	
PTB7-Th:**Qx1c**	0.82	11.72	50.27	4.81	
PBDB-T:**Qx2**	1.02	10.25	0.48	5.02	[20]
PBDB-T:**Qx3**	1	7.83	0.45	3.54	
PBDB-T:**Qx4**	1.03	2.16	0.26	0.58	
PBDB-T:**Qx2**	1	10.76	0.48	5.18	[22]
PBDB-T:**Qx7**	0.95	11.82	0.45	5.07	
PBDB-T:**Qx8**	0.98	5.16	0.32	1.62	
Qx11a	0.91	9.46	0.3	2.75	[24]
Qx11b	0.9	22.24	0.65	13.02	

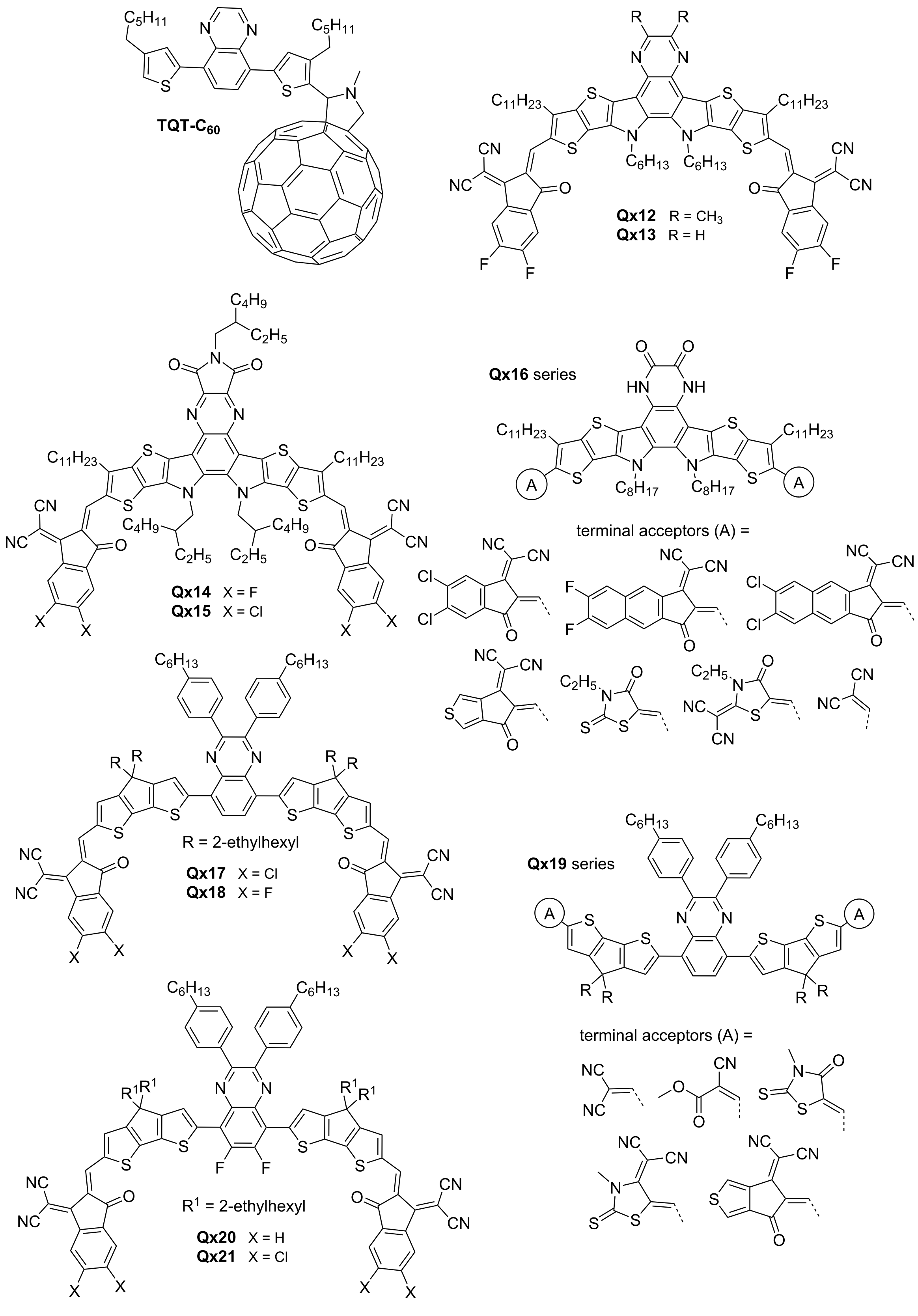

Figure 3: Qx-derived small molecule NFAs.

quinoxalinedione core and different terminal acceptor units. The modified NFAs demonstrated visible and near-infrared absorption as well as good electron mobility, suggesting their potential for experimental exploration in (OCSs) [31].

While FREAs are currently at the forefront and delivering great PCE, unfused electron acceptors have continued to garner considerable attention. Chang and co-workers focused on enhancing the aggregation and crystallinity of unfused Qx acceptors, **Qx17** and **Qx18**, containing a Qx core and different halogenated end groups. Both compounds exhibited good coplanarity through intramolecular interactions, narrow bandgaps, broad absorption in the NIR region and PCEs above 10% [32]. Ayub et al. decorated the central donor–acceptor–donor unit of **Qx17** and **Qx18** with five new terminal end groups, resulting in the **Qx19** series, and predicted their optoelectronic properties to highlight the potential of their experimental exploration [33].

The introduction of an electron-withdrawing group has been shown to be a key strategy for enhancing intermolecular interactions and improving the optical absorption, molecular packing, and charge transport ability of NFAs. Huang et al. synthesized noncovalently fused-ring electron acceptors (NFREAs), **Qx20** and **Qx21**, featuring 6,7-difluoro-2,3-diphenylquinoxaline core. The fluorine atoms of the core formed multiple noncovalent bonds (N···H and S···F) thus improving backbone coplanarity. This approach enhanced absorption, improved carrier mobility, and reduced charge recombination of NFAs. **Qx21**, bearing chlorine atoms on the end groups as opposed to **Qx20**, showed superior optoelectronic properties and a PCE of 12.32% with PBDB-T as donor in OSC device [34]. The same group explored side-chain engineering and chlorination effects on the **Qx20** series, resulting in four new NFAs, i.e., **Qx22**–**Qx25** (Figure 4). The research revealed the strategic balance between molecular crystallinity, packing, and optical properties. **Qx24** and **Qx25**, with lower steric hindrance in the alkyl side chains, showed slightly decreased crystallinity and optical absorption but a shorter π–π stacking distance. OSC devices based on **Qx23** and **Qx25** achieved the highest PCE (10.67 and 12.19%, respectively) compared to **Qx22** and **Qx24** (6.94 and 8.01%, respectively) [35].

Xiao and fellows studied the impact of side chains on molecular packing and morphology on **Qx26** and **Qx27**, employing indacenodithiophene, Qx and rhodanine as donor, acceptor and end group, respectively. The incorporation of specific side chains facilitated improved thermal stability, solubility, and broad absorption spectra (300–750 nm), narrow bandgaps (1.68–1.74 eV) and PCEs in the range of 4.03–4.81% in PSC devices [36]. The team further explored side-chain engineering (phenyl groups) and end-group modification (2-(1,1-dicyanomethylene)thiazolidin-4-one) of new NFAs, i.e., **Qx28**–**Qx30**. While removal of all side chains supported a planar conformation of the molecule, it hampered phase separation, lowering short-circuit current (J_{sc}), fill factor (FF) and PCE. Contrarily, the presence of all groups also compromised crystallinity and electron mobility. The highest PCE of 6.37% was realized for **Qx29** upon only taking away the phenyl side groups attached to the IDT units [37].

Qx29 was used to prove that employing the same acceptor unit for both donor and acceptor is an effective approach. This strategy has been shown to be successful in achieving high V_{oc} for benzotriazole materials, and now it has been extended to quinoxaline materials [38]. Ji et al. introduced fluorine atoms to the Qx moiety of **Qx29**, producing a new NFA, **Qx31**, as well as the thiophene side chains of the p-type polymer PE61 to fine-tune the optoelectronic properties. The PCE of PE62:**Qx31**-based solar cells improved from 4.19 to 9.78% with a relatively high V_{oc} of 1.09 V, and the PE61:**Qx31**-based devices gave rise to the highest PCE of 10.45% [39].

These reports provide strong evidence that the ongoing exploration and refinement of Qx-based NFAs hold tremendous promise for the future development of efficient and scalable OSC technology. The reported molecules are represented in Figure 3 and Figure 4. Photovoltaic performance of some of the reported materials is tabulated in Table 2.

Quinoxalines as auxiliary acceptors and π-bridges

Qx derivatives are highly attractive auxiliary acceptor and bridging materials for DSSCs. Their strong electron-accepting ability enables efficient electron injection and charge collection, while their extended conjugation enhances light absorption across a broad spectrum. Qx's unique structure promotes effective incorporation into the dye-sensitized layer, ensuring good intermolecular connectivity and facilitating electron transport. In addition, they enable efficient electron transfer and increased conjugation when acting as efficient π-bridge.

Krishna et al. demonstrated the significance of Qx derivatives, 2,3-diphenylquinoxaline (DPQ), and 2,3-di(thiophen-2-yl)quinoxaline as auxiliary acceptors by effectively improving the electron injection process in **Qx32** and **Qx33** (Figure 5). The charge transfer efficiency and device performance of **Qx33** was improved by aligning its LUMO energy level with the conduction band edge of the TiO_2 nanoparticles. This strategic approach highlights the importance of optimizing energy level alignment for efficient charge transport in DSSCs [40]. Similarly, Grobelny et al.'s work provides valuable insights into the impact of two quinoxaline derivatives, hexyloxy-substituted

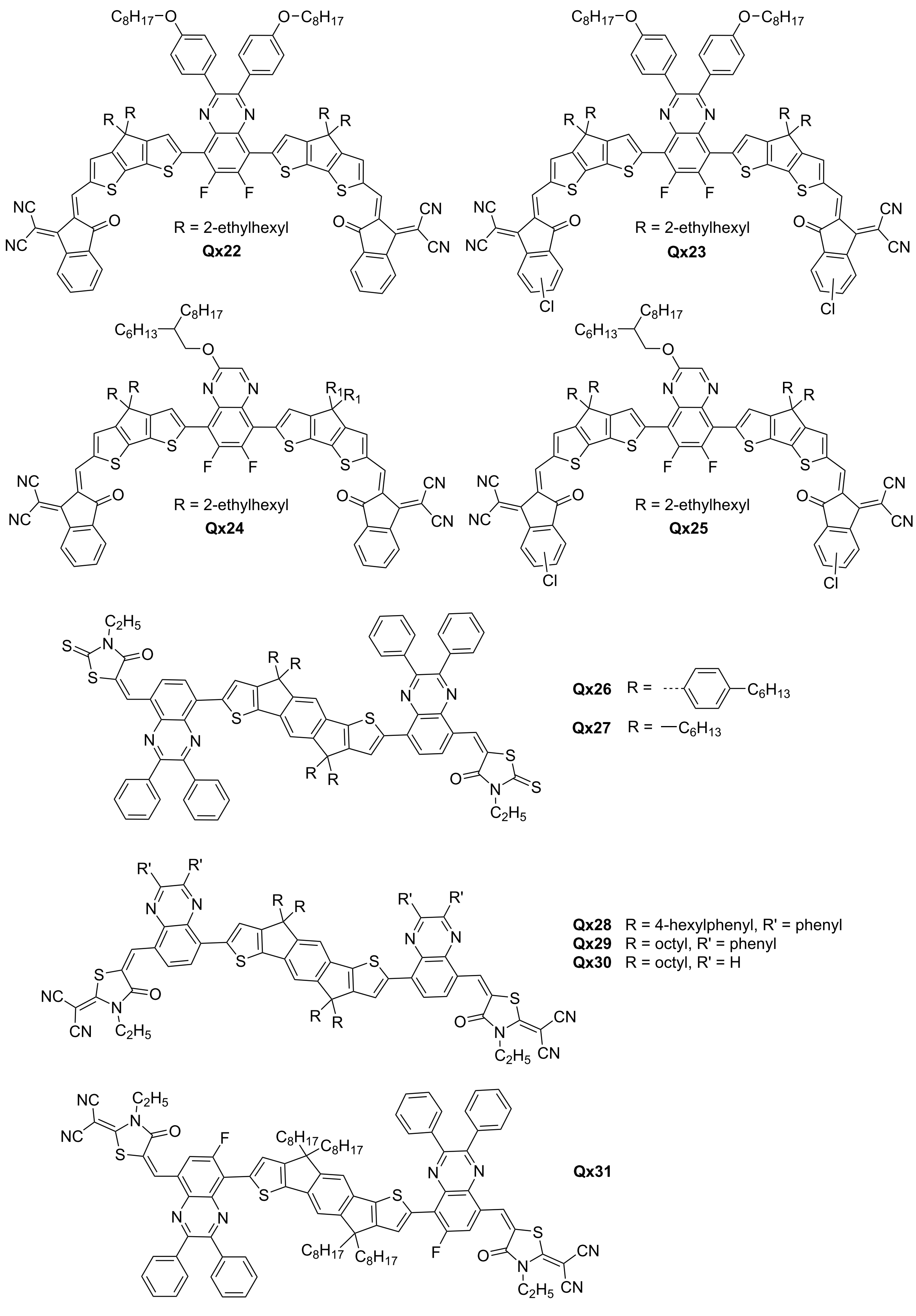

Figure 4: Qx-derived small molecule NFAs.

Table 2: Photovoltaic performance of Qx-derived NFAs in OSCs.

Active layer	V_{oc} (mV)	J_{sc} (mA/cm^3)	FF (%)	PCE (%)	Ref.
P2F-EHp:**Qx14**	0.94	18.27	70.53	12.12	[29]
P2F-EHp:**Qx15**	0.94	19.62	72.11	13.3	
J52:**Qx17**	0.78	21.64	62.12	10.54	[32]
J52:**Qx18**	0.76	22.71	63.09	10.81	
PBDB-T:**Qx20**	0.862	16.19	56.64	7.9	[34]
PBDB-T:**Qx21**	0.782	22.91	69.01	12.32	
PBDB-T:**Qx22**	0.843	17.04	48.34	6.94	[35]
PBDB-T:**Qx23**	0.824	20.74	62.44	10.67	
PBDB-T:**Qx24**	0.893	16.74	53.55	8.01	
PBDB-T:**Qx25**	0.845	21.03	68.7	12.19	
P3HT:**Qx26**	0.99	4.83	0.67	3.2	[36]
P3HT:**Qx27**	0.96	6.41	0.71	4.37	
P3HT:**Qx28**	0.89	5.57	0.68	3.37	[37]
P3HT:**Qx29**	0.75	12.87	0.66	6.37	
P3HT:**Qx30**	0.75	0.14	0.3	0.03	
PE61:**Qx29**	1.02	12.03	64.52	8.24	[39]
PE62:**Qx29**	1.12	6.47	54.97	4.19	
PE61:**Qx31**	0.98	15.44	66.28	10.45	
PE62:**Qx31**	1.09	12.53	68.96	9.78	

diphenylquinoxaline (HPQ) and naphthalene-fused-quinoxaline (NFQ), as auxiliary acceptors on DSSC performance. The comparison between **Qx34** and **Qx35** highlights the importance of the specific quinoxaline structure. **Qx34**, incorporating HPQ as the auxiliary acceptor, demonstrated enhanced electron injection and charge collection, leading to a higher PCE of 13.2% [41].

A careful choice of auxiliary acceptor is of great importance, as highlighted by Kumar and co-workers. Their study raises a concern regarding the performance of dyes with *tert*-butyl substituted DPQ acceptors, either containing benzene (**Qx74**) or thiophene (**Qx75**) as a π-conjugation linker and their benzotriazole analogue. While the incorporation of the Qx enhances the interaction between the donor and acceptor moieties, the resulting PCE falls slightly short. This observation highlights the importance of a careful choice of auxiliary acceptors to ensure optimal device performance [42]. Godfroy and colleagues also emphasized the significance of molecular structure and backbone planarity in achieving efficient charge transport in DSSCs. Their work highlights the importance of molecular structure and backbone planarity in achieving efficient charge transport in DSSCs. The sensitizers, **Qx36** and **Qx37**, employing Qx and dithieno[3,2-*f*:2',3'-*h*]quinoxaline acceptors, respectively, showed narrower absorption spectra, thus indicating well-matched energy levels, and exhibited superior performance. However, **Qx38**, featuring a thieno[3,4-*b*]pyrazine acceptor and more quinoidal backbone, suffered from reduced electron injection and increased recombination rates [43].

The challenge associated with the coplanarity of Qx-based dyes, **Qx39**–**Qx42** and the resulting device performance were highlighted by Huang et al. The use of quinoxaline-dithienothiophene and phenazine-dithienothiophene as π-bridges with the benzothiadiazole moiety as an auxiliary group did not yield the expected improvement, potentially due to the non-coplanarity of the molecular framework. DSSCs devices exhibited PCE in the range of 5.23–7.77% with **Qx41**-based device [44]. Jiang et al.'s research showcases the potential of choosing the right Qx derivatives as efficient electron-withdrawing acceptor in DSSCs. The utilization of phenanthrene-fused-quinoxaline (PFQ) in sensitizer **Qx43** resulted in exceptional PCE of 12.5%, surpassing traditional acceptor materials such as benzothiadiazole. Additionally, the improved charge recombination and stability indicate the strategic advantage of employing the right Qx derivatives for enhanced DSSC durability [45].

Several computational studies have also been performed to design dyes for optimized performance in DSSCs [46,47]. Shi and colleagues' quantum modeling study sheds light on the optoelectronic properties of Qx-based dyes containing DPQ (**Qx44a**) or methoxy-substituted DPQ (**Qx44b**) as π units, highlighting the importance of specific substitutions. While **Qx44b** demonstrated favorable properties such as a superior dipole

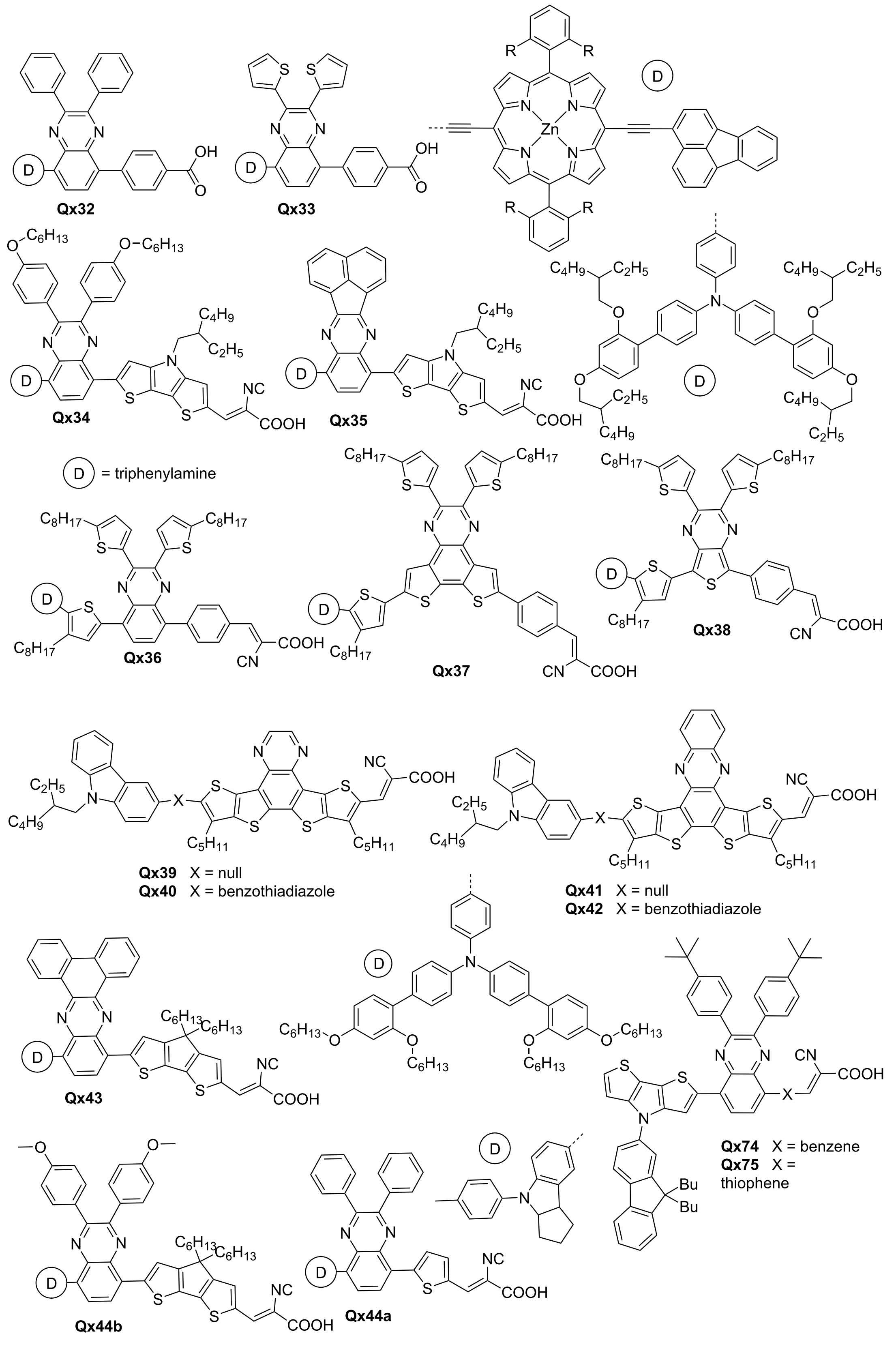

Figure 5: Dyes and sensitizers based on Qx auxiliary acceptors or bridging units.

moment, narrow bandgap, and red-shifted absorption, the reduced charge transfer rate presented a challenge. This analysis emphasizes the need for a delicate balance between desirable electronic properties and efficient charge transfer dynamics [48]. Arunkumar and colleagues demonstrated the utilization of indolocarbazole-Qx systems named ICZS4. The comprehensive investigation of ICZS4's optoelectronic properties highlighted its potential for high-performance DSSCs. The small energy gap, red-shifted absorption, good dye regeneration, and promising NLO properties underscored the multifunctional nature of Qx derivatives as auxiliary acceptors [49].

Figure 5 depicts molecular structures of Qx derivatives used as building blocks of dyes and sensitizers. The device properties of such prominent materials are summarized in Table 3. The findings from these studies contribute to the overall understanding and advancement of quinoxaline derivatives as attractive electron-transporting materials in DSSCs.

Quinoxalines as n-type transistor materials

Qxs have also emerged as promising candidates for n-type transistor materials, offering a range of properties specifically tailored for OFET applications. The tunable properties of Qxs as n-type semiconductor materials, including high electron mobility, optimal energy levels, broad absorption spectra, and processing compatibility, position them as promising candidates for OFETs and similar electronic technologies. The incorporation of Qx derivatives into electronic devices holds great potential for achieving high-performance, energy-efficient, and scalable electronic systems in diverse fields such as energy conversion, information processing, and beyond.

In the context of structural modification, the introduction of various functional groups into Qx derivatives has allowed for the precise control of energy levels, bandgaps, and carrier transport properties. For instance, Sharma et al. fine-tuned the intermolecular charge transfer (ICT) transitions and emission properties of **Qx45** series by incorporating electron-donating (methyl) and electron-withdrawing groups (bromo and nitro) (Figure 6). The observation of low-lying LUMO levels (−3.29 to −3.43 eV) and thermal stability in these dyes suggested their potential as efficient ETMs [50]. Similarly, Singh et al. explored the modulation of optoelectrochemical properties and thermal characteristics of pyridopyrazino[2,3-*b*]indole-based **Qx46** series with varying substituents, i.e., bromine, chlorine, methyl and nitro group. Their study revealed inbuilt ICT and aggregation-induced emission (AIE) effects, forming emissive nanoaggregates in a THF/H_2O mixture. Altering the substituents proved as an effective approach to tune the electrochemical properties of the compounds, resulting in comparable LUMO energy levels. The products therefore hold potential as solid-state emitters and n-type materials for organic electronics [51].

Hasegawa and colleagues focused on achieving air-stable n-channel conduction by synthesizing thiadiazole-fused quinoxalineimide derivatives, **Qx47**–**Qx49**. The team optimized the molecular packing and solubility by incorporating solubilizing N-substituted alkyl chains. The resulting molecules exhibited low LUMO levels and two-dimensional carrier transport, enabling OFET performance. The moderate air-stable n-channel mobility of 0.044 $cm^2\ V^{-1}\ s^{-1}$ demonstrated the suitability of these derivatives for electron transport [52]. Hayashi et al. introduced a new avenue for developing n-type *N*-phenylindolo-

Table 3: Photovoltaic performance of Qx-containing dyes and sensitizers in DSSCs.

Qx component	V_{oc} (mV)	J_{sc} (mA/cm^3)	FF (%)	PCE (%)	Ref.
Qx32	0.51	3.53	72	1.5	[40]
Qx33	0.56	6.28	73	2.86	
Qx34	1.05	16.3	77.1	13.2	[41]
Qx35	0.95	14.7	75	10.5	
Qx36	796	10.91	74	6.36	[43]
Qx37	828	14.11	74	8.65	
Qx38	537	15.49	64	5.31	
Qx39	661.7	12.92	75.73	6.48	[44]
Qx40	695	12.47	73.11	6.33	
Qx41	691.7	15.63	71.88	7.77	
Qx42	661.7	13.76	74.79	6.81	
Qx74	605.9	4.62	0.65	1.83	[42]
Qx75	598.6	4.98	0.66	1.97	

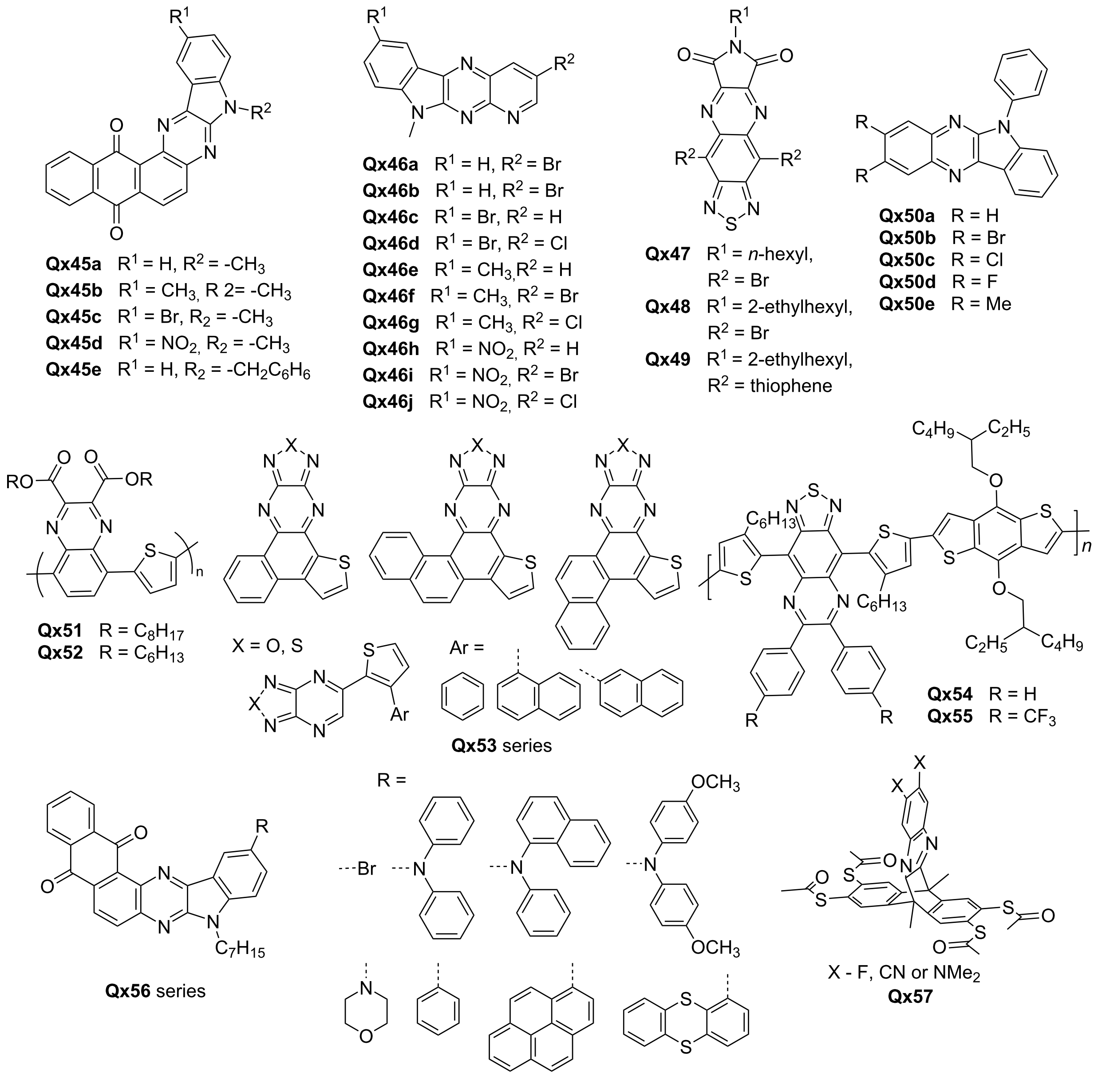

Figure 6: Qx-derived n-type transistor materials.

quinoxaline (PhIQ) derivatives, shown in Figure 6 as **Qx50** series, by chemically modifying the PhIQ groups. In particular, substituents at the 2- and 3-positions of PhIQs were introduced, allowing regulation of the reduction–oxidation potentials of the compounds. The PhIQs exhibited fluorescent solvatochromism and demonstrated n-type properties due to the electronegative Qx unit [53].

Mikie et al. explored ester-functionalized quinoxalines (QEs) as building units for both p-type and n-type polymers. They synthesized two new π-conjugated polymers, **Qx51** and **Qx-52**, with low-lying HOMO (–5.5 eV) and LUMO (–3.4 eV) levels, resulting in narrow optical bandgaps (1.6 eV). In OFETs, **Qx51** exhibited hole (μ_h) and electron (μ_e) mobilities of 1.1×10^{-3} and 6.6×10^{-4} cm^2 V^{-1} s^{-1}, which were higher than those of **Qx52** ($\mu_h = 4.4 \times 10^{-4}$ cm^2 V^{-1} s^{-1}, $\mu_e = 3.0 \times 10^{-4}$ cm^2 V^{-1} s^{-1}), due to the higher crystalline nature of the earlier [54]. Recently, Ding et al. prepared a novel air-stable n-type benzothiophene endcapped azaarene (BTPQ) and its sulfonated derivative (BSPQ). By introducing nitrogen atoms and sulfonyl groups, the researchers modulated the molecular energy levels and achieved the energy level requirements of n-type semiconductors. The strategy also involved attaching triisopropylsilyl groups to the anthracene core to balance solubility and charge carrier properties. The BSPQ derivative exhibited deeper frontier orbital energy levels and enhanced electron mobility compared to the BTPQ [55].

Several reports have highlighted the development of novel synthetic routes for producing Qx derivatives with desired properties. Kvashnin et al. reported a simple yet promising strategy for designing and synthesizing n-type semiconductors. The team developed a synthetic route to produce polycyclic (hetero)aromatic compounds (**Qx53**) with a chalcogenodiazolo[3,4-*b*]pyrazine scaffold. These compounds exhibited narrow bandgaps (from 1.25 to 1.44 eV) and demonstrated n-type organic semiconductor properties [56]. Jin and co-workers focused on improving the charge-transfer characteristics of a semiconducting copolymer, benzodithiophene-thiadiazoloquinoxaline (**Qx54**), by introducing trifluoromethyl groups to the Qx moiety (**Qx55**). This strategic modification changed the HOMO and LUMO levels, resulting in a conversion from ambipolar charge transport to n-type charge transport. The polymeric thin-film transistors (PTFTs) with **Qx54** copolymer showed ambipolar characteristics, while the PTFTs with **Qx55** copolymer exhibited only n-type charge transport [57].

Kamble et al. designed and synthesized a series of eight new indolo[2,3-*b*]naphtho[2,3-*f*]quinoxaline derivatives (**Qx56**) by incorporating an electron-accepting quinone unit on quinoxaline to achieve donor–acceptor interactions and desirable electronic properties. The compounds exhibited absorption, emission, electrochemical, and thermal properties suitable for n-type materials. Theoretical properties were also investigated using time-dependent DFT. The HOMO and LUMO energy levels of the compounds ranged from −6.51 to −6.84 eV and −3.00 to −3.30 eV, respectively. The low-lying LUMO energy levels were similar to well-known n-type materials, indicating the potential of the synthesized compounds as n-type materials in organic electronics [58].

Rohnacher et al. synthesized a tetrapodal scaffold using diazatriptycene with thiol anchors (**Qx57**) to demonstrate electrostatic dipole engineering in n-type OFETs. The scaffold was designed to enforce upright functional groups, particularly quinoxaline subunits, and utilized OFETs as prototypes to showcase the potential of self-assembled monolayer in devices. The molecular dipole and work function of gold was adjusted by using fluorine and CN as well as dimethylamino substituents on the quinoxaline. Notably, the researchers tuned the work function of gold over a range of 1.0 eV [59]. The study by You et al. quoted in the section "Quinoxalines as polymer acceptors" also fabricated OFETs using QxCN-based polymer acceptors and demonstrated unipolar n-type characteristics with moderate OFET mobilities. The well-ordered structures with tight *π*–*π* stacking in **Qx2** and **Qx3** contributed to electron mobilities greater than 1.0×10^{-4} cm^2 V^{-1} s^{-1} [20]. Figure 6 shows the molecular structures of the prominent compounds exhibiting potential as n-type materials. Table 4 lists OFET device properties of devices employing Qx derivatives.

Quinoxalines as ETL and TADF emitters

Qx derivatives have garnered substantial attention from the scientific community due to their remarkable characteristics as electron-transporting and hole-blocking layers in organic electronics [60]. Moreover, these derivatives have exhibited promising traits as thermally activated delayed fluorescence (TADF) emitters. This multifaceted nature has spurred ongoing research efforts aimed at overcoming various hurdles and enhancing the performance of Qx derivatives.

One key concern is the solubility of Qx derivatives in solution processing, as it affects their suitability for practical applications. Additionally, achieving efficient electron injection and extraction, as well as controlling the interfacial dipole, are crucial for improved device performance. The work by Kim et al. demonstrated the potential of Qx compounds (**Qx59** and **Qx60**) derived from **Qx58a** and **Q58b**, respectively, as solution-processable ETLs for OSCs and OLEDs (Figure 7). The in-

Table 4: OFET properties of Qx-derived OFET devices.

Materials	μ_e average (max) (cm^2 V^{-1} s$^{-1)}$	Threshold voltage (V)	I_{on}/I_{off}	Ref
Qx47	8.0×10^{-2} (9.0×10^{-2})	10.4	≈10^4	[52]
Qx48	2.1×10^{-4} (2.7×10^{-4})	36.8	≈10^2	
Qx49	8.0×10^{-4} (8.5×10^{-4})	43.9	≈10^3	
Qx51	6.6×10^{-4}	48	–	[54]
Qx52	3.0×10^{-4}	50	–	
Qx2	$(7.6 \pm 0.4) \times 10^{-3}$	19.9 ± 0.7	>10^3	[20]
Qx3	$(2.4 \pm 0.1) \times 10^{-2}$	23.1 ± 0.5	>10^3	
Qx4	$(7.4 \pm 0.5) \times 10^{-3}$	26.7 ± 0.4	>10^3	

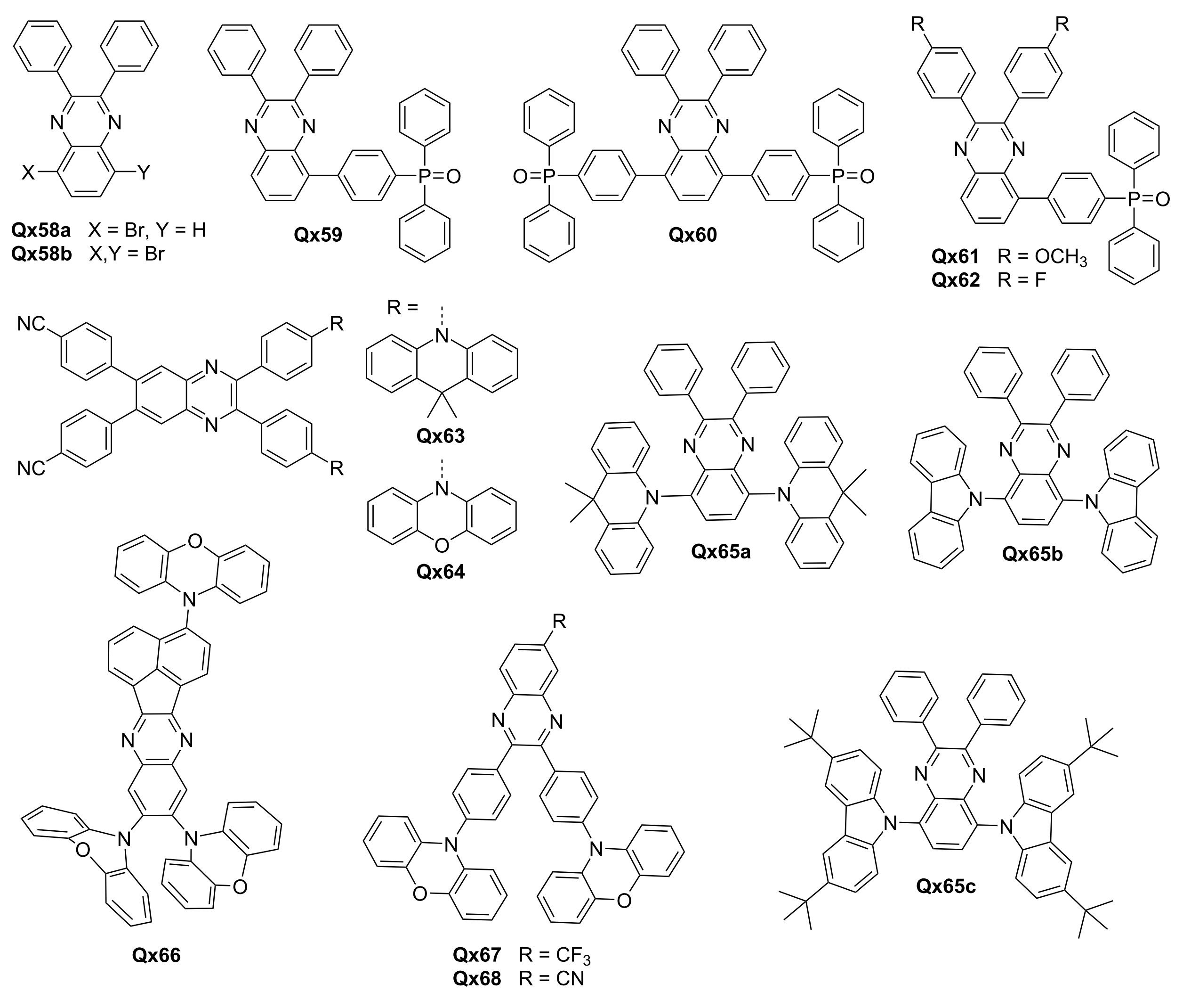

Figure 7: Qx-derived ETM and TADF emitters.

corporation of strong dipole moments in **Qx59** improves electron injection/extraction and energy level alignment, leading to enhanced device performance. The high PCE of 16.83% in OSC and excellent external quantum efficiency (EQE) of 5.00% in OLED devices highlight the efficacy of **Qx59** in facilitating efficient charge transport and emission processes [61].

To address the challenge of interfacial dipole and solubility, Lee and colleagues modified **Qx59** by introducing methoxy (**Qx61**) and fluorine (**Qx62**) groups at the 2,3-positions of the Qx ring. This modification not only facilitated easy deposition but also enhanced electron injection and transport behavior by effectively matching the band levels of the devices. The improved EQE of the OLEDs (6.12%) suggests the effectiveness of Qx derivatives as ETLs in achieving high device performance [62]. Ji et al. successfully developed TADF emitters, **Qx63** and **Qx64**, based on quinoxaline-4,4'-dicyanobenzene by manipulating the donor–acceptor conformation. The efficient TADF emission at room temperature highlighted the potential of these emitters for achieving high-performance OLEDs. The tunability of the emission peak through appropriate donor selection further demonstrates the versatility of quinoxaline derivatives in tailoring the emission properties of TADF materials. The vacuum deposited OLEDs based on **Qx63** and **Qx64** emitted yellow and red light, achieving EQEs of 17.3% and 15.6%, respectively [63].

You and co-workers reported the strategic design of a series of butterfly-shaped high-performance red/orange TADF emitters (**Qx65**). The team successfully transitioned the emission type from local excited-state to charge-transfer state by carefully tuning the molecular structure and energy levels, leading to efficient TADF. The **Qx65a**-based orange TADF OLEDs exhibit a maximum EQE of 7.4%, corresponding to a prominent contribution of 97% from the delayed fluorescence to the overall EQE [64]. Another study by Yu et al. reports the successful synthesis of a red TADF molecule, **Qx66**, based on an acenaphtho[1,2-*b*]quinoxaline acceptor. The well-separated energy levels of the molecules indicated efficient charge transfer and exciton formation within the molecule, leading to red emission. The achieved EQE of 7.4% highlighted the potential application of this Qx-based TADF emitter as dopant in red-emitting OLED devices [65].

Huang et al. developed two yellow TADF emitters, **Qx67** and **Qx68**, based on 6-(trifluoromethyl)quinoxaline or 6-cyanoquinoxaline acceptors, respectively. The small energy splitting values (0.03–0.04 eV) and long fluorescence lifetimes (5.0 μs) indicated efficient TADF processes. The utilization of these emitters in full-TADF white OLEDs, along with a sky-blue emitter, demonstrates their potential for practical applications in the lighting and display fields, with high efficiency (20.16%) and stable color rendering [66]. Gupta and co-workers designed and synthesized Y-shaped Qx derivatives with quadrupolar and tripodal arrangement. The molecules showed unique properties, including solvatochromism and AIE enhancement. These characteristics enable tunable emission and enhanced luminescence efficiency. The potential application of tripodal derivatives in white OLEDs indicates the versatility of quinoxaline-based materials in achieving diverse emission colors [67]. Figure 7 shows the prominent examples of recently reported Qx based dyes and TDAF emitters. Table 5 lists device properties and relevant information of devices employing Qx derivatives.

Quinoxalines as chromophores

Qx derivatives have emerged as promising chromophores due to their distinctive optical and electronic characteristics. To enhance their performance in sensors and electrochromic devices, researchers have concentrated on manipulating their electron transport properties. By tailoring the strength of electron acceptors, fine-tuning the electronic nature of functional groups, incorporating additional functionalities, and optimizing the π-conjugated backbone structure of Qxs, significant advancements have been made. These approaches effectively address key concerns and obstacles, resulting in red-shifted absorption and emission maxima, improved nonlinear optical properties, solvatochromism, mechanical responsiveness, acidofluorochromism, AIEE, and enhanced electrochromic performance.

One effective approach, as demonstrated by Moshkina et al., involved introducing CN and fluorine substitutions on the Qx core to give **Qx69** (Figure 8). This modification resulted in red-shifted absorption and emission maxima, indicating the potential for tunable optical properties based on the surrounding environment. The replacement of difluoroquinoxaline with cyanoquinoxaline improved the nonlinear optical properties, highlighting the importance of tailoring electron acceptor strength. Furthermore, the ability to induce changes in emission properties through mechanical stimulation offers exciting possibilities for optomechanical applications [68].

Another notable strategy, performed by Gupta and co-workers, involves fine-tuning of the electron accepting tendency of quinoxaline by incorporating various groups with different electronic natures (**Qx70a**–**Qx70g**). This approach allowed for the modulation of chromophoric properties, including solvatochromism, acidofluorochromism, and twisted-ICT. The incorporation of a pyridopyrazine derivative further expanded the range of functionalities and enabled logic gate operations, showcasing the potential of quinoxaline-based chromophores in sensor applications and molecular logic devices [69].

In terms of electrochromic performance, the work by Fu et al. emphasized the significance of the π-conjugated backbone structure in achieving desirable electrochromic properties (**Qx71**–**Qx73**). The incorporation of twisted substituents on the backbone, as observed in polymers **Qx71** and **Qx72**, led to excellent electrochromic performance attributes. In contrast, the use of a fused electron acceptor unit in polymer **Qx73** resulted in suboptimal electrochromic performance. This highlights the

Table 5: Optoelectronic properties of Qx-derived ETL and TADF emitters.

Materials	L_{max}(Cd/m^2)@bias	LE_{max}(Cd/A)@bias	EQE$_{max}$@bias	V_{on} (V)	Ref.
ITO/PEDOT:PSS/SY/**Qx59**/Al	26400@10.0	14.45@5.8	5.00@5.8	2.2	[61]
ITO/PEDOT:PSS/SY/**Qx60**/Al	8660@11.0	7.73@8.0	2.71@8.0	2.2	
ITO/PEDOT:PSS/SY/**Qx59**/Al	6211@9.1	16.69@4.3	5.65@4.3	2.5	[62]
ITO/PEDOT:PSS/SY/**Qx61**/Al	10030@8.8	17.98@4.3	6.12@4.3	2.5	
ITO/PEDOT:PSS/SY/**Qx62**/Al	3723@10.5	8.76@4.8	2.94@4.8	2.5	
Qx65	11456	19.7	7.4	3.8	[64]
DMAC-DPS:**Qx67**	6803	48.34	18.06	2.8	[66]
DMAC-DPS:**Qx68**	6858	48.22	20.16	2.8	

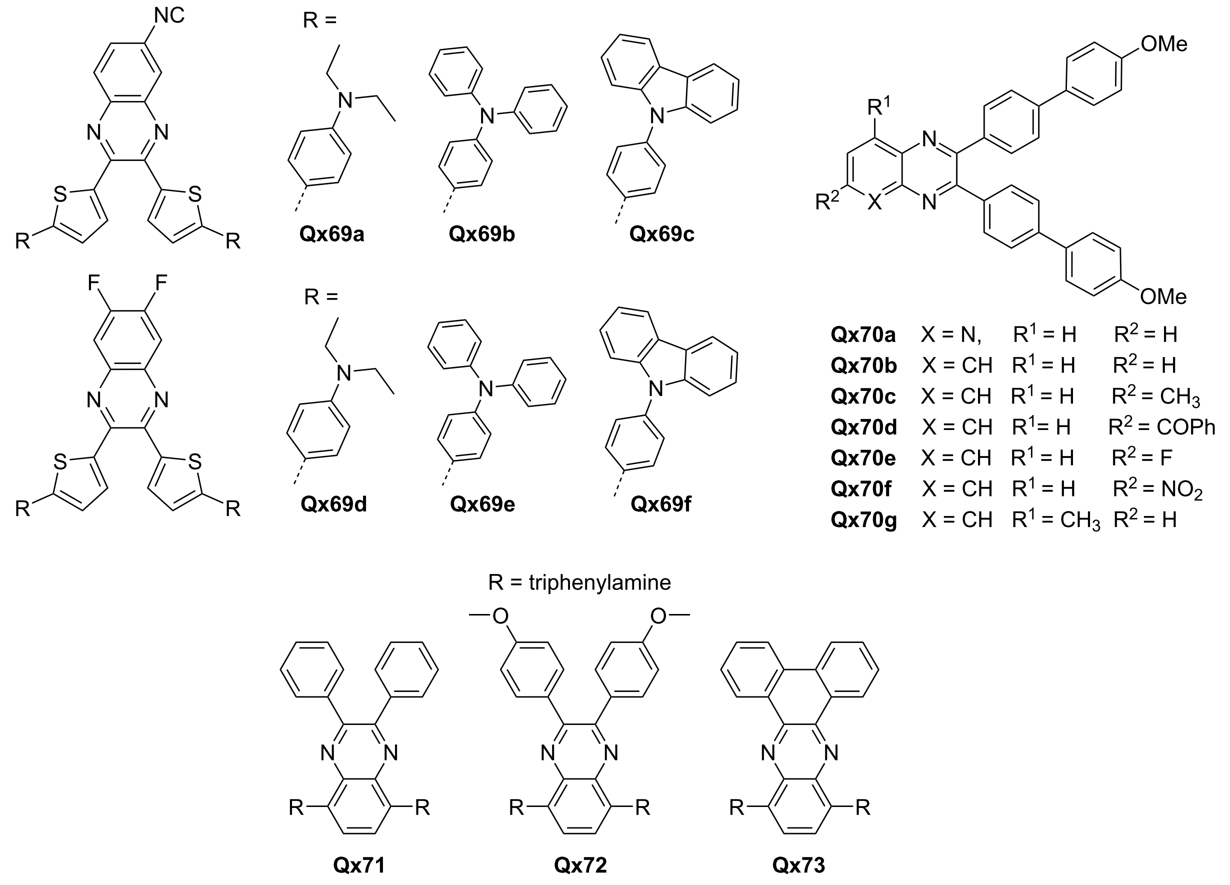

Figure 8: Qx-derived chromophores.

strategic significance of molecular design, particularly the backbone structure, for achieving high-performance electrochromic materials with up to 70% optical contrast, <3 seconds response time, over 200 $cm^2\ C^{-1}$ coloration efficiency and good cycle stability [70].

The molecular structures of the mentioned compounds are shown in Figure 8. These studies provide compelling evidence for the versatile applications of Qxs as ETMs in various fields, including sensors, electrochromic devices, optomechanics, and molecular logic devices.

Conclusion

In conclusion, the reviewed studies highlight the tremendous potential of Qx-derived ETMs across various fields, including all-PSCs, OSCs, DSSCs, OFETs, and OLEDs. Their unique properties, coupled with ongoing research, open up new avenues for their utilization in various fields.

Qx derivatives have demonstrated promise in the development of gas sensors for detection, environmental monitoring, and chemical sensing. Additionally, they can be utilized for biosensing applications by leveraging their ability to absorb and emit light in the near-infrared II range. This range allows for deeper tissue penetration, reduced scattering, and minimized autofluorescence, thereby enabling enhanced sensitivity, selectivity, and accuracy in biomarker detection, physiological parameter monitoring, and disease diagnosis. Furthermore, their efficient charge transport properties make them valuable in improving energy storage and conversion systems, including batteries and supercapacitors.

The ongoing research is focused on enhancing device efficiency through the exploration of novel device architectures, interface engineering, and material modifications. It is crucial to also address the long-term stability and durability of devices that incorporate Qx-based materials. Future advancements should focus on understanding degradation mechanisms, developing effective device encapsulation strategies, and ensuring environmental compatibility to guarantee sustained performance and viability in commercial applications. Additionally, scalability and cost-effective manufacturing processes are key for the widespread adoption of Qx-based materials. To achieve this, it is important to optimize material synthesis methods, explore solution-processable routes, and develop efficient deposition techniques. These efforts will pave the way for large-scale production of electronic devices utilizing these materials.

In addition, Qx-based materials offer notable sustainability advantages. These materials possess low environmental impact and can be synthesized from abundant precursors, making them both cost-effective and environmentally friendly compared to certain inorganic semiconductor materials. Moreover, their potential in renewable energy applications aligns with the objectives of clean energy generation and reducing dependence on fossil fuels. As research progresses, we anticipate significant advancements and breakthroughs that will pave the way for a future where quinoxaline-based materials play a vital role in shaping the next generation of electronic devices and renewable energy systems.

Funding

The authors gratefully acknowledge the Higher Education Commission (HEC) of Pakistan for their support through the IRSIP fellowship award and National Research Program for Universities (Project no. 17546), which has facilitated international collaboration and contributed to this publication.

ORCID® iDs

Zeeshan Abid - https://orcid.org/0009-0004-6946-6690
Liaqat Ali - https://orcid.org/0009-0003-0457-9996
Faiza Wahad - https://orcid.org/0009-0003-2761-7000
Raja Shahid Ashraf - https://orcid.org/0000-0003-1885-2271
Christian B. Nielsen - https://orcid.org/0000-0002-8591-1203

References

1. Jacob, M. V. *Electronics (Basel, Switz.)* **2014,** *3,* 594–597. doi:10.3390/electronics3040594
2. Bronstein, H.; Nielsen, C. B.; Schroeder, B. C.; McCulloch, I. *Nat. Rev. Chem.* **2020,** *4,* 66–77. doi:10.1038/s41570-019-0152-9
3. Fahlman, M.; Fabiano, S.; Gueskine, V.; Simon, D.; Berggren, M.; Crispin, X. *Nat. Rev. Mater.* **2019,** *4,* 627–650. doi:10.1038/s41578-019-0127-y
4. Coropceanu, V.; Cornil, J.; da Silva Filho, D. A.; Olivier, Y.; Silbey, R.; Brédas, J.-L. *Chem. Rev.* **2007,** *107,* 926–952. doi:10.1021/cr050140x
5. Yashwantrao, G.; Saha, S. *Org. Chem. Front.* **2021,** *8,* 2820–2862. doi:10.1039/d0qo01575j
6. Sun, C.; Zhu, C.; Meng, L.; Li, Y. *Adv. Mater. (Weinheim, Ger.)* **2022,** *34,* 2104161. doi:10.1002/adma.202104161
7. Gedefaw, D.; Prosa, M.; Bolognesi, M.; Seri, M.; Andersson, M. R. *Adv. Energy Mater.* **2017,** *7,* 1700575. doi:10.1002/aenm.201700575
8. Yashwantrao, G.; Saha, S. *Dyes Pigm.* **2022,** *199,* 110093. doi:10.1016/j.dyepig.2022.110093
9. Achelle, S.; Baudequin, C.; Plé, N. *Dyes Pigm.* **2013,** *98,* 575–600. doi:10.1016/j.dyepig.2013.03.030
10. McCulloch, I.; Chabinyc, M.; Brabec, C.; Nielsen, C. B.; Watkins, S. E. *Nat. Mater.* **2023,** *22,* 1304–1310. doi:10.1038/s41563-023-01579-0
11. Liu, M.; Gao, Y.; Zhang, Y.; Liu, Z.; Zhao, L. *Polym. Chem.* **2017,** *8,* 4613–4636. doi:10.1039/c7py00850c
12. Yuan, J.; Ouyang, J.; Cimrová, V.; Leclerc, M.; Najari, A.; Zou, Y. *J. Mater. Chem. C* **2017,** *5,* 1858–1879. doi:10.1039/c6tc05381e
13. Soleymani, M.; Chegeni, M. *Curr. Org. Chem.* **2019,** *23,* 1789–1827. doi:10.2174/1385272823666190926094348
14. Kim, J. H.; Yun, J. H.; Lee, J. Y. *Adv. Opt. Mater.* **2018,** *6,* 1800255. doi:10.1002/adom.201800255
15. Sun, C.; Pan, F.; Bin, H.; Zhang, J.; Xue, L.; Qiu, B.; Wei, Z.; Zhang, Z.-G.; Li, Y. *Nat. Commun.* **2018,** *9,* 743. doi:10.1038/s41467-018-03207-x
16. Wu, Y.; Zheng, Y.; Yang, H.; Sun, C.; Dong, Y.; Cui, C.; Yan, H.; Li, Y. *Sci. China: Chem.* **2020,** *63,* 265–271. doi:10.1007/s11426-019-9599-1
17. Sun, C.; Pan, F.; Chen, S.; Wang, R.; Sun, R.; Shang, Z.; Qiu, B.; Min, J.; Lv, M.; Meng, L.; Zhang, C.; Xiao, M.; Yang, C.; Li, Y. *Adv. Mater. (Weinheim, Ger.)* **2019,** *31,* 1905480. doi:10.1002/adma.201905480
18. Meng, L.; Sun, C.; Wang, R.; Huang, W.; Zhao, Z.; Sun, P.; Huang, T.; Xue, J.; Lee, J.-W.; Zhu, C.; Huang, Y.; Li, Y.; Yang, Y. *J. Am. Chem. Soc.* **2018,** *140,* 17255–17262. doi:10.1021/jacs.8b10520
19. Wang, Z.; Xiao, M.; Liu, X.; He, B.; Yang, X.; Li, Y.; Peng, J.; Huang, F.; Cao, Y. *Polymer* **2018,** *158,* 183–189. doi:10.1016/j.polymer.2018.10.062
20. You, H.; Kang, H.; Kim, D.; Park, J. S.; Lee, J.-W.; Lee, S.; Kim, F. S.; Kim, B. J. *ChemSusChem* **2021,** *14,* 3520–3527. doi:10.1002/cssc.202100080
21. Eedugurala, N.; Steelman, M. E.; Mahalingavelar, P.; Adams, D. J.; Mayer, K. S.; Liu, C.-T.; Benasco, A.; Ma, G.; Gu, X.; Bowman, M. K.; Azoulay, J. D. *Chem. Mater.* **2023,** *35,* 3115–3123. doi:10.1021/acs.chemmater.2c03548
22. You, H.; Lee, S.; Kim, D.; Kang, H.; Lim, C.; Kim, F. S.; Kim, B. J. *ACS Appl. Mater. Interfaces* **2021,** *13,* 47817–47825. doi:10.1021/acsami.1c12288
23. Zhou, L.; He, X.; Lau, T.-K.; Qiu, B.; Wang, T.; Lu, X.; Luszczynska, B.; Ulanski, J.; Xu, S.; Chen, G.; Yuan, J.; Zhang, Z.-G.; Li, Y.; Zou, Y. *ACS Appl. Mater. Interfaces* **2018,** *10,* 41318–41325. doi:10.1021/acsami.8b13949
24. Liang, S.; Xiao, C.; Xie, C.; Liu, B.; Fang, H.; Li, W. *Adv. Mater. (Weinheim, Ger.)* **2023,** *35,* 2300629. doi:10.1002/adma.202300629
25. Elavarasan, K.; Saravanan, C.; Panneer Selvam, N.; Hsieh, Y.-J.; Chang, Y.-M.; Wang, L. *Polym. Int.* **2018,** *67,* 1555–1562. doi:10.1002/pi.5678
26. Yuan, J.; Zhang, Y.; Zhou, L.; Zhang, G.; Yip, H.-L.; Lau, T.-K.; Lu, X.; Zhu, C.; Peng, H.; Johnson, P. A.; Leclerc, M.; Cao, Y.; Ulanski, J.; Li, Y.; Zou, Y. *Joule* **2019,** *3,* 1140–1151. doi:10.1016/j.joule.2019.01.004
27. Liu, Q.; Jiang, Y.; Jin, K.; Qin, J.; Xu, J.; Li, W.; Xiong, J.; Liu, J.; Xiao, Z.; Sun, K.; Yang, S.; Zhang, X.; Ding, L. *Sci. Bull.* **2020,** *65,* 272–275. doi:10.1016/j.scib.2020.01.001
28. Zhou, Z.; Liu, W.; Zhou, G.; Zhang, M.; Qian, D.; Zhang, J.; Chen, S.; Xu, S.; Yang, C.; Gao, F.; Zhu, H.; Liu, F.; Zhu, X. *Adv. Mater. (Weinheim, Ger.)* **2020,** *32,* 1906324. doi:10.1002/adma.201906324
29. Zhu, C.; An, K.; Zhong, W.; Li, Z.; Qian, Y.; Su, X.; Ying, L. *Chem. Commun.* **2020,** *56,* 4700–4703. doi:10.1039/d0cc00896f
30. Zhang, Z.; Si, W.; Wu, B.; Wang, W.; Li, Y.; Ma, W.; Lin, Y. *Angew. Chem., Int. Ed.* **2022,** *61,* e202114234. doi:10.1002/anie.202114234

31. Bhattacharya, L.; Brown, A.; Sharma, S.; Sahu, S. *J. Phys. Chem. A* **2022,** *126,* 7110–7126. doi:10.1021/acs.jpca.2c03906
32. Chang, M.; Zhang, Y.; Lu, B.-S.; Sui, D.; Wang, F.; Wang, J.; Yang, Y.; Kan, B. *Chem. Eng. J.* **2022,** *427,* 131473. doi:10.1016/j.cej.2021.131473
33. Ayub, A.; Ans, M.; Gul, S.; Shawky, A. M.; Ayub, K.; Iqbal, J.; Hashmi, M. A.; Lakhani, A. *Electron. Mater. Lett.* **2023,** *19,* 38–54. doi:10.1007/s13391-022-00378-0
34. Huang, J.; Li, S.; Qin, J.; Xu, L.; Zhu, X.; Yang, L.-M. *ACS Appl. Mater. Interfaces* **2021,** *13,* 45806–45814. doi:10.1021/acsami.1c11412
35. Huang, J.; Gao, C.-Y.; Fan, X.-H.; Zhu, X.; Yang, L.-M. *Energy Technol.* **2022,** *10,* 2100912. doi:10.1002/ente.202100912
36. Xiao, B.; Tang, A.; Yang, J.; Mahmood, A.; Sun, X.; Zhou, E. *ACS Appl. Mater. Interfaces* **2018,** *10,* 10254–10261. doi:10.1021/acsami.8b00216
37. Xiao, B.; Zhang, Q.; Li, G.; Du, M.; Geng, Y.; Sun, X.; Tang, A.; Liu, Y.; Guo, Q.; Zhou, E. *Sci. China: Chem.* **2020,** *63,* 254–264. doi:10.1007/s11426-019-9618-7
38. An, N.; Cai, Y.; Wu, H.; Tang, A.; Zhang, K.; Hao, X.; Ma, Z.; Guo, Q.; Ryu, H. S.; Woo, H. Y.; Sun, Y.; Zhou, E. *Adv. Mater. (Weinheim, Ger.)* **2020,** *32,* 2002122. doi:10.1002/adma.202002122
39. Ji, H.; Li, J.; Du, M.; Yang, J.; Tang, A.; Li, G.; Guo, Q.; Zhou, E. *J. Phys. Chem. C* **2021,** *125,* 10876–10882. doi:10.1021/acs.jpcc.1c01967
40. Krishna, J. V. S.; Prasanthkumar, S.; Dzeba, I.; Challuri, V.; Naim, W.; Sauvage, F.; Giribabu, L. *Mater. Adv.* **2021,** *2,* 7922–7931. doi:10.1039/d1ma00614b
41. Grobelny, A.; Shen, Z.; Eickemeyer, F. T.; Antariksa, N. F.; Zapotoczny, S.; Zakeeruddin, S. M.; Grätzel, M. *Adv. Mater. (Weinheim, Ger.)* **2023,** *35,* 2207785. doi:10.1002/adma.202207785
42. Kumar, S.; Thomas, K. R. J.; Li, C.-T.; Ho, K.-C. *J. Mater. Sci.: Mater. Electron.* **2017,** *28,* 18404–18417. doi:10.1007/s10854-017-7787-4
43. Godfroy, M.; Aumaitre, C.; Caffy, F.; Kervella, Y.; Cabau, L.; Pellejà, L.; Maldivi, P.; Narbey, S.; Oswald, F.; Palomares, E.; Joly, D.; Demadrille, R. *Dyes Pigm.* **2017,** *146,* 352–360. doi:10.1016/j.dyepig.2017.07.022
44. Huang, L.; Ma, P.; Deng, G.; Zhang, K.; Ou, T.; Lin, Y.; Wong, M. S. *Dyes Pigm.* **2018,** *159,* 107–114. doi:10.1016/j.dyepig.2018.06.010
45. Jiang, H.; Ren, Y.; Zhang, W.; Wu, Y.; Socie, E. C.; Carlsen, B. I.; Moser, J.-E.; Tian, H.; Zakeeruddin, S. M.; Zhu, W.-H.; Grätzel, M. *Angew. Chem.* **2020,** *132,* 9410–9415. doi:10.1002/ange.202000892
46. El Assyry, A.; Lamsayah, M.; Warad, I.; Touzani, R.; Bentiss, F.; Zarrouk, A. *Heliyon* **2020,** *6,* e03620. doi:10.1016/j.heliyon.2020.e03620
47. Daoud, A.; Cheknane, A.; Touzani, R.; Hilal, H. S.; Boulouiz, A. *J. Electron. Mater.* **2021,** *50,* 5656–5663. doi:10.1007/s11664-021-09113-1
48. Shi, X.; Zhao, D.; Wang, L.; Li, Y. *Optik (Munich, Ger.)* **2020,** *219,* 165030. doi:10.1016/j.ijleo.2020.165030
49. Arunkumar, A.; Anbarasan, P. M. *J. Electron. Mater.* **2019,** *48,* 1522–1530. doi:10.1007/s11664-018-06912-x
50. Sharma, B. K.; Shaikh, A. M.; Chacko, S.; Kamble, R. M. *J. Chem. Sci.* **2017,** *129,* 483–494. doi:10.1007/s12039-017-1252-z
51. Singh, P. S.; Shirgaonkar, A. J.; Chawathe, B. K.; Kamble, R. M. *J. Chem. Sci.* **2020,** *132,* 150. doi:10.1007/s12039-020-01851-9
52. Hasegawa, T.; Ashizawa, M.; Aoyagi, K.; Masunaga, H.; Hikima, T.; Matsumoto, H. *Org. Lett.* **2017,** *19,* 3275–3278. doi:10.1021/acs.orglett.7b01424
53. Hayashi, H.; Tsuda, E.; Koizumi, T.-a. *ChemistrySelect* **2021,** *6,* 5441–5445. doi:10.1002/slct.202101087
54. Mikie, T.; Iwasaki, Y.; Osaka, I. *Mater. Chem. Phys.* **2022,** *287,* 126225. doi:10.1016/j.matchemphys.2022.126225
55. Ding, F.; Xia, D.; Ding, X.; Deng, R.; Ge, C.; Yang, Y.; Fan, R.; Lin, K.; Gao, X. *Chin. Chem. Lett.* **2023,** *34,* 107235. doi:10.1016/j.cclet.2022.02.040
56. Kvashnin, Yu. A.; Krynina, E. M.; Medvedeva, M. V.; Svalova, T. S.; Kozitsina, A. N.; Eltsov, O. S.; Rusinov, G. L.; Verbitskiy, E. V.; Charushin, V. N. *Russ. Chem. Bull.* **2023,** *72,* 939–947. doi:10.1007/s11172-023-3857-3
57. Jin, C.-H.; Putri, S. K.; Chang, D. W.; Lee, J. *J. Imaging Sci. Technol.* **2018,** *62,* 040404-1–040404-6. doi:10.2352/j.imagingsci.technol.2018.62.4.040404
58. Kamble, R. M.; Sharma, B. K.; Shaikh, A. M.; Chacko, S. *ChemistrySelect* **2018,** *3,* 6907–6915. doi:10.1002/slct.201801208
59. Rohnacher, V.; Benneckendorf, F. S.; Münch, M.; Sauter, E.; Asyuda, A.; Barf, M.-M.; Tisserant, J.-N.; Hillebrandt, S.; Rominger, F.; Jänsch, D.; Freudenberg, J.; Kowalsky, W.; Jaegermann, W.; Bunz, U. H. F.; Pucci, A.; Zharnikov, M.; Müllen, K. *Adv. Mater. Technol. (Weinheim, Ger.)* **2021,** *6,* 2000300. doi:10.1002/admt.202000300
60. Thelakkat, M.; Schmidt, H.-W. *Polym. Adv. Technol.* **1998,** *9,* 429–442. doi:10.1002/(sici)1099-1581(199807)9:7<429::aid-pat798>3.0.co;2-e
61. Kim, J. T.; Lee, J.; Jang, S.; Yu, Z.; Park, J. H.; Jung, E. D.; Lee, S.; Song, M. H.; Whang, D. R.; Wu, S.; Park, S. H.; Chang, D. W.; Lee, B. R. *J. Mater. Chem. A* **2020,** *8,* 13501–13508. doi:10.1039/d0ta04802j
62. Lee, S. W.; Fan, X.; Whang, D. R.; Jang, J. W.; Choi, H.; Chang, D. W.; Lee, B. R. *J. Inf. Disp.* **2023,** *24,* 189–198. doi:10.1080/15980316.2023.2171145
63. Ji, S.-C.; Jiang, S.; Zhao, T.; Meng, L.; Chen, X.-L.; Lu, C.-Z. *New J. Chem.* **2022,** *46,* 8991–8998. doi:10.1039/d2nj01072k
64. Yu, L.; Wu, Z.; Zhong, C.; Xie, G.; Wu, K.; Ma, D.; Yang, C. *Dyes Pigm.* **2017,** *141,* 325–332. doi:10.1016/j.dyepig.2017.02.035
65. Yu, J.; Xiao, Y.; Chen, J. *Chin. J. Org. Chem.* **2019,** *39,* 3460. doi:10.6023/cjoc201906019
66. Huang, T.; Liu, D.; Li, D.; Jiang, W.; Jiang, J. *New J. Chem.* **2019,** *43,* 13339–13348. doi:10.1039/c9nj03184g
67. Gupta, S.; Milton, M. D. *Dyes Pigm.* **2021,** *195,* 109690. doi:10.1016/j.dyepig.2021.109690
68. Moshkina, T. N.; Nosova, E. V.; Kopotilova, A. E.; Ośmiałowski, B.; Reguant, A. I.; Slepukhin, P. A.; Lipunova, G. N.; Taniya, O. S.; Kalinichev, A. A.; Charushin, V. N. *Dyes Pigm.* **2022,** *204,* 110434. doi:10.1016/j.dyepig.2022.110434
69. Gupta, S.; Milton, M. D. *J. Mol. Struct.* **2022,** *1264,* 133275. doi:10.1016/j.molstruc.2022.133275
70. Fu, W.; Chen, H.; Han, Y.; Wang, W.; Zhang, R.; Liu, J. *New J. Chem.* **2021,** *45,* 19082–19087. doi:10.1039/d1nj04074j

License and Terms

The definitive version of this article is the electronic one which can be found at:
https://doi.org/10.3762/bjoc.19.124

BEILSTEIN JOURNAL OF ORGANIC CHEMISTRY

Charge carrier transport in perylene-based and pyrene-based columnar liquid crystals

Alessandro L. Alves[1], Simone V. Bernardino[1], Carlos H. Stadtlober[1], Edivandro Girotto[2], Giliandro Farias[2], Rodney M. do Nascimento[1], Sergio F. Curcio[3], Thiago Cazati[3], Marta E. R. Dotto[1], Juliana Eccher[1], Leonardo N. Furini[1], Hugo Gallardo[2], Harald Bock[4] and Ivan H. Bechtold*[1]

Full Research Paper

Open Access

Address:
[1]Departamento de Física, Universidade Federal de Santa Catarina, Florianópolis 88040-900, SC, Brazil, [2]Departamento de Química, Universidade Federal de Santa Catarina, Florianópolis 88040-900, SC, Brazil, [3]Departamento de Fisica, Universidade Federal de Ouro Preto, Ouro Preto 35400-000, MG, Brazil and [4]Centre de Recherche Paul Pascal, CNRS, 115 av. Schweitzer, 33600 Pessac, France

Email:
Ivan H. Bechtold* - ivan.bechtold@ufsc.br

* Corresponding author

Keywords:
charge carrier transport; columnar liquid crystal; organic electronics; perylene; pyrene

Beilstein J. Org. Chem. **2023,** *19,* 1755–1765.
https://doi.org/10.3762/bjoc.19.128

Received: 08 August 2023
Accepted: 31 October 2023
Published: 16 November 2023

This article is part of the thematic issue "Organic electron transport materials".

Associate Editor: P. J. Skabara

Abstract

Electron and hole transport characteristics were evaluated for perylene-based and pyrene-based compounds using electron-only and hole-only devices. The perylene presented a columnar hexagonal liquid crystal phase at room temperature with strong molecular π-stacking inside the columns. The pyrene crystallizes bellow 166 °C, preserving the close-packed columnar rectangular structure of the mesophase. Photophysical analysis and numerical calculations assisted the interpretation of positive and negative charge carrier mobilities obtained from fitting the space charge limited regime of current vs voltage curves. The pyrene-based material demonstrated an electron mobility two orders of magnitude higher than the perylene one, indicating the potential of this class of materials as electron transporting layer.

Introduction

Conjugated organic molecules have been widely investigated due to their interesting transport properties and promising applications as active layer in organic photovoltaics (OPVs), organic field effect transistors (OFETs), organic light-emitting diodes (OLEDs) and sensors [1,2]. Columnar liquid crystals are attractive due to their solution processability and their self-organization in highly anisotropic supramolecular architectures, which favors the mainly one-dimensional migration of charge carriers with an anisotropy of the charge carrier mobility (parallel vs perpendicular to the columnar axis) of up to ten orders of magnitude [3-7]. In 1994, Adam and collaborators obtained a hole-mobility of up to 0.1 $cm^2 V^{-1} s^{-1}$ for a triphenylene-based columnar liquid crystal [8], motivating intense research activity to understanding charge transport in columnar mesophases [9-14]. High charge carrier mobilities of 1.1 $cm^2 V^{-1} s^{-1}$ for p-type and up to 6.0 $cm^2 V^{-1} s^{-1}$ for n-type liquid-crystalline semiconductors have already been reported [15].

Among the various discotic liquid crystal materials, perylene derivatives are among the most investigated due to their easy functionalization, high chemical and thermal stability, strong photoluminescence, and n-type semiconductor character. They tend to adopt columnar organization due to the strong π–π interaction of the rigid cores, providing a path for the efficient conduction of electrons [16]. Perylene diimide derivatives display good electronic mobilities (10^{-3} to 10^{-1} $cm^2 V^{-1} s^{-1}$) and are considered suitable electron acceptors for photovoltaic applications [17-20]. Pyrene derivatives have also been widely investigated in recent decades. They exhibit excellent photoelectric properties such as strong emission, efficient excimer formation, and suitable intermolecular stacking for good charge carrier transport. They have been applied as active layer in OFETs with high ambipolar mobility due to their well-defined monocrystalline microstructures resulting from strong π–π interactions [7,21-24].

In this work, we investigated a perylene and a pyrene-based columnar liquid crystal in hole-only and electron-only devices to compare their charge carriying properties. The molecular organization and photophysical performances are coherent with the charge transport behavior. DFT calculations assisted the interpretation of electron and hole migration mechanism using the frontier orbital energies and the conjugation within the π-system.

Results and Discussion

The syntheses of **1** and **2** were previously published in [25] and [26], respectively. **1** is a benzo[*ghi*]perylene-hexacarboxylic trialkylimide and **2** a dinaphtho[2,1-*a*;1,2-*i*]pyrene-tetracarboxylic dialkylimide, both with asymmetrically branched alkyl swallow-tails derived from 7-aminohexadecane (Scheme 1 illustrates their molecular structure). In Table 1, we show the thermal characteristics and observed mesophases. Compound **1** presents a wide range columnar hexagonal phase (Col_{hex}) preserved at room temperature by cooling from the isotropic. Compound **2** shows an additional columnar rectangular phase (Col_{rect}) below the Col_{hex} and crystallizes under 166 °C. The HOMO and LUMO energy levels are also given in Table 1.

Raman spectra of both compounds were acquired off-resonance (Figure 1). Compound **1** presents the main peak at 1609 cm^{-1} assigned to C=C stretching from the chromophore, a peak of

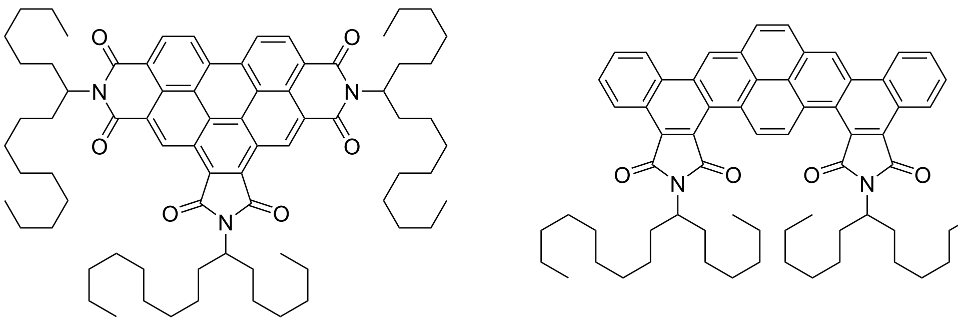

Scheme 1: Molecular structures of compounds **1** and **2**.

Table 1: Characteristics of **1** and **2** extracted from [17] and [18], respectively.

Comp.	Phase sequence (°C)[a]	HOMO (eV)	LUMO (eV)
1	Col_{hex} – 177 - Iso	–6.62	–3.79
2	Cr – 166 – Col_{rect} – 225 – Col_{hex} – 248 – Iso	–5.65	–3.32

[a]Determined by DSC, XRD and POM.

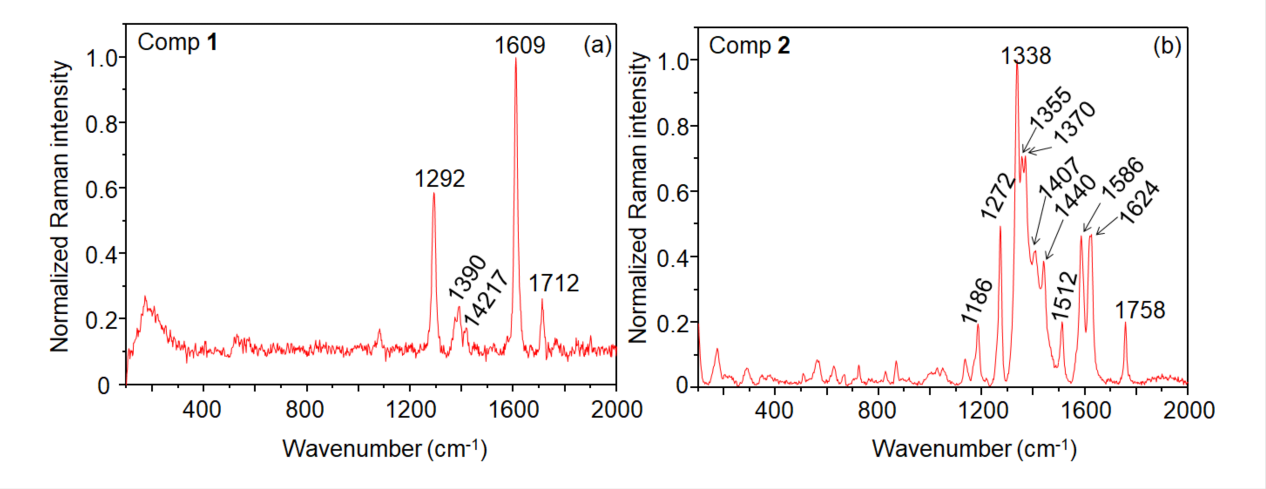

Figure 1: Raman spectra of **1** (a) and **2** (b) in powder.

intermediate intensity at 1292 cm^{-1} assigned to C–H bending and ring stretching, and a less intense peak at 1712 cm^{-1} which corresponds to C=O stretching [27]. The pair at 1390 and 1417 cm^{-1} is attributed to perylene ring stretching [28]. As observed for bis(phenethylimido)perylene (PhPTCD) [29] only a small number of peaks is observed. In contrast, compound **2** presents a larger number of peaks, with the spectrum being dominated by the peak at 1338 cm^{-1} (C–N stretching). The peak at 1272 (C–H bending and ring stretching), and the pair of peaks at 1586 and 1624 cm^{-1} are assigned to the C=C stretching mode [30]. Less intense peaks can be observed at 1186 (C–H bending), 1512 (perylene ring stretching), and 1758 cm^{-1} (C=O).

X-ray diffraction (XRD) measurements of **1** and **2** are shown in Figure 2. The Miller indices indicate the Col_{hex} and Col_{rect} character of the mesophases [31]. Despite crystallization of **2**, the Col_{rect} order is partially preserved at room temperature. The Col_{hex} lattice parameter (a) obtained is 23.7 Å for **1** and 22.9 Å for **2**. The *a*/*b* aspect ratio of the Col_{rect} phase of **2** is equal to 2.08, representing an elongation of around 20% concerning the hexagonal mesophase (where *a*/*b* = 1.73). The π-stacking distance between neighboring disks inside the columns, indicated by the (001) peak, is ≈3.5 Å for all mesophases.

Absorption and photoluminescence (PL) of **1** and **2** are presented in Figure 3 for solution and spin-coated film. Compound **1** shows the three well-defined bands typical of perylene absorption and PL in solution. The absorption becomes broader and the PL destructured and red-shifted in the film. These results indicate molecular π-stacking aggregation and excimer formation on the films [2].

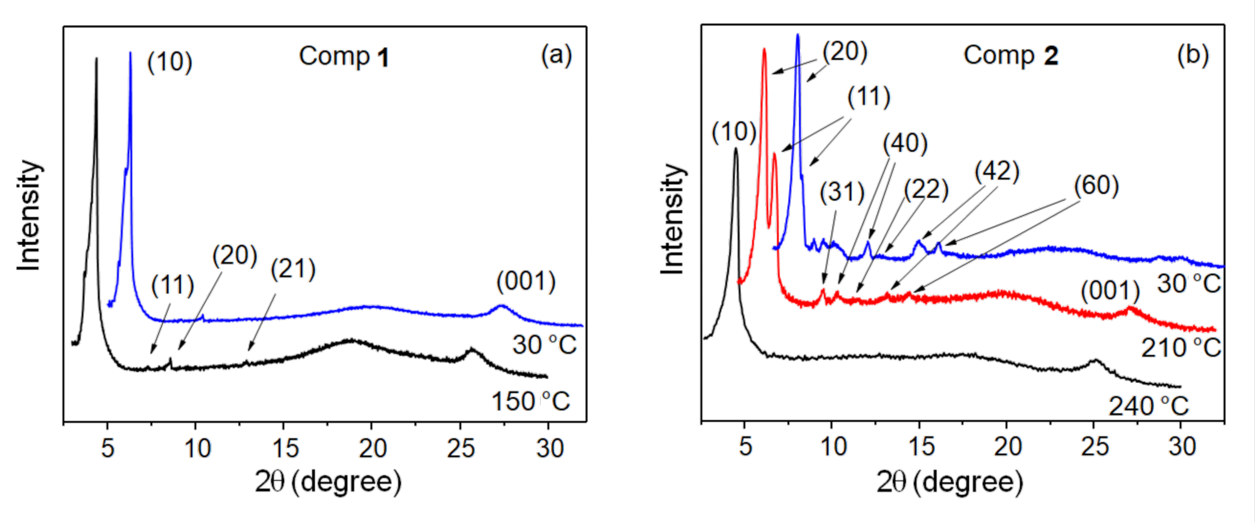

Figure 2: XRD measurements of **1** (a) and **2** (b) captured on cooling from the isotropic phase, indicating the Miller indices.

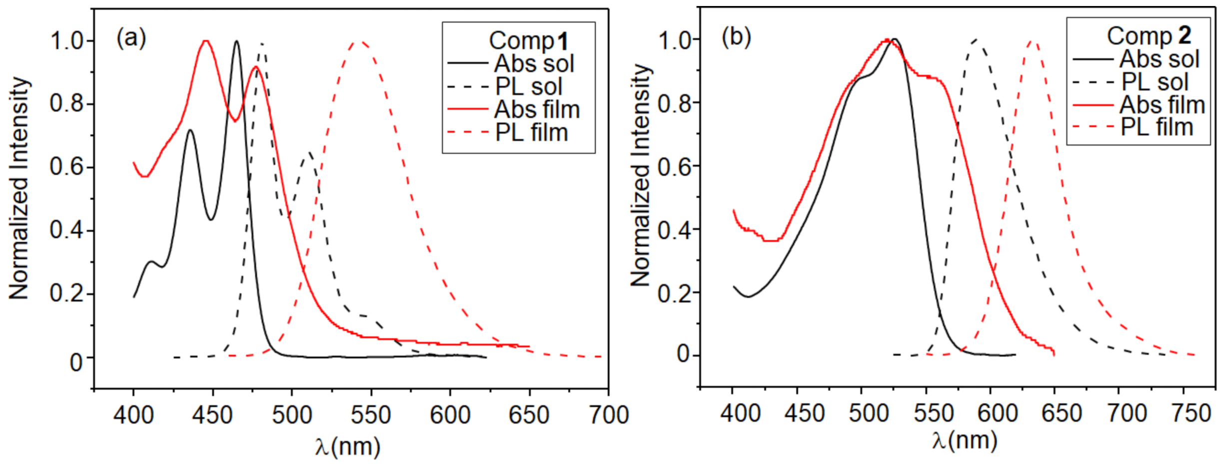

Figure 3: Absorption and PL in chloroform solution and in spin-coated films for compounds **1** (a) and **2** (b). The PL was excited at the wavelength of maximum absorption.

The PL in film was obtained as a function of temperature (Figure 4). The observed reduction of the PL intensity on heating is expected for organic semiconductors due to self-quenching aggregates and nonradiative decay processes that are thermally activated [32]. However, an increase in the emission intensity can be observed for **1** at the $\mathrm{Col_{hex}}$–Iso transition. The stronger π-stacking aggregates present in the $\mathrm{Col_{hex}}$ of **1**, reduce the emission compared to the the disordered isotropic phase. The enhanced and blue-shifted emission at the transition to the isotropic phase arise from the excited isolated molecules, where the exciton decays radiatively without diffusion. For the isolated molecules, the more localized π-orbital results in a higher energy emission state. The same effect was previously observed for another perylene-based ColLC compound, indicating the strong molecular interaction between neighboring molecules inside the columnar structure [33]. Due to the high temperature of the Iso phase for **2**, the PL intensity almost vanished. However, a slight increase could also be observed at the $\mathrm{Col_{hex}}$–Iso transition. The reduction of PL at the Cr–$\mathrm{Col_{rect}}$ transition also reflects stronger molecular π-stacking of **2** in the $\mathrm{Col_{rect}}$ phase compared to the crystalline state.

The excited state lifetimes of **1** and **2** in chloroform solutions and spin-coated films, both excited at 401 nm, are listed in Table 2. The fitted fluorescence decay curves are shown in Supporting Information File 1 (Figure S1). For diluted solutions of **1** and **2**, monoexponential lifetimes in the nanosecond timescale were observed and attributed to emission from monomeric species (6.54 and 4.14 ns, respectively). In the spin-coated films, the best fitting of the decay curves of **1** and **2** indicated three and two lifetimes, respectively. Compound **1** displayed a dominant and longer lifetime compared to solution, 25.9 ns (66.83%), attributed to excimer emission, which usually presents longer lifetimes compared to the monomeric species [34]. It agrees with the intensity inversion of the vibronic absorption bands and PL redshift in the spin-coated film compared to the solution. The intensity inversion suggests formation of H-aggregates, leading to excimer fluorescence [35]. Due to the similarity to the lifetime in solution, the 6.90 ns lifetime in the film is attributed to monomeric emission. The shortest lifetime of 0.90 ns can be related to the emission of aggregated species driven by π–π interactions [36], contributing to almost 20% of the total emission of **1**. The longer lifetime of **2** in film (3.84 ns) can be attributed to the monomeric emission as it is similar to the value observed in solution, while the shortest lifetime (1.58 ns) of aggregated π–π species dominates with 75.38% of the total emission.

Hole-only (ITO/PEDOT: PSS/**1** or **2**/Au) and electron-only devices (Al/**1** or **2**/Al) were fabricated to evaluate the positive and negative charge carrier transport of **1** and **2**. The active layers of **1** or **2** were spin-coated from chloroform solutions (10 mg/mL). Scheme S1 in Supporting Information File 1 illustrates the device structure with the energy levels of the layers.

Figure 5 shows atomic force microscopy (AFM) images to address the thickness and the morphology of the films of **1** and **2** deposited on the hole-only and electron-only device structures. The thickness of the films in these structures was 40 nm.

The films deposited on PEDOT:PSS for the hole-only devices indicate homogenous properties with low root mean square roughness (R_{rms}) of 1.7 nm and 2.8 nm for **1** (Figure 5a) and **2** (Figure 5b), respectively. The R_{rms} of the films deposited on Al for the electron-only devices are 1.1 nm for **1** (Figure 5c) and

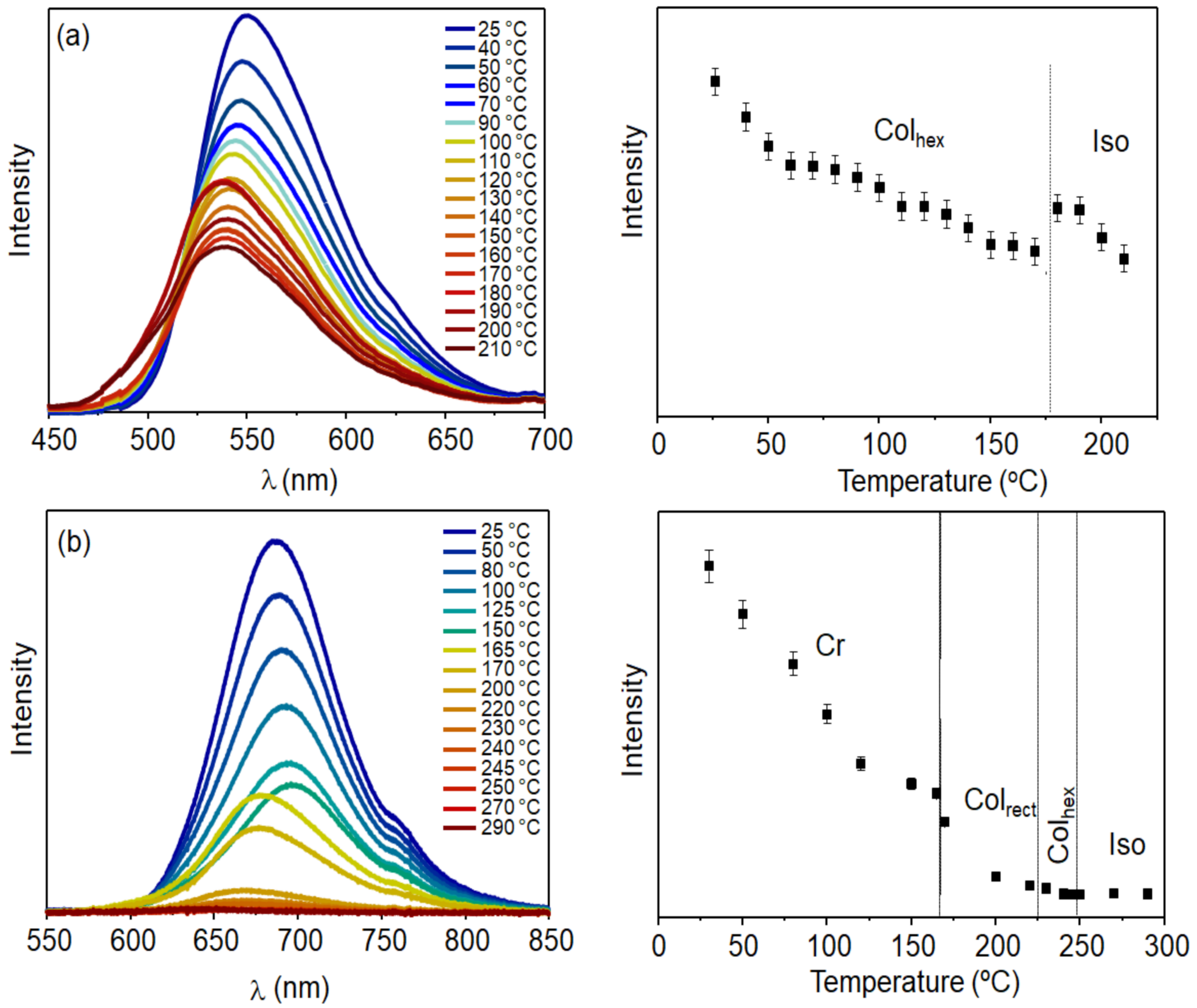

Figure 4: PL as a function of temperature for **1** (a) and **2** (b) casting films on heating. Left: PL spectra; right: intensity of the PL maximum. The PL was excited at the wavelength of maximum absorption.

Table 2: Excited state lifetimes and relative amplitudes of **1** and **2** in chloroform solutions and spin-coated films at room temperature.

Comp.	λ_{max} (nm)[a]	τ_1 (ns)	A_1 (%)	τ_2 (ns)	A_2 (%)	τ_3 (ns)	A_3 (%)	χ^2
solution[b]								
1	487	6.54 ± 0.04	100	–	–	–	–	1.063
2	589	4.14 ± 0.03	100	–	–	–	–	1.008
film								
1	542	25.90 ± 0.2	66.83	6.90 ± 0.50	13.18	0.90 ± 0.20	19.99	0.997
2	633	3.84 ± 0.05	24.62	1.58 ± 0.03	75.38	–	–	0.946

[a] Fluorescence decay collected at maximum emission (λ_{max}), excited at 401 nm. [b] Concentration of 0.17 g L^{-1}.

16.0 nm for **2** (Figure 5d). XRD measurements of as-casted spin-coated films of **1** and **2** confirm their columnar order and polarized optical microscopy show small birefringent domains, indicating locally instead of macroscopic molecular alignment of the films (see Figure S2 in Supporting Information File 1).

Figure 6 shows the log–log plots of the J–V experimental curves for **1** and **2** in both device structures. In all cases, an ohmic regime is observed at low voltages, $J \propto V^n$ with $n \approx 1.0$, followed by a space charge limited current (SCLC) trap-limited regime. To determine the charge carrier mobility, a previously

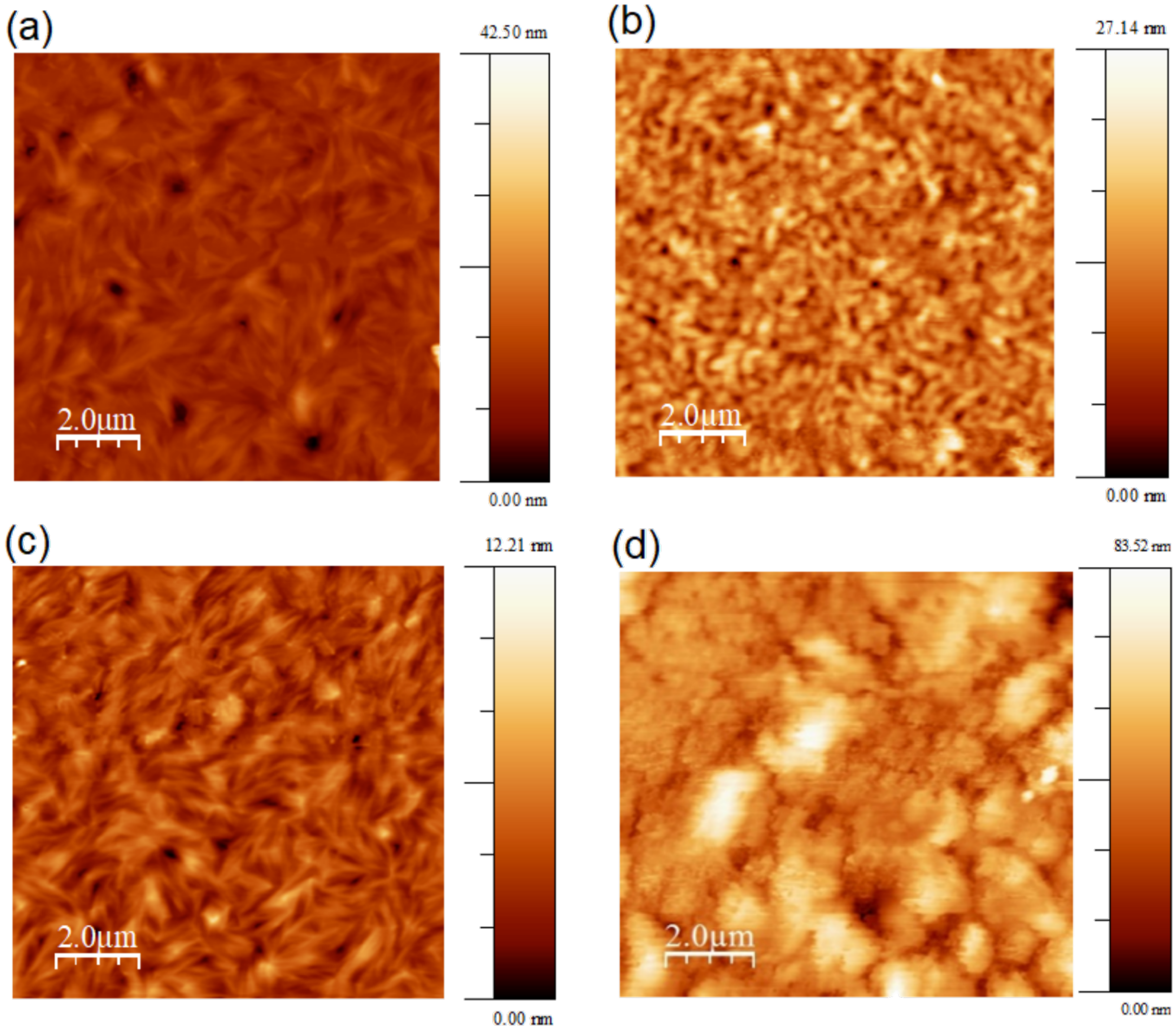

Figure 5: AFM images of spin-coated films of compound **1** (a, c) and compound **2** (b, d) on PEDOT:PSS (a, b) and Al (c, d).

published theoretical model was used [33], where an electric field dependent mobility of the form $\mu(E) = \mu_0 e^{\gamma\sqrt{E}}$ was considered. The parameters μ_0 and γ implicitly include a mono-energetic trap distribution and can be obtained from fitting the SCLC regimes of the experimental *J*–*V* curves. The fits for each device are shown as red solid lines in Figure 6, and the values of μ_0 and γ displayed in Table 3 were used to calculate the mobility $\mu(E)$ at an electric field of 6.0×10^5 V/cm.

Figure 7 shows the charge carrier mobility as a function of the applied electric field, calculated from $\mu(E) = \mu_0 e^{\gamma\sqrt{E}}$. The electron mobility of **1** is around one order of magnitude lower than that of holes, depending on the electric field. It suggests that this perylene-based material acts better as a hole-transporting material. The electron mobility of **2** is almost two orders of magnitude higher than **1**. It may be related to the closer molecular packing of the $\mathrm{Col_{rect}}$ phase preserved in the crystal at room temperature, which improves the π-stacking and corroborates with the dominant emission of aggregated π–π species in the film observed in the lifetime measurement. The hole mobility of **2** is similar to **1**, but its electron mobility is slightly higher, indicating that this pyrene-based molecule can act as an ambipolar transporting layer, in agreement with the literature [24]. It is important to emphasize that the charge carrier mobility of columnar liquid crystals can be improved by five orders of magnitude due to molecular alignment of the film in the device structure [33].

Usually, the π-system conjugation and the frontier orbitals energies dominates the charge transport [37,38]. Therefore, to better

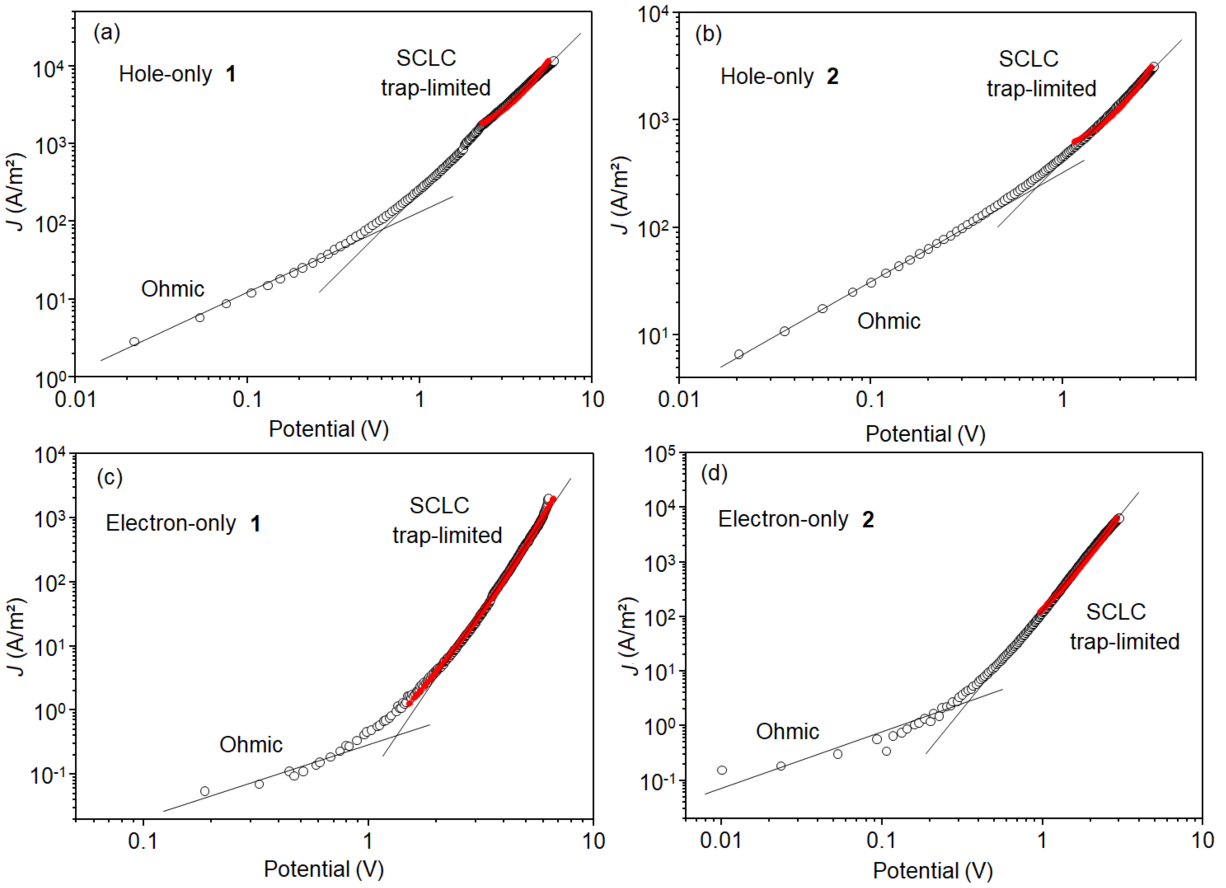

Figure 6: Log–log plot of the *J–V* curves of the hole-only (a,b) and electron-only (c,d) of **1** (a,c) and **2** (b,d). The open circles are the experimental data, and the red solid lines indicate the theoretical fitting. V_Ω is the threshold voltage between the ohmic and SCLC trap-limited regimes.

Table 3: Fitting parameters and charge carrier mobility of hole-only and electron-only devices fabricated with **1** and **2**.

Comp.	γ (cm $V^{-1})^{1/2}$	μ_0 (cm^2 V s^{-1})	μ (cm^2 V s$^{-1})^a$	Slope SCLC
hole-only				
1	2.49×10^{-3}	5.82×10^{-7}	1.2×10^{-5}	2.1
2	3.18×10^{-3}	6.62×10^{-7}	2.7×10^{-5}	1.8
electron-only				
1	7.18×10^{-3}	2.54×10^{-10}	6.4×10^{-7}	5.2
2	5.74×10^{-3}	2.24×10^{-7}	1.3×10^{-4}	3.6

[a]Mobility values for an electric field of 1.0×10^6 V cm^{-1}. Films of **1** and **2** were 40 nm thick.

understand the charge mobility of compounds **1** and **2**, we obtained their ground state geometry using DFT within the B3LYP/def2-TZVP(-f) level of theory (Figure 8a). To reduce computational efforts, isopropyl moieties were used instead of the large aliphatic substituents of molecules **1** and **2**. The π electron systems of both molecules are predominantly planar, with **2-iso** showing a slight deviation from planarity due to the steric proximity of the dicarboximide oxygens with the adjacent bay hydrogens. The frontier orbitals and their energies are shown in Figure 8b. In **1-iso**, only the two hexagonal imide groups affect the HOMO/LUMO localization, whereas the pentagonal central imide group is little affected. In **2-iso**, both pentagonal are relevant to the HOMO/LUMO localization, whereas the two terminal benzene rings are little affected. The

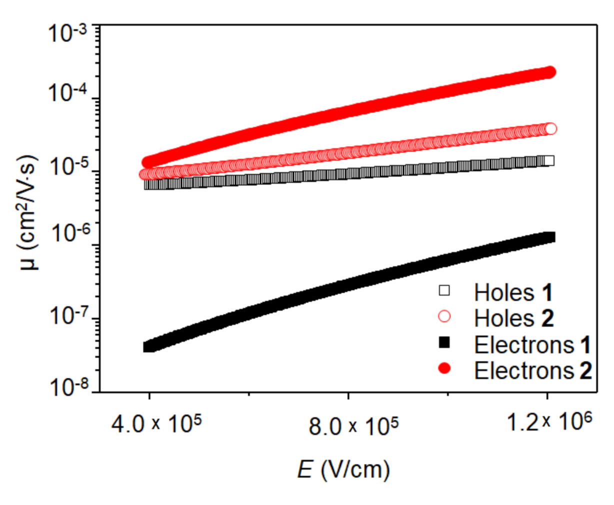

Figure 7: Charge carrier mobility as a function of the applied electric field obtained for the hole-only and electron-only devices of compounds **1** and **2**.

cartesian coordinates of the optimized isopropyl derivatives geometry are presented in Supporting Information File 1.

Conclusion

The electron and hole-transporting characteristics of two columnar liquid crystals were evaluated with electron-only and hole-only devices. Compound **1** is a perylene-based molecule presenting a columnar hexagonal mesophase stable at room temperature, and compound **2** is pyrene-based crystalline with columnar rectangular order preserved at room temperature. Photoluminescence lifetime measurements indicated that molecular aggregation and π-stacking interactions dominate the photophysics of films. While **1** presents majority hole transport, **2** is moderately ambipolar. The electron transport of **2** is around two orders of magnitude higher than **1**, which can be associated to the larger conjugation of **2**. This work highlights the potential of pyrene-based columnar liquid crystals as electron-transporting materials.

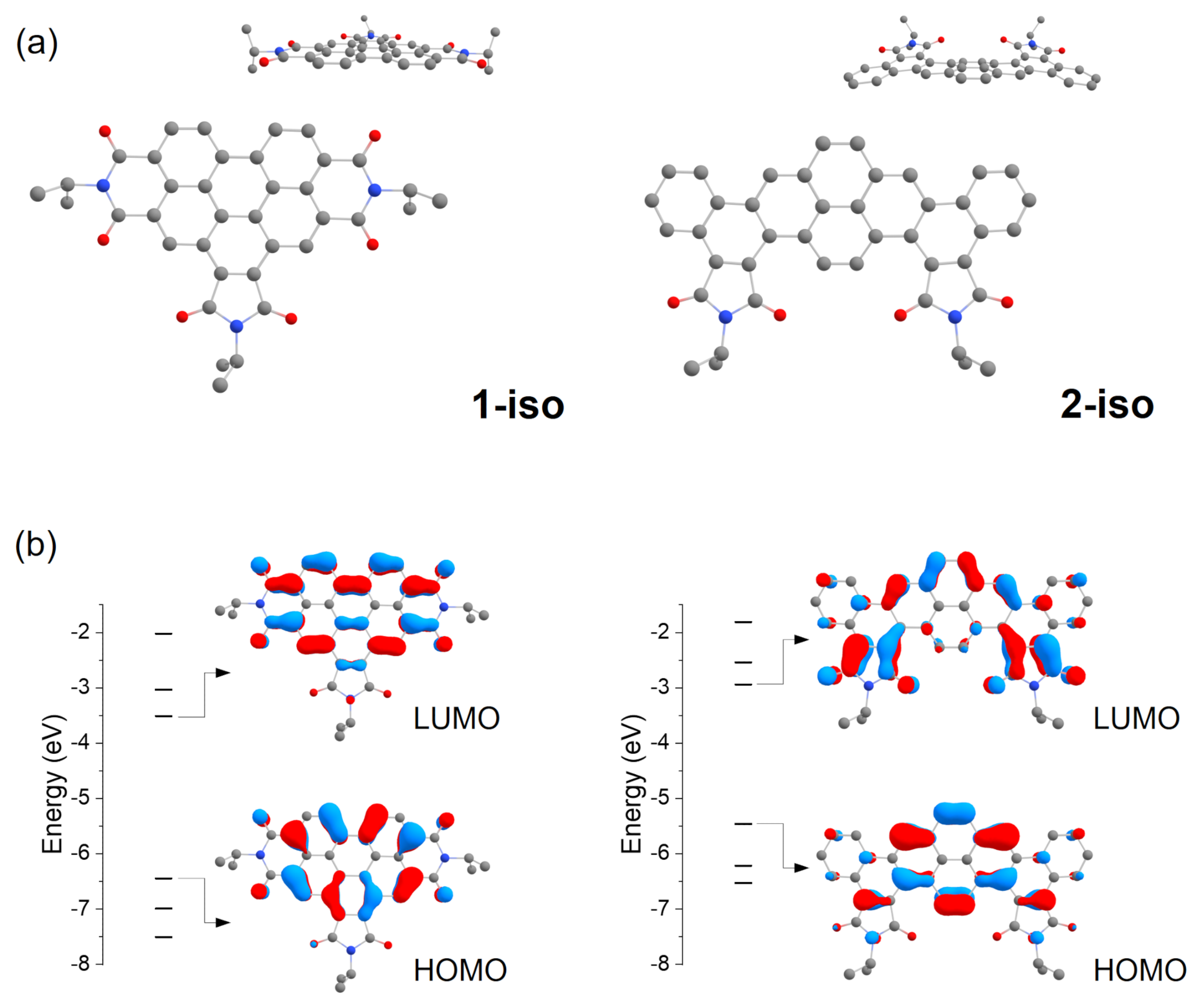

Figure 8: Ground state geometry (a) of compounds **1-iso** and **2-iso** obtained within B3LYP/def-TZVP(-f) level of theory and their frontier orbitals (b).

Experimental

Raman spectra were obtained in an Anton Paar spectrometer, Cora 5001 model, under an excitation laser line at 785 nm and 450 mW power source. The exposure time was around 160 ms and 1 accumulation. The sample powder was placed in a glass slide under the objective lens and performed the autofocus.

XRD measurements were performed with an X'Pert PRO (PANalytical) diffractometer using Cu Kα radiation (λ = 1.5418 Å) equipped with an X'Celerator detector. A small amount of **1** or **2** was deposited onto a glass substrate and heated to the isotropic liquid phase. The diffracted radiation was collected in continuous mode from 2° to 30° (2θ angle) at specific temperatures during the cooling down to room temperature. The temperature was controlled with a TCU2000-temperature control unit (Anton Paar).

The absorbance spectra in solution and in spin-coated films were collected with an Ocean Optics USB4000 spectrophotometer. The PL spectra were collected with a Hitachi fluorescence spectrophotometer (Model F-7000) and the samples were excited at the wavelength of maximal absorption. For the PL as a function of the temperature, casting films were placed on a hot stage (Mettler Toledo FP-82) and excited with a UV lamp of 365 nm wavelength. The emission spectra were captured using an optical fiber placed close to the film to guide the light until the Ocean Optics USB4000 spectrophotometer.

Time-resolved fluorescence decay curves were recorded using the technique of time-correlated single photon counting [39] with a FluoTime 200 (PicoQuant). Excitation was provided using a 401 nm pulsed diode laser with repetition rates varying from 5.0 to 20 MHz. Fluorescence was collected perpendicular to excitation and passed through a polarizer set at the magic angle. The detection system consisted of a monochromator and a multichannel bases photomultiplier (Hamamatsu R3809U-50). Lifetimes were obtained by fitting the fluorescence decay curves with exponential functions using FluoFit® software and the plots of weighted residuals and reduced chi-square were used to determine the best fits during the analysis procedure.

AFM measurements of the organic films were performed using a Nanosurf EasyScan2 apparatus in tapping mode with a scanning rate of 1.0 Hz covering 512 × 512 lines.

Hole-only devices were fabricated using indium tin oxide (ITO) coated glass plates (sheet resistance of about 15 Ω/sq) with a thin layer of PEDOT:PSS (purchased from Sigma-Aldrich) deposited by spin coating at 3000 rpm during 30 s, followed by annealing at 110 °C for 5 min as anodic electrode. For the electron-only devices, the anodic electrode consisted of a 100 nm thick Al layer vacuum deposited onto a glass substrate, 10^{-7} mbar at a rate of 2 Å/s. Compounds **1** and **2** were spin-coated from chloroform solutions (10 mg/mL) at 2000 rpm for 30 s, followed by annealing at 40 °C for 10 min. The top electrodes were vacuum deposited (10^{-7} mbar at a rate of 2 Å/s, 100 nm) onto the **1** and **2** layers, Au (for hole-only) and Al (for electron-only). The active area of the devices was 8 mm^2. The *J–V* curves were measured at room temperature (25 °C) inside a glove box under nitrogen atmosphere using Keithley's Series 2400 Source Measure Unit (SMU) instruments.

Ground state geometries of the molecules were optimized in a vacuum, using the Orca 5.0.3 [40] software package within B3LYP/Def2-TZVP(-f) level of theory [41-45]. Dispersion effects were included using Grimme's D3 correction with Becke-Johnson (BJ) damping [45,46]. The evaluation of the four-center integrals was accelerated with the RIJCOSX algorithm [47,48]. RIJ requires the specification of an auxiliary basis set for the Coulomb part (Def2/J) and a numerical integration grid for the exchange part (DefGrid-2) [49]. Analytical harmonic vibrational frequency calculations were conducted to verify if the ground state is a minimum on the potential energy surface. Images of the complex geometries were obtained using the Chemcraft program (http://www.chemcraftprog.com).

Supporting Information

Supporting Information File 1

Additional data and information.
[https://www.beilstein-journals.org/bjoc/content/supplementary/1860-5397-19-128-S1.pdf]

Acknowledgements

The XRD experiments were carried out in the Laboratório de Difração de Raios X (LDRX/UFSC).

Funding

We are grateful to INCT/INEO, CNPq, FAPESC, FAPEMIG, H2020-MSCA-RISE-2017 (OCTA, #778158), CAPES (Coordenação de aperfeiçoamento de pessoal de nível superior, Brazil. Finance code #937- 20 and #001) and COFECUB (Comité français d'évaluation de la coopération universitaire et scientifique avec le Brésil) (joint project Ph-C 962/20) for support.

ORCID® iDs

Alessandro L. Alves - https://orcid.org/0000-0002-5523-2007
Simone V. Bernardino - https://orcid.org/0000-0002-7379-0109
Carlos H. Stadtlober - https://orcid.org/0009-0005-6754-5165

Sergio F. Curcio - https://orcid.org/0000-0002-4209-7571
Thiago Cazati - https://orcid.org/0000-0002-3769-9658
Marta E. R. Dotto - https://orcid.org/0000-0001-9605-8087
Juliana Eccher - https://orcid.org/0000-0002-1878-4451
Leonardo N. Furini - https://orcid.org/0000-0002-8270-1227
Ivan H. Bechtold - https://orcid.org/0000-0001-6393-7245

References

1. Mutier, M. N.; Al-Badry, L. F. *Chin. J. Phys. (Amsterdam, Neth.)* **2020,** *63,* 365–374. doi:10.1016/j.cjph.2019.11.025
2. Eccher, J.; Almeida, A. C. B.; Cazati, T.; von Seggern, H.; Bock, H.; Bechtold, I. H. *J. Lumin.* **2016,** *180,* 31–37. doi:10.1016/j.jlumin.2016.08.012
3. Jing, T. *Sci. Insights* **2022,** *41,* 619–624. doi:10.15354/si.22.re075
4. Vishwakarma, V. K.; Roy, M.; Singh, R.; Shankar Rao, D. S.; Paily, R.; Ammathnadu Sudhakar, A. *ACS Appl. Electron. Mater.* **2023,** *5,* 2351–2364. doi:10.1021/acsaelm.3c00179
5. Cornil, J.; Lemaur, V.; Calbert, J.-P.; Brédas, J.-L. *Adv. Mater. (Weinheim, Ger.)* **2002,** *14,* 726–729. doi:10.1002/1521-4095(20020517)14:10<726::aid-adma726>3.0.co;2-d
6. Anthony, J. E.; Facchetti, A.; Heeney, M.; Marder, S. R.; Zhan, X. *Adv. Mater. (Weinheim, Ger.)* **2010,** *22,* 3876–3892. doi:10.1002/adma.200903628
7. Irla, S.; Pruthvi, M.; Raghunathan, V. A.; Kumar, S. *Dyes Pigm.* **2021,** *194,* 109574. doi:10.1016/j.dyepig.2021.109574
8. Adam, D.; Schuhmacher, P.; Simmerer, J.; Häussling, L.; Siemensmeyer, K.; Etzbachi, K. H.; Ringsdorf, H.; Haarer, D. *Nature* **1994,** *371,* 141–143. doi:10.1038/371141a0
9. O'Neill, M.; Kelly, S. M. *Adv. Mater. (Weinheim, Ger.)* **2003,** *15,* 1135–1146. doi:10.1002/adma.200300009
10. Hanna, J. *Opto-Electron. Rev.* **2005,** *13,* 259–267.
11. Pisula, W.; Zorn, M.; Chang, J. Y.; Müllen, K.; Zentel, R. *Macromol. Rapid Commun.* **2009,** *30,* 1179–1202. doi:10.1002/marc.200900251
12. Bushby, R. J.; Kawata, K. *Liq. Cryst.* **2011,** *38,* 1415–1426. doi:10.1080/02678292.2011.603262
13. O'Neill, M.; Kelly, S. M. *Adv. Mater. (Weinheim, Ger.)* **2011,** *23,* 566–584. doi:10.1002/adma.201002884
14. Kaafarani, B. R. *Chem. Mater.* **2011,** *23,* 378–396. doi:10.1021/cm102117c
15. Ruiz, C.; García-Frutos, E. M.; Hennrich, G.; Gómez-Lor, B. *J. Phys. Chem. Lett.* **2012,** *3,* 1428–1436. doi:10.1021/jz300251u
16. Rani, S.; Prasad Gupta, S.; Gupta, M.; Kumar Pal, S. *J. Mol. Liq.* **2023,** *385,* 122202. doi:10.1016/j.molliq.2023.122202
17. Fan, Y.; Wu, F.; Liu, F.; Han, M.; Chang, K.; Zhu, L.; Li, Q.; Li, Z. *J. Mater. Chem. C* **2022,** *10,* 2544–2550. doi:10.1039/d1tc04176b
18. Tong, J.; Jiang, X.; Dong, Z.; An, L.; Guo, P.; Yang, C.; Liang, Z.; Li, J.; Xia, Y. *Dyes Pigm.* **2023,** *208,* 110816. doi:10.1016/j.dyepig.2022.110816
19. Yao, J.; Chen, Q.; Zhang, C.; Zhang, Z.-G.; Li, Y. *SusMat* **2022,** *2,* 243–263. doi:10.1002/sus2.50
20. Xiao, J.; Yu, H.-J.; Xie, D.-X.; Shinohara, A.; Fan, T.; Yi, J.; Lai, J. Y. L.; Shao, G.; Yan, H. *Sustainable Energy Fuels* **2023,** *7,* 294–299. doi:10.1039/d2se01218a
21. Zhao, Y.; Yu, Y.; Zhao, X.; Zhao, Y.; Guo, Z.; Zhang, H.; Yao, R.; Ji, X.; Wang, D. *Molecules* **2022,** *27,* 7559. doi:10.3390/molecules27217559
22. Zych, D.; Slodek, A.; Krzyżanowski, N. *J. Mol. Struct.* **2022,** *1269,* 133797. doi:10.1016/j.molstruc.2022.133797
23. Pathiranage, T. M. S. K.; Ma, Z.; Udamulle Gedara, C. M.; Pan, X.; Lee, Y.; Gomez, E. D.; Biewer, M. C.; Matyjaszewski, K.; Stefan, M. C. *ACS Omega* **2021,** *6,* 27325–27334. doi:10.1021/acsomega.1c04176
24. Figueira-Duarte, T. M.; Müllen, K. *Chem. Rev.* **2011,** *111,* 7260–7314. doi:10.1021/cr100428a
25. Kelber, J.; Achard, M.-F.; Garreau-de Bonneval, B.; Bock, H. *Chem. – Eur. J.* **2011,** *17,* 8145–8155. doi:10.1002/chem.201100939
26. Girotto, E.; Ferreira, M.; Sarkar, P.; Bentaleb, A.; Hillard, E. A.; Gallardo, H.; Durola, F.; Bock, H. *Chem. – Eur. J.* **2015,** *21,* 7603–7610. doi:10.1002/chem.201500048
27. Rodríguez-llorente, S.; Aroca, R.; Duff, J. *J. Mater. Chem.* **1998,** *8,* 629–632. doi:10.1039/a707268f
28. Antunes, P. A.; Constantino, C. J. L.; Aroca, R.; Duff, J. *Appl. Spectrosc.* **2001,** *55,* 1341–1346. doi:10.1366/0003702011953450
29. Fernandes, J. D.; Alessio, P.; Silva, M. R. M.; Aroca, R. F.; de Souza, A. E.; Constantino, C. J. L. *Mater. Res. (Sao Carlos, Braz.)* **2017,** *20,* 882–890. doi:10.1590/1980-5373-mr-2016-0692
30. Aroca, R. F.; Constantino, C. J. L.; Duff, J. *Appl. Spectrosc.* **2000,** *54,* 1120–1125. doi:10.1366/0003702001950913
31. Laschat, S.; Baro, A.; Steinke, N.; Giesselmann, F.; Hägele, C.; Scalia, G.; Judele, R.; Kapatsina, E.; Sauer, S.; Schreivogel, A.; Tosoni, M. *Angew. Chem., Int. Ed.* **2007,** *46,* 4832–4887. doi:10.1002/anie.200604203
32. Benning, S.; Kitzerow, H.-S.; Bock, H.; Achard, M.-F. *Liq. Cryst.* **2000,** *27,* 901–906. doi:10.1080/02678290050043842
33. Eccher, J.; Faria, G. C.; Bock, H.; von Seggern, H.; Bechtold, I. H. *ACS Appl. Mater. Interfaces* **2013,** *5,* 11935–11943. doi:10.1021/am403681q
34. Margulies, E. A.; Shoer, L. E.; Eaton, S. W.; Wasielewski, M. R. *Phys. Chem. Chem. Phys.* **2014,** *16,* 23735–23742. doi:10.1039/c4cp03107e
35. Son, M.; Park, K. H.; Shao, C.; Würthner, F.; Kim, D. *J. Phys. Chem. Lett.* **2014,** *5,* 3601–3607. doi:10.1021/jz501953a
36. Apostol, P.; Eccher, J.; Dotto, M. E. R.; Costa, C. B.; Cazati, T.; Hillard, E. A.; Bock, H.; Bechtold, I. H. *Phys. Chem. Chem. Phys.* **2015,** *17,* 32390–32397. doi:10.1039/c5cp05582b
37. Solomon, G. C.; Andrews, D. Q.; Van Duyne, R. P.; Ratner, M. A. *ChemPhysChem* **2009,** *10,* 257–264. doi:10.1002/cphc.200800591
38. Shen, P.; Liu, H.; Zhuang, Z.; Zeng, J.; Zhao, Z.; Tang, B. Z. *Adv. Sci.* **2022,** *9,* 2200374. doi:10.1002/advs.202200374
39. O'Connor, D. V.; Phillips, D. *Time-Correlated Single Photon Counting,* 1st ed.; Academic Press: London, UK, 1984.
40. Neese, F. *Wiley Interdiscip. Rev.: Comput. Mol. Sci.* **2022,** *12,* e1606. doi:10.1002/wcms.1606
41. Becke, A. D. *Phys. Rev. A* **1988,** *38,* 3098–3100. doi:10.1103/physreva.38.3098
42. Lee, C.; Yang, W.; Parr, R. G. *Phys. Rev. B* **1988,** *37,* 785–789. doi:10.1103/physrevb.37.785
43. Weigend, F.; Ahlrichs, R. *Phys. Chem. Chem. Phys.* **2005,** *7,* 3297–3305. doi:10.1039/b508541a
44. Schäfer, A.; Huber, C.; Ahlrichs, R. *J. Chem. Phys.* **1994,** *100,* 5829–5835. doi:10.1063/1.467146
45. Pantazis, D. A.; Chen, X.-Y.; Landis, C. R.; Neese, F. *J. Chem. Theory Comput.* **2008,** *4,* 908–919. doi:10.1021/ct800047t
46. Grimme, S.; Ehrlich, S.; Goerigk, L. *J. Comput. Chem.* **2011,** *32,* 1456–1465. doi:10.1002/jcc.21759
47. Izsák, R.; Neese, F. *J. Chem. Phys.* **2011,** *135,* 144105. doi:10.1063/1.3646921

48. Izsák, R.; Neese, F.; Klopper, W. *J. Chem. Phys.* **2013,** *139,* 094111. doi:10.1063/1.4819264
49. Helmich-Paris, B.; de Souza, B.; Neese, F.; Izsák, R. *J. Chem. Phys.* **2021,** *155,* 104109. doi:10.1063/5.0058766

License and Terms

The definitive version of this article is the electronic one which can be found at:
https://doi.org/10.3762/bjoc.19.128

BEILSTEIN JOURNAL OF ORGANIC CHEMISTRY

Thienothiophene-based organic light-emitting diode: synthesis, photophysical properties and application

Recep Isci[1] and Turan Ozturk*[1,2]

Full Research Paper

Open Access

Address:
[1]Department of Chemistry, Istanbul Technical University, 34469, Maslak, Istanbul, Turkey and [2]TUBITAK UME, Chemistry Group Laboratories, 41470, Gebze, Kocaeli, Turkey

Email:
Turan Ozturk* - ozturktur@itu.edu.tr

* Corresponding author

Keywords:
OLED; organoboron; solution processes; thienothiophene; triphenylamine

Beilstein J. Org. Chem. **2023,** *19,* 1849–1857.
https://doi.org/10.3762/bjoc.19.137

Received: 07 July 2023
Accepted: 28 November 2023
Published: 07 December 2023

This article is part of the thematic issue "Organic electron transport materials".

Associate Editor: P. J. Skabara

Abstract

A donor–π–acceptor (D–π–A)-type pull–push compound, DMB-TT-TPA (**8**), comprising triphenylamine as donor and dimesitylboron as acceptor linked through a thieno[3,2-*b*]thiophene (TT) π-conjugated linker bearing a 4-MeOPh group, was designed, synthesized, and fabricated as an emitter via a solution process for an organic light-emitting diode (OLED) application. DMB-TT-TPA (**8**) exhibited absorption and emission maxima of 411 and 520 nm, respectively, with a mega Stokes shift of 109 nm and fluorescence quantum yields both in the solid state (41%) and in solution (86%). The optical properties were supported by computational chemistry using density functional theory for optimized geometry and absorption. A solution-processed OLED was fabricated using low turn-on voltage, which had performances with maximum power, current, and external quantum efficiencies of 6.70 lm/W, 10.6 cd/A, and 4.61%, respectively.

Introduction

In recent years, organic electronics have become very attractive due to their various advantages such as high flexibility, easy designability, low fabrication cost, easy processing and large-scale fabrication [1-4]. Especially in display technology, organic-based materials have found use in many applications such as OLEDs, micro-LEDs, LCDs, lasers, and photodiodes by applying thin film methods and solution processes [5-8]. The performance of organic electronics is based on the active layer composition as well as the fabrication methods and processing parameters. The organic active layers are composed of various aromatic π-conjugated small molecules/polymers including thiophene, anthracene, carbazole, and triphenylamine [9-13].

Thienothiophenes are two annulated thiophene rings having four isomers, among which the most widely used isomer is thieno[3,2-*b*]thiophene (TT) [14-19]. These compounds are electron-rich, flat and electron-delocalized systems, properties that make them promising materials for the construction of conjugated energy-based semiconductors for OLEDs [20-23], perovskite solar cells [24,25], organic field-effect transistors (OFETs) [26-28], capacitors [29,30], hybrid films [31], and photosensitizers [32-34]. Another important π-conjugated unit is triphenylamine (TPA), having an ionization potential of 6.80 eV, which is lower compared to many other organic cores, thus providing a strong electron-donating ability for organic electronic applications [12,35]. Dimesitylboron (DMB), with its unoccupied p-orbital, is an electron-acceptor organoboron compound used in several donor–acceptor systems to provide the system with pull–push interaction [36,37].

In this work, we have designed and synthesized a D–π–A model pull–push fluorophore, DMB-TT-TPA (**8**), having TPA and DMB units as donor and acceptor units that were linked through a 4-MeOPh-substituted TT core as a π-spacer. The photophysical properties of the fluorophore were investigated by spectroscopic methods. Moreover, DMB-TT-TPA (**8**) was fabricated as an emitter for an organic light-emitting diode through a solution process. DMB-TT-TPA (**8**) displayed excellent performance in both device application and photophysical properties, i.e., a maximum solution fluorescence quantum yield of 86% in THF, maximum solid-state fluorescence quantum yield of 41%, maximum current efficiency of 10.6 cd/A, and maximum power efficiency of 6.70 lm/W.

Results and Discussion

Design and synthesis

The OLED fluorophore, DMB-TT-TPA (**8**, Scheme 1), having a donor–π–acceptor (D–π–A) system, was synthesized according

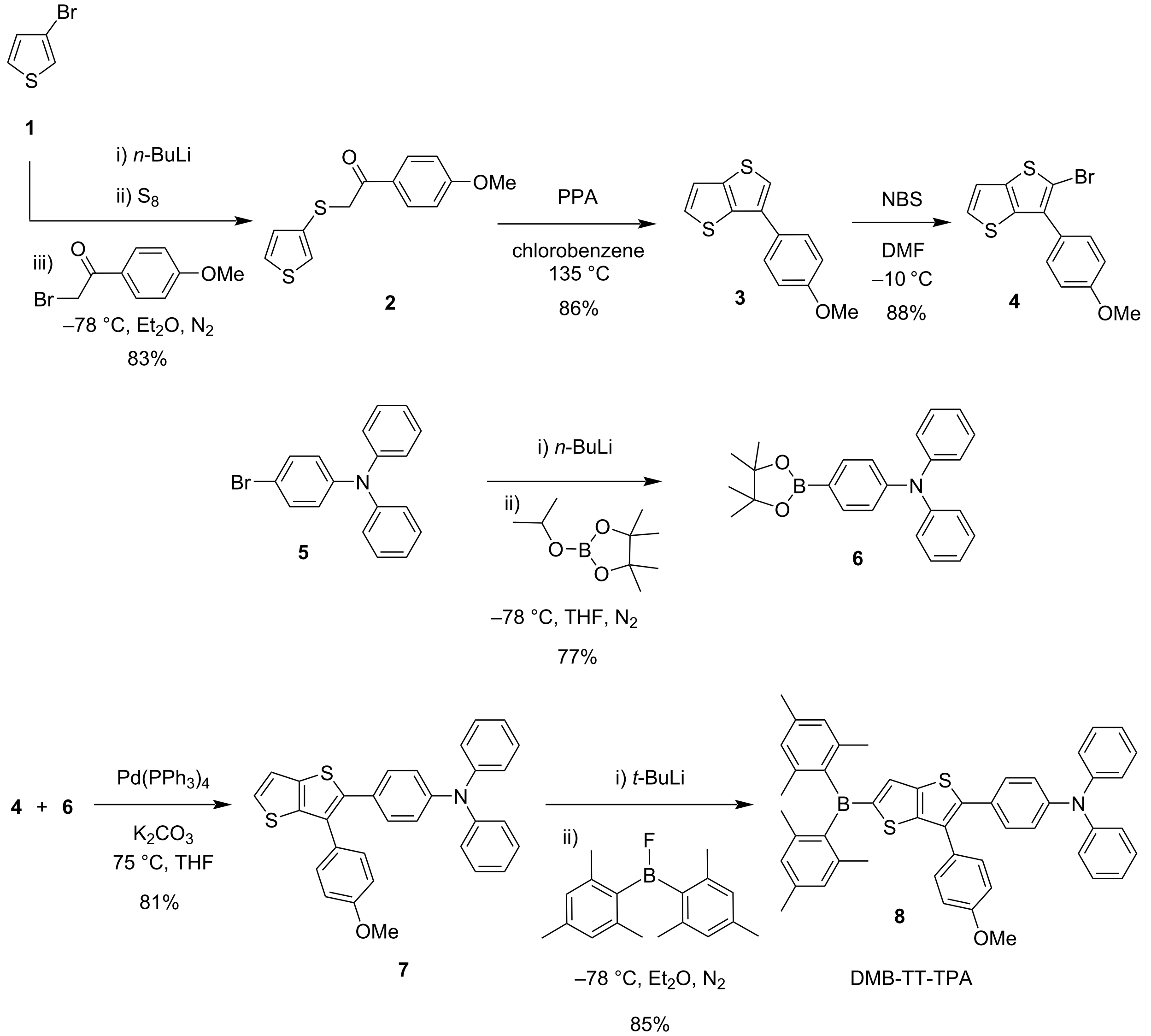

Scheme 1: Synthesis of DMB-TT-TPA (**8**).

to our previously reported methods [20-23,36,38]. The synthesis commenced with the treatment of 3-bromothiophene (**1**) with *n*-butyllithium at −78 °C, followed by the addition of elemental sulfur and subsequent reaction with 2-bromo-1-(4-methoxyphenyl)ethanone to produce compound **2** in 83% yield. The following ring-closure reaction was conducted in the presence of polyphosphoric acid (PPA) in refluxing chlorobenzene to give **3** (TT) in 86% yield. The brominated TT **4** was obtained through selective monobromination of compound **3** using NBS at −10 °C in DMF in 88% yield. The boronated triphenylamine **6** was constructed in a one-pot two-step reaction in 77% yield, by lithiation of 4-bromo-*N*,*N*-diphenylaniline (**5**) with *n*-butyllithium at −78 °C and addition of 2-isopropoxy-4,4,5,5-tetramethyl-1,3,2-dioxaborolane. The Suzuki-coupling reaction of TT **4** with borolane **6** produced the intermediate **7** in 81% yield. The target D–π–A-type fluorophore, DMB-TT-TPA (**8**), was produced by lithiation of **7** and following reaction with dimesitylboron fluoride in 85% yield (Scheme 1).

Photophysical properties

The UV–vis absorption and fluorescence spectra of DMB-TT-TPA (**8**) were recorded in THF (Figure 1 and Table 1) [38]. It showed maximum absorption and emission wavelengths of 411 and 520 nm (excitation at λ_{max}), respectively, leading to a mega Stokes shift (>100 nm) of 109 nm, which could be explained to be due to a fast relaxation from the excited state to the ground state as a result of a powerful intramolecular energy transfer between the TPA and boron groups through the thieno[3,2-*b*]thiophene (TT) core. The optical band gap (E_{optic}) of DMB-TT-TPA (**8**) was calculated to be 2.52 eV from the onset wavelength of the absorption spectrum at 491 nm. The compound demonstrates high quantum efficiencies in the solid-state and in solution (THF) of 41 and 86%, respectively. The considerable quantum efficiencies pointed out that DMB-TT-TPA (**8**) is among the best D–π–A modal fluorophores suitable for an OLED application. Moreover, the photophysical properties of DMB-TT-TPA (**8**) were investigated through time-resolved fluorescence studies (390 nm laser source in THF). The fluorescence lifetime (τ) of DMB-TT-TPA (**8**) exhibited a mono-exponential profile having a 3.20 ns fluorescence decay pattern (Figure S1 in Supporting Information File 1), demonstrating a strong pull–push interaction in steady-state time resolved fluorescence performance.

OLED application

An OLED was fabricated using a standard conventional device architecture of ITO/PEDOT:PSS/TFB/TAPC:TCTA:emitter

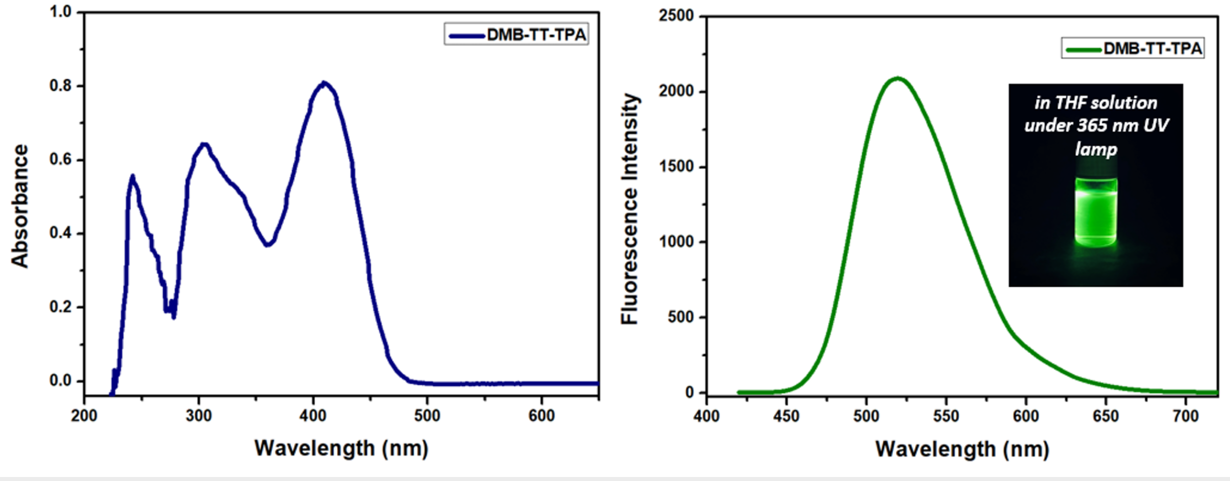

Figure 1: Absorption and emission of DMB-TT-TPA (**8**) in THF. Figure 1 was adapted with permission of Institution of Chemical Engineers (IChemE) and The Royal Society of Chemistry from [38] ("Cationic and radical polymerization using a boron–thienothiophene–triphenylamine based D-π-A type photosensitizer under white LED irradiation") by A. Suerkan et al., Mol. Syst. Des. Eng., vol. 8, issue 10, © 2023); permission conveyed through Copyright Clearance Center, Inc. This content is not subject to CC BY 4.0.

Table 1: Photophysical data of DMB-TT-TPA (**8**) [38].

Compound	$UV_{max}{}^{a}$ (nm)	UV_{onset} (nm)	$Fl_{max}{}^{a}$ (nm)	Δv^{b} (cm^{-1})	$E_{optic}{}^{c}$ (eV)	$\Phi_{solid}{}^{d}$ (%)	$\Phi_{sol}{}^{e}$ (%)
DMB-TT-TPA	411	491	520	5100	2.52	41	86

[a] Absorption and fluorescence maxima in THF. [b] Stokes shift (cm^{-1}) $\Delta v = 1/\lambda_{max} - 1/\lambda_{em}$. [c] E_{optic} from the onset of the absorption spectrum. [d] Solid-state quantum yield. [e] Solution-state quantum yield in THF.

(DMB-TT-TPA (**8**))/TPBi/LiF/Ca/Ag, where TFB, TCTA/TAPC, and TPBi acted as hole transport, hole transporting host, and electron transport materials, respectively (Figure S2 in Supporting Information File 1). The current efficiency–luminance–voltage (J–L–V) graph and power efficiency (PE), external quantum efficiency (EQE), and electroluminescence curves are depicted in Figure 2 and Figure 3, respectively. Although DMB-TT-TPA (**8**) was synthesized and OLED performance was examined in our previous study [23], a different device architecture and method, i.e., solution processing, was used in this study. In the previous study, the OLED of DMB-TT-TPA (**8**) was explained to demonstrate performance with the turn-on voltage, external quantum efficiency (EQE), and highest luminescence efficiency of 4.6 V, 0.15% and 0.40 cd/A, respectively, using a thermal evaporation method. On the other hand, in this study, the OLED of DMB-TT-TPA (**8**), prepared using a solution processing method, showed a low turn-on voltage (V_{on}) of 2.90 V, a max current efficiency (CE_{max}) of 10.6 cd/A, a max luminance of 752 cd/m^2, a max power efficiency (PE_{max}) of 6.70 lm/W, and an external quantum efficiency (EQE) of 4.61%, along with a green emitting luminescence at 512 nm (Table 2). According to the CIE color space chromaticity diagram, the device was located at the coordinates of 0.16 and 0.51. The obtained EL results are in good agreement with the fluorescence characteristic of DMB-TT-TPA (**8**). Additionally, OLED performances were significantly increased compared to the previous study [23]. In terms of the TT chemistry, the device results reached remarkable values for donor–π–acceptor-type solution processable emitters within the donor–acceptor family [39-42]. This approach also supports that the solution-processable OLED application is a perfectly suitable device preparation for DMB-TT-TPA (**8**).

Thermal properties

The thermal properties of DMB-TT-TPA (**8**) were investigated through thermal gravimetric analysis (TGA) at 750 °C at a heating rate of 10 °C min^{-1} under N_2 atmosphere (Figure 4). The initial mass loss (5%) around 120 °C could be due to residual water and/or solvent. The highest decomposition was observed at around 405 °C and 14% of DMB-TT-TPA (**8**)

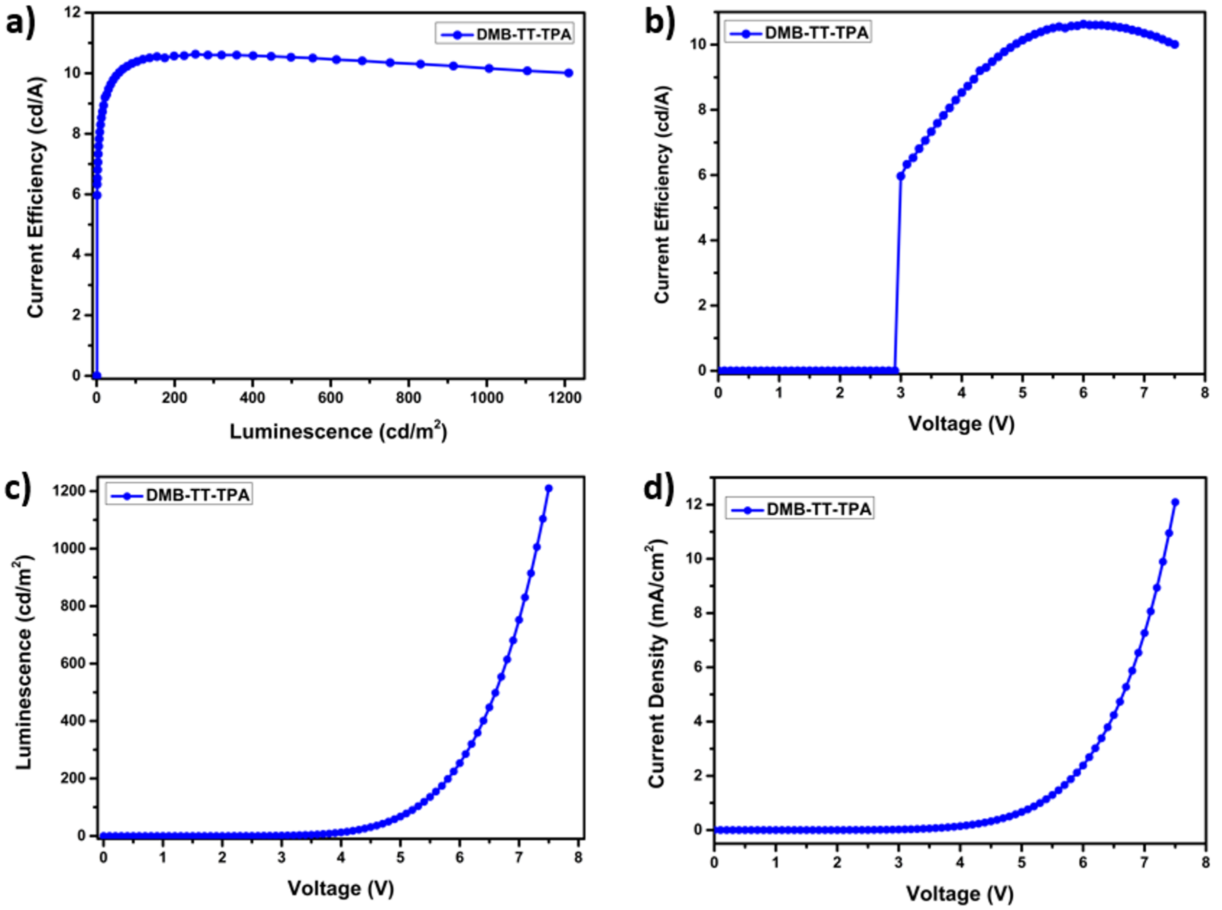

Figure 2: (a) Current efficiency–luminance, (b) current efficiency–voltage, (c) luminance–voltage, and (d) current density–voltage characteristics of DMB-TT-TPA (**8**).

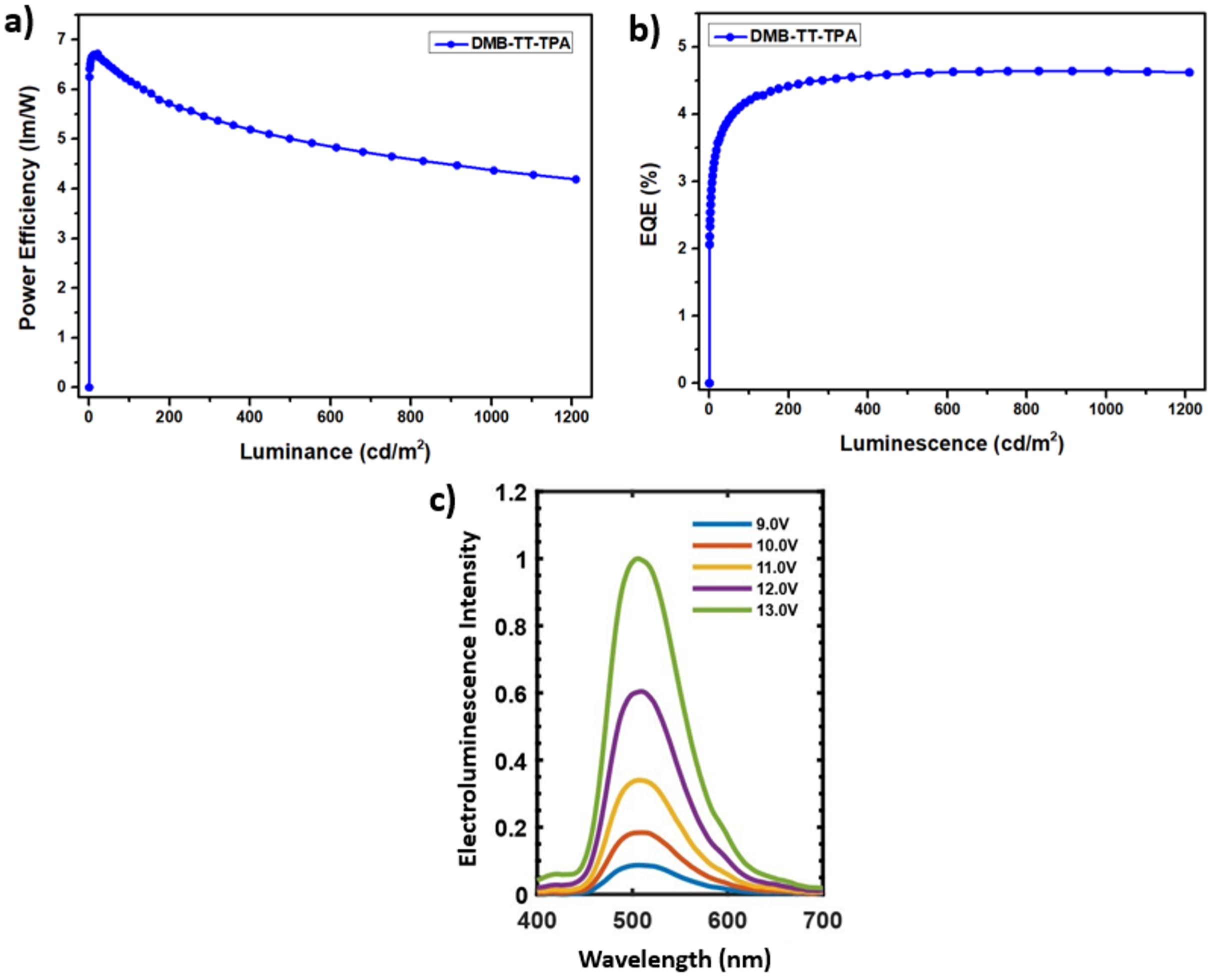

Figure 3: (a) Power efficiency–luminance, (b) external quantum efficiency–luminescence, (c) electroluminescence–wavelength characteristics of DMB-TT-TPA (**8**).

Table 2: Photophysical data of DMB-TT-TPA (**8**).

compound	V_{on}[a] (V)	CE[b] (cd/A)	L[c] (cd/m^2)	λ_{EL}[d] (nm)	EQE[e] (%)	PE_{max}[f] (lm/W)	CIE[g] (x, y)
DMB-TT-TPA	2.9	10.6	752	512	4.61	6.70	(0.16, 0.51)

[a]Turn-on voltage, recorded at the luminance of 1 cd·m^2. [b]Maximum current efficiency. [c]Maximum luminance. [e]Maximum electroluminescence wavelength. [d]Maximum current efficiency. [e]Maximum external quantum efficiency. [f]Maximum power efficiency. [g]Chromaticity coordinates according to the CIE 1931 diagram.

remained without ash up to 750 °C, indicating that the compound has an excellent thermal stability. The high thermal stability is profitable for the preparation of stable and durable OLED devices.

Computational chemistry

Ground-state geometry optimization of DMB-TT-TPA (**8**) was performed using density functional theory (DFT) calculations with the Gaussian 16 software at the B3LYP/6-31G (d,p) level (Figure S3 in Supporting Information File 1) [23,43]. The highest occupied molecular orbital (HOMO) and the lowest unoccupied molecular orbital (LUMO) energy levels were calculated to be −4.93 and −1.83 eV, respectively (Figure 5). While the HOMO electrons were distributed mainly on the triphenylamine and TT units, the LUMO was found to be delocalized through the dimesitylboron and TT ring, the results being in line with the experimental values of our previous study [23].

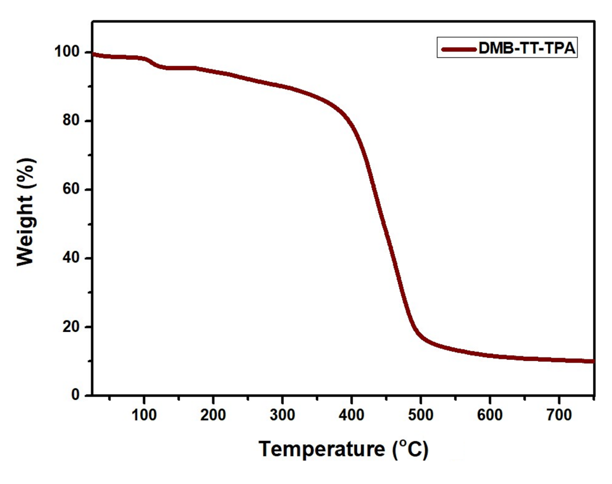

Figure 4: Thermal gravimetric analyses (TGA) of DMB-TT-TPA (**8**).

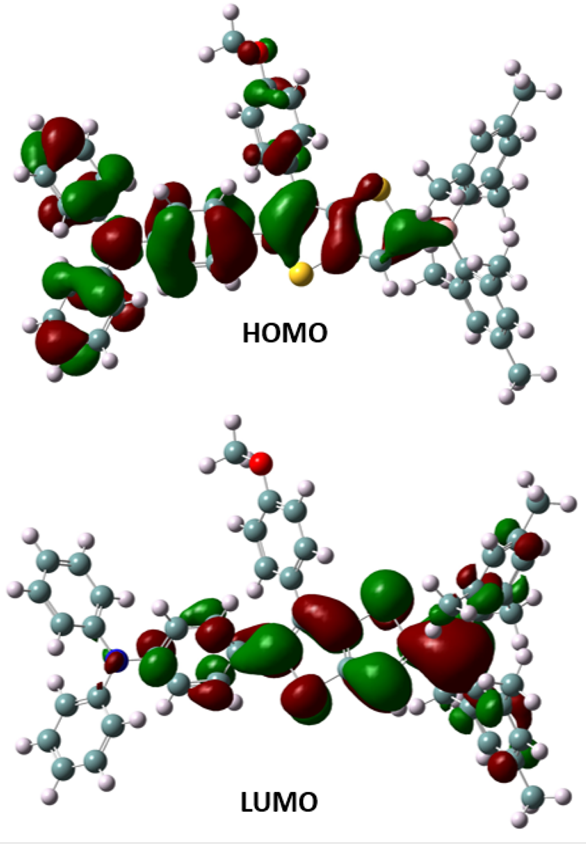

Figure 5: HOMO and LUMO diagrams calculated at the B3LYP/6-31G (d,p) level of theory.

On the basis of the optimized ground-state geometry, time-dependent DFT (TD-DFT) calculations were conducted in THF to investigate the absorption properties and theoretical band gap (Table 3). The optical band gap value (E_{optic}) was calculated to be 2.06 eV, considering the λ_{onset} (605 nm) of the UV–vis curve. The calculated absorption maximum was centered at 470 nm (Figure S4 in Supporting Information File 1), which was found to be in a good agreement with the experimentally determined UV–vis spectrum.

Conclusion

A small fluorophore molecule, DMB-TT-TPA (**8**), containing dimesitylboron as an acceptor and triphenylamine as a donor linked through a thieno[3,2-*b*]thiophene core having a 4-MeOPh group, was designed as a D–π–A model and synthesized in 85% yield. Its photophysical properties were investigated by UV–vis and fluorescence spectroscopy. The obtained experimental results were found to be in good agreement with computational investigations. An OLED fabrication, where DMB-TT-TPA (**8**) was employed as an emitter, showed a maximum luminescence efficiency of 752 cd/m^2, a maximum external quantum efficiency of 4.61%, a maximum power efficiency of 6.70 lm/W, and a maximum current efficiency of 10.6 cd/A on 2.9 V turn on voltage with CIE coordinates of 0.16 and 0.51 at λ_{EL} = 512 nm. The OLED, optical and thermal properties indicated that the composition of thienothiophene, triphenylamine, and boron is a highly suitable combination for fluorescent organic electronics in display technology.

Experimental

General methods

^{1}H and ^{13}C NMR spectra were recorded on a Varian model NMR spectrometer (500 and 126 MHz) and chemical shift values are reported in ppm downfield from tetramethylsilane (TMS). UV–vis absorption spectra were obtained using a HITACHI U-0080D spectrophotometer. Fluorescence spectra were recorded on a HITACHI F-4500 fluorescence spectrophotometer. Time-resolved fluorescence studies were performed on a Horiba, FL3-2IHR fluorescence spectrophotometer. Solid-state and solution-state quantum yields were measured using a Hamamatsu Quantaurus-QY Absolute PL Quantum Yield Spectrometer. Thermal gravimetric analysis (TGA) was performed on a PerkinElmer Diamond TA/TGA with a heating rate of 10 °C min^{-1} under nitrogen flow.

Table 3: The HOMO and LUMO energy levels and absorption values calculated by TD-B3LYP/6-31G (d,p) level of theory.

Compound	HOMO (eV)	LUMO (eV)	λ_{max} (nm)	λ_{onset} (nm)	E_{optic} (eV)
DMB-TT-TPA (**8**)	−4.93	−1.83	470	605	2.06

Materials

3-Bromothiophene (97%, Across), 2-bromo-4′-methoxyacetophenone (97% Merck), *N*-bromosuccinimide (Sigma-Aldrich), polyphosphoric acid (PPA, 115% H_3PO_4 basis, Sigma-Aldrich), *n*-butyllithium (2.5 M in hexanes, Sigma-Aldrich), sodium sulfate (Merck), 4-bromotriphenylamine (Sigma-Aldrich), dimesitylboronfluoride (90%, Sigma-Aldrich), 4,4,5,5-tetramethyl-1,3,2-dioxaborolane (Sigma-Aldrich), tetrakis(triphenylphosphine)palladium(0) ($Pd(PPh_3)_4$, 99%, Sigma-Aldrich), were used as received. Diethyl ether and THF were dried over metallic sodium. Dimethylformamide (HPLC grade) was stored over activated molecular sieves (4 Å). Dichloromethane (Aldrich), methanol (Merck), and sodium carbonate (Merck) were used as received. Compounds **2**–**6** were synthesized following our previous reports [20-23,44-47]. The characterization data of **7** and **8** are compatible with the published data in ref. [23].

Synthesis of **7**

Synthesized as described in [23]. To a mixture of thienothiophene **4** (250 mg, 0.770 mmol) and borolane **6** (320 mg, 0.845 mmol) dissolved in THF (25 mL) and degassed for 45 min with N_2 was added K_2CO_3 (2.5 mL, 2.5 M) and $Pd(PPh_3)_4$ (0.077 mmol). The mixture was then saturated with N_2, the reaction flask sealed and the mixture stirred at 75 °C for 48 h. Afterwards, the reaction mixture was filtered through celite eluting with CH_2Cl_2, extracted with CH_2Cl_2/water, and the organic phase was washed with sodium carbonate solution (10%) and water, dried over sodium sulfate, filtered, and the solvent was evaporated under reduced pressure. The crude product was purified by column chromatography eluting with *n*-hexane/CH_2Cl_2 4:1 to obtain the title compound **7** (300 mg, 81%) as a white powder. Mp 141–142 °C; ^1H NMR (500 MHz, $CDCl_3$) δ 7.42 (d, *J* = 8.8 Hz, 2H), 7.35 (d, *J* = 5.2 Hz, 1H), 7.28 (t, *J* = 8.7 Hz, 5H), 7.20 (d, *J* = 8.7 Hz, 2H), 7.13 (d, *J* = 7.6 Hz, 4H), 7.05 (t, *J* = 7.3 Hz, 2H), 6.95 (d, *J* = 8.7 Hz, 2H), 6.92 (d, *J* = 8.8 Hz, 2H), 3.86 (s, 3H); ^{13}C NMR (126 MHz, $CDCl_3$) δ 158.89, 147.36, 147.17, 142.04, 139.51, 135.73, 130.12, 129.87, 129.29, 128.34, 127.96, 125.86, 124.80, 123.24, 122.53, 119.81, 114.14, 55.22.

Synthesis of DMB-TT-TPA (**8**)

Synthesized as described in [23]. To a solution of compound **7** (200 mg, 0.410 mmol) in dry THF (50 mL) was added *tert*-butyllithium (0.3 mL, 1.7 M, 0.490 mmol) dropwise at −78 °C under a nitrogen atmosphere over a period of 45 min. Then, dimesitylborofluoride (130 mg, 0.490 mmol) was added rapidly. The mixture was further stirred at −78 °C for 1 h, then, allowed to warm to room temperature and stirring was continued overnight. The solution was extracted with dichloromethane, and the organic layer was washed with Na_2CO_3 solution (10%) and water. The organic layer was dried over Na_2SO_4, filtered and the solvent was evaporated under reduced pressure. The crude product was purified by flash column chromatography eluting with a mixture of *n*-hexane/CH_2Cl_2 3:1 and then crystallized from ethanol to give the title compound DMB-TT-TPA (**8**) as a yellow powder in 85% yield (256 mg). Mp 165–166 °C; ^1H NMR (500 MHz, $CDCl_3$) δ 7.59 (s, 1H), 7.39 (d, *J* = 8.8 Hz, 2H), 7.28 (d, *J* = 7.8 Hz, 4H), 7.19 (d, *J* = 8.7 Hz, 2H), 7.12 (d, *J* = 7.6 Hz, 4H), 7.05 (t, *J* = 7.3 Hz, 2H), 6.93 (d, *J* = 8.7 Hz, 2H), 6.87 (d, *J* = 8.8 Hz, 2H), 6.84 (s, 4H), 3.82 (s, 3H), 2.32 (s, 6H), 2.17 (s, 12H); ^{13}C NMR (126 MHz, $CDCl_3$) δ 158.92, 153.46, 151.26, 147.60, 147.20, 143.95, 141.05, 140.90, 138.50, 137.96, 132.59, 130.25, 129.86, 129.49, 129.33, 128.14, 127.85, 127.57, 125.01, 123.45, 122.08, 114.12, 55.23, 23.54, 21.22.

Supporting Information

Supporting Information File 1

General experimental device methods, life time spectra, theoretical computation data, ^1H and ^{13}C NMR spectra.
[https://www.beilstein-journals.org/bjoc/content/supplementary/1860-5397-19-137-S1.pdf]

Acknowledgements

The authors thank Dilara Gunturkun for DFT calculations, Istanbul Technical University (ITU).

Funding

The authors thank THD-2023-44904, PTA-2023-44900, TGA-2023-44077, TDA-2022-43696 numbered ITU BAP Projects and 122Z568 numbered TUBITAK 1001 Project and Unsped Global Lojistik, Turkey, for financial support. We also thank Higher Education Council of Turkey (YOK) and TUBITAK grants to Recep Isci (PhD, 100/2000 YOK, 2214A and 2211A BIDEP/TUBITAK) for financial support.

ORCID® iDs

Recep Isci - https://orcid.org/0000-0003-3086-4478
Turan Ozturk - https://orcid.org/0000-0003-3777-5320

Preprint

A non-peer-reviewed version of this article has been previously published as a preprint: https://doi.org/10.3762/bxiv.2023.28.v1

References

1. Tavasli, A.; Gurunlu, B.; Gunturkun, D.; Isci, R.; Faraji, S. *Electronics (Basel, Switz.)* **2022,** *11,* 316. doi:10.3390/electronics11030316

2. Chen, Z.; Huang, Y.; Gao, J.; Zhang, L.; Ma, Z.; Liu, M.; Emrick, T.; Liu, Y. *ACS Energy Lett.* **2022,** *7,* 4052–4060. doi:10.1021/acsenergylett.2c02153
3. M'Baye, G.; Klymchenko, A. S.; Yushchenko, D. A.; Shvadchak, V. V.; Ozturk, T.; Mély, Y.; Duportail, G. *Photochem. Photobiol. Sci.* **2007,** *6,* 71–76. doi:10.1039/b611699j
4. Takimiya, K.; Osaka, I.; Nakano, M. *Chem. Mater.* **2014,** *26,* 587–593. doi:10.1021/cm4021063
5. Monkman, A. *ACS Appl. Mater. Interfaces* **2022,** *14,* 20463–20467. doi:10.1021/acsami.1c09189
6. Yu, L.; Portale, G.; Stingelin, N. *J. Mater. Chem. C* **2021,** *9,* 10547–10556. doi:10.1039/d1tc01418h
7. Liu, X.; Lin, R.; Chen, H.; Zhang, S.; Qian, Z.; Zhou, G.; Chen, X.; Zhou, X.; Zheng, L.; Liu, R.; Tian, P. *ACS Photonics* **2019,** *6,* 3186–3195. doi:10.1021/acsphotonics.9b00799
8. Oyama, Y.; Mamada, M.; Shukla, A.; Moore, E. G.; Lo, S.-C.; Namdas, E. B.; Adachi, C. *ACS Mater. Lett.* **2020,** *2,* 161–167. doi:10.1021/acsmaterialslett.9b00536
9. Isci, R.; Rahimi Varzeghani, A.; Kaya, K.; Sütay, B.; Tekin, E.; Ozturk, T. *ACS Sustainable Chem. Eng.* **2022,** *10,* 1605–1615. doi:10.1021/acssuschemeng.1c07240
10. Jiang, H.; Tao, P.; Wong, W.-Y. *ACS Mater. Lett.* **2023,** *5,* 822–845. doi:10.1021/acsmaterialslett.2c01070
11. Tsai, M.-H.; Ke, T.-H.; Lin, H.-W.; Wu, C.-C.; Chiu, S.-F.; Fang, F.-C.; Liao, Y.-L.; Wong, K.-T.; Chen, Y.-H.; Wu, C.-I. *ACS Appl. Mater. Interfaces* **2009,** *1,* 567–574. doi:10.1021/am800124q
12. Wang, J.; Liu, K.; Ma, L.; Zhan, X. *Chem. Rev.* **2016,** *116,* 14675–14725. doi:10.1021/acs.chemrev.6b00432
13. Schipper, D. J.; Fagnou, K. *Chem. Mater.* **2011,** *23,* 1594–1600. doi:10.1021/cm103483q
14. Cinar, M. E.; Ozturk, T. *Chem. Rev.* **2015,** *115,* 3036–3140. doi:10.1021/cr500271a
15. Isci, R.; Unal, M.; Kucukcakir, G.; Gurbuz, N. A.; Gorkem, S. F.; Ozturk, T. *J. Phys. Chem. B* **2021,** *125,* 13309–13319. doi:10.1021/acs.jpcb.1c09448
16. Isci, R.; Gunturkun, D.; Yalin, A. S.; Ozturk, T. *J. Polym. Sci. (Hoboken, NJ, U. S.)* **2021,** *59,* 117–123. doi:10.1002/pol.20200635
17. Gunturkun, D.; Isci, R.; Sütay, B.; Majewski, L. A.; Faraji, S.; Ozturk, T. *Eur. Polym. J.* **2022,** *170,* 111167. doi:10.1016/j.eurpolymj.2022.111167
18. Ozturk, T.; Rice, C. R.; Wallis, J. D. *J. Mater. Chem.* **1995,** *5,* 1553–1556. doi:10.1039/jm9950501553
19. Schneider, J. A.; Dadvand, A.; Wen, W.; Perepichka, D. F. *Macromolecules* **2013,** *46,* 9231–9239. doi:10.1021/ma402018n
20. Isci, R.; Tekin, E.; Kaya, K.; Piravadili Mucur, S.; Gorkem, S. F.; Ozturk, T. *J. Mater. Chem. C* **2020,** *8,* 7908–7915. doi:10.1039/d0tc01715a
21. Isci, R.; Tekin, E.; Mucur, S. P.; Ozturk, T. *ChemistrySelect* **2020,** *5,* 13091–13098. doi:10.1002/slct.202003273
22. Isci, R.; Wan, L.; Topal, S.; Gunturkun, D.; Campbell, A. J.; Ozturk, T. *J. Mater. Chem. C* **2022,** *10,* 10719–10727. doi:10.1039/d2tc02371g
23. Turkoglu, G.; Cinar, M. E.; Buyruk, A.; Tekin, E.; Mucur, S. P.; Kaya, K.; Ozturk, T. *J. Mater. Chem. C* **2016,** *4,* 6045–6053. doi:10.1039/c6tc01285j
24. Isci, R.; Unal, M.; Yesil, T.; Ekici, A.; Sütay, B.; Zafer, C.; Ozturk, T. *Front. Mater.* **2023,** *10,* 1125462. doi:10.3389/fmats.2023.1125462
25. Chi, W.-J.; Zheng, D.-Y.; Chen, X.-F.; Li, Z.-S. *J. Mater. Chem. C* **2017,** *5,* 10055–10060. doi:10.1039/c7tc03232c
26. Ozturk, S. E.; Isci, R.; Faraji, S.; Sütay, B.; Majewski, L. A.; Ozturk, T. *Eur. Polym. J.* **2023,** *191,* 112028. doi:10.1016/j.eurpolymj.2023.112028
27. Amna, B.; Isci, R.; Siddiqi, H. M.; Majewski, L. A.; Faraji, S.; Ozturk, T. *J. Mater. Chem. C* **2022,** *10,* 8254–8265. doi:10.1039/d2tc01222g
28. Zhong, H.; Li, C.-Z.; Carpenter, J.; Ade, H.; Jen, A. K.-Y. *J. Am. Chem. Soc.* **2015,** *137,* 7616–7619. doi:10.1021/jacs.5b04209
29. Isci, R.; Balkan, T.; Tafazoli, S.; Sütay, B.; Eroglu, M. S.; Ozturk, T. *ACS Appl. Energy Mater.* **2022,** *5,* 13284–13292. doi:10.1021/acsaem.2c01830
30. Topal, S.; Isci, R.; Sezer, E.; Ozturk, T.; Ustamehmetoglu, B. *Electrochim. Acta* **2021,** *389,* 138688. doi:10.1016/j.electacta.2021.138688
31. Isci, R.; Baysak, E.; Kesan, G.; Minofar, B.; Eroglu, M. S.; Duygulu, O.; Gorkem, S. F.; Ozturk, T. *Nanoscale* **2022,** *14,* 16602–16610. doi:10.1039/d2nr04582f
32. Celiker, T.; Isci, R.; Kaya, K.; Ozturk, T.; Yagci, Y. *J. Polym. Sci. (Hoboken, NJ, U. S.)* **2020,** *58,* 2327–2334. doi:10.1002/pol.20200398
33. Kutahya, C.; Allushi, A.; Isci, R.; Kreutzer, J.; Ozturk, T.; Yilmaz, G.; Yagci, Y. *Macromolecules* **2017,** *50,* 6903–6910. doi:10.1021/acs.macromol.7b01335
34. Beyazit, S.; Aydogan, B.; Osken, I.; Ozturk, T.; Yagci, Y. *Polym. Chem.* **2011,** *2,* 1185–1189. doi:10.1039/c1py00019e
35. Farokhi, A.; Shahroosvand, H.; Monache, G. D.; Pilkington, M.; Nazeeruddin, M. K. *Chem. Soc. Rev.* **2022,** *51,* 5974–6064. doi:10.1039/d1cs01157j
36. Turkoglu, G.; Cinar, M. E.; Ozturk, T. *Eur. J. Org. Chem.* **2017,** 4552–4561. doi:10.1002/ejoc.201700679
37. Zhou, G.; Baumgarten, M.; Müllen, K. *J. Am. Chem. Soc.* **2008,** *130,* 12477–12484. doi:10.1021/ja803627x
38. Suerkan, A.; Isci, R.; Ozturk, T.; Yagci, Y. *Mol. Syst. Des. Eng.* **2023,** *8,* 1319–1326. doi:10.1039/d3me00083d
39. Sonar, P.; Soh, M. S.; Cheng, Y. H.; Henssler, J. T.; Sellinger, A. *Org. Lett.* **2010,** *12,* 3292–3295. doi:10.1021/ol1007179
40. Lee, H.; Karthik, D.; Lampande, R.; Ryu, J. H.; Kwon, J. H. *Front. Chem. (Lausanne, Switz.)* **2020,** *8,* 373. doi:10.3389/fchem.2020.00373
41. Xu, T.; Liang, X.; Xie, G. *Front. Chem. (Lausanne, Switz.)* **2021,** *9,* 691172. doi:10.3389/fchem.2021.691172
42. Fu, Q.; Chen, J.; Shi, C.; Ma, D. *ACS Appl. Mater. Interfaces* **2012,** *4,* 6579–6586. doi:10.1021/am301703a
43. *Gaussian 09,* Revision A.02; Gaussian, Inc.: Wallingford, CT, 2016.
44. Gunturkun, D.; Isci, R.; Faraji, S.; Sütay, B.; Majewski, L. A.; Ozturk, T. *J. Mater. Chem. C* **2023,** *11,* 13129–13141. doi:10.1039/d3tc02109b
45. Capan, A.; Ozturk, T. *Synth. Met.* **2014,** *188,* 100–103. doi:10.1016/j.synthmet.2013.11.018
46. Turksoy, F.; Wallis, J. D.; Tunca, U.; Ozturk, T. *Tetrahedron* **2003,** *59,* 8107–8116. doi:10.1016/j.tet.2003.08.042
47. Işçi, R.; Öztürk, T. *Turk. J. Chem.* **2023,** *47,* 1239–1248. doi:10.55730/1300-0527.3608

License and Terms

The definitive version of this article is the electronic one which can be found at:
https://doi.org/10.3762/bjoc.19.137

BEILSTEIN JOURNAL OF ORGANIC CHEMISTRY

Aromatic systems with two and three pyridine-2,6-dicarbazolyl-3,5-dicarbonitrile fragments as electron-transporting organic semiconductors exhibiting long-lived emissions

Karolis Leitonas[1], Brigita Vigante[2], Dmytro Volyniuk[1], Audrius Bucinskas[1],
Pavels Dimitrijevs[2], Sindija Lapcinska[2], Pavel Arsenyan*[2]
and Juozas Vidas Grazulevicius*[1]

Full Research Paper

Open Access

Address:
[1]Department of Polymer Chemistry and Technology, Kaunas University of Technology, Radvilenu pl. 19, LT-50254, Kaunas, Lithuania and [2]Latvian Institute of Organic Synthesis, Aizkraukles 21, LV-1006, Riga, Latvia

Email:
Pavel Arsenyan* - pavel@osi.lv; Juozas Vidas Grazulevicius* - juozas.grazulevicius@ktu.lt

* Corresponding author

Keywords:
charge transport; intramolecular charge transfer; photophysical properties; pyridine-3,5-dicarbonitrile

Beilstein J. Org. Chem. **2023,** *19,* 1867–1880.
https://doi.org/10.3762/bjoc.19.139

Received: 25 August 2023
Accepted: 18 October 2023
Published: 12 December 2023

This article is part of the thematic issue "Organic electron transport materials".

Associate Editor: P. J. Skabara

Abstract

The pyridine-3,5-dicarbonitrile moiety has gained significant attention in the field of materials chemistry, particularly in the development of heavy-metal-free pure organic light-emitting diodes (OLEDs). Extensive research on organic compounds exhibiting thermally activated delayed fluorescence (TADF) has led to numerous patents and research articles. This study focuses on the synthesis and investigation of the semiconducting properties of polyaromatic π-systems containing two and three fragments of pyridine-2,6-dicarbazolyl-3,5-dicarbonitrile. The compounds are synthesized by Sonogashira coupling reactions and characterized by steady-state and time-resolved luminescence spectroscopy. The compounds show efficient intramolecular charge transfer (ICT) from the donor to the acceptor. The photoluminescence (PL) spectra of the solutions of the compounds showed non-structured emission peaks in the visible region, which are attributed to ICT emission. The PL intensities of the solutions of the compounds are enhanced after deoxygenation, which is indicative of TADF. The photoluminescence quantum yields and TADF properties of the compounds are sensitive to the medium. Cyclic voltammetry measurements indicate good hole-blocking and electron-injecting properties due to their high ionization potentials. Photoelectron spectroscopy and time-of-flight measurements reveal good electron-transporting properties for one of the compounds. In general, polyaromatic π-systems with pyridine-3,5-dicarbonitrile fragments demonstrate promising potential for use in organic electronic devices, such as OLEDs.

Introduction

The pyridine-3,5-dicarbonitrile moiety attracted a great deal of attention in the last decade in the field of materials chemistry, precisely in the development of novel heavy-metal-free pure organic light-emitting diodes (OLEDs). Inexpensive and environmentally friendly emitters are vital for organic electronic devices including OLEDs. Thus, extensive search for organic dyes exhibiting E-type fluorescence (thermally activated delayed fluorescence (TADF)) is booming [1-3]. The majority of research results are protected by an impressive amount of patent applications.

The first example of a blue TADF emitter based on a pyridine-3,5-dicarbonitrile scaffold (to serve as an electron acceptor) directly linked to a carbazole moiety (to serve as an electron donor) was reported by the groups of Dong and Zhang in 2015 [4]. 2,6-Di(9*H*-carbazol-9-yl)-4-phenylpyridine-3,5-dicarbonitrile (CPC) showed an extremely small singlet–triplet splitting and a fair photoluminescence quantum yield (PLQY). The optimized organic light-emitting diode (OLED) based on 13 wt % CPC doped in 1,3-bis(9*H*-carbazol-9-yl)benzene (mCP) as host exhibited maximum current efficiency, power efficiency, and external quantum efficiency (EQE) of 47.7 cd A^{-1}, 42.8 lm W^{-1}, and 21.2%, respectively (Figure 1). Since then, this moiety has been modified by many scientific groups to improve its electroactive properties.

Various pyridine-3,5-dicarbonitriles bearing substituted carbazoles were synthesized using different donating and accepting groups to achieve optimal charge-transporting and fluorescent properties within one TADF compound (Figure 1) [5]. The obtained TADF emitters (453 to 550 nm) show photoluminescence quantum yields of up to 98% in oxygen-free toluene solutions. These TADF emitters are suitable for OLEDs with brightness of 10 000 cd m^{-2}, electroluminescence ranging from blue to yellow, maximum current of 15 cd/A and higher EQE than 7%.

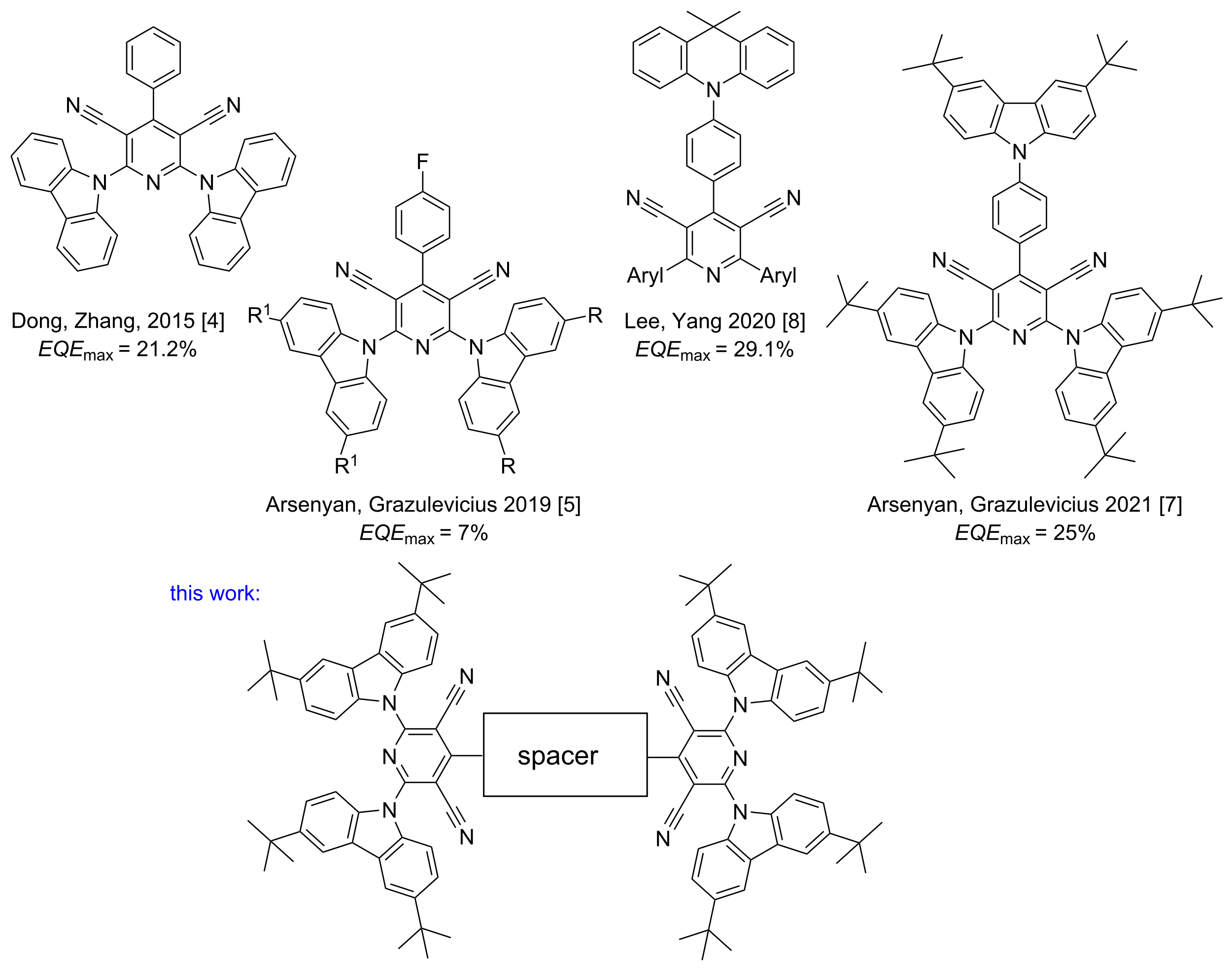

Figure 1: Chemical structures of pyridine-3,5-dicarbonitrile-based TADF emitters.

Pyridine-3,5-dicarbonitrile-based TADF materials exhibit different visible light emission spectra (Figure 1). Recently, Chen and Lu reported two new orange-red/red TADF emitters composed of pyridine-3,5-dicarbonitrile-derived electron-acceptor and acridine electron–donor moieties. The films of molecular mixtures of these emitters with the hosts exhibited excellent photophysical properties [6]. They showed PLQY of up to 91%, tiny singlet–triplet energy gaps of 0.01 eV, and ultrashort TADF lifetimes of less than 1 μs. TADF-OLEDs based on these materials exhibited EQE_{max} of up to 25.0% and well-suppressed efficiency roll-offs. Green and orange normal/dual TADF emitters were produced using compounds containing 3,6-di-*tert*-butylcarbazole and 3,7-dibromophenothiazine moieties. Pyridine-3,5-dicarbonitriles substituted with 3,6-di-*tert*-butylcarbazole were successfully leveraged as TADF emitters in the fabrication of OLED with relatively high device lifetimes and a high EQE_{max} of 25% [7]. An effective green TADF was achieved for pyridine-3,5-dicarbonitriles with highly twisted conformations that contain dimethylacridan substituents [8]. OLEDs based on phenyl-substituted pyridine-3,5-dicarbonitrile showed very high EQE_{max} of 29.1% due to a high PLQY of 89% ascribed to the rigid acceptor geometry.

In addition to the utilization of pyridine-3,5-dicarbonitriles in OLEDs, an example of their application in photocatalysis has been recently published [9]. 2,6-Bis(4-cyanophenyl)-4-(9-phenyl-9*H*-carbazol-3-yl)pyridine-3,5-dicarbonitrile) exhibits two aggregate states in aqueous dispersions: amorphous nanospheres and ordered nanofibers with π–π molecular stacking. The nanofibers promoted the photocatalytic production of H_2 while the nanospheres produced hydrogen peroxide (H_2O_2).

The introduction of the additional carbazolylphenyl moiety in the CPC molecule [4] allowed us to improve the EQE_{max} of an OLED to 25% [7]. In continuation of our studies in the field of the development of new TADF emitters [10], we would like to report our research results on the development of straightforward protocols for the synthesis and properties of polyaromatic π-systems with two and three pyridine-2,6-dicarbazolyl-3,5-dicarbonitrile fragments.

Results and Discussion

Synthesis

The sophisticated pyridine-3,5-carbonitriles **6–9** were synthesized starting with 4-bromobenzaldehyde (**1**) (Scheme 1 and

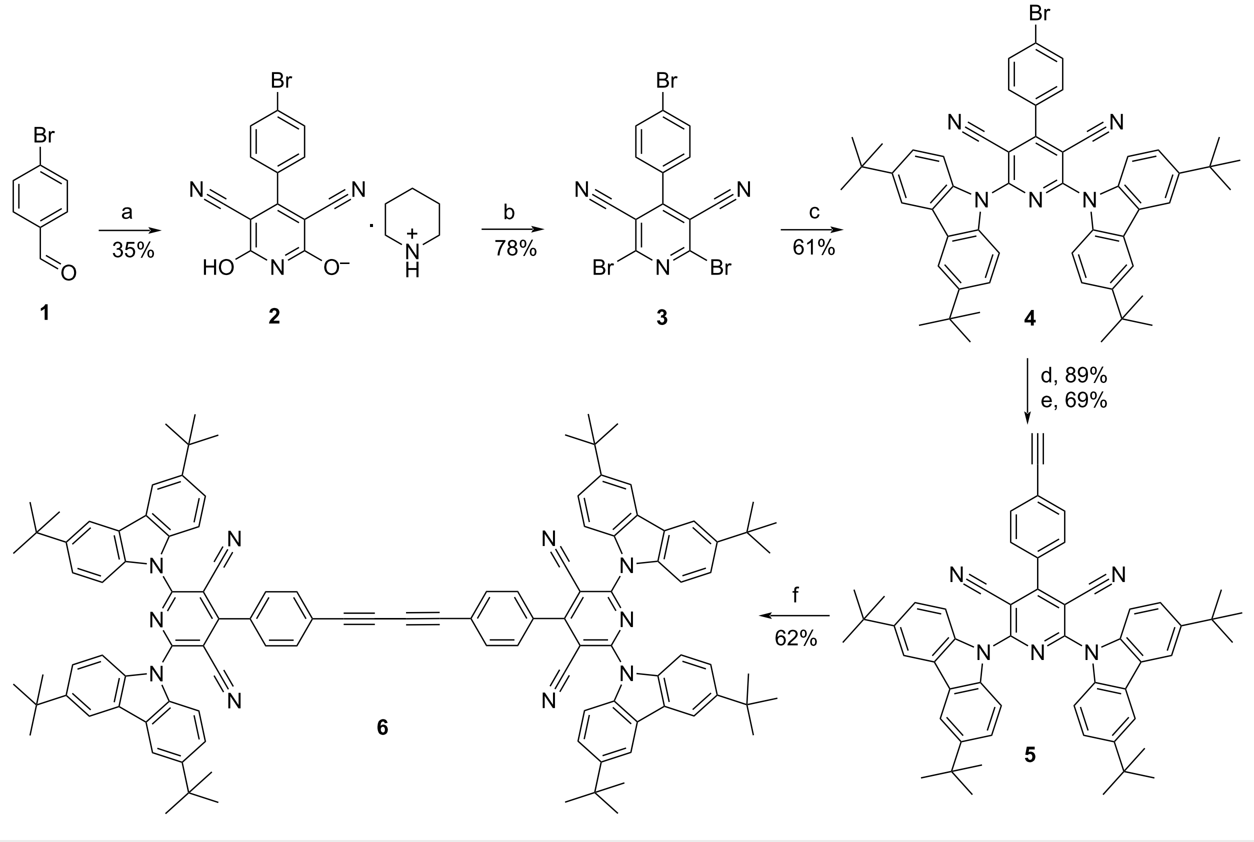

Scheme 1: Synthesis of dicyanocarbazole **6**. Reaction conditions: a) cyanoacetamide, piperidine, methanol, 40 °C, 48 h; b) $POBr_3$, 170 °C, 1 h; c) 3,6-di(*tert*-butyl)carbazole, NaH, THF, DMF, 0 → rt, 3 h; d) ethynyltrimethylsilane (2 equiv), $PdCl_2(PPh_3)_2$ (0.07 equiv), CuI (0.05 equiv), diisopropylethylamine, DMF, 55 °C, 12 h; e) K_2CO_3 (2 equiv), MeOH/Et_2O, 1 h; f) $Pd(PPh_3)_4$ (0.1 equiv), CuI (1 equiv), DMF/DIPEA, 80 °C, 48 h.

Scheme 2). Thus, piperidinium 3,5-dicyano-6-hydroxy-4-(4-bromophenyl)pyridin-2-olate (**2**) was prepared by cyclocondensation of **1** with cyanoacetamide in methanol in the presence of piperidine. The conversion of **2** to the corresponding 2,6-dibromo-4-(4-bromophenyl)pyridine-3,5-carbonitrile (**3**) was carried out by melting of compound **2** with phosphorous oxybromide without any solvent at 170 °C for 1 h in good yield. According to the previously reported procedure [4,5], 2,6-bis(3,6-di-*tert*-butylcarbazol-9-yl)-4-(4-bromophenyl)pyridine-3,5-carbonitrile (**4**) was obtained by the interaction of 3,6-di-*tert*-butyl-9*H*-carbazole with compound **3** in THF/DMF solution. The ethynylphenyl-substituted pyridine **5** was synthesized by Sonogashira coupling of **4** with ethynyltrimethylsilane in the presence of $PdCl_2(PPh_3)_2$ and copper(I) iodide in DMF/DIPEA solution at 55 °C with subsequent desilylation with potassium carbonate. Finally, butadiyne **6** was prepared by a homocoupling reaction of **5** with 80% yield. Derivatives containing two dicyanopyridyl moieties, **7** and **8**, were prepared starting with a Sonogashira coupling of compound **4** with 4,4’-diethynylbiphenyl and 5,5’-diethynyl-3,3’-dihexyl-2,2’-bithiophene, respectively. Finally, the snowflake-shaped compound **9** bearing three dicyanopyridyl moieties was constructed by the treatment of 1,3,5-triethynylbenzene with 3 equiv of **4**. The structural identity and purity of compounds **6**–**9** were confirmed by the spectral data and elemental analyses. Remarkably, despite a highly hindered structure, compound **9** exhibits good solubility in non-polar solvents.

Photophysical properties

The electronic structures of compounds **6**–**9** in the ground and excited states were investigated by steady-state luminescence spectroscopy. Meanwhile, time-resolved spectroscopy at differ-

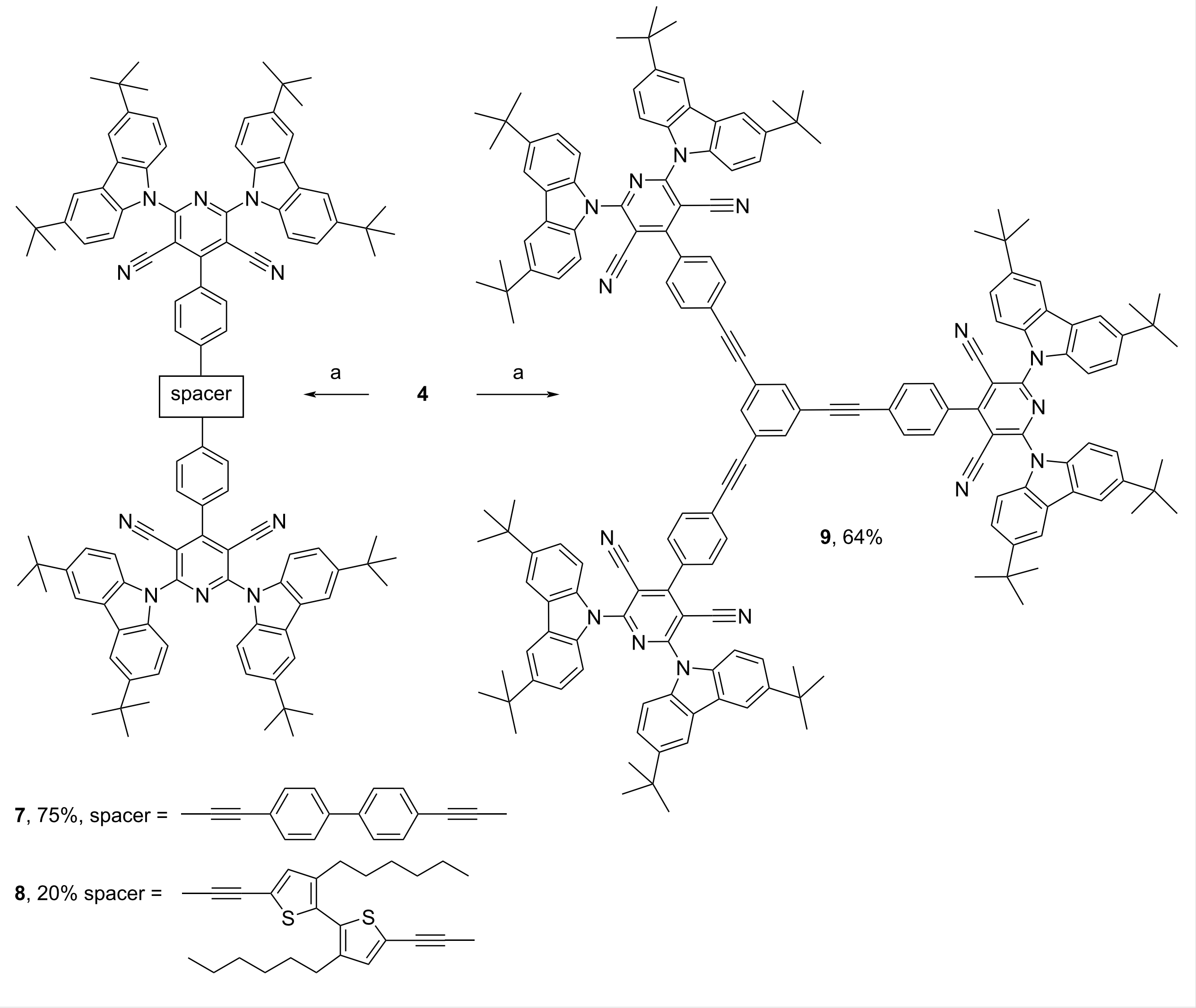

Scheme 2: Synthesis of dicyanocarbazoles **7**–**9**. Reaction conditions: a) corresponding ethynyl arene, $Pd(Ph_3P)_4$ (5 mol %), Cu(I) (3 mol %), triethylamine, DMF, 90 °C, 18 h.

ent temperatures was used to investigate the nature of long-lived emissions of **6**–**9** as it was previously done for the reference compound 2,6-bis(3,6-di-*tert*-butyl-9*H*-carbazol-9-yl)-4-(4-fluorophenyl)pyridine-3,5-carbonitrile (**REF**) [5].

Absorption spectra of dilute toluene, tetrahydrofuran (THF), and chloroform solutions as well as of the films of compounds **6**–**9** are shown in Figure 2a,b. The nonstructured low-energy bands at wavelengths of 350–450 nm are well seen in the absorption spectra of **6**–**9**. The wavelengths of peaks of these low-energy absorption bands are collected in Table 1. A similar band was previously observed for **REF** [5]. On the basis of the results of the theoretical investigations, the low-energy absorption band of **REF** has been attributed to the intramolecular charge transfer (ICT) caused by electron transfer from the donor to the acceptor. The absorption spectrum of **REF** is included in Figure 2a for comparison. Compounds **6**–**9** are characterized by similar absorption bands also caused by electron transfer from the 3,6-di-*tert*-butyl-9*H*-carbazole units to the pyridine-3,5-dicarbonitrile moiety. The number of **REF** fragments in the structures of compounds **6**–**9** does not have any strong effect on the positions of their absorption spectra. As a result, similar optical band gaps ($E_g^{\mathrm{opt.}}$) of 2.74–2.8 eV were obtained for **6**–**9**. It should be noted that the 5,5'-diethynyl-3,3'-dihexyl-2,2'-bithiophene bridge of compound **8** had a slight impact on its red-shifted absorption spectra in comparison to that of other compounds (Figure 2a,b and Table 1).

The photoluminescence spectra of toluene solutions of the compounds are characterized by non-structured shapes typical for ICT emissions (Figure 2c and Figure S1 in Supporting Information File 1) [11]. This interpretation is additionally supported by redshifted and broadened PL spectra of their THF and chloroform solutions with respect to the toluene solutions. For example, the intensity maxima at 525, 571, and 594 nm and full widths at half maxima (FWHM) of 105, 130, and 154 nm were obtained for toluene, chloroform, and THF solutions of compound **8**, respectively (Figure 2c, Table 1, and Figure S1 in Supporting Information File 1). In comparison to the PL spectrum of the toluene solution of **REF**, the PL spectra of toluene solutions of compounds **6**–**9** were redshifted. Since the freedom of movements (vibrations and rotations) of parts of **REF** are prevented in the solid state, the PL spectra of the films of compounds **6**–**9** were practically in the same spectral region (Figure 2d). It should be noted that the PL spectra of the neat films exhibit low-intensity high-energy bands and high-intensity low-energy bands. The presence of two distinct fluorescence bands is an indication of the existence of molecular conformations separated by a barrier. This is a characteristic of twisted internal charge transfer (TICT) states.

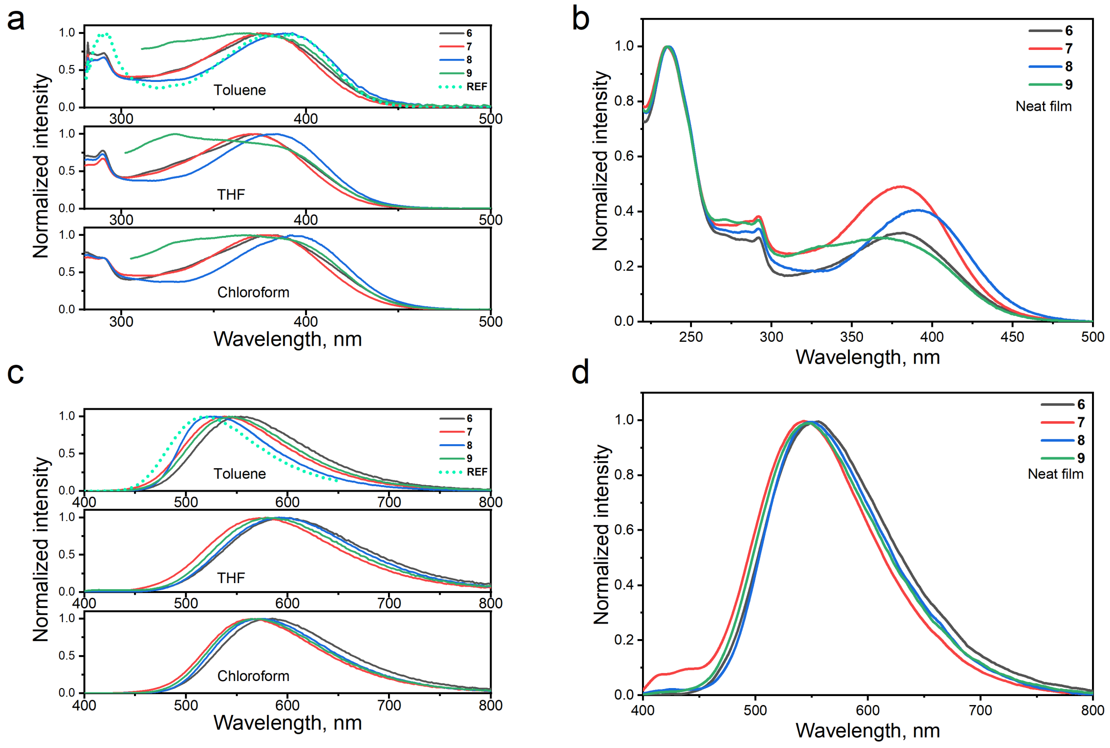

Figure 2: Absorption (a, b) and PL (c, d) spectra of dilute toluene, THF, and chloroform solutions (10^{-5} M) and of the films of compounds **6**–**9**.

Table 1: Common physical parameters of compounds **6–9**.

Compounds	Medium	**6**	**7**	**8**	**9**
λ_{abs}, nm	toluene/film/mCP-based film	379/382/385	378/381/385	391/392/394	368/369/391
λ_{PL}, nm		555/552/522	539/544/511	525/550/516	544/548/520
FWHM, nm		125/127/118	114/121/116	104/122/109	119/123/114
PLQY, %		6.7/4/6.33	7.6/6.4/7.3	17.1/7.4/9.6	9.15/6.3/8
ΔE_{ST}, eV	mCP-based film	0.14	0.21	0.25	0.24
$E_{onset,ox}$, V	CH_2Cl_2 solution	1.34	1.52	1.37	1.50
$E_{onset,ox\ vs\ Fc}$, V		1.02	1.09	1.06	1.08
$E_{onset,red}$, V		−1.15	−1.15	−1.32	−1.18
$E_{onset,red\ vs\ Fc}$, V		−1.47	−1.58	−1.63	−1.60
Fc_{onset}, V		0.32	0.43	0.31	0.42
IP_{CV}, eV[a]		5.82	5.89	5.86	5.88
EA_{CV}, eV[b]		3.33	3.22	3.17	3.20
IP^{PE}, eV	film	6.15	6.21	6.20	6.04
EA^{PE}, eV		3.37	3.41	3.46	3.28
μ_e, cm²/V·s		–	5.7×10^{-6},[c]	–	–
T_m, °C[d]	powder	–	–	–	–
T_g, °C[e]		63	75	80	90
T_d, °C[f]		449	493	433	488
M, g/mol		1566	1718	1899	2424

[a]Calculated according to equation: EA_{CV} = e ($E_{ox\ 1/2\ vs\ Fc}$ − $Fc_{1/2}$ + 4.8) [eV]; [b]calculated according to equation: IP_{CV} = −e ($E_{red\ 1/2\ vs\ Fc}$ − $Fc_{1/2}$ + 4.8) [eV]; [c]at electric field of 8.1×10^5 V/cm; [d]melting temperature at the 1st/2nd heating scan with a rate of 10 °C/min, N_2 atmosphere; [e]glass-transition temperature at the 2nd heating scan; [f]5% weight loss temperature at the scan rate of 20 °C/min, N_2 atmosphere.

It is worth of noting that the PL intensity of solutions of compounds **6**–**9** is increased after deoxygenation by argon (Figure 3a and Figure S2a in Supporting Information File 1). The increase of PL intensity is attributed to a delayed fluorescence turn-on when the triplet quenching by oxygen is omitted. This delayed fluorescence is TADF in nature as it is for compound **REF**. The increments of PL are different for the toluene, chloroform, and THF solutions. This observation shows that the TADF properties of compounds **6**–**9** are sensitive to the medium. For example, the ratios of PL intensities of deoxygenated and air-equilibrated toluene, chloroform, and THF solutions of 4.86, 7.24, and 1.41 were obtained for compound **9** (Figure 3a and Figure S2a, Supporting Information File 1). The TADF properties of derivatives **6**–**9** are discussed in more detail below. Long-lived emissions are detectable in the corresponding PL decay curves (Figure 3b and Figure S2b in Supporting Information File 1). The strongest PL intensity increment was detected for compound **9** containing the biggest number of dicyanopyridyl moieties. It can be concluded, that the TADF properties of **REF**-based molecules can be induced by linking additional **REF** moieties through the appropriate bridges. Similarly, the strongest TADF intensity was obtained for the neat films of compound **9** and of compound **9** molecularly dispersed in the host 1,3-bis(*N*-carbazolyl)benzene (mCP; Figure 3c,d and Figure S3a in Supporting Information File 1). Low-energy absorption bands of molecular mixtures of compounds **6–9** and mCP are attributed to ICT bands of **6**–**9** (see Figure S3b in Supporting Information File 1).

The temperature dependencies of PL spectra and PL decay curves of the 10 wt % molecular dispersions of compounds **6**–**9** in mCP are plotted in Figure 4a,b and Figures S4 and S5 in Supporting Information File 1. The PL intensity increased with increasing temperature and the profiles of the PL spectra were practically the same at the different temperatures proving the fluorescence nature of long-lived emission (Figure 4c and Figures S4–S6 in Supporting Information File 1). Two decay regimes were obtained for the compounds **6**–**9**. The initial decay is attributed to prompt fluorescence and the other decay is related to delayed fluorescence. The intensity of delayed fluorescence grows with the temperature rising which is typical for TADF compounds [12]. Such processes are possible because of the relatively low energy gap (ΔE_{ST}) between the lowest singlet and triplet states (Figure 4d and Figure S7 in Supporting Information File 1). A ΔE_{ST} value of 0.24 eV was obtained for compound **9**. The highest photoluminescence quantum yield (PLQY) of 17.1% was obtained for the dilute toluene solution of compound **8** (Table 1). The neat film of compound **8** showed

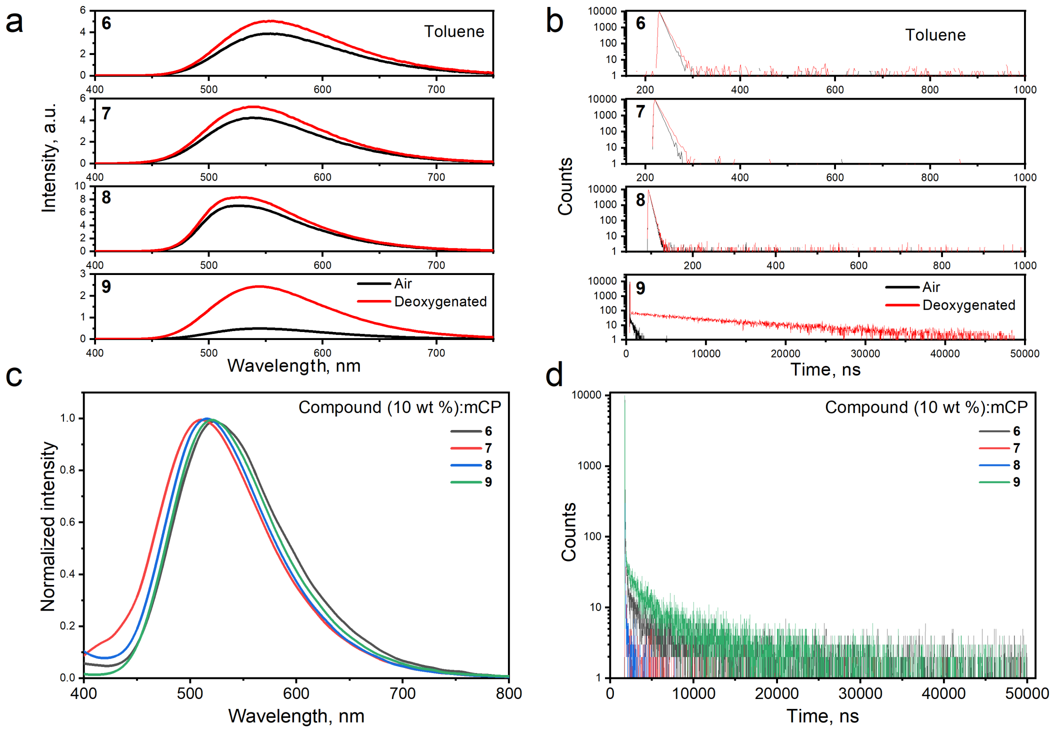

Figure 3: PL spectra (a) and PL decay curves (b) of air-equilibrated (as prepared) and deoxygenated toluene solutions of compounds **6**–**9**. PL spectra (c) and PL decay curves (d) of the films of molecular mixtures of mCP as host and compounds **6**–**9** (10 wt %).

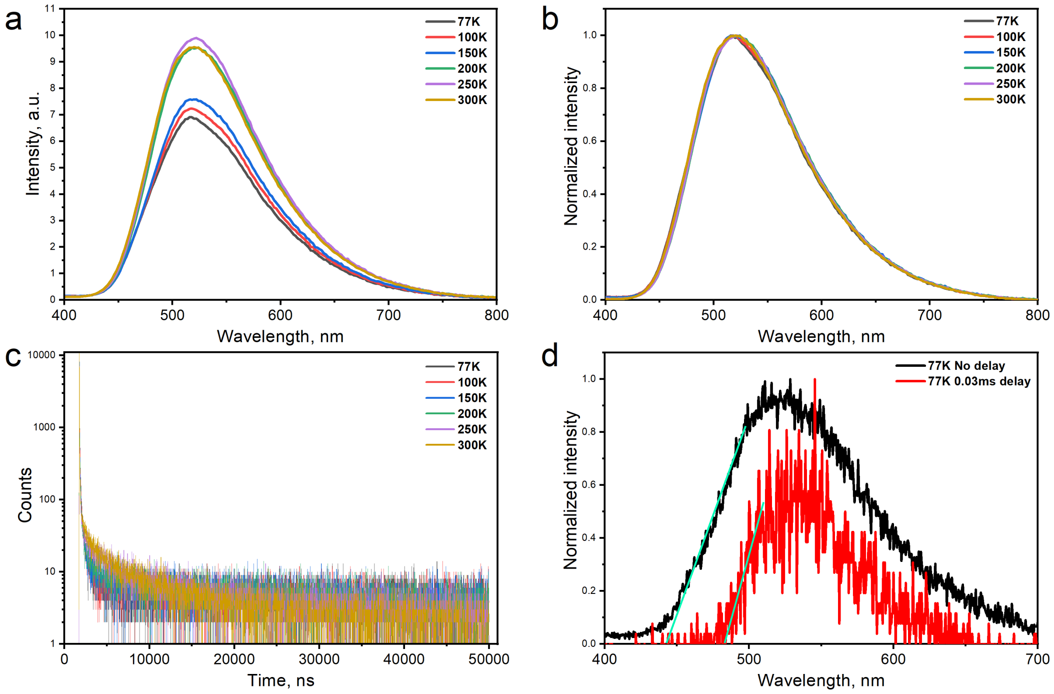

Figure 4: Non-normalized (a) and normalized (b) PL spectra and PL decay curves (c) of the film of a 10 wt % molecular dispersion of compound **9** in mCP recorded at the indicated different temperatures. PL and phosphorescence spectra of the same sample recorded at 77 K. (d) Phosphorescence was separated from fluorescence using a delay of 0.03 ms after excitation. Excitation wavelengths were 350 and 374 nm, respectively, for recording the PL spectra and PL decay curves.

a more than twice lower PLQY which was enhanced using the mCP host. The other compounds showed similar PLQY trends (Table 1).

Thermal properties

The thermal stability and phase transitions of the synthesized derivatives **6**–**9** were investigated utilizing thermogravimetric analysis (TGA) and differential scanning calorimetry (DSC), respectively. The experimental data are shown in Figure 5 and the characteristics are collected in Table 1.

An amorphous character of the derivatives was identified. No endothermic (melting) or exothermic (crystallization) transitions were observed during the 1st and 2nd DSC heating and cooling scans. However, glass transitions were detected for all the studied compounds. The glass transition temperatures (T_g) fall in the range between 63 and 93 °C (Figure 5b). A correlation between the glass transition temperature and the molecular weight of compounds **6**–**9** was observed. The T_g values of the derivatives increase gradually by 5–12 °C starting from compound **6** which possesses the lowest molecular weight (M = 1566 g/mol) up to compound **9** which possesses the highest M value (2424 g/mol) [13]. A high thermal stability was observed for all derivatives **6**–**9**. Their 5% weight loss temperatures (T_d) ranged from 433 to 493 °C (Figure 5a and Table 1).

Electrochemical properties

The electrochemical properties of compounds **6**–**9** were studied by cyclic voltammetry (CV) selecting the electrochemical window from −1.6 to 1.7 V and the CV data were corrected using ferrocene (Fc) as inner standard. The CV curves are shown in Figure 6 and the data are collected in Table 1. The reduction onset potentials ($E_{\text{red,onset}}$) of compounds **6**–**9** fall in the range from −1.63 to −1.47 V, while the onset values of the first oxidation wave range from 1.02 to 1.09 V. The values of $E_{\text{red,onset}}$ are comparable with those of recently published compounds containing a dicyanopyridyl moiety as a central electron-accepting core [7]. In case of oxidation potentials (0.96 to 1.04 V) there is only a slight effect of the extended conjugation between the dicyanopyridyl moieties. The results of CV measurements were used to obtain the ionization potential (IP_{CV}) and electron affinity (EA_{CV}) values of the compounds **6**–**9**. These values were obtained using the following equations: IP_{CV} = e ($E_{\text{onset,red}} - Fc_{\text{onset}}$ + 4.8), EA_{CV} = e ($E_{\text{onset,ox}} - Fc_{\text{onset}}$ + 4.8) [7]. The IP_{CV} values fall in a range of 5.80–5.90 eV, while the electron affinities (EA_{CV}) vary from 3.20 to 3.33 eV (Table 1). The obtained values are comparable to the corresponding ionization potentials (IP_{PE}) and electron affinities (EA_{PE}) obtained for the films by photoelectron emission spectrometry, presented and discussed in the following section. Small differences between the results obtained for the

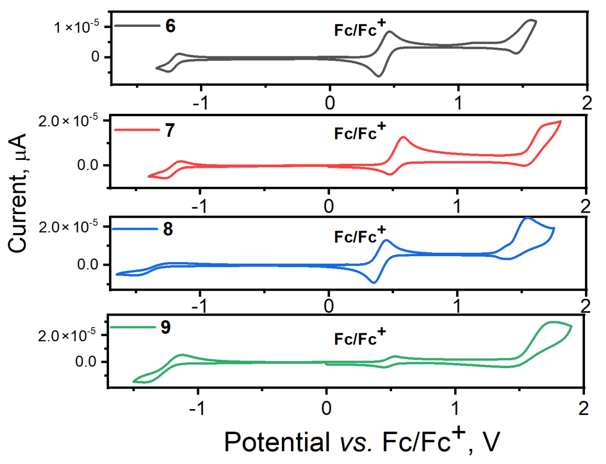

Figure 6: CV curves of compounds **6**–**9**.

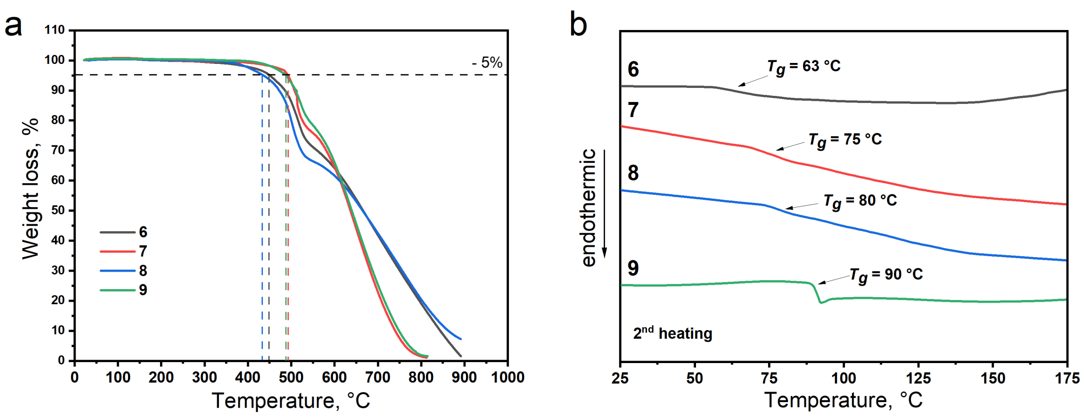

Figure 5: TGA (a) and DSC 2nd heating (b) curves of compounds **6**–**9**.

solutions and films appear to be due to different intermolecular interactions, which differ in solid films (between target molecules only) and solutions (between target molecules and molecules of the solvent) of the investigated compounds [14,15]. Compared to the results previously reported for compounds possessing a single dicyanopyridyl moiety [7,8,16], the studied compounds showed higher *IP* and *EA* values. This observation can be explained by the presence of additional dicyanopyridyl fragments in compounds **6**–**9**.

Photoelectrical and charge-transporting properties

The ionization potentials (IP^{PE}) of thin films were obtained by photoelectron emission (PE) spectroscopy in air (Figure 7 and Table 1). To generate photoelectrons detectable by a counter electrode within the PE experiments, a low-power deuterium UV lamp was used. It was previously shown that the PE technique gives practically the same IP^{PE} values as they are recorded by other methods in vacuum [17]. The PE spectra as current (i) versus photon energy ($h\nu$) dependences for thin films of compounds **6**–**9** are built in the square root of i versus linear $h\nu$ plots according to the relation $i \sim (h\nu - IP^{PE})^2$ [18]. The ionization potentials, IP^{PE}, were obtained by linear fitting of the linear parts of the plots [19], and the IP^{PE} values were taken at crossing points of the fitting curves with the baseline (x-axis). Compounds **6**–**9** are characterized by rather good hole-blocking properties due to the high IP^{PE} values of 6.04–6.21 eV. In contrast, they are characterized by pertinent electron-injecting properties because of the electron affinities (EA^{PE}) of 3.28–3.46 eV. The EA^{PE} values were calculated by the equation $EA^{PE} = IP^{PE} - E_g^{opt.}$ using $E_g^{opt.}$ taken from the low-energy edge of the absorption spectra of the corresponding films (Figure 2b, Table 1).

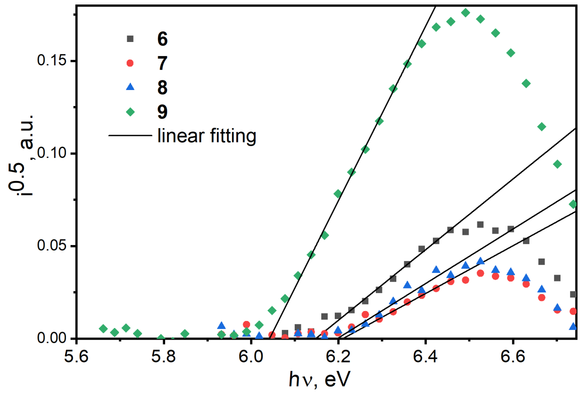

Figure 7: Photoelectron emission spectra of the vacuum-deposited films of compounds **6**–**9** on glass substrates covered by FTO electrodes.

We used time of flight (TOF) measurements to investigate the charge-transporting properties of compounds **6**–**9**. According to the current transients for electrons with clearly seen transit times in log–log scales, compound **7** is characterized by electron transport. The recorded current transients for electrons in vacuum-deposited films of compound **7** show moderate dispersion (Figure 8a). In contrast, the hole transport was not detected, apparently because of the low mobility of holes being out of the detectable range of TOF measurements. The similar situation was in the case of the other compounds which showed current transients without detectable transit times (Figure S7 in Supporting Information File 1). The electron mobility (μ_e) as the function of the electric field was substantial for **7** with the field dependence parameter (β) of 0.013 V/cm. This parameter was obtained by fitting according to the formula of Poole–Frenkel-type mobility ($\mu = \mu_0\, e^{\beta E^{1/2}}$). Compound **7** is characterized by both good electron injecting and electron-

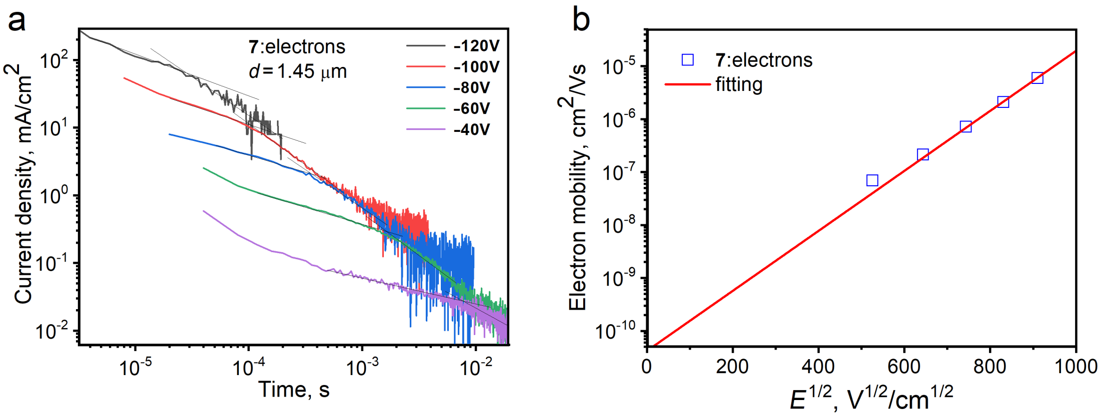

Figure 8: The current transients (a) for electrons recorded at the different voltages for the vacuum-deposited films of compound **7** in a diode-like structure ITO/film/Al. Excitation wavelength 355 nm, laser pulse duration 6 ns. b) Electric field dependence of electron mobility for the layer of **7** at room temperature (295 K).

transporting properties due to its EA^{PE} of 3.45 eV and electron mobility reaching 5.7×10^{-6} cm^2/V·s at the electric field of 8.1×10^5 V/cm (Figure 8).

Conclusion

Synthetically convenient protocols for the preparation of sophisticated pyridine-3,5-carbonitriles containing carbazole substituents in positions 2 and 6 were developed starting with 4-bromobenzaldehyde. The compounds were found to be soluble in common organic solvents and to exhibit non-structured emission peaks in the green-yellow color region of the spectrum. The PL intensity of the compounds in solution was enhanced after deoxygenation, indicating the presence of triplet harvesting by the mechanism of thermally activated delayed fluorescence. The optical band gaps of the compounds were determined to be 2.74–2.8 eV, while cyclic voltammetry measurements demonstrated that the compounds possess excellent hole-blocking properties due to their high ionization potentials. Moreover, they exhibited appropriate electron-injecting properties, as evidenced by their electron affinities. Photoelectron emission spectroscopy results confirmed the favorable electron-transporting properties with high ionization potentials, supporting their potential application as electron-transporting materials in OLEDs.

Overall, the polyaromatic π-systems with pyridine-3,5-dicarbonitrile fragments demonstrated a range of attractive properties, including efficient TADF, favorable charge transport, and thermal stability. These findings open up new possibilities for the design and development of high-performance OLEDs and other organic electronic devices. Further investigations and optimizations of the properties of such compounds may lead to the realization of environmentally friendly and cost-effective OLED technologies.

Experimental

Synthesis

Unless otherwise stated, all reagents were purchased from commercial suppliers and used without further purification. Thin-layer chromatography (TLC) was performed using Merck Silica gel 60 F254 plates and visualized by UV (254 nm) fluorescence. Zeochem silica gel (ZEOprep 60/35–70 microns – SI23501) was used for column chromatography. ^{1}H and ^{13}C NMR spectra were recorded on a Bruker 400 spectrometer at 400 and 101 MHz, respectively, at 298 K in $CDCl_3$. The corresponding spectra are given in Supporting Information File 1. The ^{1}H chemical shifts are given relative to residual $CHCl_3$ signal (7.26 ppm), ^{13}C chemical shifts are given relative to $CDCl_3$ (77.16 ppm). The melting points were determined on a "Digital melting point analyzer" (Fisher), and the results are given without correction. Reagents and solvents were purchased from common vendors such as ACROS, Fluorochem, ABCR, and others.

Piperidinium 3,5-dicyano-6-hydroxy-4-(4-bromophenyl)pyridin-2-olate (**2**). A mixture of cyanoacetamide (10.51 g, 0.125 mol, 2.5 equiv), piperidine (14.81 mL, 0.15 mol, 3 equiv), and MeOH (150 mL) was heated until complete dissolution. The mixture was cooled to rt and 4-bromobenzaldehyde (**1**, 9.25 g, 0.05 mol, 1 equiv) was added. The mixture was vigorously stirred at 40 °C for 48 h. Then solvents were evaporated to a half of volume and after cooling the precipitate was filtered. The crude product was washed with cold MeOH and EtOAc and dried under reduced pressure yielding **2** (7.40 g, 35%) as white powder, which was used in the next reaction without further purification. ^{1}H NMR (400 MHz, DMSO-d_6) 7.67–7.66 (m, 2H), 7.37–7.33 (m, 2H), 3.02–2.99 (m, 4H), 1.63–1.51 (m, 6H); MS–ESI$^-$ (*m/z*): 315 ([M − H − piperidine]$^-$, 100).

2,6-Dibromo-4-(4-bromophenyl)pyridine-3,5-dicarbonitrile (3). A mixture of compound **2** (1.16 g, 2.89 mmol, 1 equiv) and $POBr_3$ (2.49 g, 8.68 mmol, 3 equiv) was heated with stirring in an oil bath at 170 °C for 1 h. After cooling, the reaction was quenched by the addition of ice and the precipitate was filtered off. The crude product was purified by flash chromatography on silica gel using chloroform as eluent yielding compound **3** (1.0 g, 78%) as white powder. Mp > 200 °C; ^{1}H NMR (400 MHz, DMSO-d_6) 7.91–7.79 (m, 2H), 7.63–7.50 (m, 2H); GC–MS: 442 [M]$^+$.

2,6-Bis(3,6-di-*tert*-butylcarbazol-9-yl)-4-(4-bromophenyl)pyridine-3,5-dicarbonitrile (**4**). Sodium hydride (60% oil dispersion, 180 mg, 5.36 mmol, 3.2 equiv) was added to THF (15 mL) under Ar atmosphere. Then, 3,6-di-*tert*-butyl-9*H*-carbazole (1.40 g, 5.3 mmol, 3 equiv) was added at 0 °C, the suspension was stirred for 30 min and then, a DMF (5 mL) solution of compound **3** (0.74 g, 1.67 mmol, 1 equiv) was added. The mixture was stirred at rt for 3 h (TLC) before it was poured into ice-water. The suspension was extracted with chloroform (5 × 30 mL) and dried over Na_2SO_4. After the solvent was removed, the crude yellow product was carefully washed twice with acetonitrile to remove the starting materials. Further purification was achieved using flash chromatography on silica gel (eluent: dichloromethane/petroleum ether 1:2). Compound **4** (0.86 g, 61%) was obtained as bright yellow powder. Mp > 200 °C; ^{1}H NMR (400 MHz, $CDCl_3$) 8.10 (d, *J* = 1.6 Hz, 4H), 7.86 (d, *J* = 8.5 Hz, 2H), 7.76 (d, *J* = 8.5 Hz, 2H), 7.71 (d, *J* = 8.7 Hz, 4H), 7.48 (dd, *J* = 7.8, 1.9 Hz, 4H), 1.46 (s, 36H); MS–ESI$^+$ (*m/z*): 839 ([M + H]$^+$, 100); Anal. calcd for $C_{53}H_{52}BrN_5$: C, 75.88; H, 6.25; N, 8.35; found: C, 75.56; H, 6.30; N, 8.45.

2,6-Bis(3,6-di-*tert*-butylcarbazol-9-yl)-4-(4-ethynylphenyl)pyridine-3,5-dicarbonitrile (5). A mixture of compound **4** (1.0 g, 1.19 mmol, 1 equiv), $PdCl_2(PPh_3)_2$ (58 mg, 0.083 mmol, 0.07 equiv), CuI (11 mg, 0.06 mmol, 0.05 equiv) in 2 mL of DMF and 2 mL of DIPEA was degassed with Ar. Then, ethynyltrimethylsilane (0.34 mL, 2.38 mmol, 2 equiv) was added and the reaction mixture was stirred at 55 °C overnight. The mixture was poured into sat. aqueous solution of NH_4Cl and extracted with dichloromethane (4 × 60 mL). The combined extracts were washed with water, brine, and dried over Na_2SO_4. After evaporation of the solvent, the crude residue was purified by flash chromatography on silica gel using a mixture of chloroform/petroleum ether/acetone 9:12:0.4 as eluent. 2,6-Bis(3,6-di-*tert*-butyl-9*H*-carbazol-9-yl)-4-(4-(trimethylsilylethynyl)phenyl)pyridine-3,5-dicarbonitrile (0.90 g, 89%) was obtained as bright yellow powder. Mp > 200 °C; ^{1}H NMR (400 MHz, $CDCl_3$) 8.11 (d, J = 1.9 Hz, 4H), 7.87–7.76 (m, 4H), 7.72 (d, J = 8.9 Hz, 4H), 7.49 (dd, J = 8.8, 1.9 Hz, 4H), 1.47 (s, 36H), 0.31 (d, J = 1.0 Hz, 9H); ^{13}C NMR (101 MHz, $CDCl_3$) 163.16, 154.51, 146.43, 136.98, 132.85, 132.58, 129.64, 127.20, 125.71, 124.18, 116.57, 114.00, 112.34, 103.64, 99.21, 98.30, 34.90, 31.81; MS–ESI$^+$ (*m/z*): 856 ([M + H]$^+$, 100). Next, potassium carbonate (69 mg, 0.5 mmol, 1 equiv) was added to a solution of 2,6-bis-(3,6-di-*tert*-butyl-9*H*-carbazol-9-yl)-4-(4-(trimethylsilylethynyl)phenyl)pyridine-3,5-dicarbonitrile (430 mg, 0.5 mmol, 1 equiv) in methanol (70 mL) and diethyl ether (20 mL) and the mixture was stirred under Ar for 1 h (TLC control). Then, the reaction mixture was diluted with dichloromethane and poured into water. The aqueous layer was extracted with dichloromethane (2 × 50 mL), the combined organic extracts were washed with water and brine, and dried over Na_2SO_4. After removal of the solvent the residue was purified by flash chromatography on silica gel, eluting with DCM/petroleum ether 1:1.5 → 1:1. Compound **5** was obtained (270 mg, 69%) as bright yellow powder. Mp > 200 °C; ^{1}H NMR (400 MHz, $CDCl_3$) 8.10 (dd, J = 2.0, 0.6 Hz, 4H), 7.89–7.78 (m, 4H), 7.71 (dd, J = 8.7, 0.6 Hz, 4H), 7.48 (dd, J = 8.8, 2.0 Hz, 4H), 3.28 (s, 1H), 1.46 (s, 36H).

4,4'-(Buta-1,3-diyne-1,4-diylbis(4,1-phenylene))bis(2,6-bis(3,6-di-*tert*-butyl-9*H*-carbazol-9-yl)pyridine-3,5-dicarbonitrile) (6). A solution of compound **5** (130 mg, 0.166 mmol, 1 equiv) in DMF (2 mL) and DIPEA (1 mL) was bubbled with Ar. Then, $Pd(PPh_3)_4$ (19 mg, 0.0166 mmol, 0.1 equiv) and CuI (32 mg, 0.166 mmol, 1 equiv) were added and the mixture was stirred at 80 °C for 48 h. The reaction mixture was diluted with water and the product was extracted with dichloromethane (3 × 40 mL), washed with water, and brine. After evaporation of solvents the crude product was purified by flash chromatography on silica gel with DCM/petroleum ether 1:2 → 1:1. Derivative **6** was obtained as yellow powder (80 mg, 62%). Mp > 200 °C; IR ν_{max} (film): 2227, 1550; ^{1}H NMR (400 MHz, $CDCl_3$) 8.11 (dd, J = 2.0, 0.6 Hz, 8H), 7.90 (s, 8H), 7.73 (dd, J = 8.8, 0.5 Hz, 8H), 7.49 (dd, J = 8.8, 2.0 Hz, 8H), 1.46 (s, 72H); ^{13}C NMR (101 MHz, $CDCl_3$) 162.83, 154.53, 154.50, 146.56, 146.52, 136.96, 133.59, 133.50, 133.11, 129.93, 129.72, 126.17, 125.78, 125.76, 125.54, 124.23, 124.21, 116.61, 114.01, 112.43, 99.12, 99.00, 34.93, 31.83; Anal. calcd for $C_{110}H_{104}N_{10}$: C, 84.36; H, 6.69; N, 8.94; found: C, 83.97; H, 6.70; N, 8.70.

General method for the synthesis of compounds **7–9**

A mixture of 2,6-bis(3,6-di-*tert*-butyl-9*H*-carbazol-9-yl)-4-(4-bromophenyl)pyridine-3,5-dicarbonitrile (**4**, 168 mg, 0.2 mmol, 1 equiv), tetrakis(triphenylphosphine)palladium(0) (11.6 mg, 0.01 mmol, 0.05 equiv), CuI (1.2 mg, 0.006 mmol, 0.03 equiv) in 2 mL of DMF was degassed with Ar. Then, the appropriate ethynyl derivative (0.24 mmol, 1.2 equiv) and 1 mL of triethylamine were added and the resulting mixture was heated at 90 °C for 18 h. Then, the mixture was poured on ice and extracted with dichloromethane (4 × 30 mL). The solution was filtered through celite and dried over Na_2SO_4. The solvent was removed under reduced pressure and the yellow powder was purified by flash chromatography on silica gel.

4,4'-(([1,1'-Biphenyl]-4,4'-diylbis(ethyne-2,1-diyl)bis(4,1-phenylene))bis(2,6-bis(3,6-di-*tert*-butyl-9*H*-carbazol-9-yl)pyridine-3,5-dicarbonitrile) (7). Two equiv of compound **4**, 1 equiv of 4,4'-diethynylbiphenyl were employed. After evaporation of the solvent the crude product was purified by flash chromatography on silica gel with dichloromethane/petroleum ether 1:1 → 2:1. Compound **7** was isolated as yellow powder (193 mg, 75%). Mp > 200 °C; IR ν_{max} (film): 2228, 1602, 1538, 1530; ^{1}H NMR (400 MHz, $CDCl_3$) 8.12 (d, J = 2.0 Hz, 8H), 7.95–7.83 (m, 8H), 7.74 (d, J = 8.8 Hz, 8H), 7.72–7.64 (m, 8H), 7.50 (dd, J = 8.8, 2.0 Hz, 8H), 1.47 (s, 72H); ^{13}C NMR (101 MHz, $CDCl_3$) 163.18, 154.58, 146.47, 140.57, 137.01, 132.54, 132.44, 132.41, 129.87, 127.40, 127.07, 125.76, 124.22, 122.07, 116.61, 114.14, 112.40, 99.16, 34.93, 31.84; Anal. calcd for $C_{122}H_{112}N_{10}$: C, 85.28; H, 6.57; N, 8.15; found: C, 84.98; H, 6.60; N, 8.00.

4,4'-(((3,3'-Dihexyl-[2,2'-bithiophene]-5,5'-diyl)bis(ethyne-2,1-diyl)bis(4,1-phenylene)bis(2,6-bis(3,6-di-*tert*-butyl-9*H*-carbazol-9-yl)pyridine-3,5-dicarbonitrile) (8). Two equiv of **4** per 1 equiv of 5,5'-diethynyl-3,3'-dihexyl-[2,2']bithiophene were employed. After evaporation of the solvent the crude product was purified by flash chromatography on silica gel with chloroform/petroleum ether/acetone 9:15:0.4 by volume. The product **8** was obtained as orange powder (172 mg, 20%). Mp > 200 °C; IR ν_{max} (film): 2252, 2240, 1538, 1532, 1425;

^{1}H NMR (400 MHz, $CDCl_3$) 8.11 (d, *J* = 2.0 Hz, 8H), 7.93–7.80 (m, 8H), 7.73 (d, *J* = 8.7 Hz, 8H), 7.50 (dd, *J* = 8.8, 2.0 Hz, 8H), 7.27 (s, 2H), 2.56 (t, *J* = 7.8 Hz, 4H), 1.62–1.56 (m, 4H), 1.46 (s, 72H), 1.36–1.29 (m, 12H), 0.94–0.84 (m, 6H); ^{13}C NMR (101 MHz, $CDCl_3$) 163.10, 154.57, 146.47, 143.22, 137.00, 134.50, 132.46, 132.24, 130.63, 129.89, 127.06, 125.74,124.21, 122.56, 116.60, 114.11, 112.38, 99.13, 92.84, 86.01, 34.93, 31.83, 31.65, 30.67, 29.07, 28.89, 22.60, 14.12; Anal. calcd for $C_{130}H_{132}N_{10}S_2$: C, 82.24; H, 7.01; N, 7.38; found: C, 81.59; H, 7.13; N, 6.95.

4,4',4''-((Benzene-1,3,5-triyltris(ethyne-2,1-diyl)tris(benzene-4,1-diyl))tris(2,6-bis(3,6-di-*tert*-butyl-9*H*-carbazol-9-yl)pyridine-3,5-dicarbonitrile) (9). Three equiv of compound **4** per 1 equiv of 1,3,5-triethynylbenzene were employed. After evaporation of the solvent the crude product was purified by flash chromatography on silica gel eluting with DCM/petroleum ether 1:2 → 2:1. The product **9** was obtained as orange powder (280 mg, 64%). Mp > 200 °C; IR ν_{max} (film): 2229, 1608, 1532; ^{1}H NMR (400 MHz, $CDCl_3$) 8.13–8.08 (m, 12H), 7.96–7.87 (m, 12H), 7.82 (s, 3H), 7.76–7.71 (m, 12H), 7.50 (dd, *J* = 8.8, 2.0 Hz, 12H), 1.46 (s, 108H); ^{13}C NMR (101 MHz, $CDCl_3$) 163.09, 154.56, 146.50, 137.00, 132.86, 132.69, 129.93, 126.80, 125.76, 124.23, 116.61, 114.09, 112.40, 99.15, 90.69, 34.93, 31.83; Anal. calcd for $C_{171}H_{159}N_{15}$: C, 84.72; H, 6.61; N, 8.67; found: C, 84.54; H, 6.60; N, 8.55.

Measurements

In this experimental investigation, thermogravimetric analysis (TGA) and differential scanning calorimetry (DSC) were employed to characterize the thermal properties of the samples. The measurements were performed using a TA instrument TGA Q50 apparatus for TGA and a TA instrument DSC Q2000 series thermal analyzer for DSC. During the TGA experiments, the samples were subjected to controlled heating at a rate of 20 °C/min under a nitrogen atmosphere. TGA allows us to observe the weight changes of the samples as a function of temperature, providing valuable insights into processes such as decomposition, volatilization, and oxidation. In the case of DSC measurements, the samples were heated at a rate of 10 °C/min in a nitrogen environment. DSC allows us to investigate the enthalpy changes associated with phase transitions, crystallization, and other thermal events occurring in the samples. The choice of a nitrogen atmosphere in both TGA and DSC experiments is significant as it helps to prevent undesired reactions with atmospheric components, ensuring a controlled and inert environment. These optimized experimental conditions enable accurate and reproducible data acquisition.

Ionization potential (IP^{PE}) determination: The IP^{PE} analysis was conducted using electron photoemission spectrometry, a technique for investigating the energy required to remove an electron from a solid material. Thin film samples were precisely prepared through vacuum deposition onto cleaned fluorine-doped tin oxide (FTO)-coated glass substrates, maintained at a low pressure of 2×10^{-6} mbar to ensure sample integrity. During the IP^{PE} experiment, a negative voltage of 300 V was applied to the sample substrate, promoting electron emission from the surface. The photoelectron emission spectra were recorded using a Spectral Products© 30 W deep UV deuterium light source (180–400 nm) ASBN-D130-CM, coupled with the CM110 1/8 m monochromator, which allowed precise control of the incident photon wavelength. To measure the photocurrent flowing in the circuit under illumination, a Keithley 6517B electrometer/high resistance meter was utilized, providing accurate and sensitive readings. An energy scan of the incident photons was performed by systematically changing the wavelength with the monochromator in 1 nm steps, covering the range from 280 to 180 nm. The IP^{PE} was subsequently estimated by identifying the intersection points of the extrapolated linear portion of the dependence of the square root of the time derivative of voltage $(dU/dt)^{1/2}$ with respect to the incident photon energy ($h\nu$) and the $h\nu$ axis. This approach allowed for a precise determination of the IP^{PE}, facilitating a deeper understanding of the electron behavior and electronic properties of the studied materials.

UV–vis absorbance, photoluminescence (PL), and phosphorescence spectroscopy were used to study the optical properties of the compounds under investigation. For UV–vis absorbance spectra, solutions or films of the compounds were analyzed using an Avantes AvaSpec-2048XL spectrometer, which allowed us to assess the compounds' absorption characteristics across the ultraviolet and visible regions. Emission spectra of solutions and films were recorded using an Edinburgh Instruments FLS980 spectrometer, enabling a detailed investigation of the emission behavior of compounds. The choice of toluene, THF, and $CHCl_3$ as solvents in our study was based on their different polarities. By using these solvents, we aimed to investigate and visualize the charge transfer nature of the organic compounds under study through their spectra. To prepare the films, we used a spin-coating method by using a high-concentration THF solution (2 mg/mL). To study the phosphorescence spectra of Me-THF solutions, measurements were performed at an ultra-low temperature of 77 K, with and without a delay after excitation. This experimental setup ensured that we could capture the long-lived phosphorescence signals with high sensitivity and accuracy. To explore the temperature-dependent photoluminescence behavior of thin films, steady-state and time-resolved PL spectra were acquired using an Oxford Instruments Optistat DN2 cryostat, which was cooled with liquid nitrogen. The PL decay curves were obtained using a Pico-

Quant LDH-D-C-375 laser as the excitation source, operating at a wavelength of 374 nm, further allowing us to analyze the luminescence dynamics in detail. To determine photoluminescence quantum yields (PLQY), a dedicated integrated sphere with an inner diameter of 120 mm was used in conjunction with the Edinburgh Instruments FLS980 spectrometer. This specialized setup enabled accurate measurements of the PLQY, shedding light on the efficiency of light emission from the compounds. By employing this comprehensive array of spectroscopic techniques and experimental setups, we obtained a thorough understanding of the optical properties and luminescent characteristics of the studied compounds.

To accurately assess the hole and electron mobility in vacuum-deposited layers of the investigated compounds, we employed the time-of-flight (TOF) method, a reliable technique for characterizing charge transport in organic materials. Our TOF experiments involved samples with a structured configuration comprising indium–tin oxide (ITO) as the bottom electrode, a few µm thick organic layer as the active medium, and aluminum as the top electrode. The entire deposition process was carried out under a vacuum exceeding 2×10^{-6} mbar to ensure the integrity and purity of the layers. In our TOF setup, we utilized an EKSPLA NL300 laser, with a wavelength of 355 nm, as the excitation source to create charge carriers within the organic layer. By applying various positive and negative external voltages (U) to the samples using the Keithley precision 6517B electrometer, we were able to investigate hole and electron transport under different electric fields. To measure the transit time (t_{tr}) of charge carriers, we utilized the TDS 3032C oscilloscope by Tektronix to record the photocurrent transients of holes or electrons. Subsequently, we estimated the charge mobility (µ) using the formula $\mu = d^2/(U \times t_{\mathrm{tr}})$, where d represents the thickness of the organic layer, and U corresponds to the applied voltage over the sample.

Cyclic voltammetry (CV) measurements were conducted using a mAUTOLAB type III galvanostat, employing a glassy carbon working electrode in a three-electrode cell configuration. The experiments were carried out in a controlled environment with 0.1 M tetrabutylammonium hexafluorophosphate as the electrolyte and anhydrous dichloromethane as the solvent, maintaining room temperature conditions under a nitrogen atmosphere. To ensure accurate potential measurements, the system utilized silver as a quasireference electrode, while a platinum wire served as a counter electrode to facilitate the redox reactions. For calibration purposes, the potentials were standardized using the standard ferrocene/ferrocenium (Fc/Fc^+) redox system, a well-known and widely used reference for establishing electrochemical potential scales. The CV technique provided detailed cyclic voltammograms, allowing us to analyze the redox behavior and electrochemical properties of the compounds under investigation.

Supporting Information

Supporting Information File 1

Additional steady-state, time-resolved photoluminescence spectra, photoluminescence decay curves, charge transport characteristics, IR, and NMR spectra.
[https://www.beilstein-journals.org/bjoc/content/supplementary/1860-5397-19-139-S1.pdf]

Funding

This work was supported by the project of scientific co-operation program between Latvia, Lithuania, and Taiwan, "Synthesis and study of deep-blue TTF fluorescent emitters to exceed theoretical OLED external quantum efficiency reaching 15%" (grant LV-LT-TW/2023) and Research Council of Lithuania (LMTLT), agreement no. S-LLT-22-4. This project has also received funding from the Research Council of Lithuania (LMTLT), agreement No S-MIP-22-78.

ORCID® iDs

Karolis Leitonas - https://orcid.org/0000-0001-8070-0792
Dmytro Volyniuk - https://orcid.org/0000-0003-3526-2679
Pavels Dimitrijevs - https://orcid.org/0000-0002-6332-2395
Sindija Lapcinska - https://orcid.org/0000-0001-7745-8392
Pavel Arsenyan - https://orcid.org/0000-0001-5875-2799
Juozas Vidas Grazulevicius - https://orcid.org/0000-0002-4408-9727

References

1. Teng, J.-M.; Wang, Y.-F.; Chen, C.-F. *J. Mater. Chem. C* **2020,** *8,* 11340–11353. doi:10.1039/d0tc02682d
2. Bui, T.-T.; Goubard, F.; Ibrahim-Ouali, M.; Gigmes, D.; Dumur, F. *Beilstein J. Org. Chem.* **2018,** *14,* 282–308. doi:10.3762/bjoc.14.18
3. Liu, Y.; Li, C.; Ren, Z.; Yan, S.; Bryce, M. R. *Nat. Rev. Mater.* **2018,** *3,* 18020. doi:10.1038/natrevmats.2018.20
4. Liu, W.; Zheng, C.-J.; Wang, K.; Chen, Z.; Chen, D.-Y.; Li, F.; Ou, X.-M.; Dong, Y.-P.; Zhang, X.-H. *ACS Appl. Mater. Interfaces* **2015,** *7,* 18930–18936. doi:10.1021/acsami.5b05648
5. Vigante, B.; Leitonas, K.; Volyniuk, D.; Andruleviciene, V.; Simokaitiene, J.; Ivanova, A.; Bucinskas, A.; Grazulevicius, J. V.; Arsenyan, P. *Chem. – Eur. J.* **2019,** *25,* 3325–3336. doi:10.1002/chem.201805323
6. Hu, J.-X.; Jiang, S.; Zhang, D.-H.; Zhao, T.; Lin, F.-L.; Meng, L.; Chen, X.-L.; Lu, C.-Z. *Adv. Sci.* **2023,** *10,* 2300808. doi:10.1002/advs.202300808
7. Arsenyan, P.; Vigante, B.; Leitonas, K.; Volyniuk, D.; Andruleviciene, V.; Skhirtladze, L.; Belyakov, S.; Grazulevicius, J. V. *J. Mater. Chem. C* **2021,** *9,* 3928–3938. doi:10.1039/d0tc05745b

8. Liu, H.; Li, J.; Chen, W.-C.; Chen, Z.; Liu, Z.; Zhan, Q.; Cao, X.; Lee, C.-S.; Yang, C. *Chem. Eng. J.* **2020,** *401,* 126107. doi:10.1016/j.cej.2020.126107
9. Yang, H.; Li, C.; Liu, T.; Fellowes, T.; Chong, S. Y.; Catalano, L.; Bahri, M.; Zhang, W.; Xu, Y.; Liu, L.; Zhao, W.; Gardner, A. M.; Clowes, R.; Browning, N. D.; Li, X.; Cowan, A. J.; Cooper, A. I. *Nat. Nanotechnol.* **2023,** *18,* 307–315. doi:10.1038/s41565-022-01289-9
10. Leitonas, K.; Vigante, B.; Volyniuk, D.; Bucinskas, A.; Keruckiene, R.; Dimitrijevs, P.; Chiu, T.-L.; Grazulevicius, J. V.; Arsenyan, P. *J. Mater. Chem. C* **2023,** *11,* 9514–9526. doi:10.1039/d3tc00841j
11. Berenis, D.; Kreiza, G.; Juršėnas, S.; Kamarauskas, E.; Ruibys, V.; Bobrovas, O.; Adomėnas, P.; Kazlauskas, K. *Dyes Pigm.* **2020,** *182,* 108579. doi:10.1016/j.dyepig.2020.108579
12. Uoyama, H.; Goushi, K.; Shizu, K.; Nomura, H.; Adachi, C. *Nature* **2012,** *492,* 234–238. doi:10.1038/nature11687
13. Novikov, V. N.; Rössler, E. A. *Polymer* **2013,** *54,* 6987–6991. doi:10.1016/j.polymer.2013.11.002
14. Sworakowski, J. *Synth. Met.* **2018,** *235,* 125–130. doi:10.1016/j.synthmet.2017.11.013
15. Sallenave, X.; Shasti, M.; Anaraki, E. H.; Volyniuk, D.; Grazulevicius, J. V.; Zakeeruddin, S. M.; Mortezaali, A.; Grätzel, M.; Hagfeldt, A.; Sini, G. *J. Mater. Chem. A* **2020,** *8,* 8527–8539. doi:10.1039/d0ta00623h
16. Liu, H.; Li, J.; Chen, W.-C.; Lv, X.; Zhou, C.; Lee, C.-S.; Yang, C. *J. Phys. Chem. C* **2020,** *124,* 25489–25498. doi:10.1021/acs.jpcc.0c08430
17. Davis, R. J.; Lloyd, M. T.; Ferreira, S. R.; Bruzek, M. J.; Watkins, S. E.; Lindell, L.; Sehati, P.; Fahlman, M.; Anthony, J. E.; Hsu, J. W. P. *J. Mater. Chem.* **2011,** *21,* 1721–1729. doi:10.1039/c0jm02349c
18. Kane, E. O. *Phys. Rev.* **1962,** *127,* 131–141. doi:10.1103/physrev.127.131
19. Nakayama, Y.; Machida, S.; Tsunami, D.; Kimura, Y.; Niwano, M.; Noguchi, Y.; Ishii, H. *Appl. Phys. Lett.* **2008,** *92,* 153306. doi:10.1063/1.2908888

License and Terms

BEILSTEIN JOURNAL OF ORGANIC CHEMISTRY

Beyond n-dopants for organic semiconductors: use of bibenzo[*d*]imidazoles in UV-promoted dehalogenation reactions of organic halides

Kan Tang[1], Megan R. Brown[2], Chad Risko[2], Melissa K. Gish[3], Garry Rumbles[1,3,4], Phuc H. Pham[5], Oana R. Luca[1,5], Stephen Barlow*[1,3] and Seth R. Marder*[1,3,4,5]

Full Research Paper

Open Access

Address:
[1]Renewable and Sustainable Energy Institute (RASEI), University of Colorado Boulder, Boulder, Colorado 80309, United States, [2]Department of Chemistry & Center for Applied Energy Research (CAER), University of Kentucky, Lexington, Kentucky, 40506, United States, [3]National Renewable Energy Laboratory, Chemistry and Nanoscience Center, Golden, Colorado, 80401, United States, [4]Department of Chemical and Biological Engineering, University of Colorado Boulder, Boulder, Colorado 80309, United States, and [5]Department of Chemistry, University of Colorado Boulder, Boulder, Colorado 80309, United States

Email:
Stephen Barlow* - stephen.barlow@colorado.edu; Seth R. Marder* - seth.marder@colorado.edu

* Corresponding author

Keywords:
dehalogenation; n-dopant; reduction; reductive dimerization

Beilstein J. Org. Chem. **2023,** *19,* 1912–1922.
https://doi.org/10.3762/bjoc.19.142

Received: 27 September 2023
Accepted: 28 November 2023
Published: 14 December 2023

This article is part of the thematic issue "Organic electron transport materials".

Associate Editor: P. J. Skabara

Abstract

2,2’-Bis(4-dimethylaminophenyl)- and 2,2'-dicyclohexyl-1,1',3,3'-tetramethyl-2,2',3,3'-tetrahydro-2,2'-bibenzo[*d*]imidazole ((N-DMBI)$_2$ and (Cyc-DMBI)$_2$) are quite strong reductants with effective potentials of ca. −2 V vs ferrocenium/ferrocene, yet are relatively stable to air due to the coupling of redox and bond-breaking processes. Here, we examine their use in accomplishing electron transfer-induced bond-cleavage reactions, specifically dehalogenations. The dimers reduce halides that have reduction potentials less cathodic than ca. −2 V vs ferrocenium/ferrocene, especially under UV photoexcitation (using a 365 nm LED). In the case of benzyl halides, the products are bibenzyl derivatives, whereas aryl halides are reduced to the corresponding arenes. The potentials of the halides that can be reduced in this way, quantum-chemical calculations, and steady-state and transient absorption spectroscopy suggest that UV irradiation accelerates the reactions via cleavage of the dimers to the corresponding radical monomers.

Introduction

Reductive dehalogenation reactions of organic halides can be used in organic synthesis as a means of generating carbon-centered radical or anion intermediates and could have relevance to the treatment of waste halogenated polymers. While such reactions can be achieved using highly reducing metals, molecular reductants can potentially enable more selectivity, as required for the use of such reactions in the synthesis of molecules bearing various functional groups. In particular, Wanzlick dimers (C=C-bonded dimers of N-heterocyclic carbenes, Figure 1a, i) have been used by Murphy's group and others for a variety of transformations, such as the formation of indolines from *N*-allyl-2-iodoanilines [1], indanones from 3-(2-halophenyl)propanoic esters [2,3], and 3-methyl-2,3-dihydrobenzofuran from 1-allyloxy-2-halobenzenes [4]. Related species have also been used to initiate the coupling of aryl halides and arenes [5]. However, even relatively easily reduced organic halides have sufficiently cathodic reduction potentials (e.g., ca. −1.6 V and −1.8 vs ferrocenium/ferrocene ($FeCp_2^{+/0}$) for diethyl bromomalonate [6] and 4-iodotoluene, see Table 2, respectively) that simple one- or two-electron donors capable of exergonic ground-state electron transfer to these substrates will be rather air sensitive, complicating their handling and use. In addition some molecular reductants can themselves react with the reactive intermediates; for example, the dehalogenation of alkyl halides, RX, by $CoCp_2$ (Cp = η^5-cyclopentadienyl; E = −1.3 V vs $FeCp_2^{+/0}$), gives $CoCp_2^+$ and X^-, but the organic radicals $R^\bullet$ react with another molecule of $CoCp_2$ to afford $CoCp(\eta^4\text{-}C_5H_5R)$ [7]. In some cases, issues of reductant air

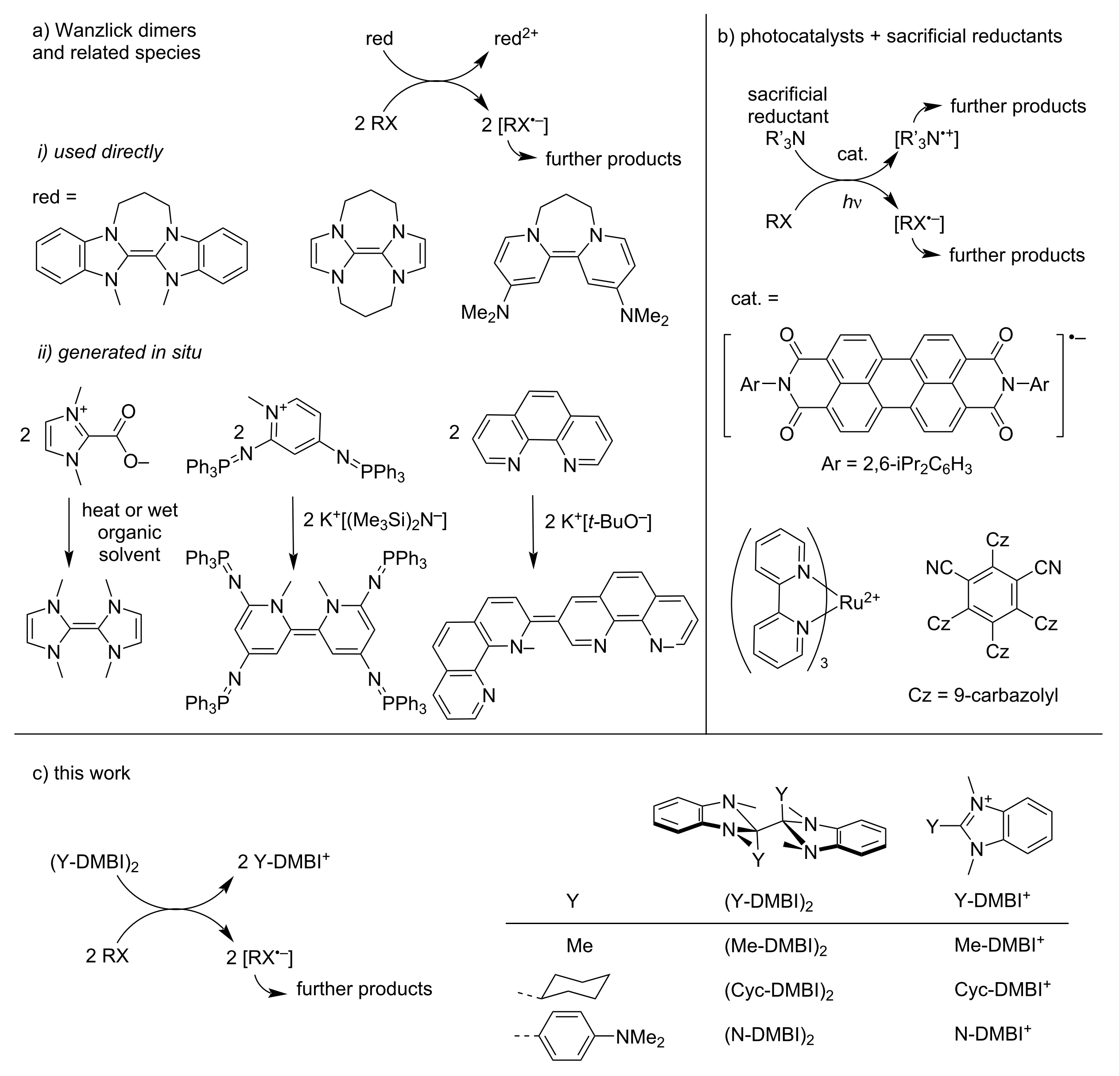

Figure 1: (a, b) Schematics of previous approaches to dehalogenation-based reactions using molecular reductants, along with representative structures of reductants and photocatalysts used, and (c) schematic for the present approach, along with structures of 1,1',3,3'-tetramethyl-2,2',3,3'-tetrahydro-2,2'-bibenzo[*d*]imidazoles, $(Y\text{-}DMBI)_2$, and the corresponding monomer cations, specifically the first reported in the literature and those used in this work.

sensitivity can be circumvented by the use of photocatalysts in concert with sacrificial weak reductants (Figure 1b) [8-11]. Another approach is to add ambient-stable precursors to reaction mixtures: for example, reducing Wanzlick dimers and related species (Figure 1a, ii) have been formed from precursors through in situ decarboxylation [12] or deprotonation [4,5], while other reducing species have been formed from in situ reactions of simple diols or diamines [13].

Another approach is to utilize dimers formed by highly reducing radicals, such the bibenzoimidazoles $(\text{Y-DMBI})_2$ (Figure 1c). $(\text{Me-DMBI})_2$ was first reported in 1984 and used as a reductant in studies of electrochemically generated reactive species [14-16]. More recently, several examples, including $(\text{Cyc-DMBI})_2$ (Y = cyclohexyl) and $(\text{N-DMBI})_2$ (Y = 4-dimethylaminophenyl) have been used as effective n-dopants for organic semiconductors [17-24] and redox mediators for the electrochemical depolymerization of poly(ethylene terephthalate) [25]. These dimers ($D_2 = (\text{Y-DMBI})_2$) undergo reactions with organic semiconductors A to afford two monomeric Y-DMBI^+ (D^+) cations and two reduced semiconductors, $A^{\bullet-}$. The effective redox potentials, $E(D^+/0.5D_2)$, are estimated to be ca. −2 V vs $\text{FeCp}_2^{+/0}$, yet the dimers are reasonably stable to air due to the kinetic barriers associated with the coupling of electron-transfer and bond-cleavage reactions [26]. Here we demonstrate that $(\text{N-DMBI})_2$ and $(\text{Cyc-DMBI})_2$ (Figure 1c) can be used to accomplish dehalogenation of benzyl, alkyl, and aryl halides (RX) and discuss the scope and possible mechanism of these reactions.

Results and Discussion

Reaction of $(\text{Y-DMBI})_2$ with benzyl bromide

We began our investigations of dehalogenation reactions using benzyl bromide (BnBr, **1a**), which has a reduction peak potential (E_{pc}) of −1.6 V vs $\text{FeCp}_2^{+/0}$, as the substrate (RX), anhydrous THF (without stabilizer) as the solvent, and $(\text{N-DMBI})_2$ or $(\text{Cyc-DMBI})_2$ as a stoichiometric reductant (0.5 equiv, assuming one electron is needed for each substrate molecule and that each dimer molecule contributes two electrons). Reaction outcomes were analyzed by GC–MS (see Supporting Information File 1 for details); products were identified based on the observed *m*/*z* values and comparison of retention times with authentic samples, while conversions and yields were based on calibration curves established using authentic samples. Table 1 summarizes the conversion of BnBr and product yields at various reaction times, with or without dimers, and with or without irradiation at a nominal wavelength of 365 nm (see Supporting Information File 1 for experimental details and

Table 1: Debromination of benzyl bromide (**1a**).

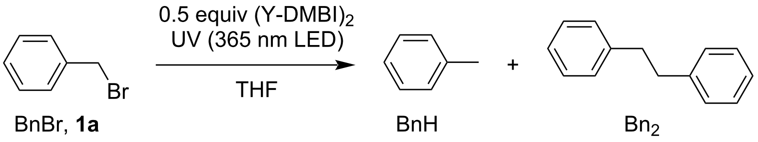

Entry	Time [h]	UV	[BnBr] [mM][a]	Reductant	Conversion [%][b]	BnH yield [%][b]	Bn_2 yield [%][b]
1	1	no	3.0	$(\text{N-DMBI})_2$	20	13	10
2	0.5	yes	3.0	$(\text{N-DMBI})_2$	90	8.6	82
3	1	yes	3.0	$(\text{N-DMBI})_2$	100	9	92
4	1	no	3.0	$(\text{Cyc-DMBI})_2$	10	5	5
5	0.5	yes	3.0	$(\text{Cyc-DMBI})_2$	70	4	65
6	1	yes	3.0	$(\text{Cyc-DMBI})_2$	100	4	95
7	1	no	18.7	$(\text{N-DMBI})_2$	29	7.5	22
8	2	no	18.7	$(\text{N-DMBI})_2$	39	9	30
9	18	no	18.7	$(\text{N-DMBI})_2$	61	7	52
10	1	yes	18.7	$(\text{N-DMBI})_2$	70	6	66
11	2	yes	18.7	$(\text{N-DMBI})_2$	80	6	74
12	2	yes	18.7	–	6	6	–[c]
13	4	yes	18.7	$(\text{N-DMBI})_2$	92	6	86
14	18	yes	18.7	$(\text{N-DMBI})_2$	100	8	93
15	18	yes	18.7	–	61	58	–[c]

[a] 3.0 and 18.7 mM BnBr concentrations used, BnBr in quantities of 12 and 75 µmol (2 and 13 mg), respectively, corresponding to dimer quantities of 6.0 and 37.5 µmol, respectively (3.2 and 20 mg for $(\text{N-DMBI})_2$; 2.8 and 17 mg for $(\text{Cyc-DMBI})_2$. [b] Conversions and yields were determined by GC–MS as described in Supporting Information File 1. [c] None detected.

see [27] for the spectrum of the excitation source used), which is anticipated to selectively excite the dimeric reductants rather than the substrate (see below and Supporting Information File 1, Figure S4 for further details). In the dark at low concentrations of substrate and reductant low conversions are observed after 1 h (Table 1, entry 1), with the dehalogenation products being a mixture of toluene and bibenzyl, i.e., RH and R_2 products, which were identified by the masses observed through GC–MS and through comparison of the GC–MS retention times with authentic samples. Higher concentrations and reaction times (entries 7–9 in Tabe 1) lead to larger extents of conversion (up to 61% at 18 h) and favor formation of bibenzyl over toluene (up to 52% yield at 18 h). $[BnBr]^{•−}$ presumably cleaves to afford $Bn^•$, which can react further to form Bn_2 (see following section) or can form toluene through reaction with THF, which is known to have a reasonably weak α-CH bond and act as a $H^•$ donor towards many radicals [28-31].

The reaction is substantially accelerated by UV excitation at 365 nm; quantitative conversion of benzyl bromide at low initial concentration (3 mM) can be achieved within 1 h using both $(N\text{-DMBI})_2$ or $(Cyc\text{-DMBI})_2$ and UV (Table 1, entries 3 and 6), while even at higher substrate concentrations (18.7 mM) 80% and near-quantitative (>90%) conversions can be obtained using $(N\text{-DMBI})_2$ within 2 h and 4 h, respectively (Table 1, entries 11 and 13). We also investigated the impact of photoexcitation in the absence of the dimeric reductant; however, extents of conversion are much lower for a given reaction time (compare entries 12 and 15 to 11 and 14 in Table 1) and the sole detected product is toluene rather than bibenzyl.

Furthermore, in one of the cases of complete conversion (Table 1, entry 14), ^1H NMR spectroscopy indicated that the reductant-based side product is a salt of the monomeric cation $N\text{-DMBI}^+$ (Supporting Information File 1, Figure S15). Thus, the overall reaction is consistent with:

$$(N\text{-DMBI})_2 + 2BnBr \longrightarrow 2(N\text{-DMBI})^+ + 2Br^- + Bn_2 \quad (1)$$

Scope of reaction $(Y\text{-DMBI})_2$ with other benzyl, alkyl, and aryl halides

Table 2 summarizes the conversions and product yields for the reactions of $(N\text{-DMBI})_2$ or $(Cyc\text{-DMBI})_2$ with several other benzyl halides (**1b–e**), an alkyl halide **2**, and several aryl halides (**3a–f**). Again GC–MS was used to identify and quantify the products; the necessary authentic samples were mostly commercially available, but the R_2 products from **1b** and **1c** were not, although well-known in the literature (for example, see ref. [32]), and were synthesized as described in Supporting Information File 1. More complete data are shown in Supporting Information File 1, Tables S1 and S2. As in the case of **1a**, conversions and yields under UV irradiation in the absence of reductant are low on a 2 h timescale (≤10%) and the main products are those in which the halide is replaced by a hydrogen atom. The more easily reduced benzyl halides examined (**1b** and **1c**) are dehalogenated by $(N\text{-DMBI})_2$ in the dark, and with $(N\text{-DMBI})_2$ and UV irradiation are quantitatively dehalogenated in 2–6 h with the corresponding substituted bibenzyls being the dominant products. These reaction conditions represent an alternative metal-free approach to the conventional synthesis of bibenzyls through the reaction of Grignard or organolithium reagents with benzyl halides, or to the use of highly active metal reagents [33-36] or metal-containing catalysts [32]. We note that another all-organic reductive dimerization of benzyl halides using 2,3,5,6-tetrakis(tetramethylguanidino)pyridine has recently been reported [37]. The less readily reduced halides examined here (**1d**,**e**, and **2**) are only sluggishly converted, even when using both $(N\text{-DMBI})_2$ (or $(Cyc\text{-DMBI})_2$) and light. Moreover, in the cases of **1d** and **1e** there are significant mismatches between conversion and the yields of the corresponding RH and R_2 species, indicating that additional products must be formed. Indeed, in the case of 4-methylbenzyl chloride GC–MS shows a product with a mass consistent with the formation of 4-methylbenzyl-substituted THF (see Supporting Information File 1, Figure S2) and a somewhat better R_2 yield is obtained in toluene (see Table S2). For 1-bromooctadecane (**2**), around half the product obtained using $(N\text{-DMBI})_2$ and UV is RH, i.e., octadecane. The remaining unidentified product may be R_2 ($C_{36}H_{74}$), but this product is not easily detected by GC–MS.

In sharp contrast to the case of benzyl derivatives, where the use of dimer reductants primarily affords R_2 products, biaryls are not observed as dehalogenation products of aryl halides by dimeric reductants and/or light. This may be attributable to the lower stability and greater reactivity of aryl radicals relative to that of their benzyl counterparts. Indeed, aryl radicals are known to abstract $H^•$ from THF [30,31] and presumably do so in the present reactions before any further reactions can occur. Resonance-stabilized benzyl radicals, on the other hand, are sufficiently long-lived to react further to afford dimeric bibenzyl derivatives (especially at higher concentrations or when photoirradiation is used, presumably affording higher steady-state $[R^•]$ concentrations). In principle, this is possible by either dimerization of $2R^•$ or by a second reduction of $R^•$ to $R^−$ (as invoked in the reductive cyclization of (2-halophenyl)propanoic esters [2]) which then acts as a nucleophile towards a second molecule of RX. However, addition of Me_3SiCl to a photoirradiated $BnBr/(N\text{-DMBI})_2$ reaction mixture did not lead to any detectable $BnSiMe_3$, thus supporting a radical dimerization pathway (see Supporting Information File 1, Table S3).

Table 2: Dehalogenation of various benzyl, alkyl, and aryl halides using $(\text{N-DMBI})_2$ (or, in parentheses Cyc-DMBI$)_2$.[a]

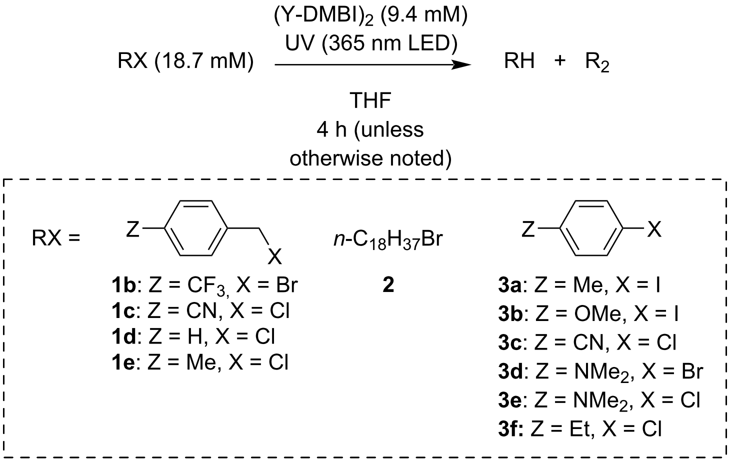

RX	E_{pc} [V][b]	Conversion [%][c]	RH yield [%][c]	R$_2$ yield [%][c]
1a	−1.6	92	6	86
1b	−1.5	80	2	75
1c	−1.6	100	14	86
1d	−2.3	39	7	5
1e	−2.4	73 (60)	3 (3)	3 (32)
2	−2.1	39	19	–[d]
3a[e]	−1.8	98	98	–[f]
3b[e]	−1.6	99	99	–[f]
3c	−1.6	55 (99)	41 (60)	–[f] (–[f])
3d	−2.4	5 (5)	5 (5)	–[f]
3e	−2.5	4 (2)	0 (2)	–[f]
3f	−2.4	1 (<1)	1 (<1)	–[f]

[a]The reaction scale in each case was 75 µmol (9.5–25 mg) RX and 37.5 µmol dimer (20 and 17 mg for $(\text{N-DMBI})_2$ and $(\text{Cyc-DMBI})_2$, respectively). [b]Peak reduction potential vs $\text{FeCp}_2^{+/0}$ in THF/0.1 M Bu_4NPF_6 (see Supporting Information File 1, Figures S7 and S8). [c]Conversions and yields were determined by GC–MS as described in Supporting Information File 1. [d]Likely not detectable by GC–MS. [e]2 h reaction time. [f]None detected.

As in the case of sp^2 R–X systems, only small extents of dehalogenation for R = aryl are observed in the absence of reductants. For the more easily reduced aryl halides (**3a**–**c**), moderate to high extents of conversion are obtained in the dark using dimeric reductants, while higher extents, in some cases near-quantitative in 2 h, are obtained using UV and reductants. In the case of **3a** and **3b** the conversion and yields of the RH compounds are in good agreement, while discrepancies in the case of **3c** indicate additional side reactions.

The observation that some of the organic halides tested in Table 2 are cleanly dehalogenated and others essentially unreactive suggested the possibility of selective dehalogenation of compounds containing different halogenated functionalities. Specifically, we examined 2-iodobenzyl chloride, in which the C–I and C–Cl bond strengths are expected to be fairly similar (C–X bond dissociation enthalpies of 280 and 310 kJ mol^{-1} have been reported for BnCl and PhI, respectively [38]), but the aryl–I bond is likely to be better coupled to the reduction process (given the reduction potentials in Table 2). As shown in Scheme 1, we found 2-iodobenzyl chloride is cleanly converted to benzyl chloride under the standard conditions used in Table 2 (see Supporting Information File 1, Table S4 for more details). This selectivity is not typically achievable using electropositive metals and may be of use in more elaborate chemical transformations.

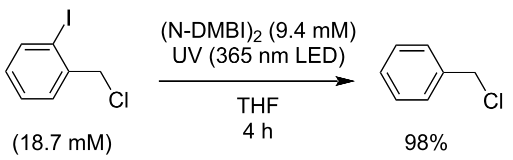

Scheme 1: Selective deiodination of 2-iodobenzyl chloride.

Mechanism of dark reactions

Doping of organic semiconductors by (Y-DMBI)$_2$ dimers [18,39] or by various dimers formed by 18-electron sandwich compounds [18,40,41], as well as redox reactions of other dimers formed by organic radicals [42,43], are known to proceed by two distinct pathways. When the dimer (D$_2$) is relatively weakly bound, its dissociation to D$^•$ can be the initial step (“cleavage-first”), which is then followed by fast electron-transfer (ET) reactions (Scheme 2). On the other hand, in the “electron-transfer first” mechanism, the first step is an ET reaction, resulting in the formation of D$_2^{•+}$, which subsequently cleaves to form D$^+$ and D$^•$, which is much more readily oxidized than the dimer itself and thus participates in a second fast ET (Scheme 2). In the present case, knowledge of the operative mechanism(s) is important to understand what substrates might be cleavable on what timescales in the dark; in particular, if the cleavage-first mechanism is viable, substrates with E_{red} as cathodic as, roughly, E(D$^+$/D$^•$), should react, whereas more strongly bonded dimers might not react with the most challenging of these substrates due to the non-viability of the cleavage-first mechanism and prohibitively endergonic initial steps for the ET-first mechanism.

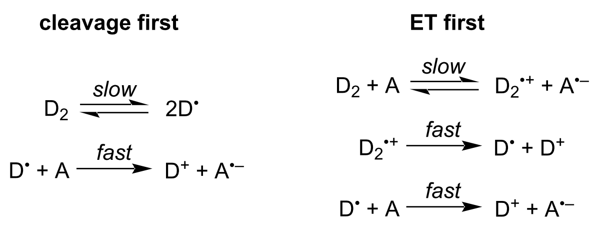

Scheme 2: Reaction mechanisms for the reactions of dimeric reductants (D$_2$) such as (Y-DMBI)$_2$ derivatives with acceptors (A) such as organic semiconductors or, in this work, organic halides that react further (the relative rates of steps are indicated for cases where the A reduction potential falls between D$_2$ and D$^•$ oxidation potentials).

We investigated the dark reactions of the two dimers with BnBr in THF, using GC–MS to determine RX conversion and R$_2$ and RH yields at various time intervals, as shown in the example of Figure 2a. We repeated these experiments for a variety of different initial reductant and RX concentrations, [D$_2$]$_0$ and [RX]$_0$ (see Supporting Information File 1, Figure S3), and plotted the initial rate normalized for dimer concentrations, (d[RX]/dt)$_0$/[D$_2$]$_0$, vs [RX]$_0$ (Figure 2b). In the case of D$_2$ = (Cyc-DMBI)$_2$, a linear plot with approximately zero intercept is obtained, consistent with a reaction first order in [RX] and [D$_2$], as expected if the reaction proceeds via an initial rate-determining ET. On the other hand, in the case of D$_2$ = (N-DMBI)$_2$, the linear plot has a distinctly non-zero intercept, a behavior which conforms with a rate law consisting of the sum of two terms, one first order in [D$_2$] and one first order in both [D$_2$] and [RX]

$$-(1/2)d[\mathrm{RX}]/dt = k_{\mathrm{cl}}[\mathrm{D}_2] + k_{\mathrm{ET}}[\mathrm{D}_2][\mathrm{RX}] \qquad (2)$$

and is similar to doping behavior we have recently seen for some weakly bonded dimers where both “cleavage-first” and

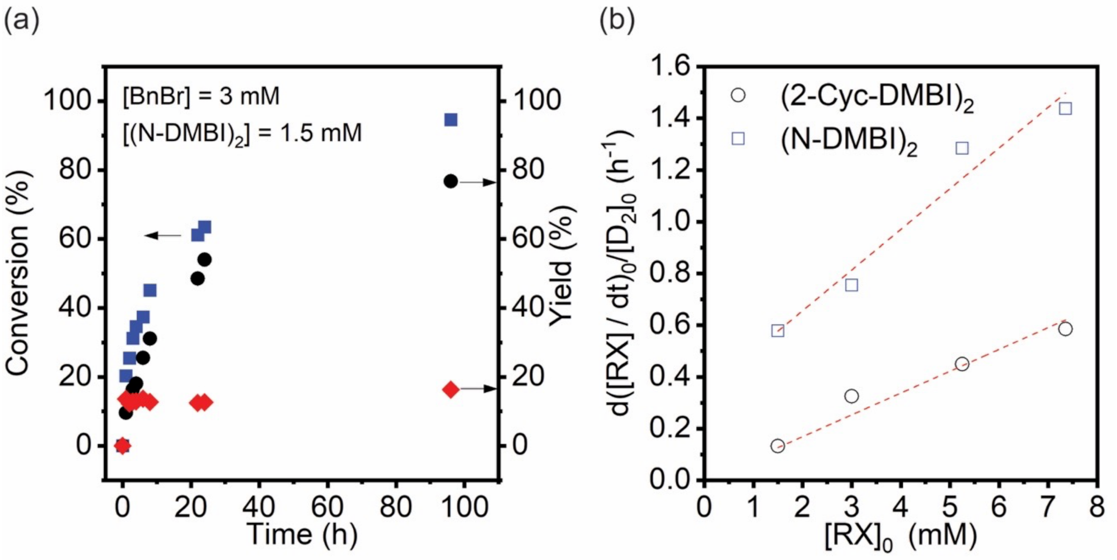

Figure 2: (a) A representative temporal evolution of % conversion (blue squares), % toluene yield (red diamonds), and % bibenzyl yield (black circles) during the dark dehalogenation reaction of benzyl bromide (BnBr) using (N-DMBI)$_2$ in THF (these data were acquired using 3 mM BnBr and 1.5 mM of (N-DMBI)$_2$. (b) Plot of [D$_2$]$_0$-normalized initial reaction rate (d([RX]/dt)$_0$/[D$_2$]$_0$) as a function of the initial benzyl bromide concentration ([RX]$_0$) obtained from several experiments of the type shown in part (a) for different [D$_2$] and [RX] for both D$_2$ = (Cyc-DMBI)$_2$ and (N-DMBI)$_2$. For these slow reactions, the “initial” rates were estimated from the change of substrate concentration over the first 30 min reaction time.

“ET-first” mechanisms are competitive. In the case of (Cyc-DMBI)$_2$, the second-order rate constant, k_{ET}, is estimated as 6.0×10^{-3} M^{-1} s^{-1}, whereas for (N-DMBI)$_2$, $k_{\mathrm{cl}} = 4.7 \times 10^{-5}$ s^{-1} and $k_{\mathrm{ET}} = 1.0 \times 10^{-2}$ M^{-1}s^{-1}. The difference in k_{ET} values is qualitatively consistent with the peak oxidation potentials, $E_{\mathrm{pa}}(\mathrm{D_2}^{\bullet+}/\mathrm{D_2})$, of the two dimers; values of −0.06 and −0.13 V vs $\mathrm{FeCp_2}^{+/0}$ are found for (Cyc-DMBI)$_2$ and (N-DMBI)$_2$, respectively [18,44], indicating that ET from the former to benzyl bromide is more endergonic than from the latter. The rate constant for (Cyc-DMBI)$_2$-to-BnBr ET is also much smaller than that previously determined for the doping of 6,13-bis(triisopropylsilylethynyl)pentacene (TIPS-pentacene, $E_{1/2}{}^{0/-} = -1.45$ V, $k_{\mathrm{ET}} \approx 0.15$ M^{-1}s^{-1}) by (Cyc-DMBI)$_2$ [18], consistent with the differences in the reduction potentials between BnBr and TIPS-pentacene. The observation of the “cleavage-first” mechanism for (N-DMBI)$_2$ and not for (Cyc-DMBI)$_2$ is consistent with DFT estimates of bond dissociation energies for these two dimers (ΔU_{diss} = 163 and 210 kJ mol^{-1}, respectively [18,44]) and with their reactivity towards TIPS-pentacene [18,39].

Impact of photoexcitation

The absorptivities, ε, of (N-DMBI)$_2$ and (Cyc-DMBI)$_2$ at 365 nm in THF are ca. 420 and 43 M^{-1} cm^{-1}, respectively. Figure 3a and b show the absorption spectra of the two dimeric reductants in THF (see Supporting Information File 1, Figure

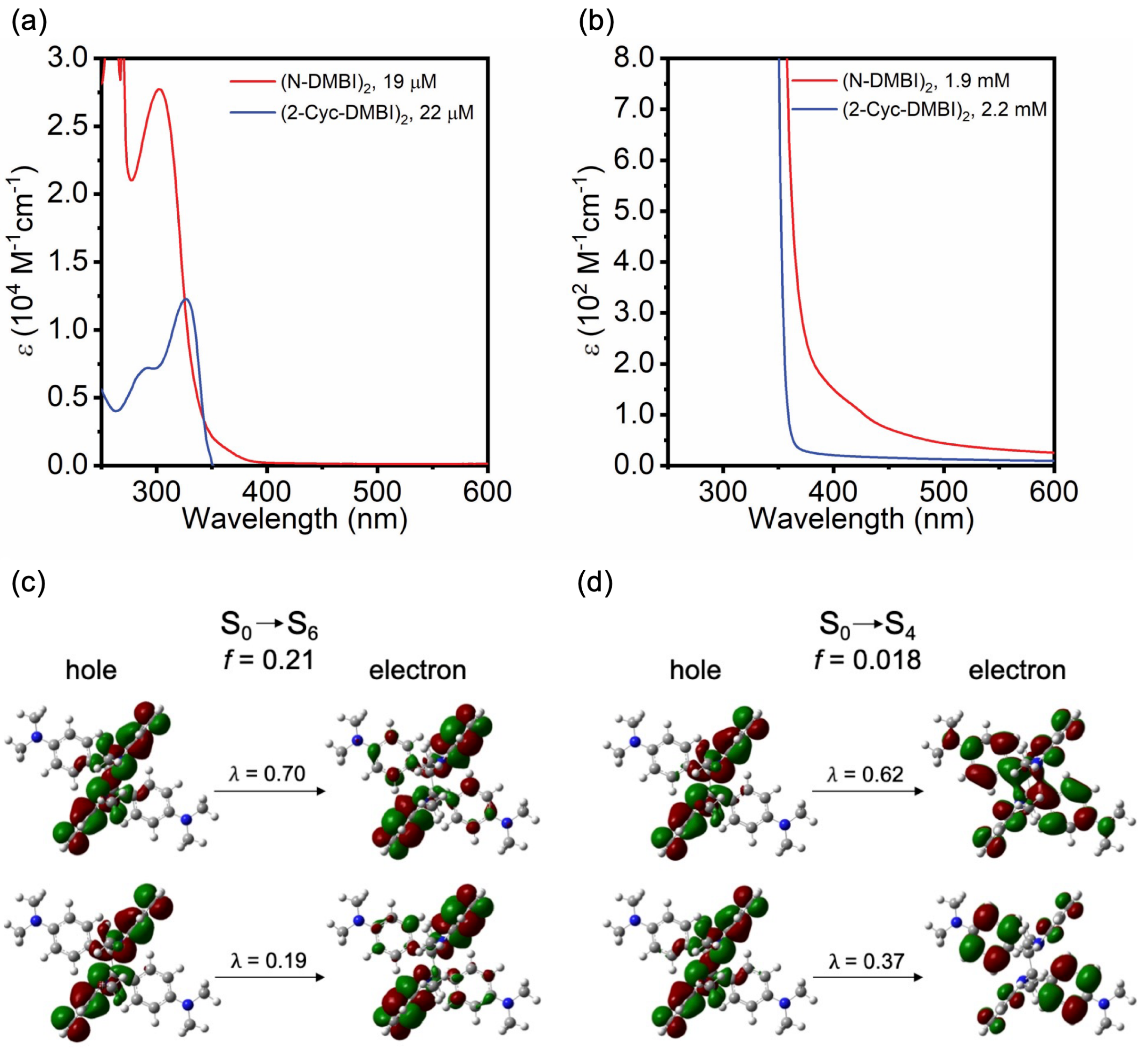

Figure 3: Top: UV–vis absorption spectra for the two dimeric reductants in THF emphasizing (a) the different positions of the relatively strong absorption peaks and (b) the presence of a low-energy shoulder in the spectrum of (N-DMBI)$_2$. Bottom: TD-DFT (M06/6-31G(d, p)) natural transition orbitals for selected (N-DMBI)$_2$ transitions that are thought to be primarily responsible for (c) the main absorption peak and (d) the weak shoulder seen experimentally.

S6 for data in toluene). (N-DMBI)$_2$ shows a strong absorption feature with a maximum at 304 nm (ε_{max} = 28000 M^{-1} cm^{-1}) and a weak shoulder at ca. 400 nm (ε_{400} ≈ 150 M^{-1} cm^{-1}), whereas (Cyc-DMBI)$_2$ exhibits only a strong feature with a maximum at 327 nm (ε_{max} = 13000 M^{-1} cm^{-1}). TD-DFT calculations (M06/6-31G(d,p), isolated molecules) qualitatively reproduce the different behavior of the two dimers: for (Cyc-DMBI)$_2$ the $S_0 \rightarrow S_1$ transition is calculated to be strong (oscillator strength, f = 0.27). The natural transition orbitals (NTOs, see Supporting Information File 1, including Figure S10, for more information) indicate that this excitation is largely confined to the bibenzoimidazole portion of the molecule. In the case of (N-DMBI)$_2$ the lowest reasonably strong (f = 0.21) transition is $S_0 \rightarrow S_6$ and has bibenzoimidazole-dominated NTOs (Figure 3c) similar to those for the $S_0 \rightarrow S_1$ transition of (Cyc-DMBI)$_2$, but is seen at higher energy. The strongest of the weaker lower energy transitions are $S_0 \rightarrow S_4$ (f = 0.018), which is calculated to lie lower in energy than the $S_0 \rightarrow S_1$ transition of (Cyc-DMBI)$_2$ and presumably corresponds to the shoulder observed in the experimental spectrum of (N-DMBI)$_2$, and $S_0 \rightarrow S_5$, which lies very close to $S_0 \rightarrow S_6$. For both of these transitions, the NTOs indicate considerable charge transfer from the bibenzo-imidazole portion of the molecules to the $C_6H_4NMe_2$ Y substituents (see Figure 3d and Supporting Information File 1, Figure S11).

Most of the above-mentioned substrates exhibit little or no absorption at 365 nm (see Supporting Information File 1, Figure S4 for comparison of spectra of the reductants and BnBr); thus, although slight overlap between the tail of substrate absorption and the tail of the output of the nominally 365 nm LED may be responsible for the reactivity seen in the absence of dimeric reductants, the stronger absorption of the two dimeric reductants examined suggests photo-acceleration of the reactions involves the excited states of the dimers. In principle excitation of the dimers might result in cleavage of the dimers to the corresponding radical monomers, $D^{\bullet}$, which can then reduce RX, or to ET from dimer excited states, D_2*, to RX. The results in Table 2 support the former effect: if photoinduced cleavage occurs we would expect the scope of RX cleavage to be more-or-less limited by the reducing strength of $D^{\bullet}$ ($E(D^{+}/D^{\bullet})$ = ca. −2.4 V for both species used here), whereas the singlet excited state of the dimer, D_2*, should be more reducing, allowing more challenging substrates to be reduced ($E(D_2^{\bullet+}/D_2^*)$ can be estimated as ca. −3.4 and −2.8 V for (Cyc-DMBI)$_2$ and (Cyc-DMBI)$_2$, respectively, using values of $E(D_2^{\bullet+}/D_2)$ and estimated absorption onsets). Furthermore, the NTOs for the strong absorptions of both dimers and the weak low-energy absorption of (N-DMBI)$_2$ both involve some depopulations of the bibenzoimidazole-based HOMO, which, as well as π-character also has significant C–σ-bonding character associated with the inter-monomer bond, suggesting that excitation should weaken the bond (in a similar way to oxidation associated with removal of an electron from the same orbital). To investigate this possibility in more detail we recorded transient absorption spectra of the dimers following excitation at 350 nm. Importantly, the samples did not degrade during the experiment, indicating that the species observed eventually reform the dimers. The transient absorption spectra of (N-DMBI)$_2$ (Figure 4a) show significant spectral evolution within the first 1 ps following photoexcitation at 350 nm in MeCN. The (negative) bleach feature at 450 nm and photoinduced absorption (PIA) peaking at 775 nm transform into a broad PIA spanning the visible wavelengths with a notable isosbestic point at 600 nm. There is a secondary evolution occurring with a time constant of approximately 60 ps resulting in a long-lived feature existing beyond the 5 ns window of the ultrafast experiment. In toluene (Figure 4b), the spectral features at early times are different; however, the kinetics at 654 nm are the same between solvents suggesting that the initial features dominating the spectra at 250 fs in MeCN are present in toluene.

The (Cyc-DMBI)$_2$ exhibits faster decay kinetics (Figure 4c) than (N-DMBI)$_2$ under the same experimental conditions. The spectral shape is similar to the late time spectra of the (N-DMBI)$_2$ with a broad PIA spanning the visible wavelengths, which may suggest that the initial evolution observed in the (N-DMBI)$_2$ occurs within our instrument response. In toluene, the signal amplitude at 5 ns for (Cyc-DMBI)$_2$ is significantly smaller than that of the (N-DMBI)$_2$ and 96% of the signal amplitude at 654 nm decays with a 1 ps lifetime. The isosbestic point in Figure 4a is consistent with a clean transformation such as monomer formation. The corresponding monomeric radicals are calculated using TD-DFT (M06/6-31G(d,p)) (Figure 4e) to have absorptions at similar energies to those seen in the longer-time spectra with Cyc-DMBI$^{\bullet}$ having a blue-shifted absorption relative to N-DMBI$^{\bullet}$, consistent with the observed features arising from the monomeric radicals. Intersystem crossing (ISC) from the singlet to triplet excited state is also a possibility and TD-DFT calculations suggest that the dimer T_1 states absorb at similar wavelengths to the monomer radicals (see Supporting Information File 1, Figure S12). However, ISC is typically much slower than 1 ps in organic molecules, especially so for those lacking heavy atoms [45].

Conclusion

Dimeric reductants of the (Y-DMBI)$_2$ type can accomplish the dehalogenation of a variety of organic halides with peak reduction potentials less cathodic than ca. −2.0 V vs $FeCp_2^{+/0}$, affording essentially quantitative conversions in a few hours under 365 nm illumination. In the case of benzyl halides the primary products are bibenzyls, some of which may be

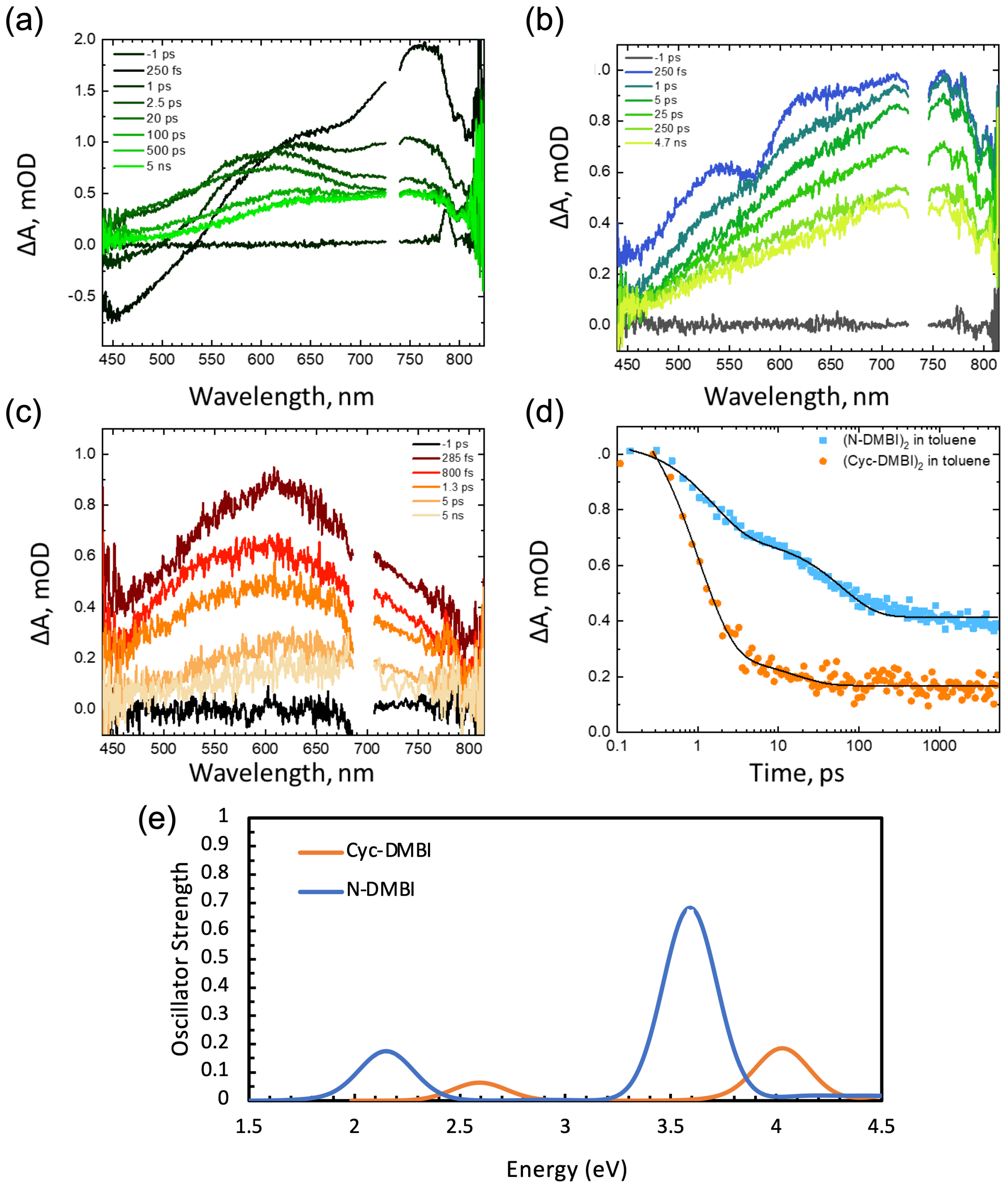

Figure 4: Transient absorption spectra of (a) $(N\text{-}DMBI)_2$ in MeCN, (b) $(N\text{-}DMBI)_2$ in toluene, and (c) $(Cyc\text{-}DMBI)_2$ in toluene with excitation at 350 nm in the absence of oxygen. (d) Comparison of temporal evolution of the absorption at 654 nm for both dimers in toluene. (e) Spectra for the two monomeric radicals obtained from M06/6-31G(d,p) TD-DFT calculations.

challenging to synthesize by other methods, whereas aryl halides afford dehalogenated arenes. One example also demonstrates that the approach may have utility for selectively dehalogenating compounds containing different halogens. The photoacceleration of these reactions appears to occur through photocleavage of the dimers to the more strongly reducing monomers, which may help inform the use of these and related reductants in achieving other chemical transformations.

Supporting Information

Supporting Information File 1

Synthetic and other experimental procedures, additional data, additional TD-DFT results, and NMR spectra of compounds.
[https://www.beilstein-journals.org/bjoc/content/supplementary/1860-5397-19-142-S1.pdf]

Funding

This work was authored in part by the National Renewable Energy Laboratory (NREL), operated by Alliance for Sustainable Energy, LLC, for the U.S. Department of Energy (DOE) under Contract No. DE-AC36-08GO28308. This work was primarily supported by the Laboratory Directed Research and Development (LDRD) Program at NREL. The DFT and TD-DFT calculations, performed at the University of Kentucky, were supported by the Center for Soft PhotoElectroChemical Systems (SPECS), an Energy Frontier Research Center funded by the U.S. Department of Energy, Office of Science, Basic Energy Sciences under award No. DE-SC0023411. The views expressed in the article do not necessarily represent the views of the DOE or the U.S. Government. The U.S. Government retains and the publisher, by accepting the article for publication, acknowledges that the U.S. Government retains a nonexclusive, paid-up, irrevocable, worldwide license to publish or reproduce the published form of this work, or allow others to do so, for U.S. Government purposes.

ORCID® iDs

Kan Tang - https://orcid.org/0000-0003-0012-0224
Megan R. Brown - https://orcid.org/0000-0003-3105-4688
Chad Risko - https://orcid.org/0000-0001-9838-5233
Phuc H. Pham - https://orcid.org/0000-0002-7086-6948
Oana R. Luca - https://orcid.org/0000-0002-2988-4909
Stephen Barlow - https://orcid.org/0000-0001-9059-9974
Seth R. Marder - https://orcid.org/0000-0001-6921-2536

References

1. Murphy, J. A.; Khan, T. A.; Zhou, S.-z.; Thomson, D. W.; Mahesh, M. *Angew. Chem., Int. Ed.* **2005,** *44,* 1356–1360. doi:10.1002/anie.200462038
2. Murphy, J. A.; Zhou, S.-z.; Thomson, D. W.; Schoenebeck, F.; Mahesh, M.; Park, S. R.; Tuttle, T.; Berlouis, L. E. A. *Angew. Chem., Int. Ed.* **2007,** *46,* 5178–5183. doi:10.1002/anie.200700554
3. Murphy, J. A.; Garnier, J.; Park, S. R.; Schoenebeck, F.; Zhou, S.-z.; Turner, A. T. *Org. Lett.* **2008,** *10,* 1227–1230. doi:10.1021/ol800134g
4. Hanson, S. S.; Doni, E.; Traboulsee, K. T.; Coulthard, G.; Murphy, J. A.; Dyker, C. A. *Angew. Chem., Int. Ed.* **2015,** *54,* 11236–11239. doi:10.1002/anie.201505378
5. Zhou, S.; Anderson, G. M.; Mondal, B.; Doni, E.; Ironmonger, V.; Kranz, M.; Tuttle, T.; Murphy, J. A. *Chem. Sci.* **2014,** *5,* 476–482. doi:10.1039/c3sc52315b
6. Huang, M.; Tang, J.; Kim, J. K.; Gong, M.; Zhang, J.; Li, Y.; Wu, Y. *Org. Biomol. Chem.* **2022,** *20,* 6459–6463. doi:10.1039/d2ob00835a
7. Herberich, G. E.; Bauer, E.; Schwarzer, J. *J. Organomet. Chem.* **1969,** *17,* 445–452. doi:10.1016/s0022-328x(00)88230-3
8. Narayanam, J. M. R.; Tucker, J. W.; Stephenson, C. R. J. *J. Am. Chem. Soc.* **2009,** *131,* 8756–8757. doi:10.1021/ja9033582
9. Furst, L.; Matsuura, B. S.; Narayanam, J. M. R.; Tucker, J. W.; Stephenson, C. R. J. *Org. Lett.* **2010,** *12,* 3104–3107. doi:10.1021/ol101146f
10. Ghosh, I.; Ghosh, T.; Bardagi, J. I.; König, B. *Science* **2014,** *346,* 725–728. doi:10.1126/science.1258232
11. Constantin, T.; Zanini, M.; Regni, A.; Sheikh, N. S.; Juliá, F.; Leonori, D. *Science* **2020,** *367,* 1021–1026. doi:10.1126/science.aba2419
12. Tintori, G.; Fall, A.; Assani, N.; Zhao, Y.; Bergé-Lefranc, D.; Redon, S.; Vanelle, P.; Broggi, J. *Org. Chem. Front.* **2021,** *8,* 1197–1205. doi:10.1039/d0qo01488e
13. Zhou, S.; Doni, E.; Anderson, G. M.; Kane, R. G.; MacDougall, S. W.; Ironmonger, V. M.; Tuttle, T.; Murphy, J. A. *J. Am. Chem. Soc.* **2014,** *136,* 17818–17826. doi:10.1021/ja5101036
14. Ludvík, J.; Volke, J.; Pragst, F. *J. Electroanal. Chem. Interfacial Electrochem.* **1986,** *215,* 179–190. doi:10.1016/0022-0728(86)87014-0
15. Ludvík, J.; Pragst, F.; Volke, J. *J. Electroanal. Chem. Interfacial Electrochem.* **1984,** *180,* 141–156. doi:10.1016/0368-1874(84)83576-5
16. Pragst, F.; Niazymbetov, M. *J. Electroanal. Chem. Interfacial Electrochem.* **1986,** *197,* 245–264. doi:10.1016/0022-0728(86)80153-x
17. Naab, B. D.; Zhang, S.; Vandewal, K.; Salleo, A.; Barlow, S.; Marder, S. R.; Bao, Z. *Adv. Mater. (Weinheim, Ger.)* **2014,** *26,* 4268–4272. doi:10.1002/adma.201400668
18. Zhang, S.; Naab, B. D.; Jucov, E. V.; Parkin, S.; Evans, E. G. B.; Millhauser, G. L.; Timofeeva, T. V.; Risko, C.; Brédas, J.-L.; Bao, Z.; Barlow, S.; Marder, S. R. *Chem. – Eur. J.* **2015,** *21,* 10878–10885. doi:10.1002/chem.201500611
19. Naab, B. D.; Gu, X.; Kurosawa, T.; To, J. W. F.; Salleo, A.; Bao, Z. *Adv. Electron. Mater.* **2016,** *2,* 1600004. doi:10.1002/aelm.201600004
20. Yuan, D.; Huang, D.; Zhang, C.; Zou, Y.; Di, C.-a.; Zhu, X.; Zhu, D. *ACS Appl. Mater. Interfaces* **2017,** *9,* 28795–28801. doi:10.1021/acsami.7b07282
21. Schwarze, M.; Gaul, C.; Scholz, R.; Bussolotti, F.; Hofacker, A.; Schellhammer, K. S.; Nell, B.; Naab, B. D.; Bao, Z.; Spoltore, D.; Vandewal, K.; Widmer, J.; Kera, S.; Ueno, N.; Ortmann, F.; Leo, K. *Nat. Mater.* **2019,** *18,* 242–248. doi:10.1038/s41563-018-0277-0
22. Al Kurdi, K.; Gregory, S. A.; Jhulki, S.; Conte, M.; Barlow, S.; Yee, S. K.; Marder, S. R. *Mater. Adv.* **2020,** *1,* 1829–1834. doi:10.1039/d0ma00406e
23. Un, H.-I.; Gregory, S. A.; Mohapatra, S. K.; Xiong, M.; Longhi, E.; Lu, Y.; Rigin, S.; Jhulki, S.; Yang, C.-Y.; Timofeeva, T. V.; Wang, J.-Y.; Yee, S. K.; Barlow, S.; Marder, S. R.; Pei, J. *Adv. Energy Mater.* **2019,** *9,* 1900817. doi:10.1002/aenm.201900817

24. Lungwitz, D.; Joy, S.; Mansour, A. E.; Opitz, A.; Karunasena, C.; Li, H.; Panjwani, N. A.; Moudgil, K.; Tang, K.; Behrends, J.; Barlow, S.; Marder, S. R.; Brédas, J.-L.; Graham, K.; Koch, N.; Kahn, A. *J. Phys. Chem. Lett.* **2023,** *14,* 5633–5640. doi:10.1021/acs.jpclett.3c01022
25. Pham, P. H.; Barlow, S.; Marder, S. R.; Luca, O. R. *Chem Catal.* **2023,** *3,* 100675. doi:10.1016/j.checat.2023.100675
26. Mohapatra, S. K.; Marder, S. R.; Barlow, S. *Acc. Chem. Res.* **2022,** *55,* 319–332. doi:10.1021/acs.accounts.1c00612
27. https://www.hepatochem.com/product/hck1012-xx-011/ (accessed Sept 27, 2023).
28. Newcomb, M.; Park, S. U. *J. Am. Chem. Soc.* **1986,** *108,* 4132–4134. doi:10.1021/ja00274a046
29. Bietti, M.; Martella, R.; Salamone, M. *Org. Lett.* **2011,** *13,* 6110–6113. doi:10.1021/ol202561z
30. Jing, L.; Nash, J. J.; Kenttämaa, H. I. *J. Am. Chem. Soc.* **2008,** *130,* 17697–17709. doi:10.1021/ja801707p
31. Higginson, B.; Sanjosé-Orduna, J.; Gu, Y.; Martin, R. *Synlett* **2021,** *32,* 1633–1636. doi:10.1055/a-1457-2399
32. Yu, D.; To, W.-P.; Tong, G. S. M.; Wu, L.-L.; Chan, K.-T.; Du, L.; Phillips, D. L.; Liu, Y.; Che, C.-M. *Chem. Sci.* **2020,** *11,* 6370–6382. doi:10.1039/d0sc01340d
33. Inaba, S.; Matsumoto, H.; Rieke, R. D. *J. Org. Chem.* **1984,** *49,* 2093–2098. doi:10.1021/jo00186a003
34. Burns, T. P.; Rieke, R. D. *J. Org. Chem.* **1987,** *52,* 3674–3680. doi:10.1021/jo00392a033
35. Kim, S.-H.; Rieke, R. D. *J. Org. Chem.* **2000,** *65,* 2322–2330. doi:10.1021/jo991478s
36. Suh, Y.; Lee, J.-s.; Kim, S.-H.; Rieke, R. D. *J. Organomet. Chem.* **2003,** *684,* 20–36. doi:10.1016/s0022-328x(03)00500-x
37. Wiesner, S.; Walter, P.; Wagner, A.; Kaifer, E.; Himmel, H.-J. *Eur. J. Org. Chem.* **2016,** 5045–5054. doi:10.1002/ejoc.201600978
38. Blanksby, S. J.; Ellison, G. B. *Acc. Chem. Res.* **2003,** *36,* 255–263. doi:10.1021/ar020230d
39. Mohapatra, S. K.; Al Kurdi, K.; Jhulki, S.; Bogdanov, G.; Bacsa, J.; Conte, M.; Timofeeva, T. V.; Marder, S. R.; Barlow, S. *Beilstein J. Org. Chem.* **2023,** *19,* 1651–1663. doi:10.3762/bjoc.19.121
40. Guo, S.; Mohapatra, S. K.; Romanov, A.; Timofeeva, T. V.; Hardcastle, K. I.; Yesudas, K.; Risko, C.; Brédas, J.-L.; Marder, S. R.; Barlow, S. *Chem. – Eur. J.* **2012,** *18,* 14760–14772. doi:10.1002/chem.201202591
41. Longhi, E.; Risko, C.; Bacsa, J.; Khrustalev, V.; Rigin, S.; Moudgil, K.; Timofeeva, T. V.; Marder, S. R.; Barlow, S. *Dalton Trans.* **2021,** *50,* 13020–13030. doi:10.1039/d1dt02155a
42. Bennett, R. W.; Wharry, D. L.; Koch, T. H. *J. Am. Chem. Soc.* **1980,** *102,* 2345–2349. doi:10.1021/ja00527a036
43. Colter, A. K.; Lai, C. C.; Parsons, A. G.; Ramsey, N. B.; Saito, G. *Can. J. Chem.* **1985,** *63,* 445–451. doi:10.1139/v85-073
44. Jhulki, S.; Un, H.-I.; Ding, Y.-F.; Risko, C.; Mohapatra, S. K.; Pei, J.; Barlow, S.; Marder, S. R. *Chem* **2021,** *7,* 1050–1065. doi:10.1016/j.chempr.2021.01.020
45. Imran, M.; Zhang, X.; Wang, Z.; Chen, X.; Zhao, J.; Barbon, A.; Voronkova, V. K. *Phys. Chem. Chem. Phys.* **2021,** *23,* 15835–15868. doi:10.1039/d1cp01937f

License and Terms